Optical Superlenses: Quality and Fidelity in Silver-Dielectric Near-Field Imaging Systems

Ciaran P. Moore, B.E. (Hons. I)

A thesis presented for the degree of
Doctor of Philosophy
in
Electrical and Electronic Engineering
at the
University of Canterbury,
Christchurch, New Zealand.

24 May 2011

To my parents, Michael and Ronél.

Abstract

In the year 2000 John Pendry described a new kind of lens that could focus both the propagating and evanescent components of light. This 'super' lens, which took the form of a thin slab of silver with a negative effective index of refraction under certain conditions, had the ability to reproduce images much smaller than the wavelength of light, seemingly in violation of the diffraction limit that governed the performance of conventional optics. Despite significant controversy regarding the purported operation of such superlenses, the first experimental samples were fabricated in 2005, with features as small as 63 nm successfully imaged with 365 nm light. These results put to rest disbelief in the feasibility of superlenses and ushered in an era of intense interest in near-field phenomena and negative index materials (NIMs).

Despite sustained effort, progress on the practical implementation of superlenses was slow, with a further five years passing before improved experimental results were published. In the meantime, a proliferation of analytical and modelling studies appeared on the behaviour and properties of superlenses, as well as numerous suggestions for improved physical designs, very few of which had accompanying experimental evidence. The primary aim of this thesis arose from these many proposals, namely, to reconcile predictions made about the behaviour of superlenses with observed experimental results.

The measurement of the theoretical and practical behaviour of superlenses is addressed in this thesis by the development of a set of characterisation metrics that can be used to describe the imaging performance of a number of near-field imaging systems. These metrics are initially calculated via transfer matrix modelling (TMM), which is a one-dimensional analytical technique traditionally used to find the transmission and reflection coefficients of planar structures. Two families of metrics are derived; one that describes imaging systems in terms of their abilities in generic situations and the other

that gives the suitability of an imaging system for application to a given class of object. Transfer functions, bandwidth and peak wavenumber measurements form this first group of characterisation functions, while contrast, pseudo-contrast and correlation coefficients are used to assess the quality of imaging systems when exposed to well-defined input profiles. Both sets of metrics show that the performance of superlenses is highly application-specific, with the fidelity or otherwise of a generated image dependent more on the construction of the superlens than on the maximum spatial frequencies present in the object. The results from the characterisation metrics are also used to guide the design of hypothetical superlens structures; these suggest that sub-diffraction limited resolution may still be available with almost a full wavelength separation between object and image.

The quantitative accuracy of the TMM method is assessed by comparison to full-field vector simulations performed via finite element modelling (FEM), these reveal systematic inadequacies in the application of the TMM technique to superlensing applications. These inadequacies stem from near-field mask-lens interactions that are present in superlens experiments but are not accounted for in TMM calculations. A new technique, based on a modified transfer matrix model (M-TMM), is proposed that accounts for the effects between masks and superlenses by approximating masks as solid slabs of known thickness. Results generated via M-TMM are shown to be in better agreement with FEM models than similar TMM data, even when the duty cycle of the actual mask becomes significant and the approximation in M-TMM is at its most coarse.

Finally, experiments are designed and executed that directly measure the transfer functions of superlenses and other near-field imaging techniques. The problem of intimate contact between optics components, which normally hinders any such attempts to perform lithography in the near-field, is mitigated by including a flexible layer of poly (dimethylsiloxane) (PDMS) between various components in the mask:lens:resist stack. Furthermore, high spatial frequency data corresponding to low nanometre-scale features are retrieved from masks with periodic, micron-scale patterns, greatly easing the requirements on mask construction for these experiments. The end results show good agreement with FEM and M-TMM data and satisfy the aim of this thesis, which was to bridge the divide between the performance expected and experienced from silver superlenses.

Preface

Preparation for this thesis began in November 2006, with a summer project based on analytical work first laid out in a PhD disertation published by David Melville in February of that year. After a brief sojourn, the author began formal studies in September 2007. Work continued for the next three and a half years, with the twin goals of building an improved understanding of near-field imaging systems and then disseminating this new knowledge in as wide an arc as possible — to undergraduate students, to postgraduate researchers and to colleagues and mentors in the academic community.

The first of these goals was marked by the publication of several academic papers, including two journal papers that between them accrued 24 references in a little over three years. The second objective, the success of which was more difficult to judge, was addressed by a series of posters, short talks, research seminars and informal discussions conducted for audiences throughout New Zealand and Australia. Perhaps a more effective means of achieving this goal were the email discussions and collaborations with colleagues in Australia, China, Germany, India, Indonesia and the United States of America. On three separate occasions these discussions prefigured publications, giving a clear indication that at least some of the new knowledge described in this thesis was shared beyond its source.

A list of the publications and presentations that are based on results described in this thesis are given below. In addition, preparations are underway to publish excerpts from this thesis as a number of independent manuscripts. These include Sections 4.4 and 5.7, which shed new light on the imaging properties of 'thick' superlenses, and Chapter 6, which describes the experimental techniques documented in this work. Lastly, work has begun on submitting Chapter 7 for inclusion in the academic liter-

ature, on the basis that it contains previously unpublished results that reconcile the practical behaviour of superlenses with predicted models.

Publications in Refereed Journals
C. P. Moore, M. D. Arnold, P. J. Bones and R. J. Blaikie, "Image fidelity for single-layer and multi-layer silver superlenses," *Journal of the Optical Society of America A: Optics, Image Science and Vision*, vol. 25, no. 4, pp. 911–918, April 2008 (17 citations as at 17 May 2011, according to Google Scholar and ISI Web of Knowledge)

C. P. Moore, R. J. Blaikie and M. D. Arnold, "An improved transfer-matrix model for optical superlenses," *Optics Express*, vol. 17, no. 16, pp. 14260–14269, July 2009 (7 citations as at 17 May 2011, according to Google Scholar and ISI Web of Knowledge)

Invited Journal Publication
C. P. Moore and R. J. Blaikie, "Plasmonic superlenses: theory, practice and recent developments," *Asian Journal of Physics*, vol. 18, no. 1, pp. 7–16, February 2009

Publications in Refereed Conference Proceedings
R. J. Blaikie, C. P. Moore, M. D. Arnold and D. O. S. Melville, "Near-field imaging through plasmonic superlenses," *Proceedings of the International Society for Optics and Photonics (SPIE)*, vol. 6801, no. 680102 (invited), 14 pp., January 2008

C. P. Moore, M. D. Arnold, P. J. Bones and R. J. Blaikie, "Analysis and comparison of simulation techniques for silver superlenses," *Proceedings of the International Conference on Nanoscience and Nanotechnology (ICONN08)*, Melbourne, Australia, IEEE Press, pp. 210–213, February 2008 (3 citations as at 17 May 2011, according to Google Scholar and ISI Web of Knowledge)

C. P. Moore, R. J. Blaikie and M. D. Arnold, "Improved analytical models for single- and multi-layer silver superlenses," *Materials Research Society (MRS) Proceedings*, vol.1182, no. 1182-EE11-02, August 2009

Invited Talks at International Conferences (presenter in bold)
R. J. Blaikie, C. P. Moore and M. D. Arnold, "Near-field imaging through plasmonic superlenses," *SPIE Conference on Microelectronics, microelectromechanical systems (MEMS), and Nanotechnology*, Canberra, Australia, December 2007

C. P. Moore, **R. J. Blaikie** and M. D. Arnold, "Improved analytical models for single- and multi-layer silver superlenses," *2009 MRS Spring Meeting Symposium EE: Materials for Nanophotonics — Plasmonics, Metamaterials and Light Localisation*, San Francisco, California, United States of America, April 2009

R. J. Blaikie, C. P. Moore, M. Schøler and M. D. Arnold, "Nanolithography using Optical Near Fields and Surface Plasmons," *Nanophotonics Down Under 2009: Devices and Applications. Sir Mark Oliphant International Frontiers of Science and Technology Conference Series (SMONP09)*, Melbourne, Australia, June 2009

Oral and Poster Presentations at International Conferences and Workshops (presenter in bold)

C. P. Moore and R. J. Blaikie, "Image fidelity for single- and multi-layer silver superlenses," *2008 International Conference on Nanoscience and Nanotechnology (ICONN08)*, Melbourne, Australia, February 2008

C. P. Moore and R. J. Blaikie, "Modelling evanescent behaviour in silver superlenses," *Australia Japan Nanophotonics Workshop 2008*, Canberra, Australia, December 2008

C. P. Moore and R. J. Blaikie, "Thick silver superlenses - not too bright but very sharp," *Fourth Advanced Materials and Nanotechnology Conference (AMN4)*, Dunedin, New Zealand, February 2009

C. P. Moore and R. J. Blaikie, "Spatial frequency characterisation of near-field imaging systems," *Fifth Advanced Materials and Nanotechnology Conference (AMN5)*, Wellington, New Zealand, February 2011

Oral and Poster Presentations at National and Local Conferences and Meetings (presenter in bold)

C. P. Moore and R. J. Blaikie, "Spatial frequency characterisation of near-field imaging systems," *Microfabrication Laboratory Group Meeting*, University of Canterbury, Christchurch, New Zealand, 10 May 2011

C. P. Moore and R. J. Blaikie, "Spatial frequency characterisation of near-field imaging systems," *MacDiarmid Institute Student and Post-Doc Symposium*, Victoria University, Wellington, New Zealand, 18–19 November 2010

C. P. Moore and R. J. Blaikie, "An introduction to superlensing photolithography," *Electrical and Computer Engineering Departmental Seminar*, University of Canterbury, Christchurch, New Zealand, 31 July 2009

C. P. Moore and R. J. Blaikie, "Superlens model verification," *Microfabrication Laboratory Group Meeting*, University of Canterbury, Christchurch, New Zealand, 27 April 2009

C. P. Moore and J. E. Foulkes, "Finite Element Modelling with COMSOL," *MacDiarmid Institute Student and Post-Doc Symposium*, Victoria University, Wellington, New Zealand, 10-11 November 2008

C. P. Moore and R. J. Blaikie, "Thick silver superlenses: bigger is (sometimes) better," *Microfabrication Laboratory Group Meeting*, University of Canterbury, Christchurch, New Zealand, 29 September 2008

C. P. Moore and R. J. Blaikie, "Understanding superlenses," *Microfabrication Laboratory Group Meeting*, University of Canterbury, Christchurch, New Zealand, 21 January 2008

C. P. Moore M. D. Arnold, P. J. Bones and R. J. Blaikie, "Image Fidelity for Single- and Multi-Layer Silver Superlenses," *MacDiarmid Institute Student and Post-Doc Symposium*, Massey University, Palmerston North, New Zealand, 26–27 November 2007

Acknowledgements

I would like to thank my supervisor, Richard Blaikie, for his guidance during the course of my studies. His sure, professional direction and genuine care for my best interests have made my days as a postgraduate student both pleasant and productive. I also thank and acknowledge Maan Alkaisi and Phil Bones, who have been responsible and helpful associate supervisors. Furthermore, Helen Devereaux and Gary Turner have consistently maintained a first-class laboratory in which to conduct research. This thesis would stop at Chapter 5, were it not for them.

I am grateful for funding I received to conduct my PhD studies, this was provided by the MacDiarmid Institute for Advanced Materials and Nanotechnology and the Electrical and Computer Engineering Department at the University of Canterbury. I also acknowledge Don Eigler and the IBM Distinguished Scholars programme that he established between the IBM Almaden Research Centre and universities in New Zealand. Through this initiative I was able to spend three productive, exciting months working for IBM in San Jose, California, on a topic unrelated to my thesis. The break that this gave me at the midpoint of my studies provided much of the inspiration necessary to design and implement the experiments described in Chapters 6 and 7.

Almost without fail, it is a condition of dissertations that the students who write them will be confronted with vast new fields of knowledge in the course of their research. When starting work in a new area, guidance from a more experienced person can drastically reduce the learning time required to become productive. Frequently during my studies I was lucky to work closely with expert researchers who were both generous and obliging with their support: firstly, Matt Arnold put up with three months of almost daily meetings as I learnt about T-matrices and spatial frequency analysis. Later on, Trey Holzwarth explained the principles of interference lithography to me and helped me to fabricate mask patterns. Volker Nock also came to my aid innumerable

times as I attempted to pry meaningful results from the equipment in the microfabrication laboratory; most recently he gave me instructions and advice on working with PDMS. I thank these men for the time and the patience that they invested in me.

There were many others who lent me assistance and comfort over the last four years: in particular, I thank those with whom I shared an office for experiencing the highs and lows of academic life with me: Martin Allen, Jessica Chai, John Foulkes, Jeff Hsiao, Prateek Mehrotra, Mikkel Schler and Chuck Yoon. I thank Tom Cronje, Mark Noonchester and Steve Weddell, who have been good friends to me and who have never wavered from sharing my latest triumph or despair, often over a cup of coffee. I also thank Fr John Adams, Eddie Caudel, Ken Joblin and the members of CathSoc who provided me with encouragement, companionship and distraction, all of which proved to be vital at different times.

Lastly, I would like to thank my wife, Angel, who has patiently shared me with this thesis since I enrolled in 2007. I thank and acknowledge my family, too, who have stood by me, believed in me, and taught me to always try my best. Perhaps unsurprisingly, this tutelage has often involved snippets of advice, repeated often and believed firmly. I conclude by listing a few of these sage words below:

'The more you put in, the more you get out.'

'Work hard — you won't regret it.'

And, my favourite:

'Nothing succeeds like success.'

Table of Contents

List of Figures

List of Tables

List of Acronyms

AFM	atomic force microscope
Ag	silver
Al	aluminium
AMN	Advanced Materials and Nanotechnology
Ar	argon
ArF	argon fluoride
ARC	anti-reflective coating
ASCII	American standard code for information interchange
BW	bandwidth
CAMFR	cavity modelling framework
Cr	chrome
DFT	discrete Fourier transform
DIW	de-ionised water
DOF	degree of freedom
EBL	electron beam lithography
EMA	effective medium approximation
ENFOL	evanescent near-field optical lithography
FEM	finite element modelling

FFT fast Fourier transform

FIB focused ion beam

FOM figure of merit

FSL far-field superlens

Ge germanium

He-Cd helium-cadmium

HMW high molecular weight

IC integrated circuit

IL interference lithography

InAs indium antimonide

IPA isopropyl alcohol

ITRS International Technology Roadmap for Semiconductors

LWIR long wave infra-red

MEMS microelectromechanical systems

MIBK methyl isobutyl ketone

MLP maskless laser patterning

MRS Materials Research Society

M-TMM modified transfer matrix model

NiCr nichrome

NIL nanoimprint lithography

NIM negative index material

NSOM near-field scanning microscopy

ODE ordinary differential equation

OL optical lithography

O_2	oxygen
PDE	partial differential equation
PDMS	poly (dimethylsiloxane)
PGMEA	Propylene glycol monomethyl ether acetate
PLL	planar lensing lithography
PML	perfectly matched layer
PMMA	poly (methyl methacrylate)
Λ_{peak}	peak wavenumber
PVA	poly (vinyl alcohol)
RF	radio frequency
RIE	reactive ion etching
RMS	root mean square
SEM	scanning electron microscope
SiC	silicon carbide
SiN	silicon nitride
SiO	silicon monoxide
SiO_2	silicon dioxide
SF_6	sulphur hexaflouride
SNOM	scanning near-field optical microscope
SNR	signal-to-noise ratio
SP	surface plasmon
SPIE	International Society for Optics and Photonics
SPR	surface plasmon resonance
SRR	split ring resonator

TE transverse electric

TF transfer function

TM transverse magnetic

TMM transfer matrix modelling

TMAH tetramethyl ammonium hydroxide

T-matrix transfer matrix

UCSD University of California, San Diego

UV ultra-violet

EUV extreme ultra-violet

W tungsten

Chapter 1

Introduction

Since the dawn of the electronic age, engineers have strived to make circuits smaller, pack components more densely, and increase the complexity of devices by integrating more and more functionality onto ever shrinking substrates. The motivation for this continuous decrease in size is fuelled not only by technological factors but also by economics: smaller components lead to faster devices that are cheaper to build and more efficient to operate [1]. Hence, manufacturers and consumers mutually benefit from reducing the size of the electronics inside the devices that increasingly dominate our lives.

This trend toward nanoscale devices, which was predicted by Richard Feynman in 1959 [2], was first observed and formalised by Gordon Moore* in 1965. Writing in Electronics magazine, Moore studied the data shown in Fig. 1.1 and observed that '[t]he complexity for minimum component costs has increased at a rate of roughly a factor of two per year... [c]ertainly over the short term this rate can be expected to continue, if not to increase.' [3] This exponential rate of progress, which came to be known as Moore's law, proved valid long past the ten year time period [3] that Moore originally envisioned, as shown in Fig. 1.2. Despite a gradual increase in the law's time constant from one year towards two, it became a self-fulfilling prophecy that continues to govern the pace of development in the electronics industry today, through collaborative ventures such as the International Technology Roadmap for Semiconductors (ITRS) [4].

*No relation to author.

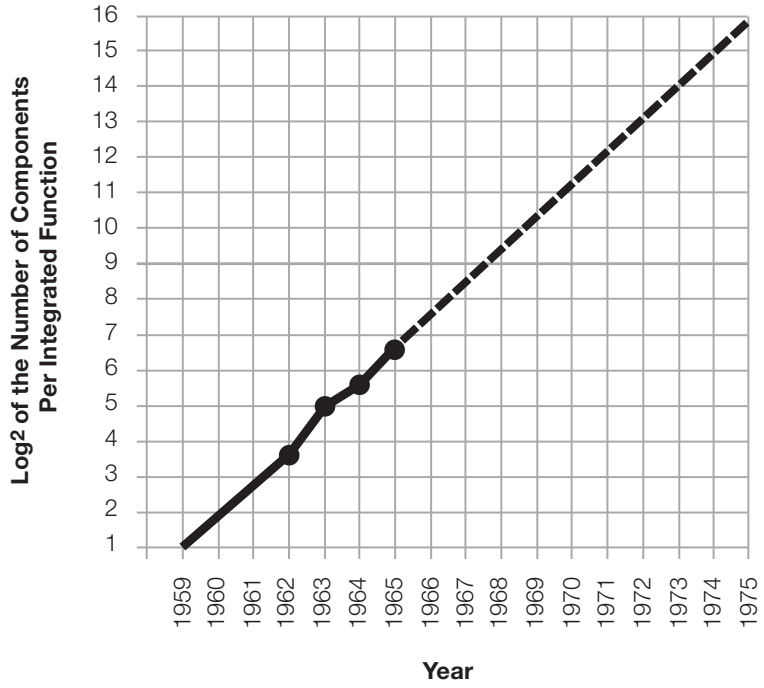

Figure 1.1: Plot of Moore's law from 1965, predicting that the number of electrical components per IC would increase exponentially over time [3].

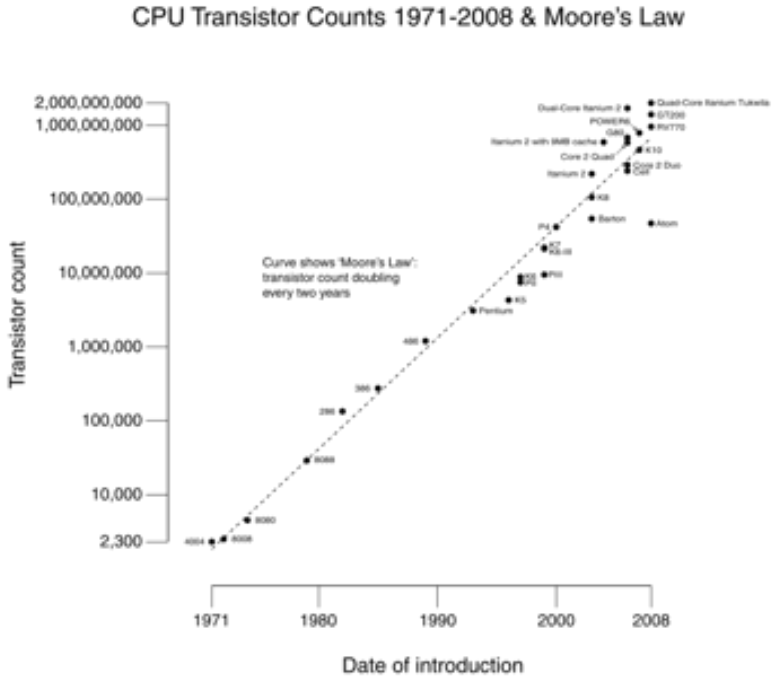

Figure 1.2: Logarithmic plot of transistor count on Intel microprocessors vs. release date. The constant rate of increase confirms that Moore's law is still valid forty years after it was first proposed [5].

1.1 Optical Lithography and the Diffraction Limit

The rapid decrease in component sizes articulated by Moore's law has been sustained only as a result of huge amounts of research and development into the processes involved with manufacturing electronic devices. Chief among these processes is the art of optical lithography, which involves the reproduction of a pattern from a mask into a resist using electromagnetic waves [6] to affect the transfer, as shown in Fig. 1.3. This process is suitable for arbitrary mask patterns and, with the addition of appropriate lenses, the phase of the propagating waves passing through the mask can be manipulated to produce focussed features in the photoresist layer, with sizes down to the order of the wavelength of the light source.

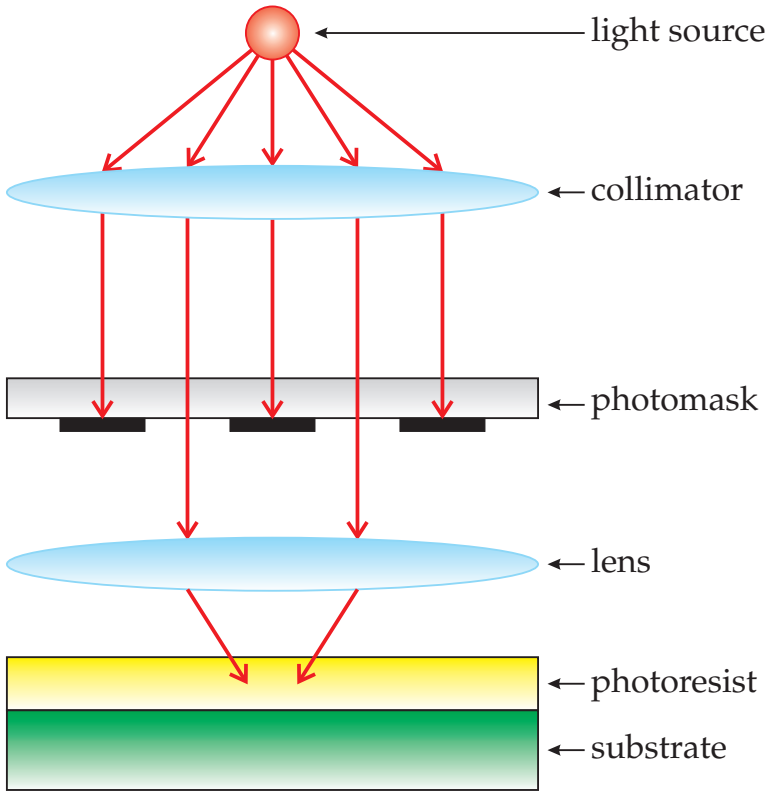

Figure 1.3: Optical lithography schematic [7].

This limit on the minimum size of features that can be resolved is known as the diffraction limit, d [6], defined as

$$d = \frac{k_1 \lambda}{2\,\mathrm{NA}}, \tag{1.1}$$

where k_1 is a constant determined by the lithography process, λ is the exposing wavelength and NA is the numerical aperture of the optics used between the mask and

resist. Shown in Fig. 1.4, NA is a measure of the maximum angle, θ, at which light can enter or exit a lens from a given point, P. NA is commonly defined as

$$\mathrm{NA} = n \sin \theta, \tag{1.2}$$

where n is the refractive index of the medium between the final lens and the image plane.

Eq. (1.1) includes several variables that can be used to reduce the diffraction limit and thus decrease the minimum feature size that can be fabricated. For instance, if the illumination approaches the mask at normal incidence, k_1 has a minimum value around 0.25 for the half pitch of dense features; however, this value decreases if an angle is introduced between the mask and the direction of propagation of the light source [6]. Similarly, multiple light sources can be used to give interferometric patterns with further reduced k_1 [9]. Alternatively, improved optics or immersion systems can be used to increase the numerical aperture of the system [10], as shown in Fig. 1.5a. Lastly, λ can be reduced from visible wavelengths into the ultra-violet (UV) spectrum [11] and even to extreme ultra-violet (EUV) wavelengths [12].

Alternative approaches that are not subject to the diffraction limit are also available; for example, the light source and collimator in Fig. 1.3 can be replaced with electron [13] or ion [14] beams. Electron beam lithography (EBL) and focused ion beam (FIB) techniques allow much finer resolution than optical lithography but only at the expense of longer write times. In yet another approach, the mask itself can affect the pattern transfer into the resist by means of imprinting [15], as shown in Fig. 1.5b. Nanoimprint lithography (NIL) is similar to optical lithography in that the whole mask pattern can be imaged at once, however, component wear and contamination

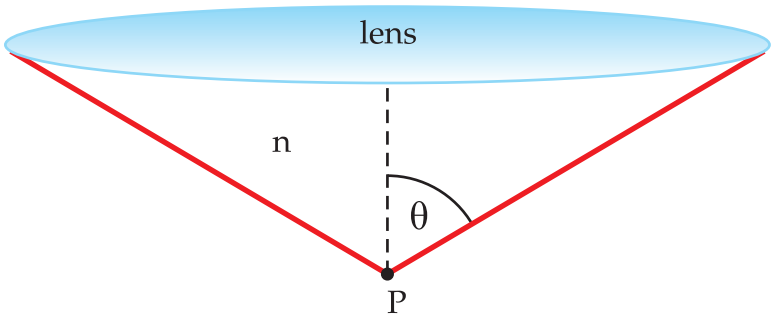

Figure 1.4: Numerical aperture schematic [8], illustrating the terms defined in Eq. (1.2).

rates are higher due to repeated contact between the mask and resist-coated wafers. For these reasons UV immersion lithography is still the preferred technology for industry leaders such as Intel, Samsung and GlobalFoundries [16], with 193 nm argon fluoride (ArF) lasers scheduled to image features at the 22 nm lithography node in 2011 [17].

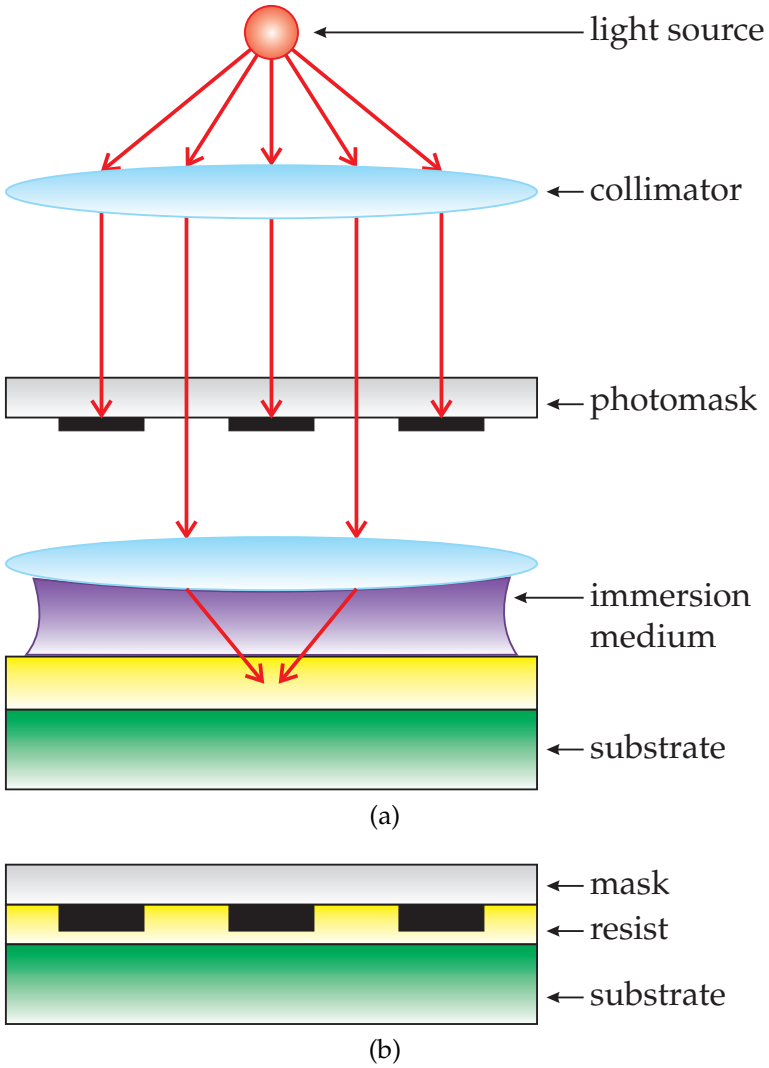

Figure 1.5: Schematics for various lithography technologies. Immersion lithography is shown in (a), where a droplet of liquid or some solid material is placed between the final lens and photoresist. Nanoimprint lithography, which involves pressing the mask into the resist, is shown in (b).

1.2 Breaking the Diffraction Limit for Optical Lithography Systems

Given the attraction that the semiconductor industry has for optical lithography, it is worth considering the diffraction limit in detail and investigating what can be done to remove or surpass it, without going to the expense of changing to a completely separate lithography system, such as electron beam lithography (EBL). For optical lithography (OL) systems, the diffraction limit comes about when imaged features are significantly smaller than the wavelength of the light source, as shown in Fig. 1.6. As the dimensions of the mask shrink, diffraction from the feature edges begins to dominate and propagating waves are not able to travel from the mask to the subsequent optics and photoresist, as shown in Fig. 1.6b. Instead, only evanescent modes escape from the mask, decaying exponentially as they approach the photoresist, as shown in Fig. 1.7. Although these evanescent modes contain all of the deep sub-wavelength information from the mask, they decay to negligible levels within $\lambda/10$ and are not typically captured in the photoresist. For this reason, the resolution of conventional OL systems remains limited.

Fortunately, there are techniques available for capturing and manipulating evanescent modes. Examination of Fig. 1.7 leads to the intuitive approach of removing any optics

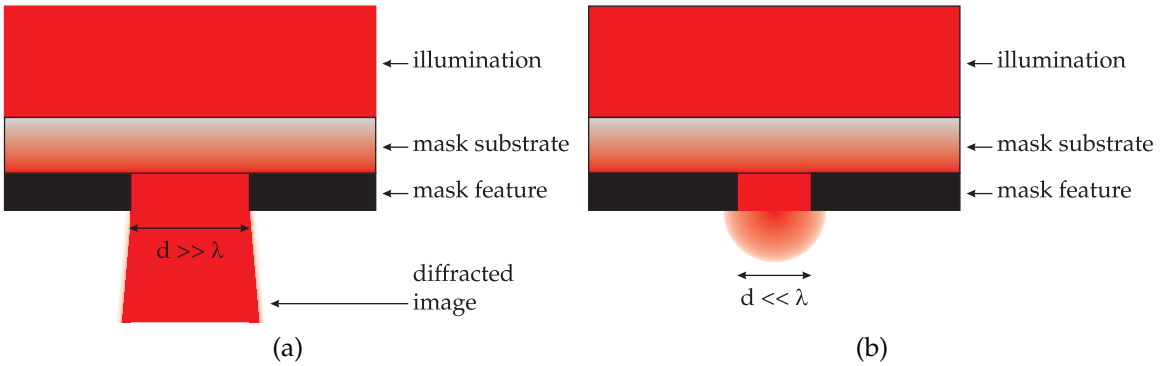

Figure 1.6: Light diffraction through a mask with super-wavelength (a) and sub-wavelength (b) sized features. As the light travels past the mask features it diffracts, leading to a slightly blurred or 'spread out' light beam. This has only a minor effect on the image when the mask features are large relative to the wavelength (a) but it can prevent an image from being formed at all if the mask features are much smaller than the wavelength of the light (b).

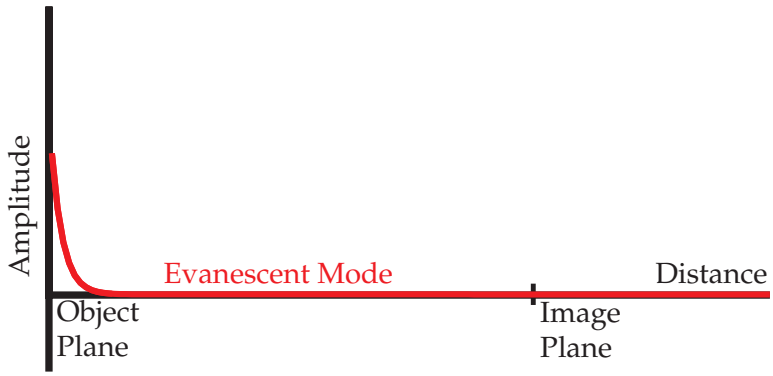

Figure 1.7: Typical amplitude profile of evanescent modes as they travel away from the mask or object plane.

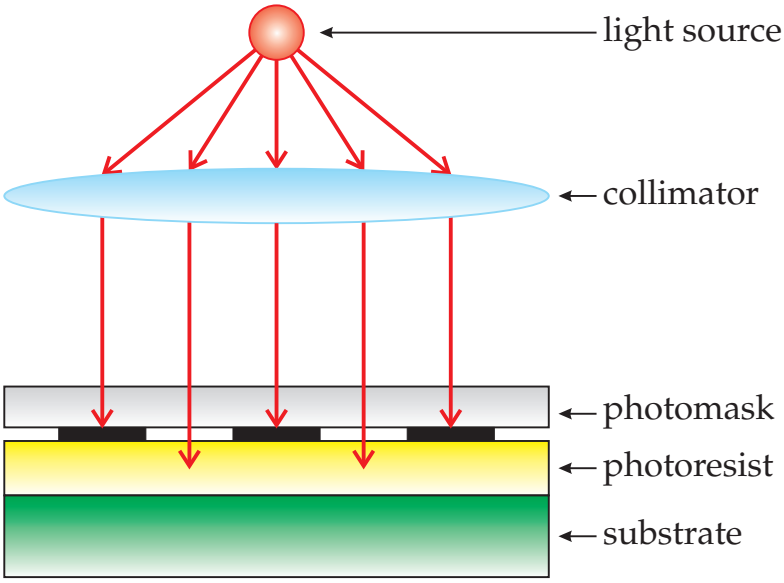

Figure 1.8: ENFOL schematic: the mask and photoresist are placed in intimate contact, allowing evanescent modes to be captured in the resist before they decay significantly.

and placing the resist in intimate contact with the mask, so that the evanescent modes have much less distance over which to decay before they are absorbed by the photoresist, as shown in Fig. 1.8. This approach is known as evanescent near-field optical lithography (ENFOL) [18] and it has produced features as small as $\lambda/11$ [19].

A second, less intuitive solution involves placing a specialised lens between the mask and resist. It is already apparent that conventional lenses cannot eliminate the diffraction limit, as they will always have finite NA. Furthermore, conventional lenses work by altering the phase of waves travelling through them, yet the behaviour of evanescent modes is dominated by their exponentially decaying amplitude response, rather

than their phase behaviour. Ideally, what is needed is a 'perfect' lens that can enhance the amplitude of evanescent modes while also focusing propagating waves. John Pendry suggested that such a device may be possible, if it were constructed from materials with negative indices of refraction [20], that is, materials with simultaneously negative electric permittivity, ϵ, and magnetic permeability, μ. Unfortunately, such materials do not occur naturally and are particularly difficult to fabricate at optical wavelengths. Instead, Pendry proposed a planar 'super' lens [20] that could enhance the amplitude of evanescent modes under certain polarisations, so that a complete, diffraction-free image of the mask could be reconstructed at the photoresist, as shown in Fig. 1.9. This resulted in a new form of lithography known as planar lensing lithography (PLL) [21], with sub-diffraction limited features first imaged in 2005 [22, 23] and best performance reported below $\lambda/12$ [24].

1.3 This Thesis

Both ENFOL and PLL represent new and exciting ways of performing lithography below the diffraction limit. The theory behind their operation is increasingly well understood in the literature [25–27] and several experiments have confirmed their performance for sub-wavelength, periodic line-space features [28, 29]. However, there is still much to be learnt about their behaviour for non-typical applications and their performance over a range of feature sizes.

For this reason an extended study of evanescent imaging systems is documented in this thesis. After a description of the development of ENFOL, superlensing, and other relevant techniques in Chapter 2, Chapter 3 describes the methods that were used to model evanescent systems and predict their behaviour. Metrics and data from Ref. [30] are presented in Chapter 4; these describe lens performance for a variety of mask features, large and small, densely packed and sparse. These stand in contrast to typical experimental results presented in the literature, which tend to describe only the minimum period width that a system can resolve [18, 19, 22–24, 29].

As much as the metrics describe the imaging systems, differences in metric values calculated using alternative modelling techniques identify discrepancies in the models themselves. The causes of these discrepancies are discussed in Chapter 5 and an im-

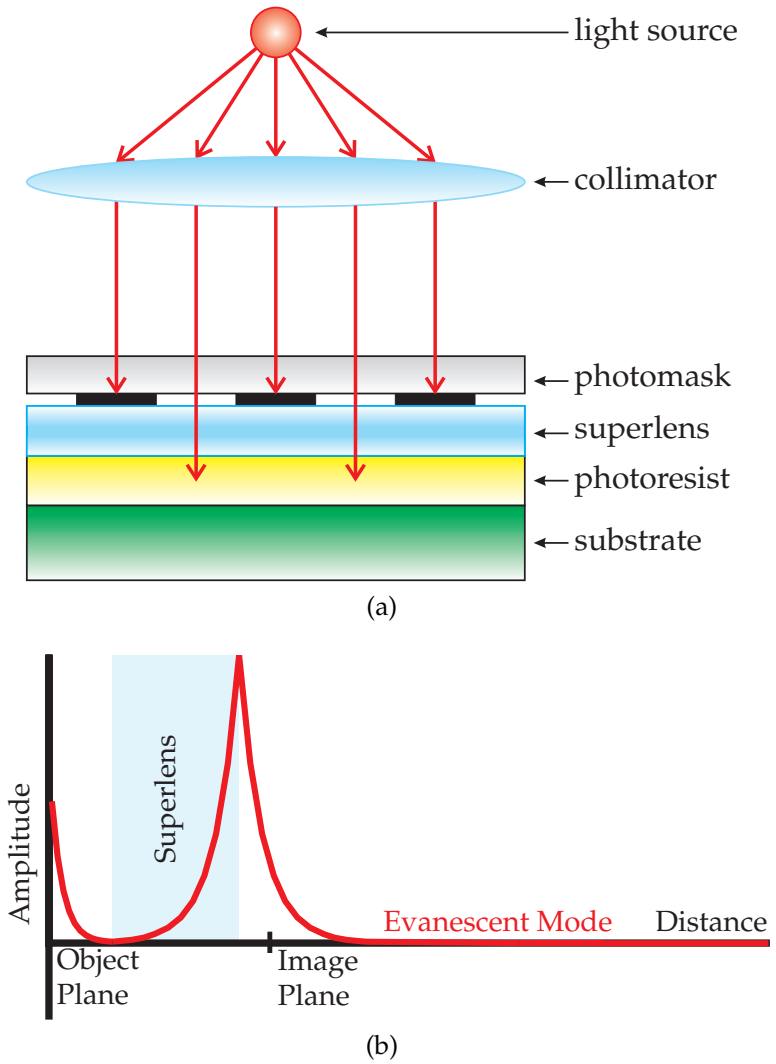

Figure 1.9: Planar lensing lithography schematic (a). A superlens is held in intimate contact between mask and resist. Evanescent modes are enhanced as they travel through the lens (b), allowing a diffraction-free image to be captured in the resist.

proved modelling technique, known as the modified transfer matrix model (M-TMM) [31], is proposed as a result. M-TMM is subsequently used to optimise the design [32] of a superlensing system to give improved image fidelity and resolution.

The final part of this thesis deals with the implementation, in Chapter 6, and analysis, in Chapter 7, of a set of experiments that attempts to reconcile the performance predicted by models of evanescent imaging systems with the results observed in the laboratory. Work in these chapters also includes an improved protocol for contact lithography experiments, which have had low yield and poor durability in the past [7]. Lastly,

the image processing techniques necessary to relate the patterns in the resist back to the spatial frequency metrics covered in Chapter 4 are described and implemented.

Chapter 2

Background

Although the PLL and ENFOL processes described in Chapter 1 have many similarities, they evolved over different routes from unrelated areas of research. PLL came about largely as a result of research in the field of negative refraction and metamaterials, which sought to control the macroscopic effective permittivity, ϵ_{eff}, and permeability, μ_{eff}, of materials by altering their microscopic structure. Tuning materials to have negative ϵ_{eff} and μ_{eff} led to negative refraction of electromagnetic waves, which was very similar to the enhancement of evanescent modes affected by superlenses. ENFOL, on the other hand, followed on directly from previous imprint and contact lithography experiments. The development of both of these techniques is traced here, in an attempt to provide some context for the new research that is described in later chapters of this thesis.

2.1 Snell's Law and Negative Refraction

In order to meaningfully discuss negative refraction and metamaterials it is first necessary to have an understanding of the causes and effects of optical refraction. Since the phase velocity of light, v, is dependent on the medium that it is travelling through, interesting effects are observed at the junction between two different materials, shown in Fig. 2.1. If v increases from the first medium to the second, i.e. $v_1 < v_2$, then the angle between the light beam and the interface normal, θ, will be larger in the sec-

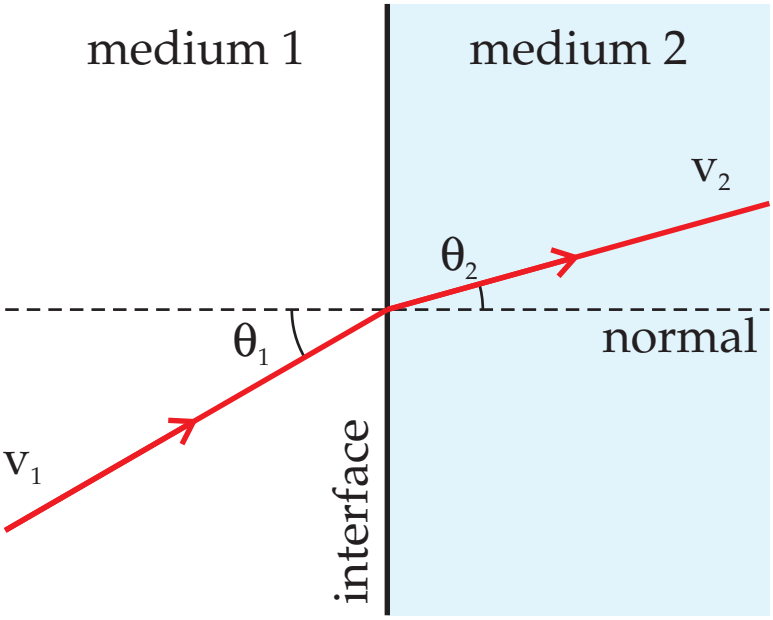

Figure 2.1: Refraction at an interface between two materials [34]. Lower phase velocity in the second medium than in the first leads to a reduced angle between the light beam and the interface normal in the second medium.

ond medium than in the first, i.e. $\theta_1 < \theta_2$. Similarly, a decrease in v from the first to the second medium will result in a smaller angle of incidence in the second medium, as illustrated in Fig. 2.1. This effect of light changing direction as it moves from one medium to another is known as refraction and the relationship between the velocities and angles in the two media is given by Snell's law [33], defined as

$$\frac{\sin\theta_1}{\sin\theta_2} = \frac{v_1}{v_2}. \tag{2.1}$$

If v_1 and v_2 are calculated as ratios of the velocity of light in a vacuum, defined as $c_0 = 299,792,458 m/s$ [35], then so-called indices of refraction, n, can be derived for each medium:

$$n_1 = c_0/v_1, \tag{2.2a}$$

$$n_2 = c_0/v_2. \tag{2.2b}$$

Snell's law then becomes

$$\frac{\sin\theta_1}{\sin\theta_2} = \frac{n_2}{n_1}. \tag{2.3}$$

Conveniently, n is also given by the square root of the product of the relative permittivity, ϵ_r, and permeability, μ_r, of a medium, i.e.

$$n = \sqrt{\epsilon_r \cdot \mu_r}; \tag{2.4}$$

this relationship allows the optical behaviour of a material to be calculated from its electromagnetic properties.

For natural materials n is always positive but, if ϵ_r and μ_r can be made negative, then n must change sign [20] and the angles of refraction must change from positive to negative. This behaviour provides many new possibilities to be explored, such as the planar lens shown in Fig. 2.2. It is this phenomenon of negative refraction, made possible by simultaneously negative permittivity and permeability, that is one of the driving forces behind interest in the field of metamaterials.

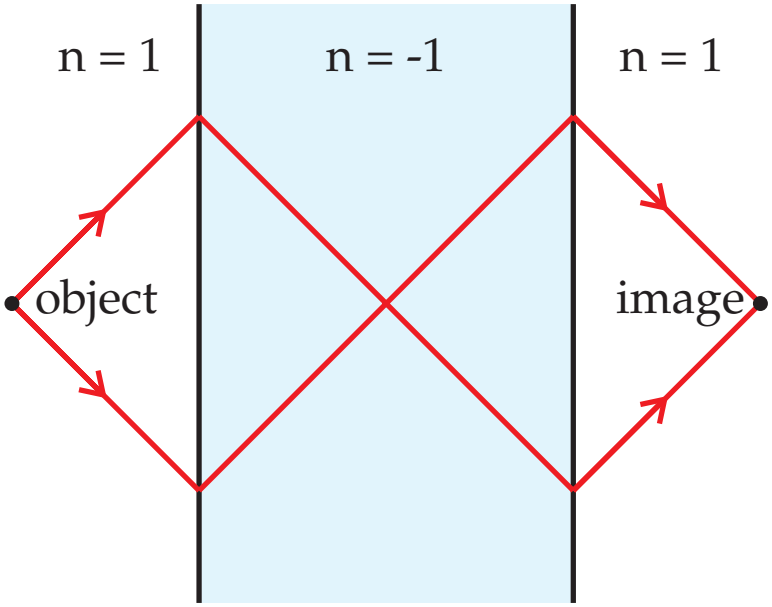

Figure 2.2: Planar lens made from a metamaterial slab with $n = -1$, surrounded by free space. Negative refraction between the metamaterial and its surroundings allows a focussed image of an object to be projected through the lens.

2.2 Metamaterials

Metamaterials with a negative refractive index, n, arising from negative ϵ_r and μ_r were first examined thoroughly by Veselago in 1968 [36]. He speculated that such negative

index materials (NIMs) would be of great interest, correctly pointing out that, due to their negative n, their phase- and group-velocities would be in opposite directions. He predicted that this would lead to a reversal of the Doppler and Vavilov-Čerenkov [37] effects and of Snell's law. He also considered NIM lenses, observing that a planar slab could be used to focus propagating light waves and that concave and convex NIM lenses had the opposite effect on light compared to conventional lenses of equivalent geometries, as shown in Fig. 2.3.

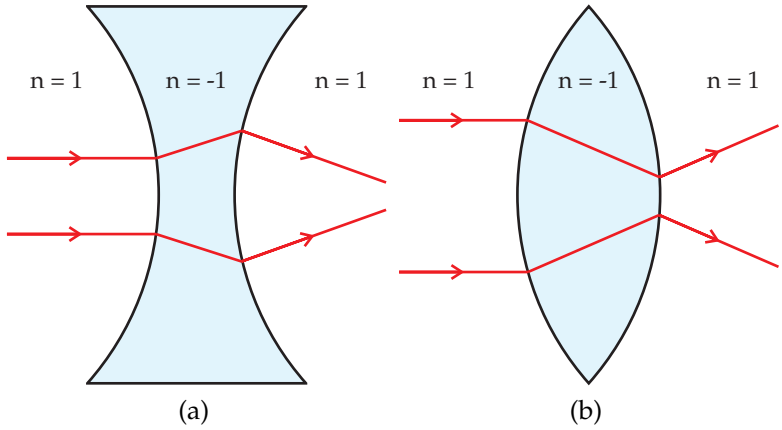

Figure 2.3: Negative refraction leads to reversed ray bending in concave (a) and convex (b) structures.

Although Veselago's theoretical work could not be faulted, it did not gain much popularity and its experimental implementation was delayed for several decades. Despite the production of compounds that behaved as NIMs under certain conditions, refraction experiments could not be conducted due to the compounds' gyrotropic nature—their μ, and hence n, were only negative over a small range of angles of incidence. The problem, as Veselago put it, was that "...we do not know of even a single substance which could be isotropic and have $\mu < 0$" [36].

It was not until 1999 that Pendry and co-workers finally succeeded in solving Veselago's isotropy dilemma by showing that a plane of concentric split rings made up of electrically conducting, magnetically inert material could behave as a metamaterial, exhibiting an effective magnetic permeability, μ_{eff} [38]. This property could be tuned, even to negative values, depending on the geometry of the rings and the frequency of the incident radiation. Significantly, by arranging these split ring resonators (SRRs) in a three-dimensional lattice, shown in Fig. 2.4, they were able to overcome the restric-

tions on the angle of incidence that plagued every other known NIM, thus creating a genuine "isotropic magnetic material," complete with negative μ_r [38].

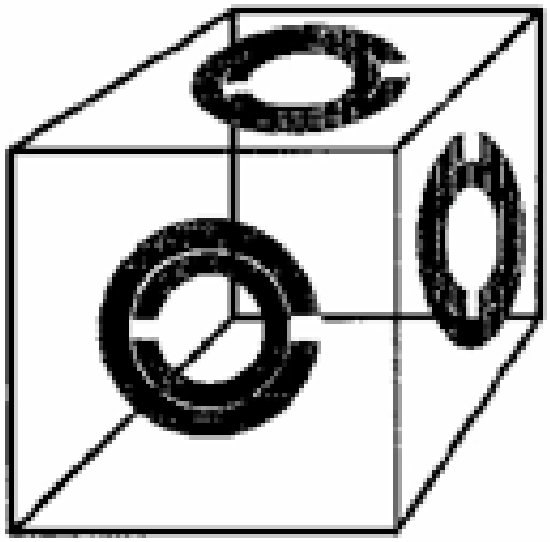

Figure 2.4: Three-dimensional split-ring resonator unit cell used by Pendry et al. to build an isotropic microstructure with $\mu < 0$ [38].

Previously, Pendry had also lead a team which, in 1996, proposed a microstructure based on very thin wires arranged in a periodic fashion that displayed a negative effective permittivity, ϵ_{eff}, at frequencies in the gigahertz band [39]. They were able to verify their theory experimentally in 1998 [40]. The achievement was not that a negative-ϵ metamaterial had been formed—after all, plasmas have $\epsilon < 0$—but that plasma-like characteristics had been observed at microwave frequencies, rather than at the much higher visible or near UV frequencies required by conventional plasmas. It fell to a group from University of California, San Diego (UCSD) to combine these two pieces of research to produce a two-dimensional, isotropic metamaterial [41], shown in Fig. 2.5, with simultaneously negative permeability and permittivity over a band of microwave frequencies [42]. Subsequent experiments showing transmission through such wire-resonator arrays [41] and verifying the metamaterial's negative index of refraction [43] meant that Veselago's theoretical studies were finally validated.

Although metamaterials were now realisable, their potential applications were somewhat limited by the restrictions placed on their physical dimensions — to work effectively, the lattice constant of the split ring resonator and wire arrays had to be much smaller than the free-space wavelength of operation [38]. For example, the metamate-

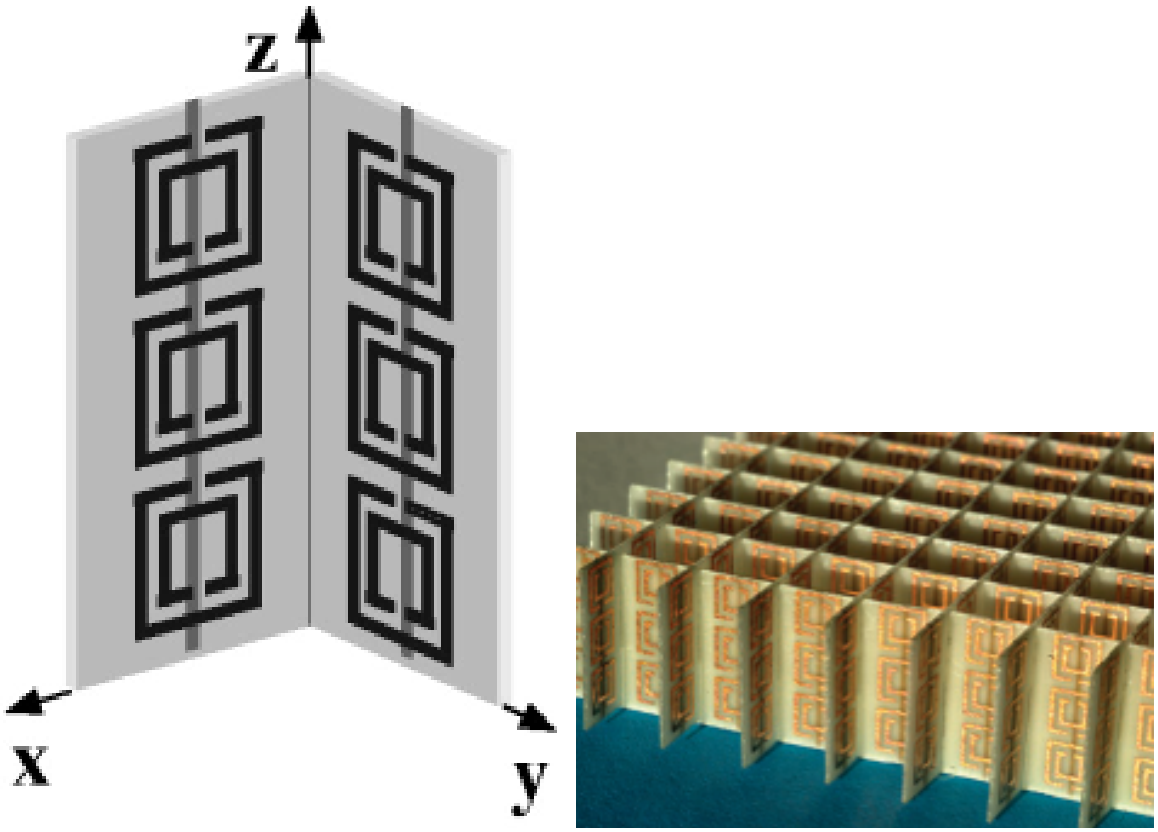

(a) (b)

Figure 2.5: Unit cell schematic (a) [41] and photograph (b) [44] of the first two-dimensional isotropic metamaterial. Negative ϵ_r is given by 1 cm high wire strips (vertical lines), while on the other side of the fibreglass support copper split-ring resonators generate negative μ_r.

rial described in Fig. 2.5 operated at wavelengths between 27.0 mm and 29.1 mm, yet required a lattice constant of 5 mm with wire thickness of 0.25 mm. This meant that the lattice constant had to be at least five times smaller than the free-space operating wavelength, with the minimum wire thickness more than 100 times smaller. This effectively precluded metamaterials from visible wavelength lensing applications, albeit temporarily.

2.3 A Perfect Lens

The next great advance in metamaterials research came when Pendry predicted that planar lenses based on NIMs could act as perfect, diffraction-free lenses by focusing

evanescent, near-field electromagnetic waves, as well as their propagating counterparts [20]. Veselago had predicted the focusing of propagating waves, noting that the NIM served to correct the phase distortion acquired by radiation as it travelled away from its source [36], but he had not considered evanescent modes. Pendry showed that, as well as providing a phase correction for propagating waves, i.e. negative refraction, a NIM could also enhance evanescent modes, thus reversing their exponential decay to restore them and the sub-wavelength information that they contain to their original intensity at a point some distance away from their source, as shown in Fig. 2.6. Furthermore, he showed that if all of the component dimensions in a metamaterial are much smaller than the wavelength of incident radiation and imaging takes place only in the near-field, then the electrostatic and magnetostatic fields due to ϵ and μ, respectively, become quasi-independent of each other and are effectively decoupled. By polarising the radiation incident on his NIM to have all of its magnetic field in the p-plane, i.e. transverse magnetic (TM) polarisation, he was able to ignore the magnetostatic field and hence, the value of μ. This allowed him to focus on finding non-fabricated materials with $\epsilon < 0$, which could be used to fabricate near-field superlenses or what he later called a "poor-man's" perfect lens [44].

This relaxation on the requirement of $\mu < 0$ meant that NIMs were no longer strictly necessary for evanescent enhancement. Instead, natural materials with $\epsilon < 0$ were sufficient to act as near-field lenses, as shown in Fig. 2.7 [20]. The noble metals, in particular, have $\epsilon < 0$ over wide frequency bands below their plasma frequency, with silver, gold and copper all having negative ϵ in the optical spectrum. For this reason, Pendry chose silver as the subject of his analysis.

Pendry's work generated huge interest around NIMs, not least because it gave reason to believe that they were capable of sub-diffraction limited optical imaging, thanks to their transmission and enhancement of evanescent modes. It also showed that negative μ materials were not essential for NIM applications, as had previously been thought. Not surprisingly, such a dramatic revision of what was understood about the subjects of NIMs and near-field physics did not go unchallenged and caused much controversy in the scientific community. Numerous comments and replies were published [45–52], with objections being raised regarding Pendry's calculations, his assumptions about causality and his method of energy transport. M. C. K. Wiltshire explained the energy transport question, and its answer, as follows [53]:

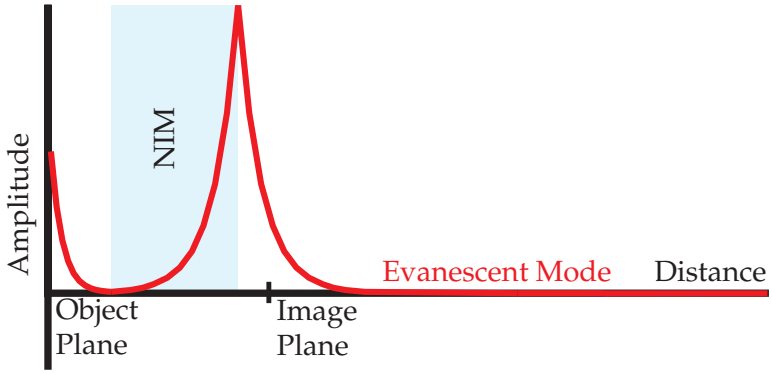

Figure 2.6: Evanescent mode enhancement through an NIM, repeated from Fig. 1.9b. Although the mode decays exponentially outside of the NIM, inside it is enhanced well beyond its initial amplitude. This allows the mode to be observed much further away from the object plane than would be possible without the NIM.

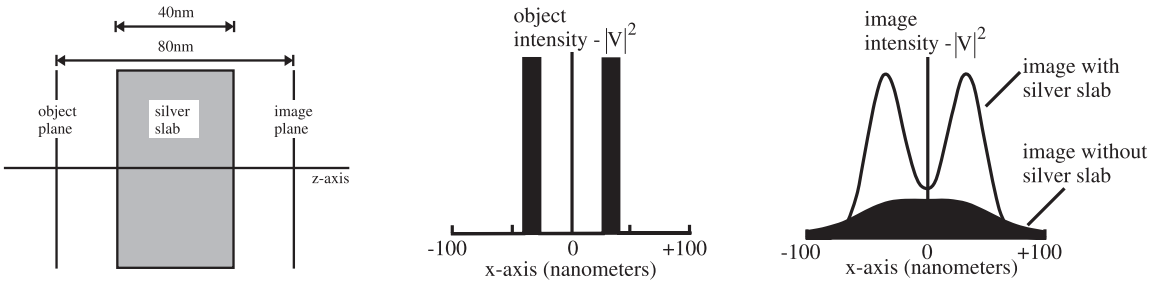

Figure 2.7: Silver superlens operation, as proposed by John Pendry [20]. A slab of silver (a) is exposed to a quasi-electrostatic potential (b) and causes an image to form (c). The resolution of the image formed by the silver is much improved compared to the case where no slab is present.

> Does a negative refractive index mean that light travels backward? Not in any conventional sense... [There is] a difference between the group velocity of light, which measures the speed at which information or energy is transported, and the phase velocity, which measures the speed of the individual light wavefronts. The wavefronts do indeed move backward, consistent with the negative n, but energy is still transported forward. Hence, the materials do obey the laws of physics while opening up new possibilities for manipulating radiation.

Remaining doubts about Pendry's theory were answered definitively in 2005, when two independent groups from the University of Canterbury, New Zealand [22] and the University of California, Berkeley [23] constructed planar NIM superlenses using thin layers of silver, according to the schematic shown in Fig. 2.8. The lenses used plasmon resonances on the surface of the silver to enhance and couple evanescent modes, achieving 72.5 nm and 60 nm half-pitch resolution, respectively, for periodic line arrays illuminated with 365 nm light. This was more than 2.5 times better than the theoretical diffraction-limited resolution, and confirmed that superresolution was indeed possible at optical frequencies. Micrographs of surfaces patterned by these superlenses are shown in Figs. 2.9 and 2.10.

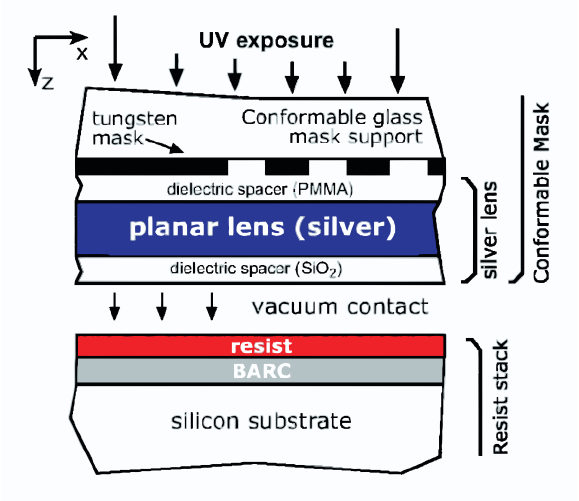

Figure 2.8: The first superlens consisted of 50 nm of silver sandwiched between silicon dioxide and poly (methyl methacrylate) [22].

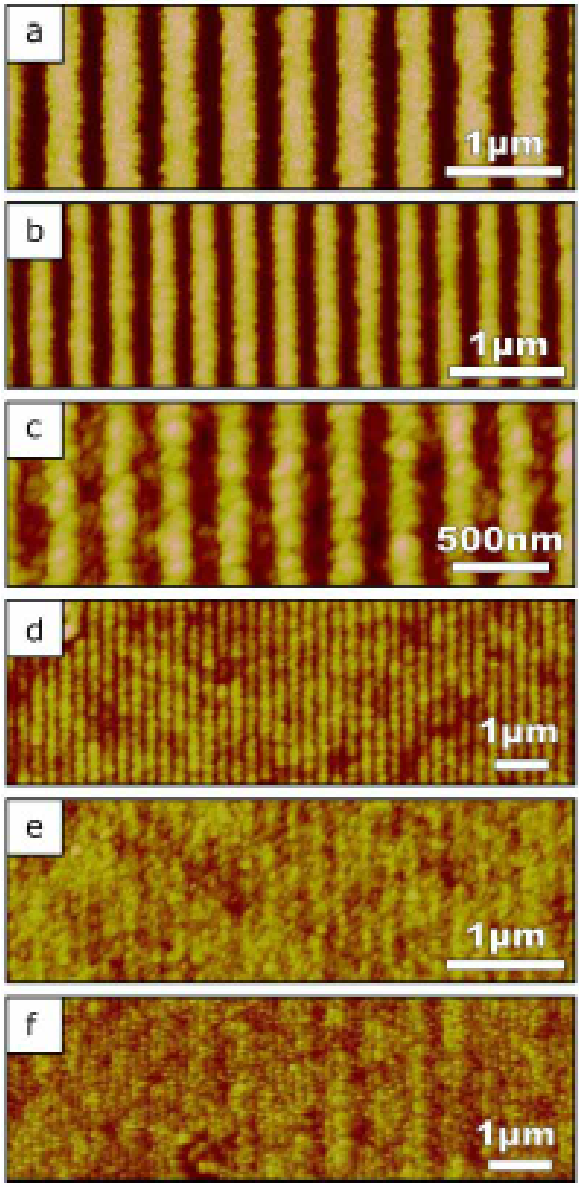

Figure 2.9: Atomic force micrographs of photoresist features imaged via superlens [22]. Periods of (a) 500 nm, (b) 350 nm, (c) 290 nm and (d) 250 nm are all well resolved, as would be expected of a conventional lens illuminated with λ_0 = 365 nm. Superresolution is confirmed by sub-wavelength features with periods of (e) 200 nm and (f) 170 nm.

2.4 Near-Field Nanolithography

Around the same time that the first metamaterials were being constructed, interesting steps were being made in the area of nanophotonics. Reluctant to merely reduce wavelength, scientists were starting to explore methods of imaging beyond the diffraction

Figure 2.10: Atomic force micrograph of developed photoresist patterned by a silver superlens [23]. Scale bar is 2 μm and average line width is 89 nm.

limit by harnessing the near field. Surprisingly, the easiest path to near field success lay not with advanced optics or complicated imaging systems, but with conceptually simple mask-less contact lithography.

As early as 1997, George Whitesides' group at Harvard fabricated conformal phase masks from poly (dimethylsiloxane) (PDMS), a soft, flexible material that had previously been used to make contact stamps [54]. The group found that if a PDMS mask was merely brought into intimate contact with an imaging layer, and not necessarily driven into it, then the near field modulations resulting from phase discontinuities in the mask could be coupled into the imaging layer and sub-wavelength features could be captured. Using this method, they were able to capture features as small as 90 nm [55], shown in Fig. 2.11, from a polychromatic, incoherent light source with λ between 330 nm and 460 nm [56].

The following year, 1998, researchers at the University of Canterbury were able to replace the PDMS masks with conformal silicon nitride (SiN) membranes, which allowed the minimum feature size to be varied according to the depth and profile of the mask [57]. A switch to nichrome (NiCr)-patterned shadow masks and the addition of a reactive ion etch recipe, which allowed deep transfer of nanometre-scale features, resulted in a technique known as ENFOL [18]. Using ENFOL, researchers were able to image well below the diffraction limit, patterning 50 nm features from a broadband (365–600 nm) source, as shown in Fig. 2.12 [18]. Sub-50 nm features were later patterned from a 220 nm source [58], before a variant of ENFOL was adopted by Canon, Inc. [59], who were able to add their own tri-layer resist to the process in order to image 32 nm half pitch lines from a 365 nm source, as shown in Fig. 2.13 [19].

This early work in contact lithography lent itself well to superlens fabrication, as many of the key aspects between the two technologies are similar. Both rely on intimate contact between the mask and lens or imaging layer; both require the transfer of low

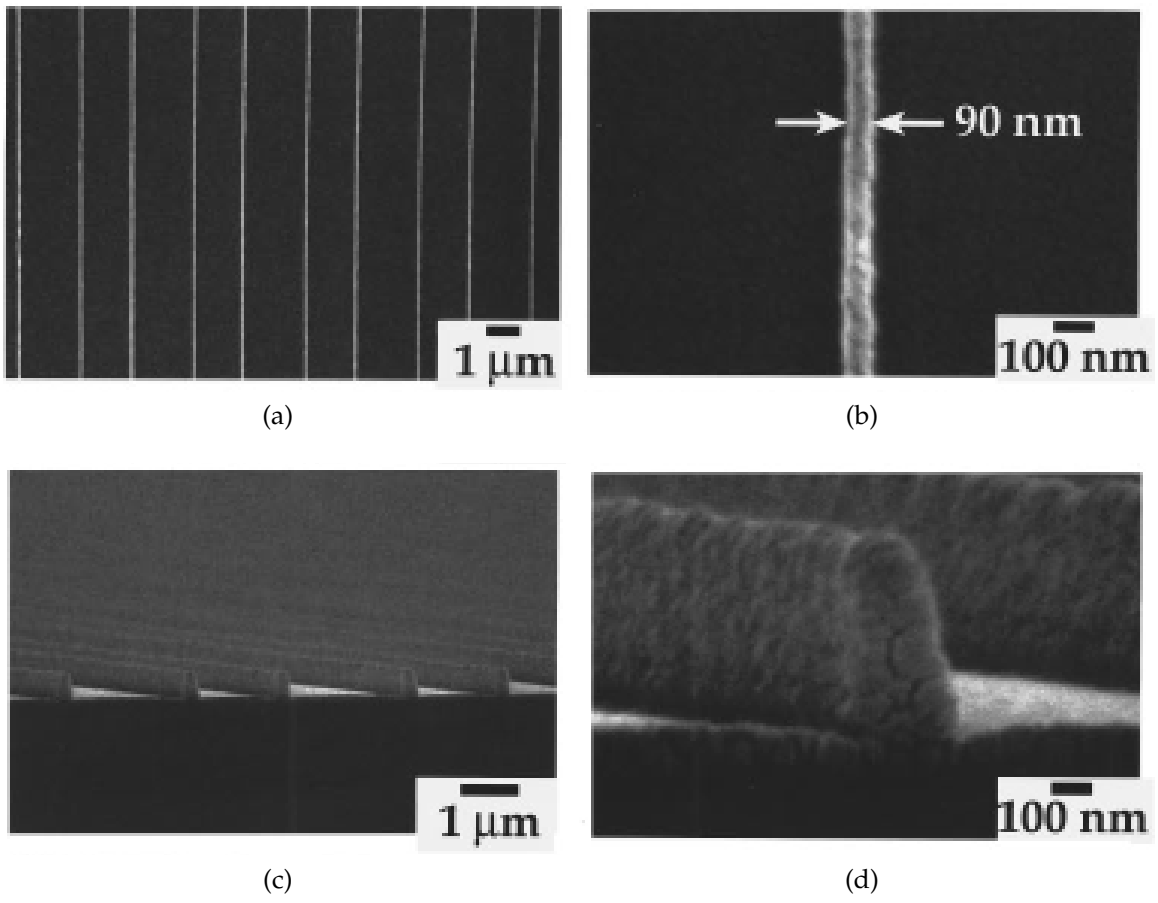

(a) (b)

(c) (d)

Figure 2.11: Scanning electron micrographs showing plane (a) and cross-sectional (b) views of 90 nm wide, 2 μm period lines imaged via PDMS phase masks [55]. Images (c) and (d) are enlargements of (a) and (b), respectively.

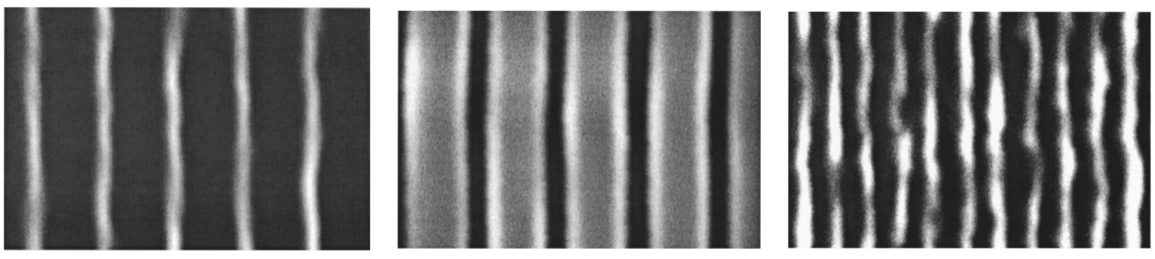

(a) (b) (c)

Figure 2.12: Scanning electron micrographs of photoresist features imaged via ENFOL [18]. 70 nm wide, 240 nm period line (a) and aperture (b) mask features are successfully imaged, as well as a 70 nm wide, 140 nm period grating (c).

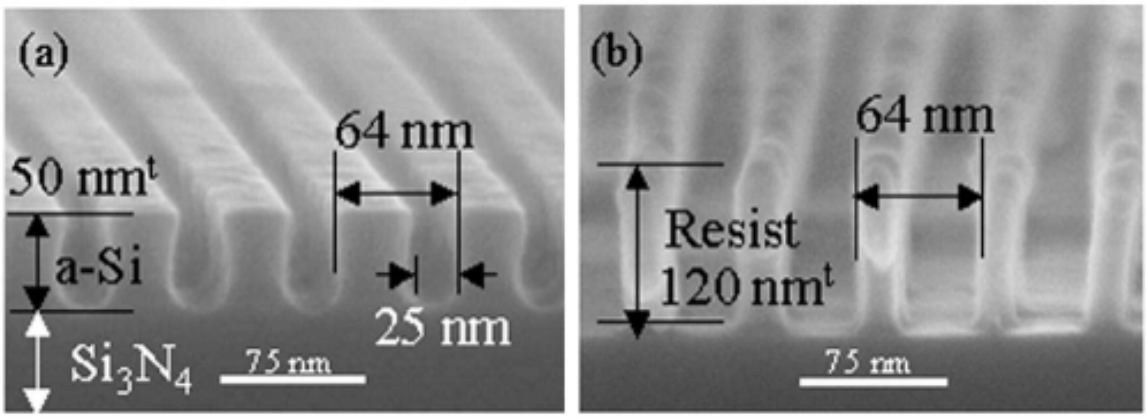

Figure 2.13: Scanning electron micrographs of 32 nm half-pitch mask (a) and resist pattern (b), imaged via ENFOL [19].

amplitude profiles deep into photoresist and both attempt to achieve relatively small features from the relatively large wavelengths generated by i-line sources. In fact, the work on contact lithography described here, especially Ref. [56], forms much of the basis for the superlensing experiments carried out in this thesis.

2.5 State of the Art

Pendry's perfect lens theory had a huge effect on the field of nanophotonics [60, 61], growing it in several ways. Most importantly, it prompted a surge of interest in optical and near-optical superresolving systems [22, 23, 28, 62–66]. Research into fabricated NIMs [27, 67–70], cloaking materials [71, 72] and photonic crystals [73–76] was also positively affected. Recent developments in each of these areas are outlined below.

2.5.1 Superlenses

One of the most significant additions to Pendry's original work on superlenses was the idea that several superlenses could be laminated together to create a multilayered superlens [25, 27, 77, 78], as shown in Fig. 2.14. Theoretically, such designs would have vastly increased resolution with much lower absorption in the lens itself [25]. However, experiments with multilayered structures revealed that the expected increase in resolution over single Ag-layer superlenses was not fully realised, due mainly to the

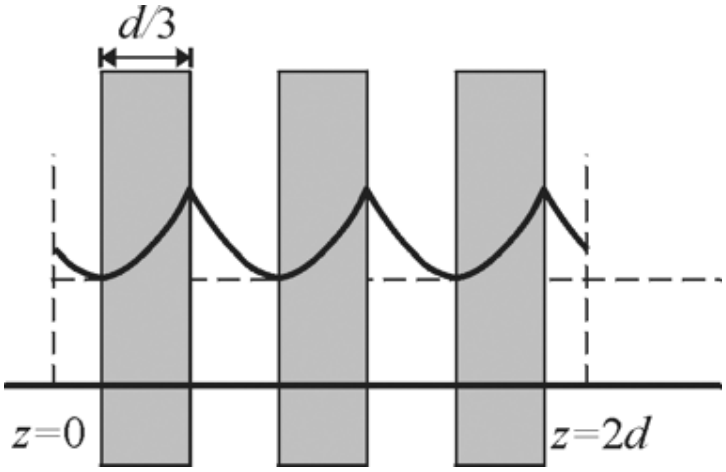

Figure 2.14: Schematic of a multilayered superlens with Ag films shown as shaded areas. An evanescent mode, incident on the lens from the left, is enhanced as it passes through each Ag layer, arriving at the right-most boundary of the lens with its original amplitude [25].

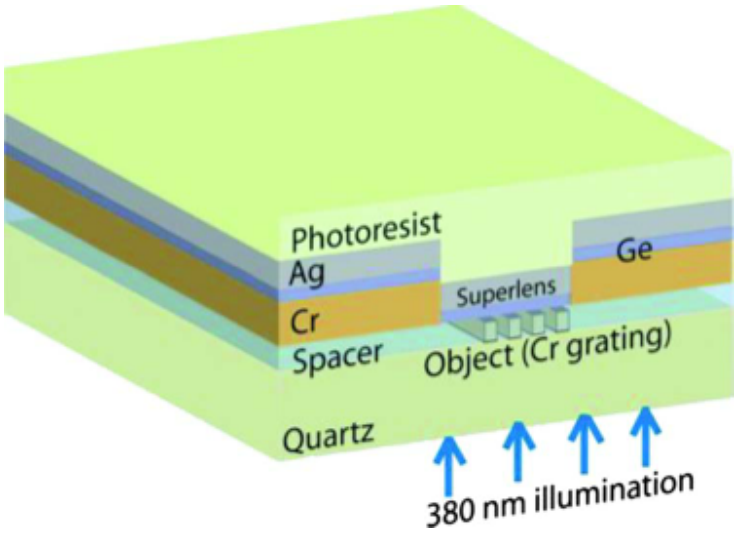

Figure 2.15: Ultrasmooth Ag superlens, grown with the aid of a Ge wetting layer [24].

roughness of the Ag layers, which increased rapidly above 1 nm RMS once the Ag film thickness dropped below ~35 nm [28]. Recently, the surface roughness of 15 nm Ag films was successfully reduced to 0.8 nm RMS [24], simply by depositing the Ag on top of a 1 nm germanium (Ge) wetting layer [79], as shown in Fig. 2.15. Unfortunately, this approach has yet to be applied to multilayered lens designs.

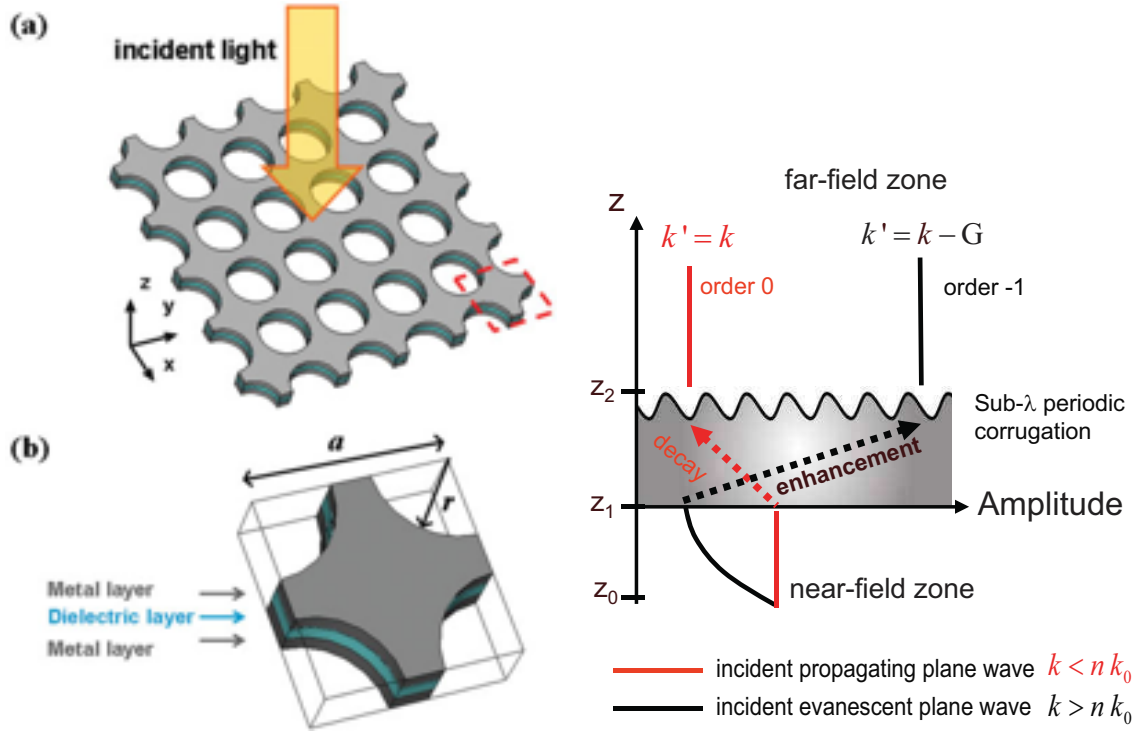

(a) (b)

Figure 2.16: Superlens designs based on perforated (left) [67] and corrugated (right) [86] layers of Ag.

Further research into optical superlenses involved attempts to better understand surface plasmon resonance (SPR) [80, 81], which Pendry identified in 2000 as being a key component required for superresolution [20]. This led to a reexamination of earlier work [82, 83], inspiring novel superlens designs made up of layers of Ag patterned with periodic holes, slits [66, 67, 84, 85] or corrugations [86, 87], examples of which are shown in Fig. 2.16. One unique design was a superlens imagined by Xiang's group at University of California, Berkeley, that used a corrugated NIM layer, shown in Fig. 2.17, to selectively couple and amplify first order diffracted waves. The scattering of evanescent modes reduced their wave vectors—which were normally well beyond the diffraction limit—to create equivalent propagating waves that were detectable by conventional, diffraction-limited devices, as shown in Fig. 2.18. Hence the lens was able to uniquely map information normally stored in evanescent modes into propagating waves [64], giving a far-field optical superlens.

As well as new applications, theoretical performance limits for superlenses were explored [26, 88]. The performance of lossy lenses was considered in much detail [81].

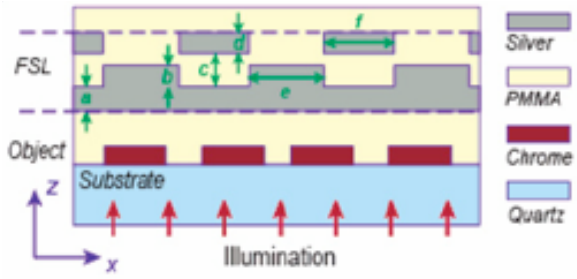

Figure 2.17: Far-field optical superlens design [64].

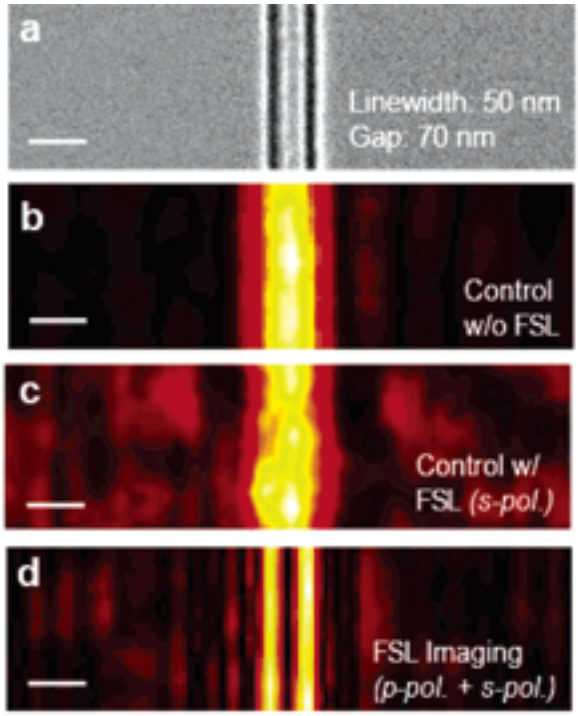

Figure 2.18: Far-field optical superlens performance. Two closely-spaced 50 nm lines (a) are unresolved by a conventional microscope with λ_0 = 377 nm (b). Adding a FSL improves resolution (d) due to surface plasmon resonance, which only occurs for p-polarised light (c) [64].

Non-symmetrical superlens designs [63, 81] and designs that used metals other than silver, such as aluminium, copper, gold, potassium, sodium and related alloys, were also explored [66, 67, 85, 89, 90]. Lastly, semiconductor-based superlenses were built using either doped indium antimonide (InAs) [68] or silicon carbide (SiC) [91]; however, these operate in the long wave infra-red (LWIR) part of the spectrum and are unlikely to have optical applications.

2.5.2 Negative Index Materials

In a similar fashion to the patterned superlenses of Refs. [66, 67, 84, 85], fabricated NIM research focused on different geometries that could be used to create negative effective indices of refraction. As well as the dual split ring and continuous wires used at UCSD at the start of the millennium [41, 42], single split loops [92, 93], Ω-shaped particles [94], singly split double rings [95] and accoustic Helmholtz resonating chambers [70] were all studied. The frequency of operation for these NIMs ranged from approximately 2.6 GHz to more than 12 GHz [95]. Different NIM applications were also explored, for example, harmonic generation [96], optical switching [97], image magnification [98] and (non-linear) waveguides [99].

2.5.3 Cloaking

Of all of these applications, the concept of electromagnetic cloaking [100] has garnered the most interest, from scientific [101–106] and lay [107, 108] circles alike. Gbur [109] evaluated the underlying theoretical concepts in a review published in 2003, this led to parallel proposals from Leonhardt [71] and Pendry, Schurig and Smith [72] in 2006 for an "invisibility device," that "should guide light around an object as if nothing were there" [71]. As shown in Fig. 2.19, they proposed a two dimensional cylinder, made of engineered metamaterials with anisotropic ϵ and μ, as a means of exponentially reducing the shadow and reflection of an otherwise visible object through a perceived squeezing of its dimensions. Numerical [110] and experimental [100] verification of this work followed in the same year, with Schurig et al. publishing details of a SRR-based cloak that operated in the gigahertz band. Further collaboration between Schurig, Smith and Pendry led to the derivation of theory required for a three dimensional cloak [111], while other groups contributed theory detailing cloaking with isotropic [101] and non-magnetic [106] materials.

The first experimental demonstration of a three dimensional invisibility cloak came in 2010, when a group from the Karlsruhe Institute of Technology in Germany collaborated with Pendry to build a woodpile photonic crystal that could cloak a bump on a gold surface, as shown in Fig. 2.20. The crystal was composed of polymer rods, with the index of refraction proportional to their volume filling fraction, f. The group

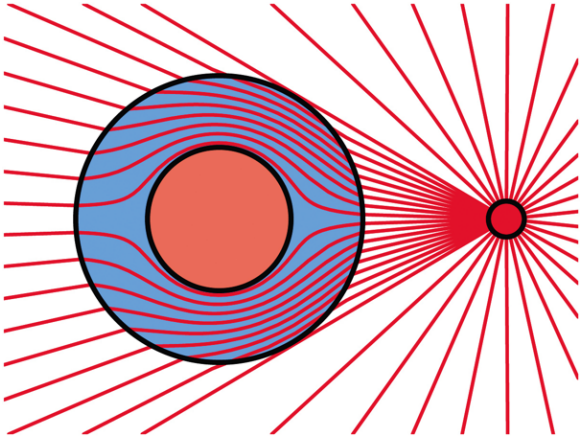

Figure 2.19: The electric displacement field emanating from a point source does not penetrate a cloaking cylinder, yet emerges beyond it completely intact [72].

used a direct laser writing technique to vary f, which led to good cloaking performance over a range of wavelengths (1.4 to 2.7 μm) and viewing angles (up to 60°). A summary of their results is given in Fig. 2.21.

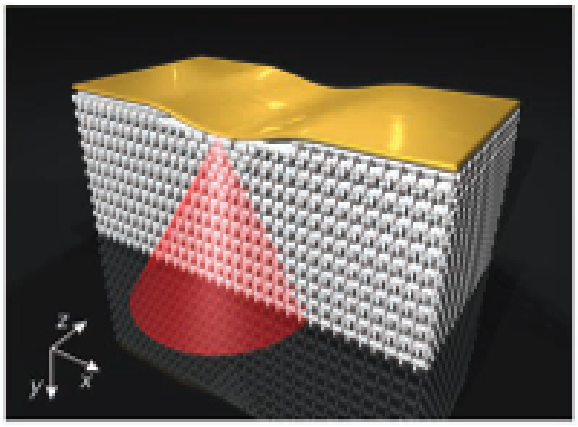

Figure 2.20: Three-dimensional invisibility cloak [112]. A bump in a gold layer is effectively hidden by polymer rods (coloured silver in this figure). The red cone corresponds to light from a microscope lens.

2.5.4 Photonic Crystal Superlenses

Finally, research has gone into photonic crystals, which were identified as alternative media capable of superresolution [73–76]. The structure of the crystals, shown in Fig. 2.22, was conceptually similar to the perforated-plane geometries presented in

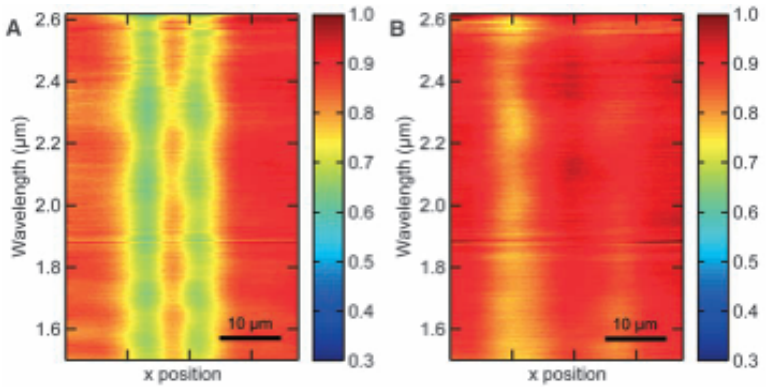

Figure 2.21: Image intensity of a bump of gold viewed with unpolarised light. (A) Without an invisibility cloak, the sloping sides of the bump are clearly visible as two parallel intensity peaks. (B) With an invisibility cloak covering the bump, there is very little change in intensity over a range of wavelengths [112].

Refs. [66, 67] and negative refraction was observed by several groups at microwave and optical frequencies [74, 76, 113–115]. Superresolution was achieved through coupling between incident evanescent modes and bound photon states [75] and it was shown that the crystals did not need negative ϵ_{eff} or μ_{eff} for this to occur [75, 78, 116].

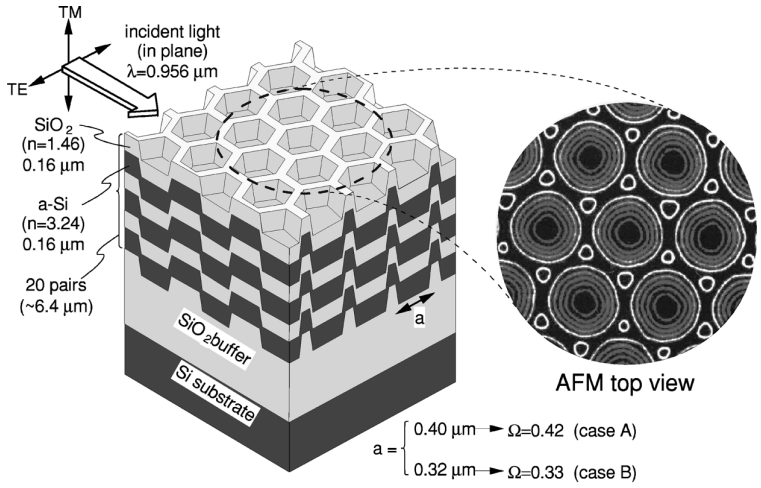

Figure 2.22: Three-dimensional graphite photonic crystal, operating at a wavelength of 956 nm [113].

2.6 Summary

Even in the light of great progress, much work still remains to fully characterise and understand superlenses and the ways in which they behave. For instance, a system of metrics are needed to classify superlens performance and to allow comparison between different superlens designs. Many theoretical performance results predicted of superlenses have yet to be validated and the experimental characterisation of superlenses is still almost non-exist, other than for minimum resolution [22, 23] measurements. This thesis aims to address some of these shortcomings, with the goal of giving a more complete, detailed picture of the performance and peculiarities of silver superlenses.

Chapter 3

Modelling Techniques

The ENFOL and PLL techniques discussed in Chapters 1 and 2 possess the exciting ability to reproduce images with features much smaller than conventional lithography would allow, all at UV wavelengths close to the visible spectrum of light. Their capabilities have been tested numerous times both in theoretical studies [20, 25, 81] and in practical experiments [18, 19, 22–24], with their capacity to break the diffraction limit now widely accepted. However, the suitability of such systems, particularly PLL, for general purpose lithography applications is still far from certain, since their behaviour has been calculated only for a small sample of test cases and their experimental performance was characterised almost exclusively in terms of the minimum resolvable grating period. The performance of PLL systems when exposed to arbitrarily shaped masks is yet to be fully quantified. Furthermore, it is not known what effect, if any, the period or shape of a mask profile may have on the surface plasmon resonance (SPR) taking place in a superlens. If there is any interaction it is bound to affect imaging performance, since the evanescent enhancement necessary for superresolution in PLL is mediated by SPR. Hence, one of the key questions addressed in this thesis asks whether PLL is an inherently robust approach that can be used for a range of lithography applications, or is it destined to fill a small niche in the endlessly changing technological landscape?

The attempt to answer this question begins first with modelling and analytical studies, which provide ideal, uncontaminated guidelines from which experimental work can be directed. Two techniques used to predict ENFOL and PLL behaviour are described

in this chapter, with the corresponding results based on these techniques presented in Chapters 4 and 5. The experimental methods and results used to test the practical efficacy of ENFOL and PLL are discussed after this, in Chapters 6 and 7, respectively.

3.1 Overview

Analytical modelling was used extensively in this work to explore the characteristics and behaviour of different near-field imaging systems. This was done for three reasons. Firstly, simulations allowed for increased understanding of the image formation process. This was useful as the concept of imaging using planar lenses has only recently been developed [20]. Secondly, the high number of delicate, low-yield steps required to fabricate a superlens was a deterrent to try novel designs; numerical analysis provided an inexpensive way of trialling the performance of such designs and served to focus attention on the most promising geometries. Thirdly, modelling allowed for comprehensive system optimisation that experimental data alone could not practically provide.

In order to get the most value out of the analysis, it was preferable to make the data on each design as complete and accurate as possible. Hence, two separate techniques were used: one technique, transfer matrix modelling (TMM), was a semi-analytic technique used to model lens performance in the spatial frequency domain; and another, finite element modelling (FEM), was used to generate spatial domain visualisations. The TMM results allowed general characterisation of superlenses without necessarily referencing a particular mask or input pattern, while the FEM technique was used to study individual cases of interest. The use of multiple techniques also had the advantage that similar data produced by differing means could be compared together, in order to show self-consistency and to provide some degree of validation.

The details of the theory and implementation of both the TMM and FEM techniques are included in this chapter, along with some example results from the spatial frequency and spatial domains. Methods of converting data from the different techniques into compatible forms are also described. Finally, comparisons are made to data in the literature in an effort to authenticate the implementation of these techniques.

3.2 Transfer Matrix Modelling

Transmission matrices (transfer matrices (T-matrices)) can be used to model wave behaviour at the interface between two materials with differing electromagnetic characteristics, as well as to describe propagation through a uniform material. The technique works for both propagating and evanescent modes, travelling through either conventional media or metamaterials with negative ϵ and/or μ. Interface behaviour is calculated by defining modes in terms of their electric, $\mathbf{E}$, and magnetic, $\mathbf{H}$, fields, which are incident or reflecting on either side of an interface at some angle θ. The transmitted modes on the far side of the interface are found by equating components of $\mathbf{E}$ and $\mathbf{H}$ to form a pair of simultaneous equations. Same-medium propagation is modelled by exponential multipliers, the coefficients of which are determined by the electromagnetic properties of the medium and the distance travelled. These features can be repeated and combined, allowing a single T-matrix to predict wave behaviour through several interfaces at various spacings.

The relative simplicity of T-matrices and their speed of calculation make them attractive tools for analysis; however, they do suffer some limitations when applied to near-field imaging systems. The first of these limitations arises due to the strictly one dimensional nature of T-matrices, which means that their use is based on the assumption of regular and perfectly smooth interfaces. In practice, no fabricated film is completely smooth. Furthermore, the specific roughness of layers within a superlensing system has a strong effect on performance and should not be ignored [117]. The other main shortcoming of T-matrices is that they do not account for the near field interactions that occur between a structured mask and a near-field lens. For most conventional imaging systems these interactions will be negligible; however, they are significant for superlensing systems where intimate contact is required between mask and lens [31].

Even accounting for their limitations, which are more fully addressed in Chapter 5, T-matrices offer a quick and convenient means of predicting the spatial-frequency domain behaviour of multi-layered systems. For this reason they are used extensively in this thesis. A brief summary of their derivation is included here, with a full formulation documented in Ref. [7].

3.2.1 Derivation

A schematic illustrating the parameters involved in the T-matrix model (TMM) [7] is given in Fig. 3.1. The illustration describes two media with arbitrary permittivities, ϵ_1 and ϵ_2, forming an interface at the z-origin. Four waves, A, B, C and D, are present, characterised by their electromagnetic fields. Note that these waves can be either evanescent or propagating, i.e. there is no restriction on their wavenumber, $\mathbf{k}$, except that the waves are all of the same temporal frequency. For this study the waves are also restricted to TM polarisation; this is permissible due to the negligible effect that transverse electric (TE) polarised waves have on the superlensing process [23] and is desirable as it reduces the complexity of the model. Accordingly, the electric field shown in Fig. 3.1, $\mathbf{E}$, is defined as

$$\mathbf{E}|_{z<0} = \mathbf{E}^A e^{i(k_x^A x + k_z^A z - \omega t)} + \mathbf{E}^B e^{i(k_x^B x - k_z^B z - \omega t)} \tag{3.1a}$$

$$\mathbf{E}|_{z>0} = \mathbf{E}^C e^{i(k_x^C x + k_z^C z - \omega t)} + \mathbf{E}^D e^{i(k_x^D x - k_z^D z - \omega t)} \tag{3.1b}$$

and the magnetic field, $\mathbf{H}$, is

$$\mathbf{H}|_{z<0} = \mathbf{H}^A e^{i(k_x^A x + k_z^A z - \omega t)} - \mathbf{H}^B e^{i(k_x^B x - k_z^B z - \omega t)} \tag{3.2a}$$

$$\mathbf{H}|_{z>0} = \mathbf{H}^C e^{i(k_x^C x + k_z^C z - \omega t)} - \mathbf{H}^D e^{i(k_x^D x - k_z^D z - \omega t)}, \tag{3.2b}$$

where k_x and k_z are the cartesian components of the wavenumber, $\mathbf{k}$, corresponding to the waves described by $\mathbf{E}$ and $\mathbf{H}$. x and z are cartesian unit vectors with their origin at the intersection of waves A, B, C and D; ω is the angular frequency of the waves and t is time, measured in arbitrary units.

From this point, several simplifications are made to Eqs. (3.1) and (3.2). Firstly, we note that the angles of incidence and reflection are equivalent for waves on the same side of the interface [118]:

$$\theta^A = \theta^B = \theta_1 \tag{3.3a}$$

$$\theta^C = \theta^D = \theta_2. \tag{3.3b}$$

This observation holds for both propagating and evanescent modes, although it is not intuitive to talk of the 'angle' of an evanescent mode. Instead, the equivalent

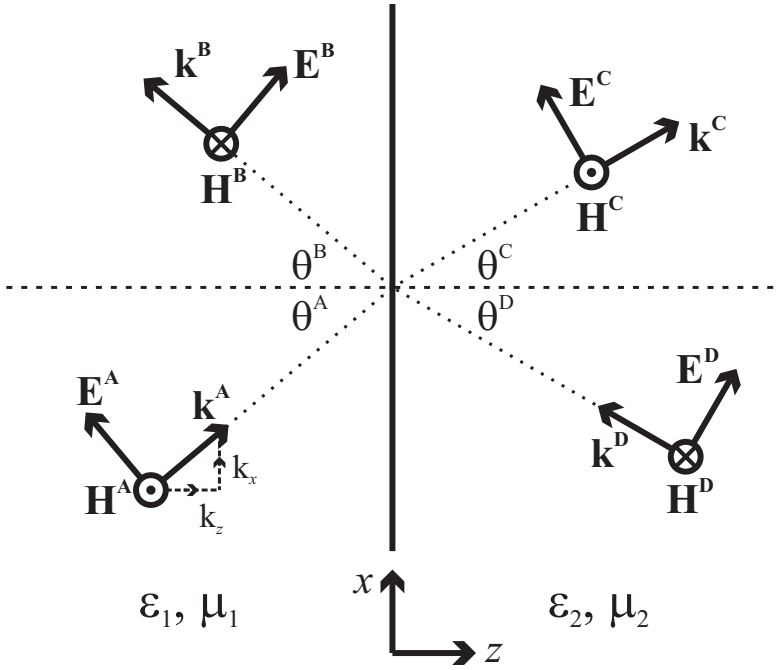

Figure 3.1: Domain setup for T-matrix simulations, after [7]. Propagating waves are shown; however, this formalism is equally valid for evanescent modes.

quantity may be referred to as the 'decay constant' of that mode. In order to avoid this confusion, the derivation that follows is phrased in terms of wavevectors and their components, which apply equally well to both evanescent and propagating modes.

The relationship between wavevector and angle of incidence is given by

$$\theta = \tan^{-1}\left(\frac{k_x}{k_z}\right), \tag{3.4}$$

where θ is the angle of incidence for propagating modes or the decay constant for evanescent modes; k_x and k_z are the x- and z-components of the corresponding wavevector, $\mathbf{k}$, such that $\mathbf{k}^2 = k_x^2 + k_y^2$. Note that k_z is real for propagating waves and imaginary for evanescent modes. Furthermore, the y-component of $\mathbf{k}$, k_y, is always zero as a result of the construction of the coordinate system and the choice of TM polarisation for all modes. Hence, Eq. (3.3) is rephrased as:

$$\frac{k_x^A}{k_z^A} = -\frac{k_x^B}{k_z^B} = \frac{k_{1x}}{k_{1z}} \tag{3.5a}$$

$$\frac{k_x^C}{k_z^C} = -\frac{k_x^D}{k_z^D} = \frac{k_{2x}}{k_{2z}}. \tag{3.5b}$$

The magnitudes of the wavevectors for waves on the same side of the interface are also identical, since all of the waves share the same temporal frequency:

$$|\mathbf{k^A}| = |\mathbf{k^B}| = |\mathbf{k_1}| \tag{3.6a}$$

$$|\mathbf{k^C}| = |\mathbf{k^D}| = |\mathbf{k_2}|. \tag{3.6b}$$

Secondly, the steady-state forms of $\mathbf{E}$ and $\mathbf{H}$ are chosen, allowing the removal of the $-\omega t$ terms from Eqs. (3.1) and (3.2). These simplifications yield Eqs. (3.7), (3.8) and (3.9), which show $\mathbf{E}$ and $\mathbf{H}$ in terms of their cartesian components:

$$E_x|_{z<0} = E_x^A e^{i(k_{1x}x + k_{1z}z)} + E_x^B e^{i(k_{1x}x - k_{1z}z)} \tag{3.7a}$$

$$E_x|_{z>0} = E_x^C e^{i(k_{2x}x + k_{2z}z)} + E_x^D e^{i(k_{2x}x - k_{2z}z)} \tag{3.7b}$$

$$E_z|_{z<0} = -E_z^A e^{i(k_{1x}x + k_{1z}z)} + E_z^B e^{i(k_{1x}x - k_{1z}z)} \tag{3.8a}$$

$$E_z|_{z>0} = -E_z^C e^{i(k_{2x}x + k_{2z}z)} + E_z^D e^{i(k_{2x}x - k_{2z}z)} \tag{3.8b}$$

$$H_y|_{z<0} = \mathbf{H}|_{z<0} = H_y^A e^{i(k_{1x}x + k_{1z}z)} - H_y^B e^{i(k_{1x}x - k_{1z}z)} \tag{3.9a}$$

$$H_y|_{z>0} = \mathbf{H}|_{z>0} = H_y^C e^{i(k_{2x}x + k_{2z}z)} - H_y^D e^{i(k_{2x}x - k_{2z}z)}. \tag{3.9b}$$

Lastly, expressions for the fields on opposite sides of the x-axis (i.e. at $z = 0$) are equated, since both $\mathbf{E}$ and $\mathbf{H}$ are continuous in that plane. For even greater simplicity, the equations are expressed at the arbitrary plane $x = 0$, giving:

$$E_x^A + E_x^B = E_x^C + E_x^D \tag{3.10a}$$

$$-E_z^A + E_z^B = -E_z^C + E_z^D \tag{3.10b}$$

and

$$H_y^A - H_y^B = H_y^C - H_y^D. \tag{3.11}$$

Eq. (3.10a) is the first of the simultaneous equations required to form a T-matrix. The second is derived from Eq. (3.11) by equating the magnetic, $\mathbf{H}$, and electric, $\mathbf{E}$, fields

in terms of their plane-wave impedance, η [118]:

$$\eta = \frac{\mathbf{E}}{\mathbf{H}} = \frac{\mathbf{k}}{\omega\epsilon}. \tag{3.12}$$

Rearranging,

$$\mathbf{H} = \frac{\omega\epsilon}{\mathbf{k}}\mathbf{E}. \tag{3.13}$$

Eq. (3.13) can be expressed in terms of cartesian coordinates to give

$$|\mathbf{H}| = \frac{\omega\epsilon}{|\mathbf{k}|\cos(\theta)}|\mathbf{E}|\cos(\theta), \tag{3.14}$$

which simplifies to

$$H_y = \frac{\omega\epsilon}{k_z}E_x. \tag{3.15}$$

This is allowed since

$$|\mathbf{H}| = H_y, \tag{3.16}$$

$$|\mathbf{E}|\cos(\theta) = E_x, \tag{3.17}$$

and

$$|\mathbf{k}|\cos(\theta) = k_z. \tag{3.18}$$

Substituting Eq. (3.15) into Eq. (3.11), the complementary equation to Eq. (3.10a) is found:

$$\frac{\omega\epsilon_1}{k_{1z}}\left(E_x^A - E_x^B\right) = \frac{\omega\epsilon_2}{k_{2z}}\left(E_x^C - E_x^D\right). \tag{3.19}$$

By substituting Eq. (3.10a) into Eq. (3.19), E_x^C and E_x^D can be found, followed by the T-matrix that describes the domain shown in Fig. 3.1:

$$E_x^C = \frac{1}{2}\frac{k_{2z}}{\epsilon_2}\left(E_x^A\left(\frac{\epsilon_1}{k_{1z}} + \frac{\epsilon_2}{k_{2z}}\right) + E_x^B\left(\frac{\epsilon_2}{k_{2z}} - \frac{\epsilon_1}{k_{1z}}\right)\right), \tag{3.20}$$

and

$$E_x^D = \frac{1}{2}\frac{k_{2z}}{\epsilon_2}\left(E_x^A\left(\frac{\epsilon_2}{k_{2z}} - \frac{\epsilon_1}{k_{1z}}\right) + E_x^B\left(\frac{\epsilon_2}{k_{2z}} + \frac{\epsilon_1}{k_{1z}}\right)\right), \tag{3.21}$$

yielding

$$\begin{aligned}\begin{bmatrix} E_x^C \\ E_x^D \end{bmatrix} &= \frac{1}{2}\frac{k_{2z}}{\epsilon_2}\begin{bmatrix} \frac{\epsilon_2}{k_{2z}} + \frac{\epsilon_1}{k_{1z}} & \frac{\epsilon_2}{k_{2z}} - \frac{\epsilon_1}{k_{1z}} \\ \frac{\epsilon_2}{k_{2z}} - \frac{\epsilon_1}{k_{1z}} & \frac{\epsilon_2}{k_{2z}} + \frac{\epsilon_1}{k_{1z}} \end{bmatrix}\begin{bmatrix} E_x^A \\ E_x^B \end{bmatrix} \\ &= \begin{bmatrix} T_{11} & T_{12} \\ T_{21} & T_{22} \end{bmatrix}\begin{bmatrix} E_x^A \\ E_x^B \end{bmatrix}. \end{aligned} \tag{3.22}$$

In order to find the transmission and reflection coefficients of the interface from the matrix defined by Eq. (3.22), E_x^A is set to unity, representing a source wave travelling in the $+z$ direction. E_x^D is set to zero, removing any interference from source waves on the opposite side of the interface. This means that the transmission coefficient, t_0, is given by E_x^C and the reflection coefficient, r_0, is given by E_x^B. The T-matrix now becomes

$$\begin{bmatrix} t_0 \\ 0 \end{bmatrix} = T(0) \begin{bmatrix} 1 \\ r_0 \end{bmatrix}, \tag{3.23}$$

where

$$T(0) = \begin{bmatrix} T_{11} & T_{12} \\ T_{21} & T_{22} \end{bmatrix}. \tag{3.24}$$

Multiplying and expanding,

$$r_0 = \frac{-T_{21}}{T_{22}} \tag{3.25a}$$

$$= \frac{\epsilon_1 k_{2z} - \epsilon_2 k_{1z}}{\epsilon_2 k_{1z} + \epsilon_1 k_{2z}} \tag{3.25b}$$

and

$$t_0 = \frac{T_{11}T_{22} - T_{12}T_{21}}{T_{22}} \tag{3.26a}$$

$$= \frac{2\epsilon_1 k_{2z}}{\epsilon_2 k_{1z} + \epsilon_1 k_{2z}}. \tag{3.26b}$$

The coefficients defined in Eqs. (3.25) and (3.26) are valid for an interface at the $z = z_0 = 0$ plane, for interfaces elsewhere on the z-axis a displacement transform has to be applied. Accordingly, an electric field at the point $z = d$ is defined as follows:

$$\begin{aligned} E|_{z=d} &= E e^{i(k_x x + k_z(z_0+d))} \\ &= E e^{i(k_x x + k_z z_0)} e^{i(k_z d)} \\ &= E|_{z=0} e^{i(k_z d)}. \end{aligned} \tag{3.27}$$

Substituting this definition into Eq. (3.22) allows the T-matrix for an arbitrary interface at $z = d$, $T(d)$, to be expressed in terms of $T(0)$:

$$\begin{bmatrix} E_x^C e^{i(k_{2z}d)} \\ E_x^D e^{-i(k_{2z}d)} \end{bmatrix} = T(0) \begin{bmatrix} E_x^A e^{i(k_{1z}d)} \\ E_x^B e^{-i(k_{1z}d)} \end{bmatrix}$$

$$\begin{bmatrix} e^{i(k_{2z}d)} & 0 \\ 0 & e^{-i(k_{2z}d)} \end{bmatrix} \begin{bmatrix} E_x^C \\ E_x^D \end{bmatrix} = T(0) \begin{bmatrix} e^{i(k_{1z}d)} & 0 \\ 0 & e^{-i(k_{1z}d)} \end{bmatrix} \begin{bmatrix} E_x^A \\ E_x^B \end{bmatrix}$$

$$\begin{bmatrix} E_x^C \\ E_x^D \end{bmatrix} = \begin{bmatrix} e^{-i(k_{2z}d)} & 0 \\ 0 & e^{i(k_{2z}d)} \end{bmatrix} T(0) \begin{bmatrix} e^{i(k_{1z}d)} & 0 \\ 0 & e^{-i(k_{1z}d)} \end{bmatrix} \begin{bmatrix} E_x^A \\ E_x^B \end{bmatrix}. \tag{3.28}$$

Hence

$$T(d) = \begin{bmatrix} e^{-i(k_{2z}d)} & 0 \\ 0 & e^{i(k_{2z}d)} \end{bmatrix} T(0) \begin{bmatrix} e^{i(k_{1z}d)} & 0 \\ 0 & e^{-i(k_{1z}d)} \end{bmatrix}, \tag{3.29}$$

and

$$\begin{bmatrix} t_d \\ 0 \end{bmatrix} = T(d) \begin{bmatrix} 1 \\ r_d \end{bmatrix}, \tag{3.30}$$

giving

$$r_d = r_0 e^{i2k_{1z}d} \tag{3.31a}$$

$$t_d = t_0 e^{i(k_{1z}-k_{2z})d}. \tag{3.31b}$$

Lastly, although substituting $T(d)$ for $T(0)$ in Eq. (3.23) gives coefficients for an interface at $z = d$, the coefficients are referred to the $z = 0$ plane. Hence, a final phase shift is applied to the coefficients to project them into the $z = d$ plane:

$$T_d(d) = \begin{bmatrix} e^{ik_{z2}d} & 0 \\ 0 & e^{-ik_{z2}d} \end{bmatrix} T(d). \tag{3.32}$$

3.2.2 Transfer Functions

In order to find the T-matrix for a multi-interface system, such as may be used to represent a superlens, the steps outlined in Section 3.2.1 are repeated for each interface with the resulting matrices from Eq. (3.32) multiplied together. Calculating the transmitted intensity, $|t|^2$, and phase, $\angle t$, of this combined T-matrix over a range of wavenumbers, k_x, gives intensity and phase transfer funcitons for the system, which are useful tools for analysing superlens performance as discussed in Section 4.2.1. This section explains superlens transfer functions and explores, by way of example, some of the information that they contain.

Exemplar transfer functions (TFs) for three different imaging systems, shown in Fig. 3.2, are plotted in Fig. 3.3. These systems are (1) an 80 nm wide vacuum gap, approx-

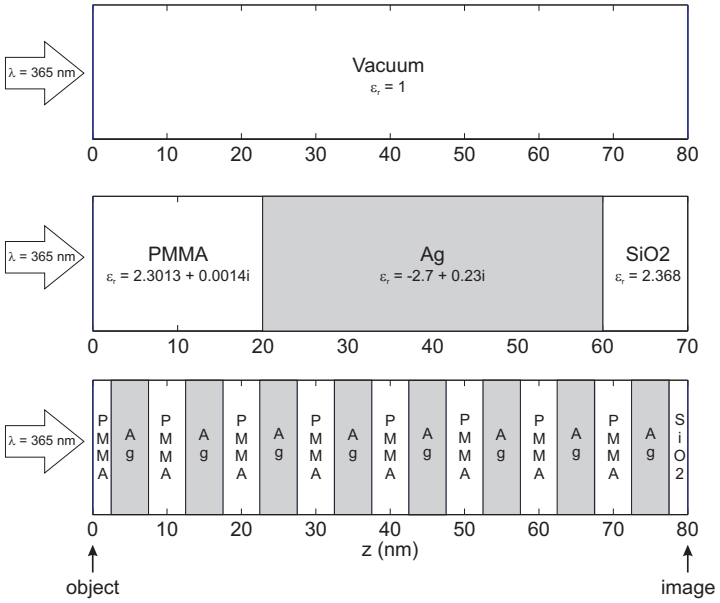

Figure 3.2: Lens composition and dimensions. Top: 80 nm vacuum gap used for proximity imaging. Middle: Single active Ag layer superlens with 10 nm SiO_2 final layer in accordance with practical experimental conditions [63]. Bottom: Multiple active layer superlens made up of eight individual 5 nm Ag laminations. Total Ag thickness is 40 nm, as for the single-layer lens. Input object patterns are applied from the left of the lenses and output images are retrieved from the right, as indicated.

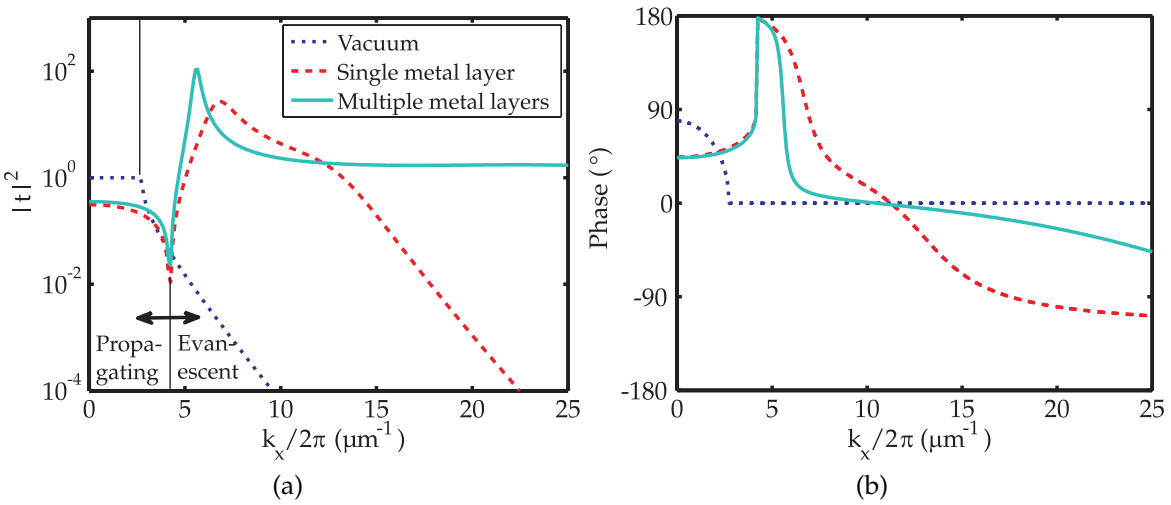

Figure 3.3: Intensity (a) and phase (b) transfer functions for single and multiple Ag layer superlenses and an 80 nm vacuum gap. The dimensions and composition of these systems are described in Fig. 3.2.

imating the case of conventional lithography with a diffraction-limited lens; (2) a 20:40:10 nm PMMA:Ag:SiO_2 superlens, based on the experiments reported in [22],

and (3) a multi-layered superlens made up of eight 5 nm Ag layers separated by 5 nm PMMA layers, with 2.5 nm layers of PMMA and SiO_2 capping the Ag layers at the entrance and exit of the superlens, respectively. For the intensity transfer function of Fig. 3.3a, the vertical axis of the plot represents total transmission through the system, given by the magnitude of the transmission coefficient squared, $|t|^2$. Values of $|t|^2$ greater than 1 represent an enhancement of electric fields in the system, while values less than 1 correspond to attenuation. A logarithmic scale is used to better display the vastly different resonant and attenuated regions that are typical of superlens transfer functions.

The horizontal axis of Fig. 3.3a represents the x-component of the wavenumber of modes within the system, k_x. This axis is scaled by $1/2\pi$, making its values the inverse of the spatial period, Λ, of the electric field profile in the x-direction, E_x; such that $k_x \,/\, 2\pi \;=\; \Lambda^{-1}$. Wavenumbers on the left part of the axis represent propagating waves with $\Lambda \leqslant \frac{\lambda_0}{n}$, while wavenumbers on the right represent evanescent modes where $\Lambda > \frac{\lambda_0}{n}$. The transition between the two occurs at $k_x/2\pi = n/\lambda_0$, which is representative of the diffraction limit in conventional systems. Here λ_0 is the incident wavelength and n is the refractive index of the source medium. The transition points between propagating and evanescent modes for the different imaging systems are marked by solid vertical hairlines in Fig. 3.3a.

The three curves shown in Fig. 3.3a are transfer functions (TFs) for the systems described in Fig. 3.2, all of which are illuminated with $\lambda_0 = 365$ nm. The dotted curve represents transmission through the 80 nm vacuum gap with n = 1. Transmission is uniform below $\frac{1\times 2\pi}{365 \text{ nm}} \approx 2.7\ \mu\text{m}^{-1}$, at which point it decreases exponentially with increasing wavenumber. This is consistent with the evanescent decay of modes with $k_x > \frac{2\pi}{\lambda_0}$.

The dashed curve represents transmission through the experimental superlens [63], with a generic glass source medium (n = 1.5). At a wavelength of 365 nm, the relative permittivities of the Ag and the PMMA and SiO_2 that surround it are $\epsilon_{r,Ag} = -2.7 + 0.23i$, $\epsilon_{r,PMMA} = 2.3013 + 0.0014i$ and $\epsilon_{r,SiO_2} = 2.368 + 0i$, respectively. Transmission for large periods, i.e. small k_x, is lower than for the vacuum gap due to reflection at the various interfaces and attenuation of propagating waves in the silver due to the skin effect [119]. Conversely, transmission is up to five orders of magnitude greater in the evanescent regime, which begins at $\frac{n}{\lambda_0} = \frac{1.5}{365 \text{ nm}} = 4.1\ \mu m^{-1}$. This enhancement per-

sists up to $\sim$15 μm^{-1}, after which transmission decays exponentially with increasing wavenumber. This suggests that the superlens will have better minimum resolution than the vacuum gap but will have poor performance for propagating waves.

The last, solid curve in Fig. 3.3a is for the hypothetical, multilayered superlens made up of eight individual 5 nm thick Ag layers. Relative permittivity values are as for the single Ag layer case. This design has a sharper resonant peak in transmission than the single layer lens, with enhanced transmission through the entire evanescent spectrum to beyond 25 μm^{-1}. When considered in combination with a relatively flat phase response, this suggests that half-pitch resolution below 20 nm is theoretically possible with such systems. The price for this increased performance is further decreased transmission of propagating modes relative to the vacuum and single layer cases, not to mention greatly increased manufacturing complexity.

The complementary analytical tool to the intensity transfer function is the phase transfer function, which measures the phase response, $\angle t$, of a system over a range of wavenumbers. Phase transfer functions for the imaging systems described in Fig. 3.2 are shown in Fig. 3.3b. Similar to transfer function plots, vertical wavenumber is shown on the horizontal axis, with the phase in degrees plotted on the vertical axis. Note that the initial, 0 μm^{-1} phase for the vacuum gap is 78.9°, which is consistent with the phase change a 365 nm period wave would experience over a free space distance of 80 nm. Furthermore, the overall shape of the phase response for the 80 nm gap is complementary to the shape of the amplitude response shown in Fig. 3.3a. According to the transfer function, the amplitude of propagating waves is not affected by the vacuum gap, whereas the amplitude of evanescent waves decreases sharply with increasing wavenumber. This is reversed in the phase response, where evanescent waves have constant phase and propagating waves experience a phase change dependent on their wavenumber. Unfortunately, such decoupling is not present for sub-diffraction limited systems, such as the superlenses described here.

3.2.3 Validation and Improved Implementation

The TMM source code used to generate a TF, listed in Appendix A, was validated by comparison with data from the literature, which modelled a 36 nm Ag slab suspended in vacuum [120]. Fig. 3.4 showed good agreement for low to mid-sized wavenum-

bers, with the results calculated by TMM identical to earlier published data [7, 20, 26]. Unfortunately, the simulations became unstable at very high wavenumbers, around $k_x/2\pi \geqslant 100$, as shown in Fig. 3.5a. These numerical instabilities are due to a computational error that results from the calculation of the $T_{12}(d)$ coefficient in Eq. (3.29). The arguments in the exponential functions of Eq. (3.29) can obtain positive real parts for wavenumbers greater than the diffraction limit, which cause the exponential functions to return increasingly large numbers that eventually exceed the maximum floating-point value ($\mathcal{O}(308)$) that can be calculated by the computer running the simulation. Once this hardware-dependent maximum value is exceeded, the Matlab [121] program used to compute the T-matrix treats the variable as infinite, causing subsequent calculations to return ill-defined results. The $T_{21}(d)$ coefficient also has non-complex arguments in its precursor exponential functions but they remain negative at all times, causing it to approach 0, rather than ∞, and to remain well-behaved.

Such numerical inconveniences are avoided by rearranging Eq. (3.23) to solve for r_0 instead of t_0:

$$\begin{bmatrix} 1 \\ r_0 \end{bmatrix} = T(0)^{-1} \begin{bmatrix} t_0 \\ 0 \end{bmatrix} = R\,(0) \begin{bmatrix} t_0 \\ 0 \end{bmatrix}. \tag{3.33}$$

This expands to give

$$t_0 = \frac{1}{R_{11}} \tag{3.34a}$$

$$r_0 = \frac{R_{21}}{R_{11}}, \tag{3.34b}$$

where

$$\begin{bmatrix} R_{11} & R_{12} \\ R_{21} & R_{22} \end{bmatrix} = R\,(0) = \frac{1}{2}\frac{k_{1z}}{\epsilon_1} \begin{bmatrix} \frac{\epsilon_2}{k_{2z}} + \frac{\epsilon_1}{k_{1z}} & -\frac{\epsilon_2}{k_{2z}} + \frac{\epsilon_1}{k_{1z}} \\ -\frac{\epsilon_2}{k_{2z}} + \frac{\epsilon_1}{k_{1z}} & \frac{\epsilon_2}{k_{2z}} + \frac{\epsilon_1}{k_{1z}} \end{bmatrix}. \tag{3.35}$$

Similarly, $R(d)$ is given by $T(d)^{-1}$, with the phase changes necessary to find r_d and t_d being identical to those shown in Eq. (3.31).

This rearrangement is successful, despite $R_{12}(d)$ suffering from the same tendency towards instability as $T_{12}(d)$, because the calculation of the transmission coefficient in Eq. (3.34a) is no longer dependent on a potentially ill-defined coefficient, as it was in Eq. (3.26a). This is demonstrated in Fig. 3.5b, which shows results obtained with a rearranged T-Matrix. Unlike Fig. 3.5a, the data are valid for $k_x/2\pi \geqslant 100\mu m^{-1}$, corresponding to spatial periods below 10 nm.

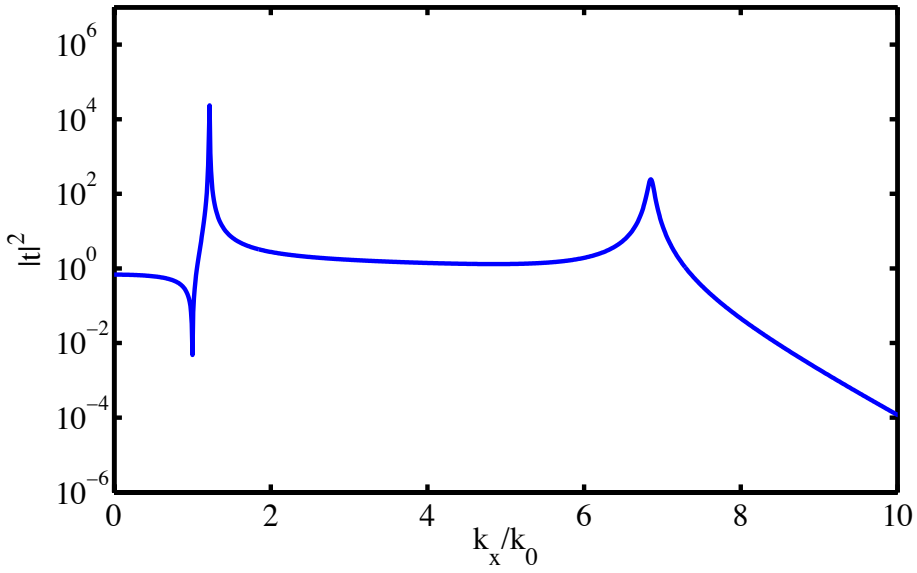

(a)

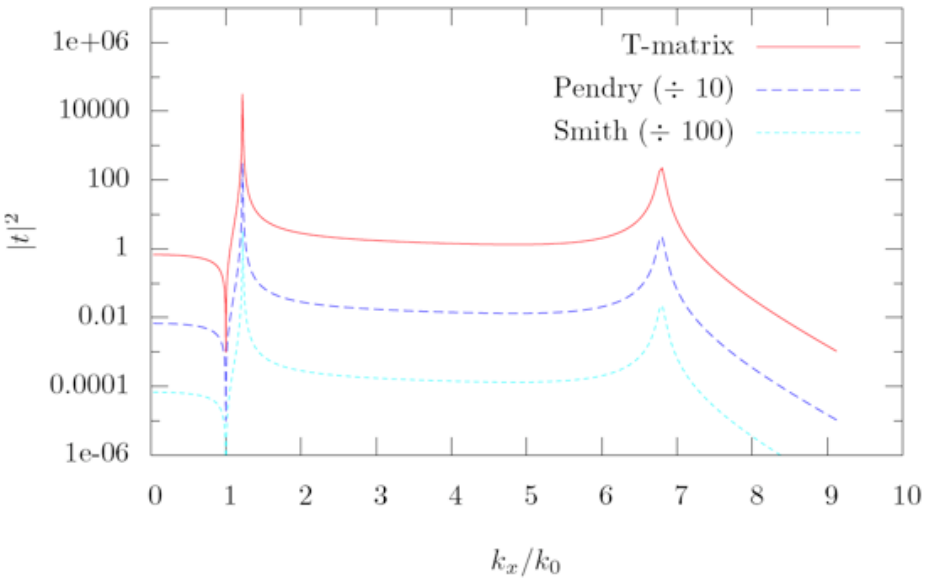

(b)

Figure 3.4: T-Matrix results (a) for a 36 nm-thick Ag slab suspended in vacuum, as described in Ref. [120]. Identical results obtained via different techniques [7, 20, 26] are shown in (b) [7].

3.2.4 Image Performance Calculation from Transfer Matrix Results

The goal of calculating transfer functions for different imaging systems is to use them to predict the behaviour of such systems when exposed to different object waveforms.

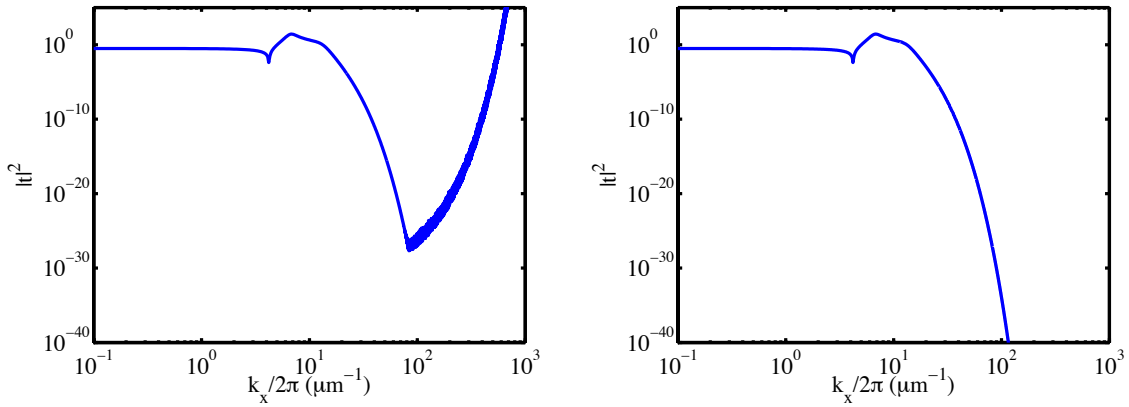

Figure 3.5: Transfer functions for a 20:40:10 nm PMMA:Ag:SiO_2 superlens [30], calculated using (a) Eq. (3.22) and (b) Eq. (3.35).

Hence, the discrete Fourier transform (DFT) was used to convert object waveforms to equivalent spectra in the spatial frequency domain; these could be multiplied directly with the TMM transfer functions, such as the ones shown in Fig. 3.3a. Inverse transforms were then used to give the expected image waveforms from the multiplied spectra.

This process of switching between the spatial and spatial-frequency domains, summarised in Fig. 3.6, allowed not only the simulation of individual cases but also allowed performance metrics to be calculated for an imaging system exposed to a series of standard object profiles, as described in Chapter 4. Furthermore, it allowed results computed by TMM to be compared with results from spatial-domain simulation techniques such as FEM, performed using COMSOL [122], and eigenmode expansion, implemented by cavity modelling framework (CAMFR) [123], as discussed in Chapter 5 and Ref. [31]. The individual steps involved in translating results to the spatial domain are detailed below.

Firstly, the discrete spatial-frequency spectrum, $IP(k)$, of an object or 'input' waveform, $ip(x)$, was calculated in Matlab [121]:

$$IP(k) = \mathcal{F}\{ip(x)\}$$

$$= \frac{1}{\sqrt{N}} \cdot \sum_{x=1}^{N} ip\,(x)\, e^{-i2\pi(k-1)(x-1)/N}, 1 \leqslant k \leqslant N, \tag{3.36}$$

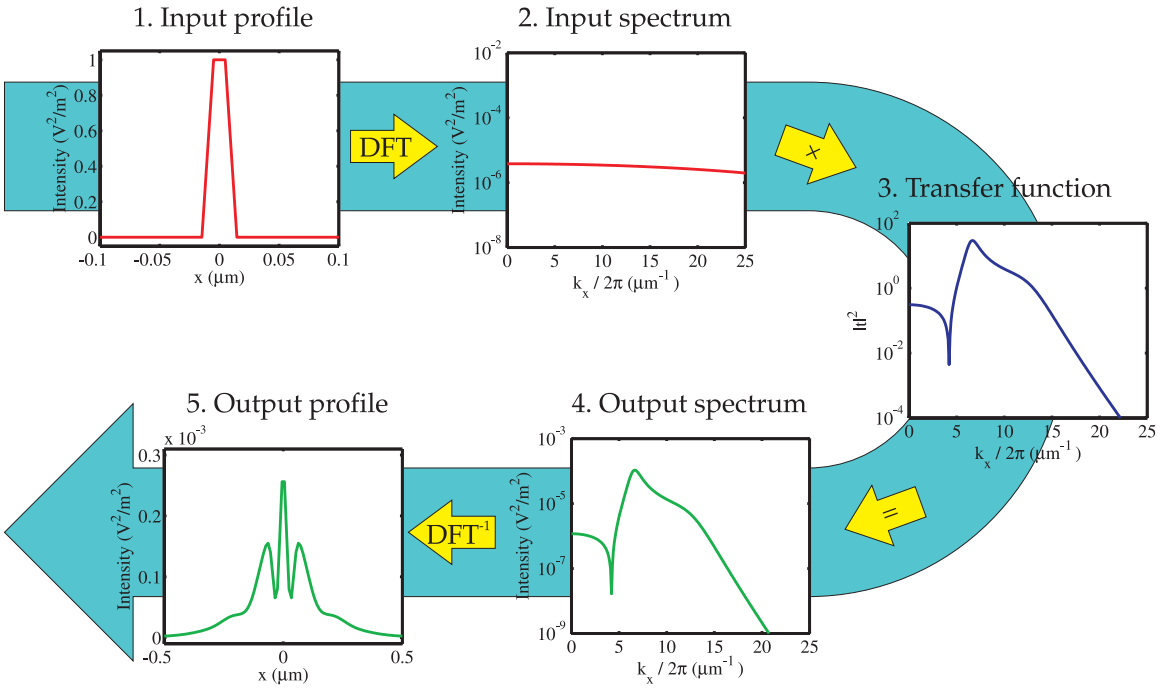

Figure 3.6: Schematic of the TMM data conversion process used to calculate spatial image profiles from spatial frequency domain TF data: a spatial domain input profile (1) is converted to the spatial frequency domain (2) via a Fourier transform. The resulting input spectrum is multiplied with a transfer function (3), which here describes the single Ag layer superlens shown in Fig. 3.2. This multiplication produces an output spectrum (4), which is converted back to the spatial domain via an inverse Fourier transform to give a spatial output profile (5).

where $\mathcal{F}\{\}$ is the fast Fourier transform (FFT). Note that $ip(x)$, shown in Fig. 3.6(1), was zero-padded to increase spatial-frequency resolution and $IP(k)$, shown in Fig. 3.6(2), was normalised by $\frac{1}{\sqrt{N}}$, where N was its length.

For the example in Fig. 3.6, $ip(x)$ was a single, 10 nm wide feature on a 1 μm support, which gave $IP(k)$ as an almost constant function with intensity of $\sim 2 \times 10^{-6}\mathrm{V}^2/\mathrm{m}^2$ over the spatial frequencies of interest, i.e. 0 – 25 $\mu\mathrm{m}^{-1}$. Once calculated, $IP(k)$ was multiplied by a transfer function, $H(k)$, shown in Fig. 3.6(3), in order to give an output spectrum, $OP(k)$, shown in Fig. 3.6(4):

$$OP(k) = IP(k) \cdot H(k). \tag{3.37}$$

In turn, the inverse DFT of $OP(k)$ was taken to yield an output waveform, $op(x)$, normalised by $\frac{1}{\sqrt{N}}$ and shown in Fig. 3.6(5). Finally, $op(x)$ was resampled to reduce its length to that of $ip(x)$, thus removing any side effects from the zero-padding opera-

tion in Eq. (3.36):

$$op(x) = \mathcal{F}^{-1}\{OP(k)\}$$
$$= \frac{1}{\sqrt{N}} \cdot \sum_{k=1}^{N} OP\,(k)\, e^{i2\pi(k-1)(x-1)/N}, 1 \leqslant x \leqslant N. \tag{3.38}$$

The end result, $op(x)$, showed a tri-peaked profile consisting of a single, central peak flanked by two smaller shoulders. Recall that such complex features were not present in $ip(x)$. This unexpected distortion between input and output profiles is an example of one of the complexities of the near-field systems that are studied in this thesis and illustrates the need for a series of specialised metrics to characterise their behaviour, as discussed in Chapter 4.

3.3 Finite Element Modelling

To complement the transfer functions (TFs) calculated by TMM, FEM was used to calculate the spatial distribution of electromagnetic fields around a superlens. This method was more sophisticated than TMM as it could handle true two-dimensional geometries, allowing such phenomena as the near-field interaction between mask and lens to be incorporated into the modelled solutions. The advantage of this added complexity was that the results produced were no longer mere approximations of physical phenomena, as the TMM results had been, but were actual calculations of what could be expected from practical experiments. The solutions calculated via FEM could also be used to validate individual TMM results, provided an appropriate Fourier transformation was applied, as discussed in Section 3.3.3. The details of these FEM models and the software used to implement them are discussed in this section, along with descriptions of some of the typical initial conditions, problem domains, and boundary conditions that were used.

3.3.1 Theory

FEM works by approximating a system of partial differential equations (PDEs), which are not conducive to being solved computationally, with an equivalent set of ordinary

differential equations (ODEs), which can be solved numerically. Individual solutions to the ODEs are calculated at numerous points or subdomains within the problem geometry, which are defined in terms of an interconnected mesh. The density of the mesh and number of subdomains that it contains are both variable, allowing for locally-varied resolution across the problem domain. This varied resolution is essential to reduce computational intensity, which is much heavier than for TMM.

3.3.1.1 From Maxwell's laws to the Helmholtz equation

In the case of time-varying electromagnetic waves, which apply to the analysis of superlenses, the governing PDEs are derived from Maxwell's equations [124, 125]. Faraday's law and Ampère's circuital law with Maxwell's correction, which describe the generation of magnetic and electrical fields and are given in Eq. (3.39) and Eq. (3.40), respectively, are rewritten in common terms to give Eq. (3.46), which is a single equation for the magnetic potential, $\mathbf{A}$. From Eq. (3.46), independent PDEs for the electric field, $\mathbf{E}$, and magnetising field, $\mathbf{H}$, can be found, as per Eqs. (3.51) and (3.53). Limiting the source radiation within the domain to transverse magnetic (TM) waves then allows the definition of Eq. (3.58), a simplified PDE in the form of the Helmholtz equation, with the expression for $\mathbf{H}$ reduced from a vector to a scalar term.

In detail, Faraday's law is given by

$$\nabla \times \mathbf{E} = -\frac{\partial \mathbf{B}}{\partial t}, \tag{3.39}$$

and the Maxwell-Ampére law is

$$\nabla \times \mathbf{H} = \mathbf{J} + \frac{\partial \mathbf{D}}{\partial t}, \tag{3.40}$$

according to the terms defined in Table 3.1 [125].

Using the constituent relations

$$\mathbf{B} = \mu \mathbf{H}, \tag{3.41}$$

$$\mathbf{D} = \epsilon \mathbf{E}, \tag{3.42}$$

and

$$\mathbf{J} = \sigma \mathbf{E}. \tag{3.43}$$

Eqs. (3.39) and (3.40) can be rephrased to give equations in $\mathbf{E}$ and $\mathbf{H}$:

$$\nabla \times \mathbf{E} = -\frac{\partial \mu \mathbf{H}}{\partial t}, \tag{3.44}$$

and

$$\nabla \times \mathbf{H} = \sigma \mathbf{E} + \frac{\partial \epsilon \mathbf{E}}{\partial t}. \tag{3.45}$$

These in turn lead to a wave equation describing the magnetic potential in the system, $\mathbf{A}$,

$$\nabla \times \left(\mu^{-1} \nabla \times \mathbf{A}\right) + \sigma \frac{\partial \mathbf{A}}{\partial t} + \frac{\partial}{\partial t} \epsilon \frac{\partial \mathbf{A}}{\partial t} = 0, \tag{3.46}$$

defined according to the dependencies [124]

$$\mu \mathbf{H} = \nabla \times \mathbf{A} \tag{3.47}$$

and

$$\mathbf{E} = -\frac{\partial \mathbf{A}}{\partial t}. \tag{3.48}$$

Using Eq. (3.48) again with Eq. (3.46), $\mathbf{E}$ can be separated from $\mathbf{H}$ to form its own independent equation, as follows:

$$\nabla \times \left(\mu^{-1} \nabla \times - \int \mathbf{E}\, dt\right) - \sigma \mathbf{E} - \frac{\partial \epsilon \mathbf{E}}{\partial t} = 0. \tag{3.49}$$

If the time-harmonic form of $\mathbf{E}$ is used,

$$\mathbf{E}\left(x, y, z, t\right) = \mathbf{E}\left(x, y, z\right) e^{i\omega t}, \tag{3.50}$$

Table 3.1: Definition of electromagnetic terms.

Symbol	**Description**	**Unit**
$\mathbf{E}$	electric field	V/m
$\mathbf{D}$	electric displacement field	C/m^2
$\mathbf{H}$	magnetising field	A/m
$\mathbf{B}$	magnetic field	T
$\mathbf{J}$	current density	A/m^2
$\mathbf{A}$	magnetic potential	Vs/m
σ	conductivity	S/m
ϕ	electric potential	V

then Eq. (3.49) simplifies to

$$\nabla \times \left(\mu^{-1} \nabla \times -\frac{1}{i\omega} \mathbf{E} \right) - \sigma \mathbf{E} - i\omega\epsilon \mathbf{E} = 0$$

$$\nabla \times \left(\mu^{-1} \nabla \times \mathbf{E} \right) + i\omega\sigma \mathbf{E} - \omega^2 \epsilon \mathbf{E} = 0$$

$$\nabla \times \left(\mu^{-1} \nabla \times \mathbf{E} \right) - \omega^2 \epsilon_c \mathbf{E} = 0, \tag{3.51}$$

where ϵ_c is complex permittivity:

$$\epsilon_c = \epsilon - i\frac{\sigma}{\omega}. \tag{3.52}$$

Applying the same steps to Eqs. (3.46) and (3.47) yields a similar expression for $\mathbf{H}$:

$$\nabla \times \left(\epsilon_c^{-1} \nabla \times \mathbf{H} \right) - \omega^2 \mu \mathbf{H} = 0. \tag{3.53}$$

From this point, simplifications can be made by restricting the orientation of source waves in the domain to TM polarisation and by forcing ϵ_r and μ_r to be isotropic in the y-direction. This reduces $\mathbf{H}$ to a scalar, H_y, and changes Eq. (3.53) to

$$\nabla \times \left(\epsilon_c^{-1} \nabla \times H_y \right) - \omega^2 \mu_{yy} H_y = 0, \tag{3.54}$$

where μ_{yy} is the component of the permeability in the y-direction. Next, the expansions $\epsilon_c = \epsilon_0 \epsilon_{rc}$ and $\mu_{yy} = \mu_0 \mu_{ryy}$ are inserted, where ϵ_{rc} and μ_{ryy} are the relative complex permittivity and relative permeability, respectively. Furthermore, ω^2 is replaced with $k_0^2/\epsilon_0\mu_0$, where k_0 is the fundamental wavenumber. This yields

$$\nabla \times \left(\epsilon_0^{-1} \epsilon_{rc}^{-1} \nabla \times H_y \right) - k_0^2 \epsilon_0^{-1} \mu_0^{-1} \mu_0 \mu_{ryy} H_y = 0$$

$$\nabla \times \left(\epsilon_{rc}^{-1} \nabla \times H_y \right) - k_0^2 \mu_{ryy} H_y = 0. \tag{3.55}$$

Expanding Eq. (3.55),

$$\epsilon_{rc}^{-1} \nabla \left(\nabla \cdot H_y \right) - \nabla \cdot \left(\epsilon_{rc}^{-1} \nabla H_y \right) - k_0^2 \mu_{ryy} H_y = 0$$

$$- \nabla \cdot \left(\epsilon_{rc}^{-1} \nabla H_y \right) - k_0^2 \mu_{ryy} H_y = 0, \tag{3.56}$$

since $\nabla \cdot H_y = 0$, as described by Gauss' law for magnetism [125]. Recognising that ϵ_{rc} in Eq. (3.56) is potentially a 2×2 tensor, as it does not need to be isotropic in the xz-plane, its inverse is given by

$$\epsilon_{rc}^{-1} = \frac{\epsilon_{rc}^{T}}{\det\left(\epsilon_{rc}\right)} = \tilde{\epsilon}_{rc}, \tag{3.57}$$

and the PDE that the FEM attempts to solve becomes [124]:

$$-\nabla \cdot \left(\tilde{\epsilon}_{rc} \nabla H_y\right) - k_0^2 \mu_{ryy} H_y = 0, \tag{3.58}$$

which is a form of the well-known and solvable Helmholtz equation. Calculation of other fields within the domain is done by applying the appropriate constituent relations and dependencies to Eq. (3.58).

3.3.1.2 Solving the Helmholtz equation

In order to find a solution to the Helmholtz equation given in Eq. (3.58), it is necessary to first reformulate the problem from a boundary value problem to a functional or weak form. This is done as follows [126]: firstly, Eq. (3.58) is multiplied by the variational, δH_y, and the integral over the entire domain, Ω, is found:

$$\int_{\Omega} \delta H_y \left[-\nabla \cdot \left(\tilde{\epsilon}_{rc} \nabla H_y\right) - k_0^2 \mu_{ryy} H_y\right] d\Omega = 0. \tag{3.59}$$

Setting $u = \delta H_y$ and $v = \nabla H_y$, integration by parts [127] yields the functional form of Eq. (3.58), $\mathcal{F}$:

$$\mathcal{F} = \frac{-1}{2} \int_{\Omega} \left[\tilde{\epsilon}_r |\nabla H_y|^2 - k_0^2 \mu_{ryy} H_y^2\right] d\Omega = 0, \tag{3.60}$$

provided the boundary conditions are all well-behaved, i.e. either homogeneous, Dirichlet or Neumann types [126]. Once the functional form is found, a solution can be determined simply by finding conditions on $\mathcal{F}$ such that it satisfies each of the boundary conditions and also becomes stationary, i.e. $\delta\mathcal{F} \rightarrow 0$ [126].

This technique effectively replaces the problem of solving a PDE with the much simpler one of minimising a function, which computers are well suited to solve using numerical techniques. In order to reduce the approximation inherent in this step, Eq. (3.60) is evaluated at many closely-spaced coordinates within Ω. In practice, a meshing algo-

rithm is used to ensure that each evaluation of Eq. (3.60) is made over a suitably small area, with the individual areal elements connected via a scalable, adjustable mesh. This gives rise to the controlled variable resolution of FEM, which is one of its main advantages over other modelling techniques.

3.3.2 Implementation

The finite element modelling method discussed in Section 3.3.1 was implemented using COMSOL [122], a multi-physics modelling and analysis environment. A dedicated radio frequency (RF) software module, together with bi-directional Matlab [121] integration, allowed for detailed models and extensive data post-processing. The specific details of the COMSOL models used in this thesis are discussed in this section, with a discussion of the post-processing and data conversion steps given in Section 3.3.3.

Individual models were constructed using COMSOL's in-plane TM wave module, which was set to use the built-in stationary solver to give harmonic propagation results. Different subdomains within the model domain were specified according to the permittivities shown in Table 3.2. The domain for an exemplar model, showing an Ag superlens exposed to a tungsten mask, is illustrated in Fig. 3.7.

Table 3.2: Material permittivites as used in FEM and T-matrix simulations.

Material	**Permittivity**	**Reference**
W	$1.497 + 7.69i$	[128]
PMMA	$2.3013 + 0.0014i$	[129]
Ag	$-2.7 + 0.23i$	[129]
SiO_2	2.368	[128]
AZ 1518 Photoresist - unbleaced	$2.933 + 0.1226i$	[130]
AZ 1518 Photoresist - bleached	$2.888 + 0.0197i$	[130]
BARLi-II ARC	$2.561 + 1.011i$	[131]
Quartz - ordinary direction	2.442	[132]
Quartz - extraordinary direction	2.473	[132]

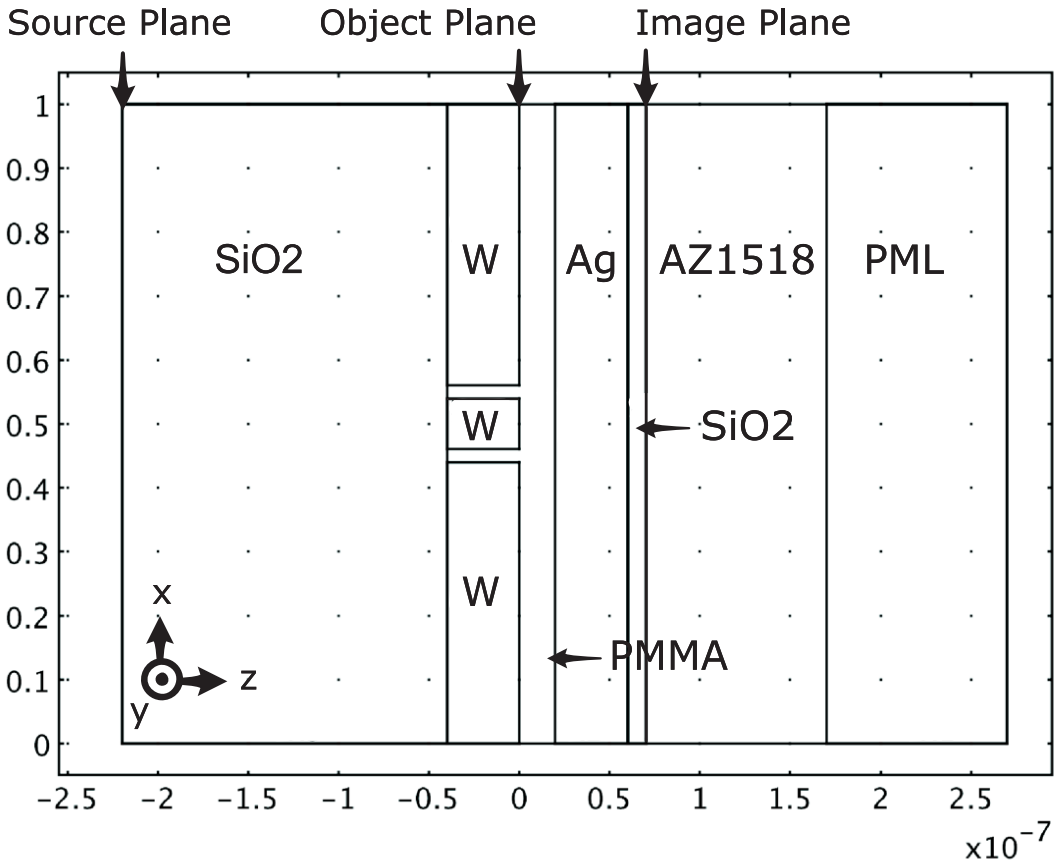

Figure 3.7: Annotated two-dimensional FEM geometry and composition, showing an Ag superlens [22] exposed to a dual-slit W mask [25]. Horizontal axis units are metres; vertical axis units are 10^{-5} metres.

Starting from the left side, this exemplar model comprised an SiO_2 subdomain that joined a 40 nm thick tungsten mask comprised of two slits, each 20 nm wide and separated by a gap of 80 nm. A 20 nm wide PMMA spacer region appeared between the mask and a 40 nm wide Ag subdomain. These two subdomains, together with a 10 nm SiO_2 region on the right face of the Ag formed the superlens under consideration.

The domain to the right of the superlens was AZ 1518 photoresist, 100 nm thick, which was terminated by an equally thick perfectly matched layer (PML). The PML absorbed energy in the z-direction without creating reflections, this attenuated standing waves in the model and mitigated the effects introduced due to the finite size of the model domain. The right-most boundary, beyond the image plane, was set as a plane wave scatterer.

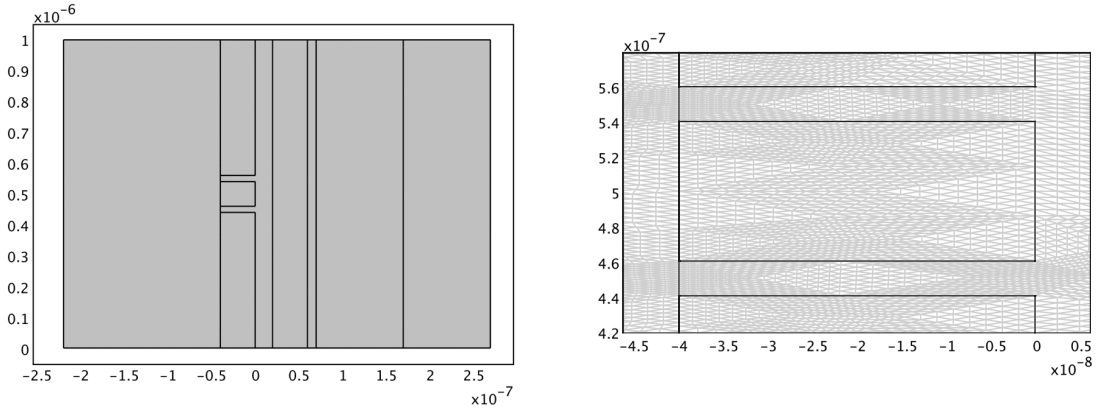

(a) (b)

Figure 3.8: Two-dimensional FEM mesh (a) for the geometry shown in Fig. 3.7, with detail of the mask features shown in (b). Horizontal and vertical axis units are metres.

At the vertical extremes of the model the top and bottom horizontal boundaries were set as periodic, in-phase boundaries. This further reduced the problem of boundary reflections by creating the illusion of infinite length in the x-direction, similar to the images produced by a pair of mirrors placed opposite and parallel to each other. Unlike the external boundaries of the model, all internal boundaries were made continuous.

The source boundary condition, that is, the boundary at the left-most edge of the model, was specified individually for each model. Unless otherwise noted, this boundary was set to a scattering condition with a magnetic source field, $\mathbf{H_0 y} = e^{ik_0 z}$ A/m. The wave type was set to 'planar' with direction vector $\mathbf{k} = -z$ and the free space wavelength of the source was set to 365 nm. This configuration corresponded to the i-line of a mercury-vapour lamp spectrum radiating along the z-axis.

Once constructed, models were meshed using the automated 'free mesh' functions. Subsequent manual refinement was performed to give between 100,000 and 200,000 mesh points per model, as shown in Fig. 3.8. Solutions to the meshed models, shown in Fig. 3.9, were exported to the Matlab environment, where post-processing allowed the extraction of electrical intensity profiles at the object and image planes. The intensity profiles for the example model detailed in Fig. 3.9 are shown in Fig. 3.10. With these data, further analysis could be done to find spatial frequency spectra and transfer functions that were compatible with data from TMM, as discussed in Section 3.3.3.

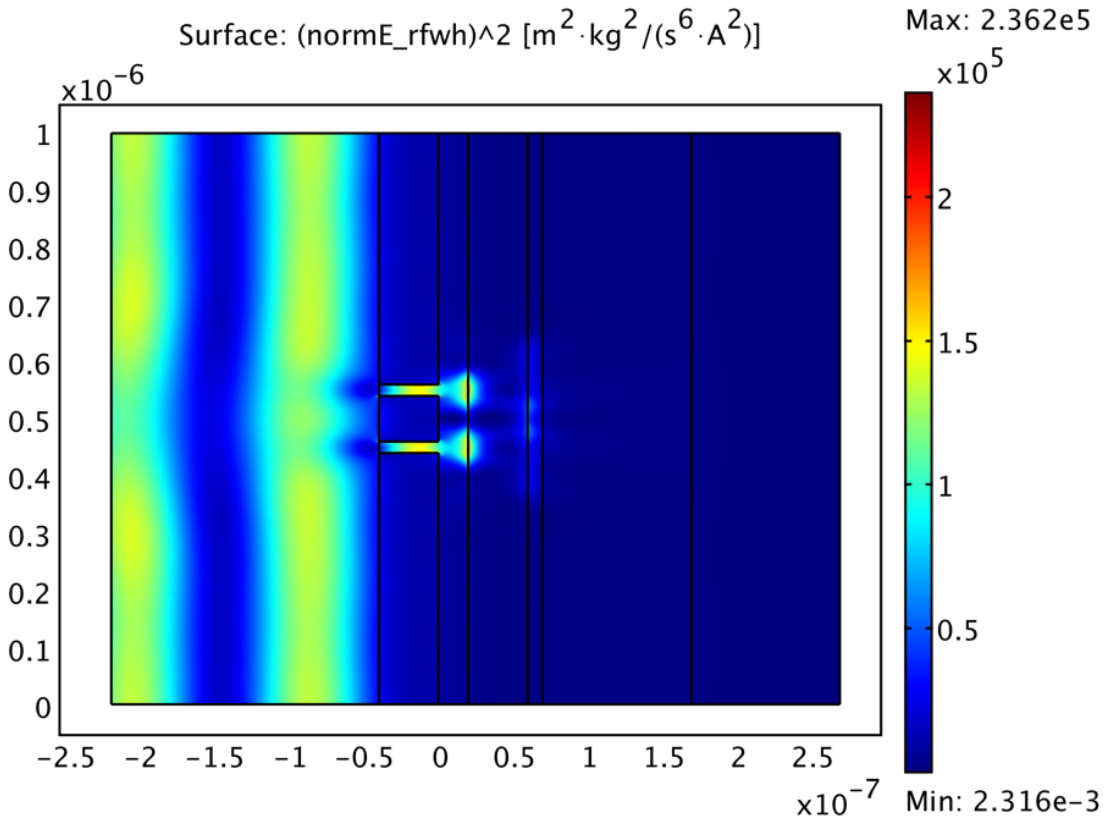

Figure 3.9: Norm square of simulated electric field for the geometry shown in Fig. 3.7. Horizontal and vertical axis units are metres. Colour bar units are V^2/m^2.

It is worth noting that care had to be taken when selecting which field to calculate. For comparison with TMM results, the x-component of the electric field is relevant, as the transmission and reflection coefficients described in Section 3.2.1 are calculated in terms of E_x. However, for practical experiments, such as those described in Chapter 7, the entire electrical field, $\mathbf{E} = \sqrt{E_x^2 + E_z^2}$, is required to correctly model photoresist exposure patterns.

3.3.3 Transfer Function Estimation from Finite Element Model Results

In a similar manner to that described in Section 3.2.4, FEM line profiles were converted to spectra in the spatial frequency domain. This allowed TFs to be calculated, which

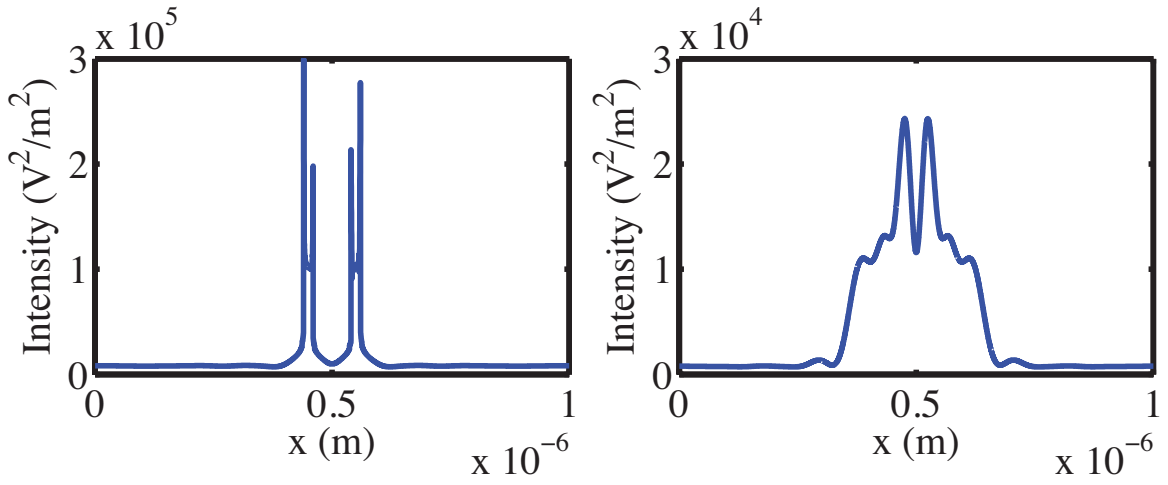

(a) (b)

Figure 3.10: Electric field intensity line profiles extracted at the object plane (a) and image plane (b), from the superlens model described in Fig. 3.7.

could be compared with TMM data. The details of this conversion process are presented in this section.

Semi-aperiodic masks containing a single, 10 nm wide slit feature were used as input stimuli in order to illicit an approximate lens impulse response that was rich in high frequency components. Taking $ip(x)$ and $op(x)$ from line scans of these simulations, transfer functions were calculated as follows:

$$IP(k) = \mathcal{F}\{ip(x)\}, \tag{3.61a}$$

$$OP(k) = \mathcal{F}\{op(x)\}, \tag{3.61b}$$

hence

$$H(k) = \frac{OP(k)}{IP(k)}, \tag{3.62}$$

where $\mathcal{F}\{\}$ is the FFT and $ip(x)$, $op(x)$, $IP(k)$ and $OP(k)$ are the input profile, output profile, input spectrum and output spectrum of the model, as per the definitions given in Section 3.2.4. A graphical representation of this process is given in Fig. 3.11.

To ensure that the reconstructed TFs were characteristic of the superlenses in the models, rather than the masks used to stimulate them, tests were run using several different masks as input stimuli, as shown in Fig. 3.12. The TFs produced by these masks

were approximately identical, indicating that the size of the mask features was not colouring the reconstructed TFs, as shown in Fig. 3.13. What little variation there was between TFs appeared to be due to noise related to the unique mesh matrices specified for each FEM model. This noise was minimised as the number of mesh points was increased, as shown in Fig. 3.14. For this reason the number of mesh points in each FEM simulation was never lower than 150,000, with some simulations having upwards of 400,000 mesh points.

3.4 Summary

The TMM and FEM techniques described here provide complementary approaches to analysing different lithographic systems. The speed of TMM and the spatial frequency domain transfer functions that it calculates for ideal, smooth interfaces are supported by FEM intensity profiles, which are extracted from rigorous solutions to more complex geometries that require more computational time and power to generate. When used together, these tools form a comprehensive suite that can characterise imaging systems over a range of different levels of detail and complexity. They are therefore adequate tools to address the question posed at the start of this chapter, concerning the suitability of PLL to general purpose lithography applications. The first part of the answer to that question, which deals with the difference between single-Ag layer and multi-Ag layer superlens designs and the different ways in which their performance can be characterised, is presented in Chapter 4.

3.4.1 Agreement between Transfer Matrix and Finite Element Model Results

Despite this convenient symbiosis between techniques, close analysis of equivalent results derived by TMM and FEM often reveals subtle differences that should be considered carefully. For instance, the transfer functions calculated by different techniques in Figs. 3.6 and 3.11, reproduced here in Fig. 3.15, do not have exactly the same shape. Similarly, the sidelobes on the image profiles in Figs. 3.6 and 3.11, again reproduced

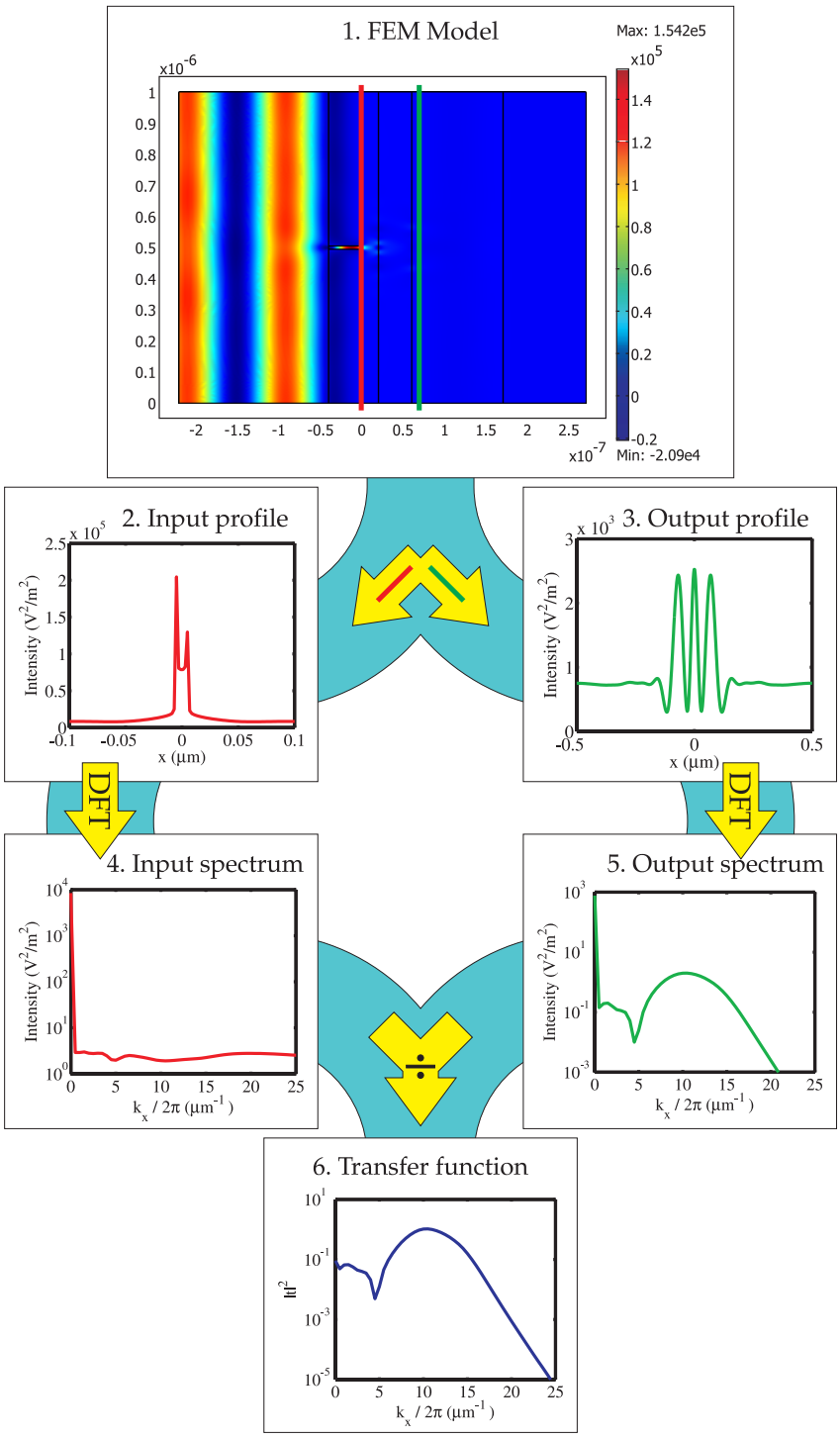

Figure 3.11: Schematic of the FEM data conversion process used to calculate transfer functions from spatial domain data: a FEM model (1), which in this example describes an isolated, 10 nm wide feature on a 40 nm thick W mask in contact with the single Ag layer superlens shown in Fig. 3.2, is used to generate spatial domain input (2) and output (3) waveforms, which are converted to the spatial frequency domain via a DFT (4, 5). The resulting output spectrum (5) is divided by the input spectrum (4), to give the transfer function (6) of the lens described by the FEM model.

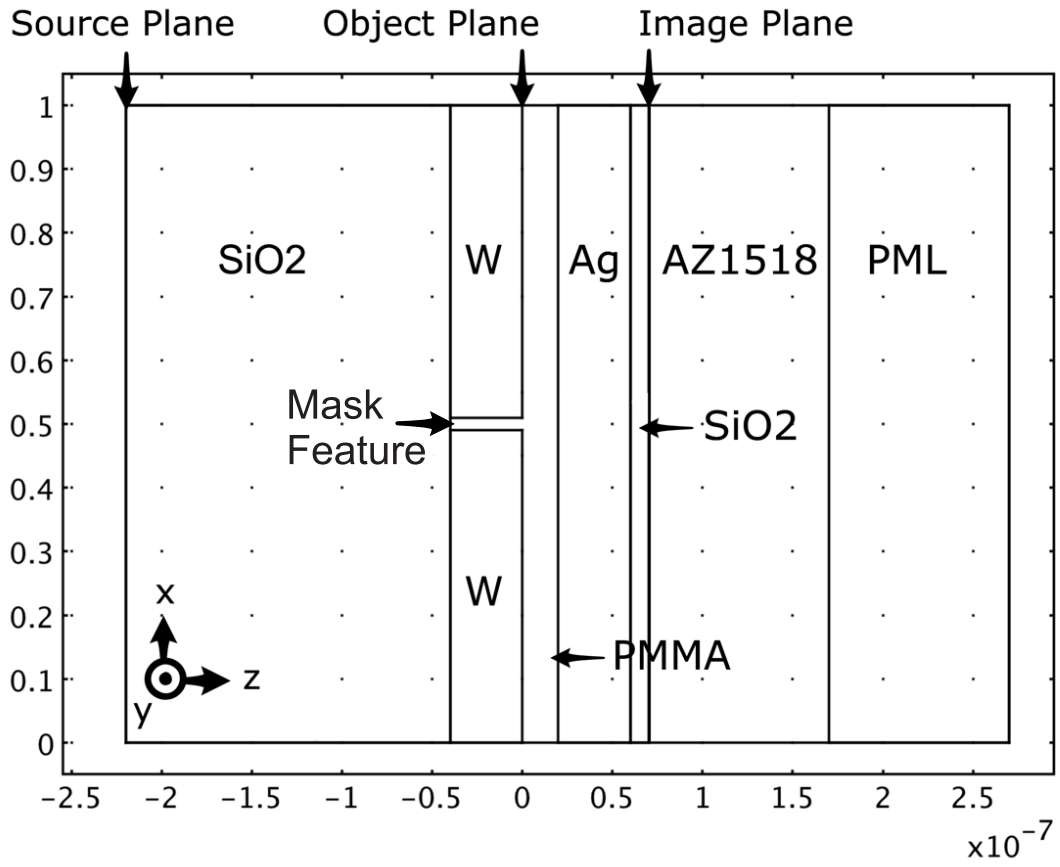

Figure 3.12: Annotated two-dimensional FEM geometry showing the mask and superlens used to test the TF retrieval process described in Fig. 3.11. The size of the feature in the mask is varied between 5 nm and 20 nm in 5 nm steps. The total mask width is kept constant at 10 μm. Horizontal axis units are metres; vertical axis units are 10^{-5} metres.

for convenience in Fig. 3.16, are less pronounced in the TMM calculated results than in the FEM solution.

These differences arise mainly from near-field interactions between the mask and superlens [31], which are included in the FEM simulations that contain an explicitly defined mask. TMM, on the other hand, is concerned only with the superlens stack, and is reliant on a synthetic input profile to generate images, thus any interactions between a mask and lens are not calculated. Hence differences between TMM and FEM results appear mainly due to the different scope of each technique, with TMM limited to only isolated lens stacks composed of perfectly smooth layers.

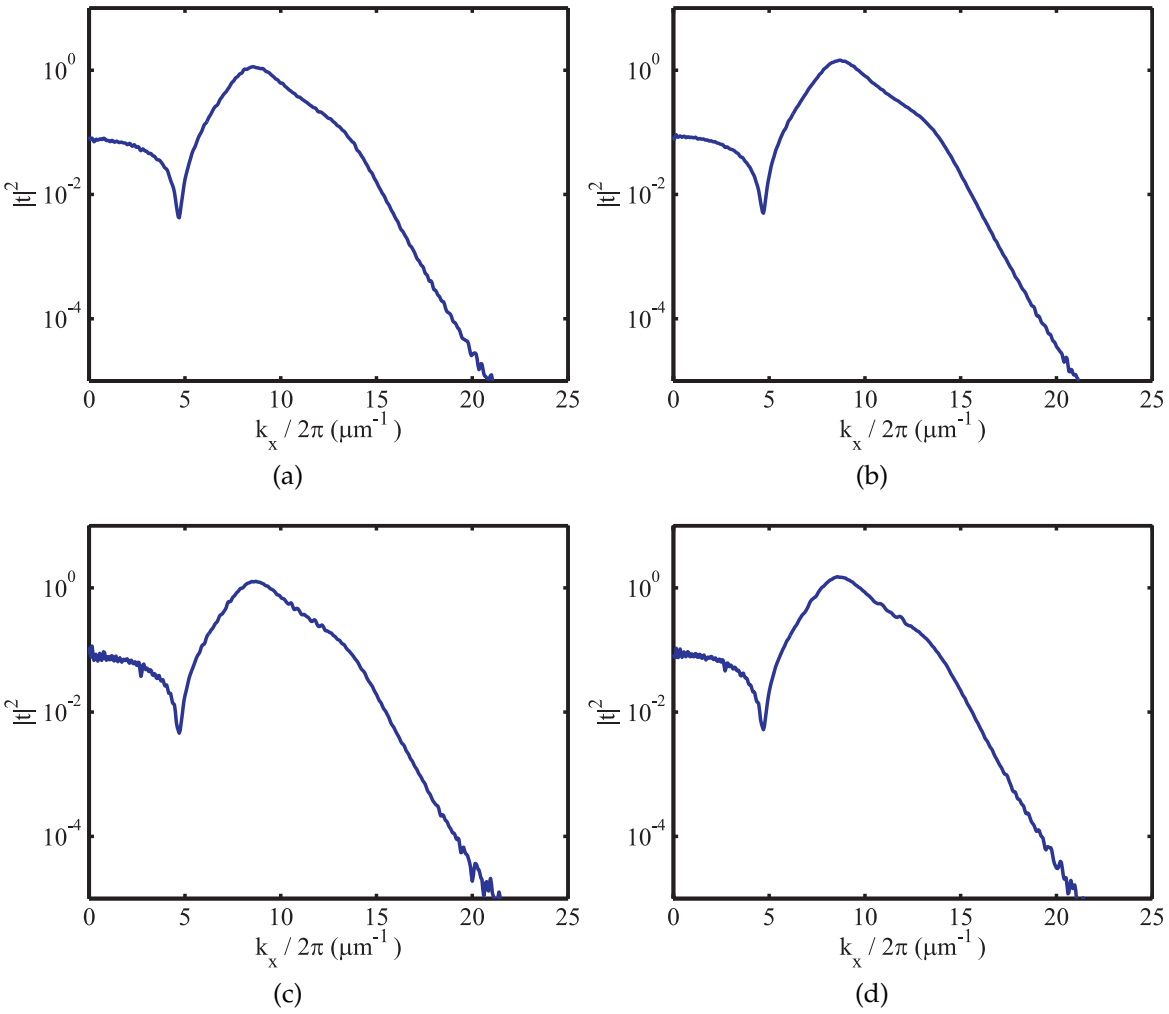

Figure 3.13: Transfer functions reconstructed from FEM simulations of the geometry shown in Fig. 3.12. The size of the feature in the mask is varied between (a) 5 nm, (b) 10 nm, (c) 15 nm and (d) 20 nm.

Although these conditions on TMM analysis allow only qualitative conclusions to be drawn from the resulting data, the level of detail is still sufficient to thoroughly explore the potential and capabilities of different ENFOL and PLL systems, as is done in Chapter 4. The many uses of TMM in the literature support this view [24–27, 41, 63, 81, 82, 96, 133–142] and hence the analysis in Chapter 4 is performed with this method. Nevertheless, the challenge of incorporating mask effects into TMM calculations is an interesting one and Chapter 5 is dedicated to solving this problem.

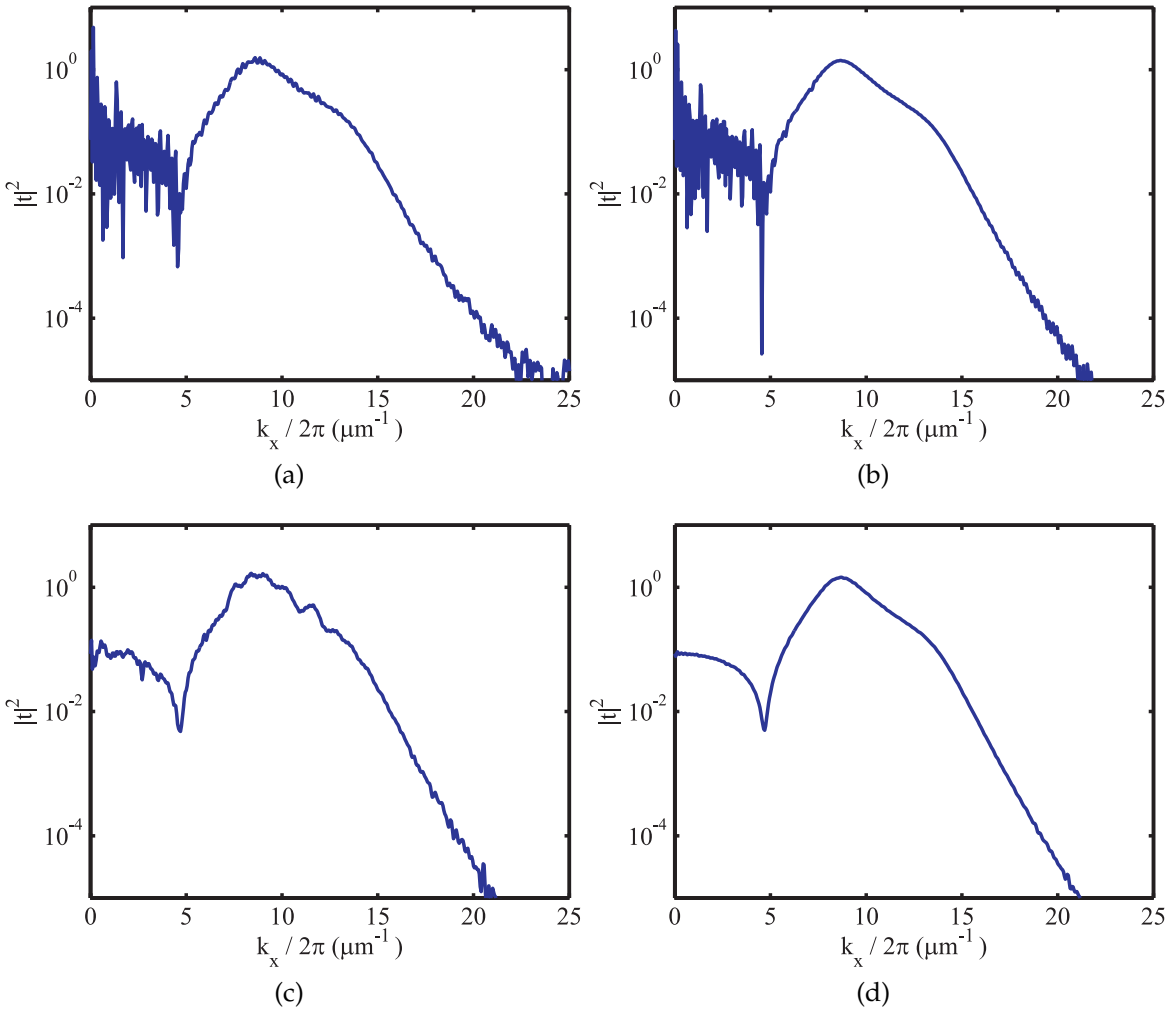

Figure 3.14: Transfer functions reconstructed from FEM simulations containing the masks shown in Fig. 3.12. The size of the feature in the mask is fixed at 10 nm, with the number of mesh points in the FEM model varied between approximately (a) 30,000 points, (b) 80,000 points, (c) 120,000 points and (d) 330,000 points.

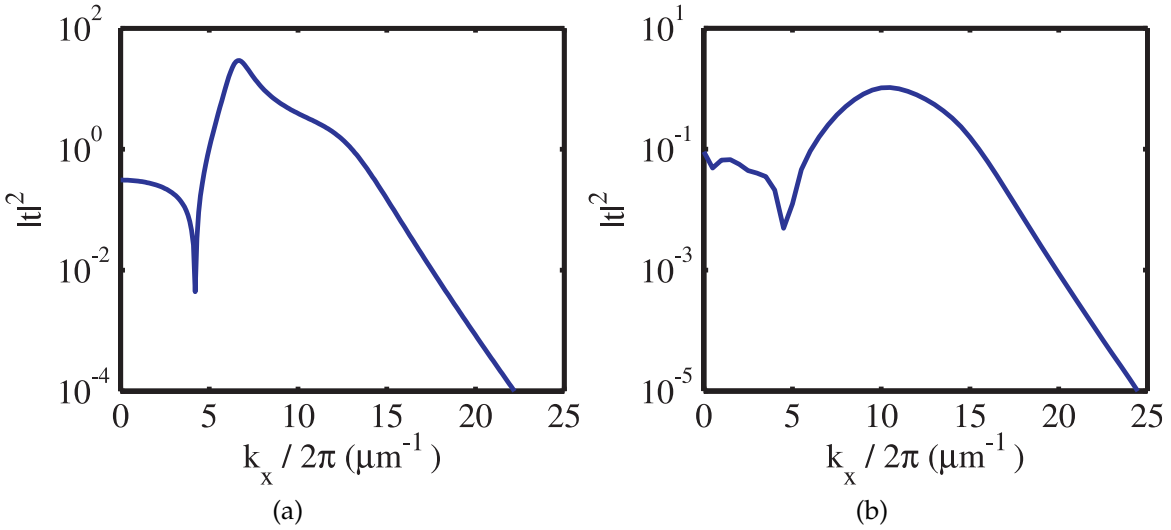

Figure 3.15: Transfer functions for a 20:40:10 nm PMMA:Ag:SiO_2 superlens, calculated via TMM (a) and FEM (b). Subtle differences in the two results, such as a more pronounced resonant peak in the TMM curve, are due to mask-lens interactions that are only calculated by FEM.

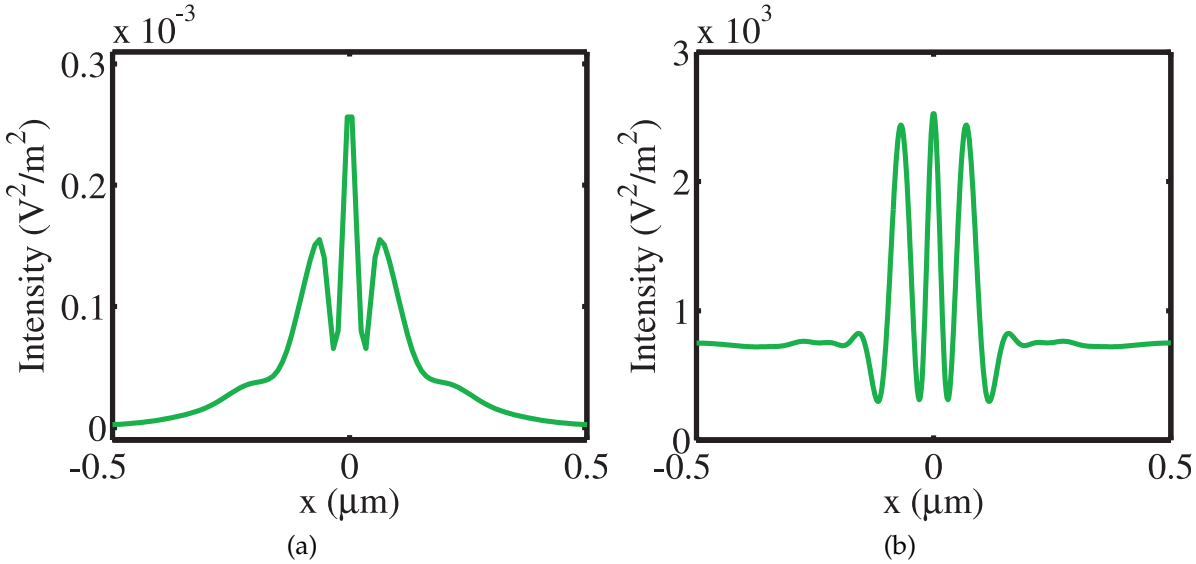

Figure 3.16: Images formed by a 20:40:10 nm PMMA:Ag:SiO_2 superlens exposed to a mask with a single, 10 nm wide feature, calculated via TMM (a) and FEM (b). Differences in the two results, such as more pronounced sidelobes in the FEM result, are due to mask-lens interactions that are only calculated by FEM.

Chapter 4

Image Fidelity for Single-Layer and Multi-Layer Silver Superlenses*

There was much excitement within the scientific community after the proposal [20] and initial implementation [22, 23] of silver (Ag)-based superlenses. Theory [81] as well as negative refraction experiments at microwave frequencies [38, 40–42] predicted that such planar structures would be able to break the diffraction limit; however, the extent of their potential remained unknown since loss in the Ag layers [81] and surface roughness in engineered examples [28] limited their ultimate resolution. For want of a better alternative, simple optical transfer functions became the de facto standard for the theoretical and numerical characterisation of superlenses [7, 22, 26, 27, 63, 75, 120, 143], with only a few representative line objects, such as Pendry's double-peak profile [20], used occasionally for characterisation in the spatial domain. In contrast, most experimental studies [22, 23, 28] used semi-infinite line gratings as standard test objects and quoted the period of the smallest features that could be resolved from such gratings.

Although these metrics are convenient to quote and compare, their usefulness is limited if superlens imaging is to progress from a scientific curiosity towards real imaging applications. Transfer functions work well as a rough measure of the charateristics of

*Aspects of the work presented in this chapter were published as: C. P. Moore, M. D. Arnold, P. J. Bones and R. J. Blaikie, "Image fidelity for single-layer and multi-layer silver superlenses," *Journal of the Optical Society of America A: Optics, Image Science and Vision*, vol. 25, no. 4, pp. 911–918, April 2008 (17 citations as at 17 May 2011, according to Google Scholar and ISI Web of Knowledge.)

a lens but they often lack the ability to predict how a superlens design will fare for a given application. Conversely, the conclusions gained from the semi-infinite gratings are specific to a given type and size of object but are not easily generalised. Hence, new tools for describing superlens performance are necessary in order to better understand their behaviour and assess their capabilities.

To illustrate the need for a careful image quality analysis, examples of different images from single Ag layer and multi-Ag layer silver superlenses are shown in Fig. 4.1. The fundamental difference between the lens stacks, both of which have the same object-image separation and total Ag thickness, is that one has a single 40 nm thick silver layer and the other has eight 5 nm thick silver laminations. Two input objects are used to test the superlenses: firstly, a pair of 20 nm wide bright lines with 80 nm centre-to-centre spacing [27], followed by a pair of 20 nm wide dark lines with the same spacing. Both objects are illuminated with TM polarised, 365 nm wavelength light. These objects have the same information content and the same spatial-frequency spectral extent, however, they differ only in the fact that the dark-line-pair object has a significantly higher DC spatial-frequency component. The imaging of these objects is carried out using TMM; line scans of the images of the bright- and dark-line-pair objects are shown in Fig. 4.1(a) and (b), respectively.

For the bright-line-pair object shown in Fig. 4.1(a), the performance of the multilayer superlens is clearly superior to the single-layer lens, even though they both have the same silver thickness. This case was considered previously [27, 77] and seems to support the conclusion that multilayer superlenses are superior to single-layer lenses. However, when studying the performance of the same lenses for the dark-line-pair object in Fig. 4.1(b) the situation is more complicated; neither lens performs particularly well and the resulting images are not as sharply defined as the images of the bright-line-pair object imaged through the multilayer lens. If a qualitative distinction has to be made between the two lenses, it is that the single-layer lens produces an image more in keeping with the dual troughs of the original object.

It is clear from this simple example that superlens behaviour is not trivial and that performance can vary greatly, even between similar applications. Hence, there is a need to develop a more general set of image classification techniques to complement existing transfer function analysis and example-image comparisons that are usually reported in the literature. To address this shortcoming, quantitative image quality

measures have been developed and are presented here, with the aim of providing robust tools that clearly express the strengths and weaknesses of different near field imaging systems.

4.1 Method

To demonstrate the image quality metrics considered here, several different practical and theoretical Ag-based superlenses were simulated using the TMM method described in Section 3.2. Analysis is carried out for 365 nm wavelength light, mimicking the i-line wavelength produced by mercury vapour bulbs typically used in practical experiments. The dimensions of the different imaging systems are given in Fig. 4.1c, with the relative permittivities of the constituent materials given in Table 4.1. Materials are specified as non-magnetic at optical wavelengths, hence their relative permeability, μ_r, is fixed at 1.0.

Table 4.1: Material permittivities used to model superlenses.

Material	**Relative Permittivity, ϵ_r**	**Reference**
Ag	$-2.7 + 0.23i$	[129]
PMMA	$2.3013 + 0.0014i$	[129]
SiO_2	2.368	[128]
Vacuum	1	

Two groups of imaging metrics were calculated, with a distinction made between metrics that depended only on the composition of the lens, known as 'lens-specific' metrics, and those that depended jointly on the construction of the lens and the object that it images, i.e. 'object-lens' metrics. For the object-lens metrics, a comprehensive set of source objects were chosen from the four families of intensity profiles shown in Fig. 4.2. These are: a single bright slit on an otherwise dark background; a single dark slit on a bright background; two bright slits on a dark background, and two dark slits on a bright background. Total pattern width is set at 10 μm for the single-slit patterns, whereas 30 μm is used for the dual-slit patterns because of their larger overall feature size. Slit widths are varied between 1 nm and 2.5 μm. The space between adjacent slits in the dual-slit profiles is set to be the same width as the slits themselves.

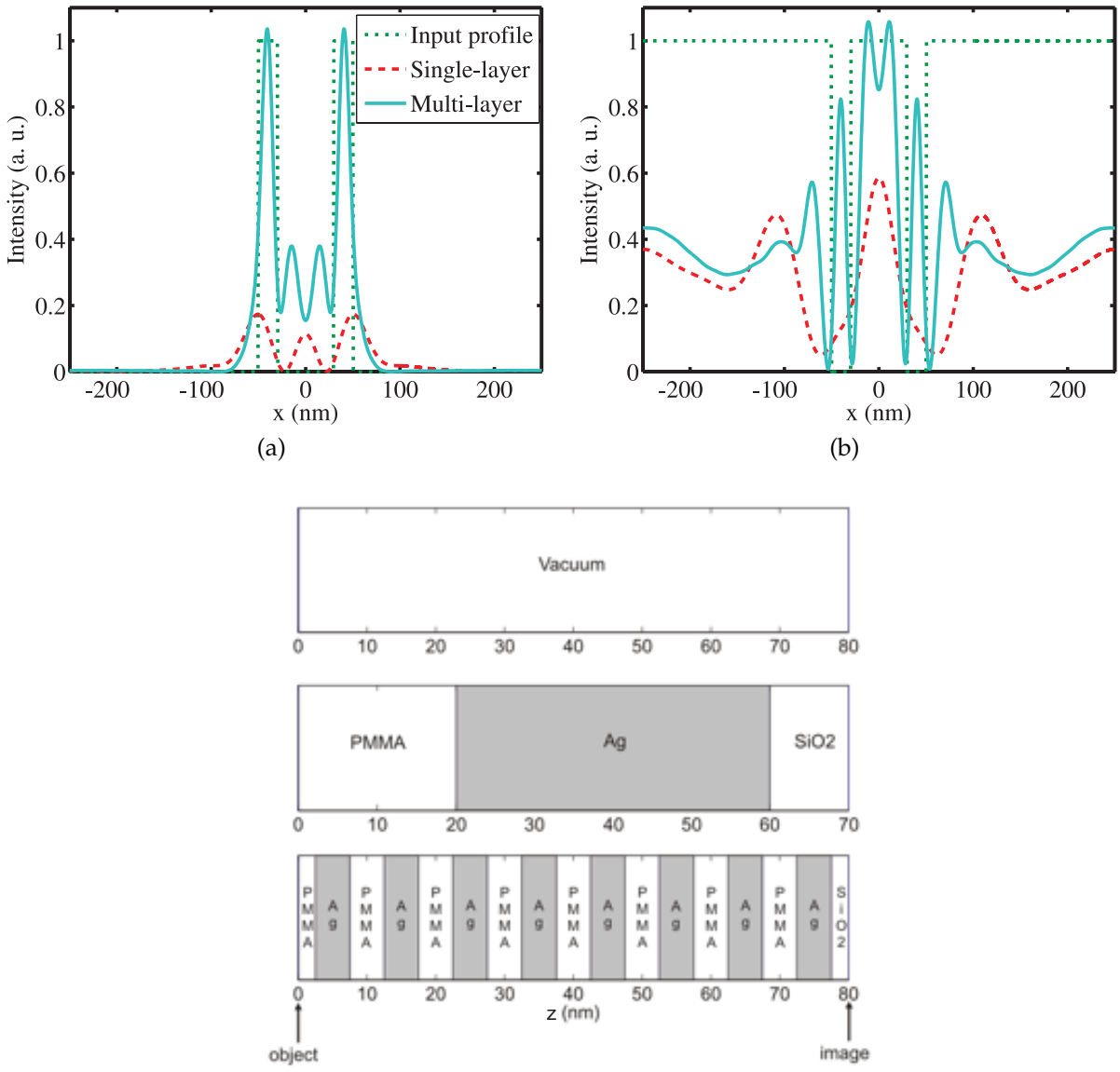

Figure 4.1: Comparison of 20 nm bright-line-pair (a) versus dark-line-pair (b) images for single layer and multilayer superlenses. Note that the multilayer lens (solid) outperforms the single layer lens (dashed) when imaging the bright features (a) but not when imaging the dark features (b). The composition and dimensions of the superlenses are given in (c). Top: 80 nm vacuum gap used for proximity imaging. Middle: Single layer silver superlens with 10 nm SiO_2 final layer in accordance with practical experimental conditions [63]. Bottom: Multilayer superlens made up of eight individual 5 nm silver laminations. Total silver thickness is 40 nm, as for the single layer lens. Input object patterns are applied from the left of the lenses and output images are retrieved from the right, as indicated.

More conventional input patterns, such as line grating profiles, were avoided in this analysis, since the performance of a superlens when exposed to a grating can be readily predicted to first order based only on the transfer function of the superlens. In other words, the transmission coefficient of a superlens corresponding to the fundamental period of a grating is usually all that is required to predict how well the lens will image the grating. Any more complicated metrics would thus likely be redundant.

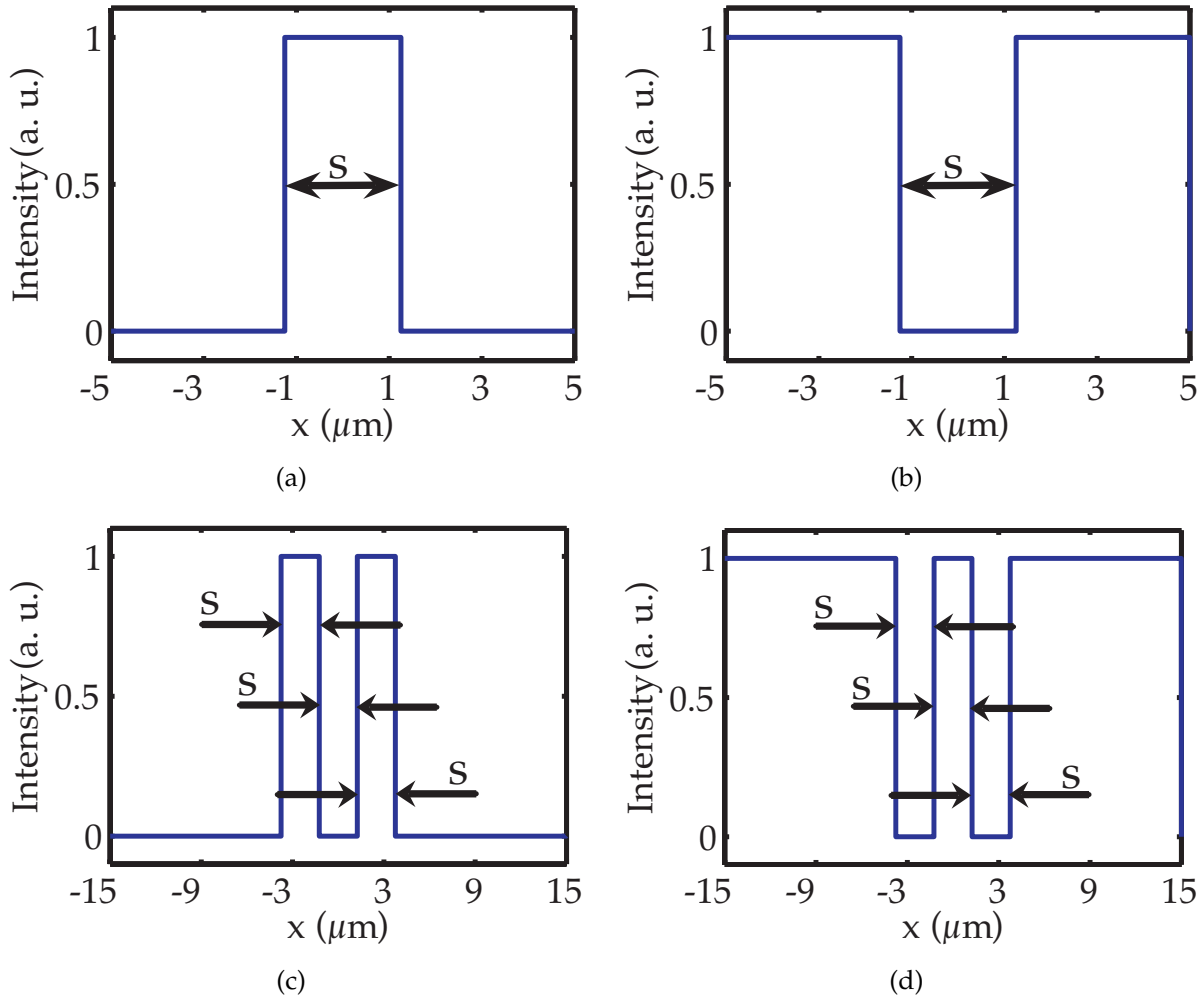

Figure 4.2: (a) Single bright slit, (b) single dark slit, (c) dual bright slit, and (d) dual dark slit input intensity patterns used to generate contrast, error, and correlation profiles. Slit widths are varied between 1 nm and 2.5 μm.

4.2 Lens-Specific Metrics

Different superlens designs are characterised first in the spatial frequency domain by means of their transfer function (TF). This allows the relative magnitude of their transmission coefficients at high spatial frequencies to be used to predict their sub-wavelength performance in the spatial domain. A simple improvement to this analysis involves calculating bandwidth, BW, and peak wavenumber, Λ_{peak} figures of merit. This is done because it is not only the absolute values of the TF coefficients but also the shape of the TF that determines image fidelity. The details of this analysis are presented in this section, along with an interpretation and explanation of the accompanying results.

4.2.1 Transfer Functions

The first indicator considered was a lens transfer function, which is by far the most common imaging metric presented in the literature to date [7, 23, 26, 27, 63, 75, 77, 120]. This figure of merit (FOM) depends only on the construction of the superlens, i.e. it is lens-specific; it can be calculated analytically and it provides an easy way to see what happens to individual spatial frequency components as they pass through a lens. The TF also provides an indication of the minimum feature size that can be transmitted through a lens for a given loss in intensity. Fig. 4.3 shows the simulated TFs of the imaging systems described in Fig. 4.1c. These systems are a single-Ag layer superlens, a multi-Ag layer superlens and an 80 nm vacuum gap, which is included to give an estimate of the characteristics of conventional lenses. The superlenses, which both have total Ag thickness of 40 nm, were used to produce the spatial profiles shown in Fig. 4.1.

The comparison of transfer functions in Fig. 4.3 highlights the rich spatial-frequency behaviour that is present in these superlenses. Looking at the performance for high spatial frequencies, the multilayer lens gives a significant response up to $k_x/2\pi \geqslant 25\ \mu\mathrm{m}^{-1}$, corresponding to image features at a scale below 40 nm — an impressive performance that would be desirable to have in practical imaging systems using visible light. This multilayer lens also responds better to these high spatial frequency components than either of the other lenses. However, the performance of the TFs

around and below the diffraction limit, i.e. in the range of 2.7 μm^{-1} to 4 μm^{-1}, is rather complicated, exhibiting a resonant response for the superlenses, and differing greatly from system to system. This low-wavenumber behaviour can significantly affect image quality, as poor transmission of the DC component of the object and distortion due to introduced resonance can drastically reduce image fidelity, as was illustrated in Fig. 4.1.

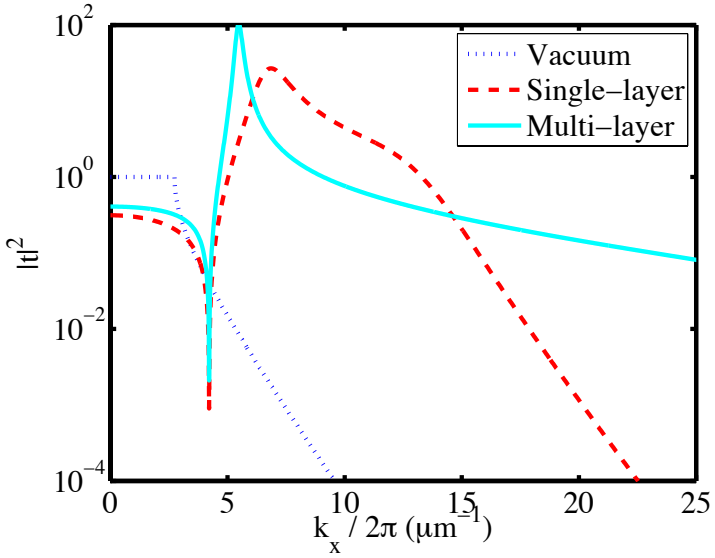

Figure 4.3: Transfer functions for single-layer and multilayer superlenses and an 80 nm vacuum gap. The single-layer lens is 40 nm thick, sandwiched between PMMA and SiO_2 spacers, whereas the multilayer lens consists of eight 5 nm thick silver laminations (separated by 5 nm) with the same PMMA and SiO_2 outer layers.

4.2.2 Bandwidth and Peak Wave Number

The TFs described in Section 4.2.1 could be summarised by their bandwidth (BW) and peak wavenumber (Λ_{peak}), which provide two lens-specific FOMs with which to compare different superlens designs. For the purposes of this thesis, BW is defined as the range of spatial wavenumbers over which the transmission of a system, e.g. a superlens, is greater than half of the maximum transmission of that system, as shown in Fig. 4.4. A specific peculiarity of superlens systems is that there is a dip in transmission at wavenumbers around the conventional diffraction limit. This leads to two passbands with different bandwidths, one in the propagating region of the spectrum, $\mathrm{BW}_{\mathrm{prop}}$, and the other in the evanescent regime, $\mathrm{BW}_{\mathrm{evan}}$. The total bandwidth of the

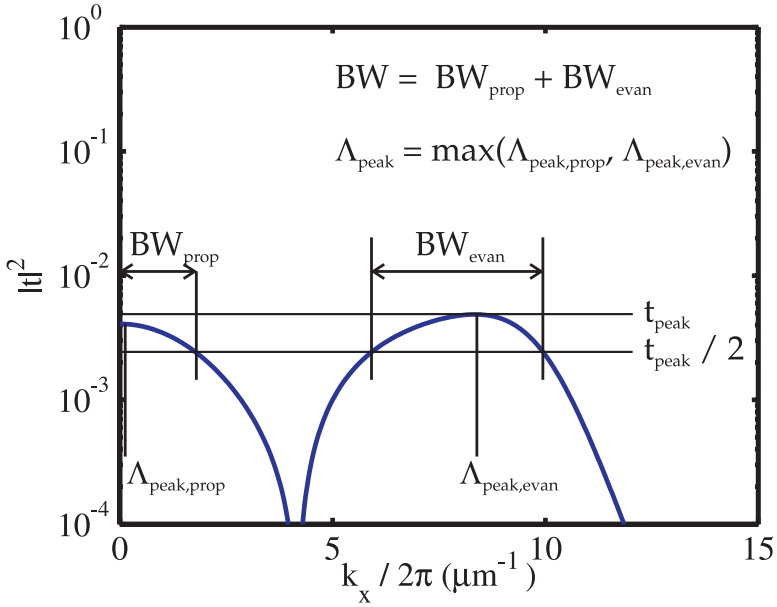

Figure 4.4: Transfer function for a 20:90:20 nm PMMA:Ag:PMMA superlens, annotated with measurements that are used to define the BW and Λ_{peak} metrics.

system, BW, is given by the sum of $\mathrm{BW}_{\mathrm{prop}}$ and $\mathrm{BW}_{\mathrm{evan}}$:

$$\mathrm{BW} = \mathrm{BW}_{\mathrm{prop}} + \mathrm{BW}_{\mathrm{evan}}. \tag{4.1}$$

Also shown in Fig. 4.4, Λ_{peak} is defined as the wavenumber at which maximum transmission occurs. Similarly to the BW metric, local peak wavenumbers (Λ_{peak}s) can be defined for both the propagating, $\Lambda_{peak,prop}$, and evanescent, $\Lambda_{peak,evan}$, parts of the spectrum, with Λ_{peak} of the system given by the larger of these two values:

$$\Lambda_{peak} = \max(\Lambda_{peak,prop}, \Lambda_{peak,evan}). \tag{4.2}$$

Hence, an ideal imaging system would have sub-wavelength Λ_{peak} and high BW, indicating a wide range of object profiles that could be transmitted by that system. In contrast, systems with low BW would be better suited to single-purpose applications.

Table 4.2 contains the values of these metrics for the imaging systems defined in Fig. 4.1c. The similar values of BW for the vacuum gap and single-Ag layer superlens confirm that the superlens has a similar range of operation compared to a conventional lens but with much better resolution, as indicated by the larger Λ_{peak} of the superlens. On the other hand, the small BW and high Λ_{peak} of the multi-Ag layered superlens suggest

that, although it may have greater evanescent transmission than the single-layered lens, its optimum imaging range is much narrower, indicating that this design is better suited to single-purpose applications.

Table 4.2: Bandwidth and peak wavenumber metrics for the lenses described in Fig. 4.1c.

Design	**BW (μm^{-1})**	Λ_{peak} **(μm^{-1})**
Vacuum gap	3.15	3.08
Single-Ag layer superlens	2.93	8.53
Multi-Ag layer superlens	0.56	6.60

4.3 Object-Lens Metrics

Even with the improved analysis in the spatial frequency domain, spatial domain examples were occasionally necessary to illustrate and improve the interpretation of spectral results. To this end, new superlens imaging metrics were calculated for a range of semi-aperiodic objects whose fundamental periods ranged from several wavelengths to a few thousandths of a wavelength. These metrics, which calculated the contrast and correlation coefficients for different images, gave a sense of the ideal object type for a given lens, predicting which object and lens combinations would fare well in practical imaging experiments and estimating the amount of distortion introduced into an image.

4.3.1 Contrast and Pseudo-Contrast

One of the most important image qualities is contrast, an object-lens metric which needs to be as high as possible for an image to be of use in a microscopy or lithography process [144]. Accordingly, the Michelson contrast, C_M, of an intensity profile or image is defined as [145]

$$C_M = \frac{I_{max} - I_{min}}{I_{max} + I_{min}}, \tag{4.3}$$

where I_{min} and I_{max} are the extreme intensities of the image's electric field, illustrated in Fig. 4.5. The example shown in Fig. 4.5 is for the case of a 75 nm dark feature

imaged through a 20:40:10 nm PMMA:Ag:SiO_2 superlens. The Michelson contrast for the resulting image is $C_M = 0.998$.

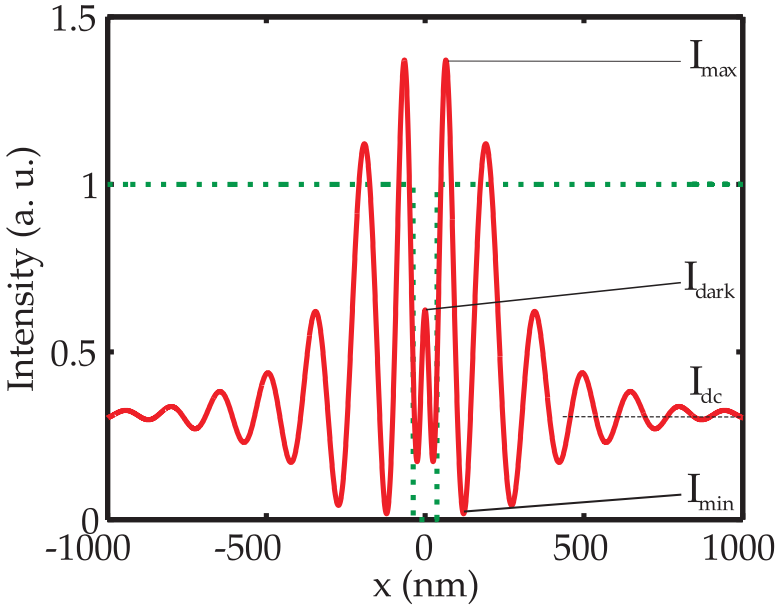

Figure 4.5: Input (dashed) and output (solid) intensity profiles for a 75 nm feature imaged through a 20:40:10 nm PMMA:Ag:SiO_2 realisable superlens. The definitions for the maximum intensity I_{max}, minimum intensity I_{min}, background intensity I_{dc}, and the intensity at the centre of the dark-line feature in the object I_{dark}, are shown for use in the contrast and pseudo-contrast calculations.

The Michelson contrast values of the lenses shown in Fig. 4.1c were calculated for the dark-slit input profiles shown in Fig. 4.2(b) and Fig. 4.2(d). The resulting profiles are shown in Fig. 4.6. As expected, contrast is high for all lenses when the slit width is much greater than the wavelength of the exposing light. In the sub-wavelength regime, the contrast for the superlenses is noticeably higher than for the proximity gap, illustrating the diffraction limit which hinders such conventional systems and giving an indication of the benefits that superlenses can provide. Interestingly, the single-Ag layer superlens has higher contrast than the multi-Ag layer variant over much of the evanescent spectrum, despite the higher transmission of the multi-layer lens shown in the TFs.

Although Michelson contrast can predict which images will be suitable for lithography, it cannot identify the level of similarity or difference between source objects and their images. This problem is shown most clearly in Fig. 4.5, where the output profile with high contrast of 0.998 is nevertheless a poor representation of its source profile, due to the extensive ringing that is induced outside the spatial extent of the 75 nm

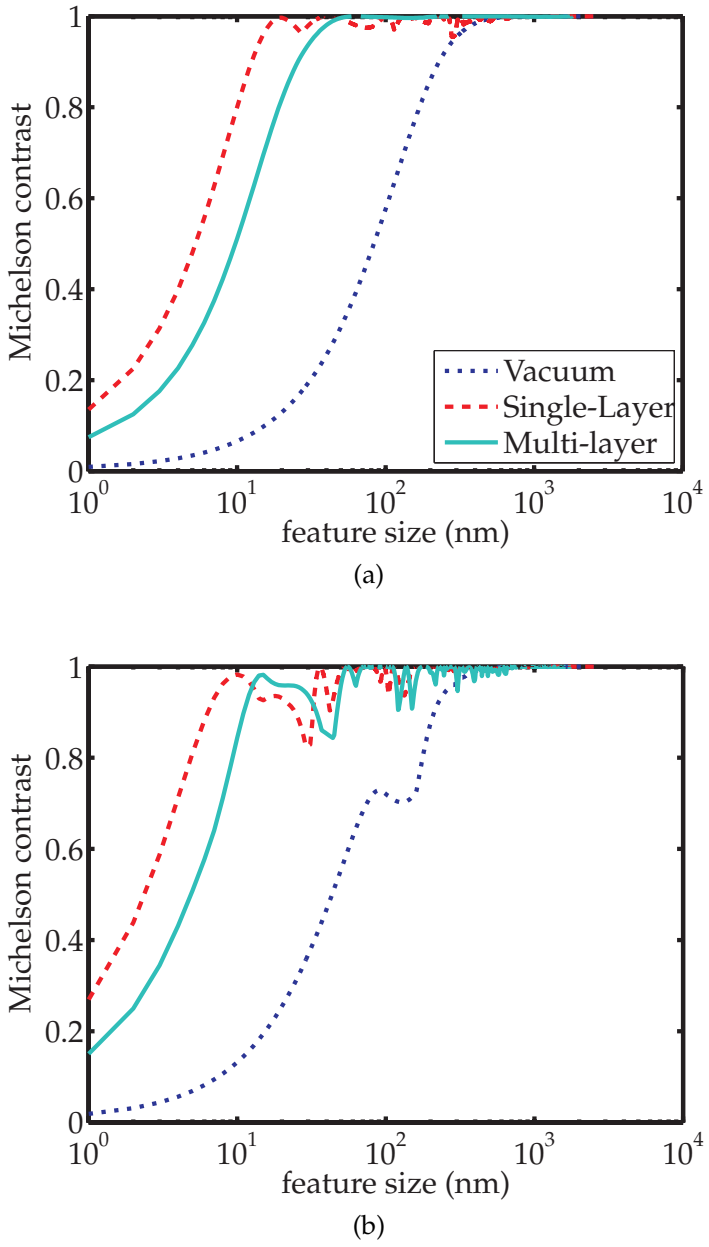

Figure 4.6: (a) Single and (b) dual dark-slit contrast profiles for single-layer and multilayer superlenses and an 80 nm vacuum gap.

dark-line object. As an improvement, these Michelson contrast profiles, which evaluate output images independently of the input profiles that are used to make them, can be combined with simple heuristics based on the locations of the intensity extrema in the input profiles to give a pseudo-contrast measurement that measures both the suitability of an image for lithography and the fidelity of that image to the original. Provided the input pattern is relatively simple and largely non-zero, the following

definition of pseudo-contrast can be used,

$$C_{pseudo} = \frac{I_{DC} - I_{dark}}{I_{DC} + I_{dark}}, \tag{4.4}$$

where I_{DC} represents the mean or DC intensity of the output and I_{dark} represents the output intensity value corresponding to the location of the minimum intensity in a dark-line or dark-point input profile, as illustrated in Fig. 4.5. If a bright-line input profile is used, then I_{bright} is used in place of I_{dark} and the definition of pseudo-contrast is rewritten as

$$C_{pseudo} = \frac{I_{bright} - I_{DC}}{I_{DC} + I_{bright}}. \tag{4.5}$$

For the example shown in Fig. 4.5, the pseudo-contrast is only $C_{pseudo} = -0.309$, giving a clear indication that the image is distorted relative to the input pattern. The negative value also shows that image reversal or frequency doubling may have taken place, as the intensity at the image centre, which should be at a minimum, is greater than the background intensity. Note that pseudo-contrast is not sensitive to ringing in the image; instead, it is only affected by distortion of the extreme intensity value and DC component of the image.

The pseudo-contrast profiles for the dark slit input profiles described in Fig. 4.2(b) and Fig. 4.2(d) are given in Fig. 4.7. Here the single layer lens outperforms the multi-layer lens over a range of sub-wavelength slit widths for single slit patterns, an example of which is shown in Fig. 4.8. Furthermore, the pseudo-contrast of the multi-Ag layer superlens varies slowly and stays below 0.6 for all periods below 1300 nm. This indicates weak differentiation between light and dark areas of the object mask in the image. These observations agree with other analyses for periodic patterns [75], which attribute the decrease in performance of multilayer lenses to increased suppression of the DC component in their transfer functions. On the other hand, for the dual slit case analysed in Fig. 4.7(b), the multi-Ag layer superlens has a resonant, rapidly changing pseudo-contrast profile, making its performance highly application specific. Michelson and pseudo-contrast profiles are not shown for the bright line patterns of Fig. 4.2(a) and Fig. 4.2(c), as the low DC offset in these profiles reduces the contrast ratio to

$$C \approx \frac{I_{ex} - 0}{I_{ex} + 0} = 1, \tag{4.6}$$

making the calculations meaningless.

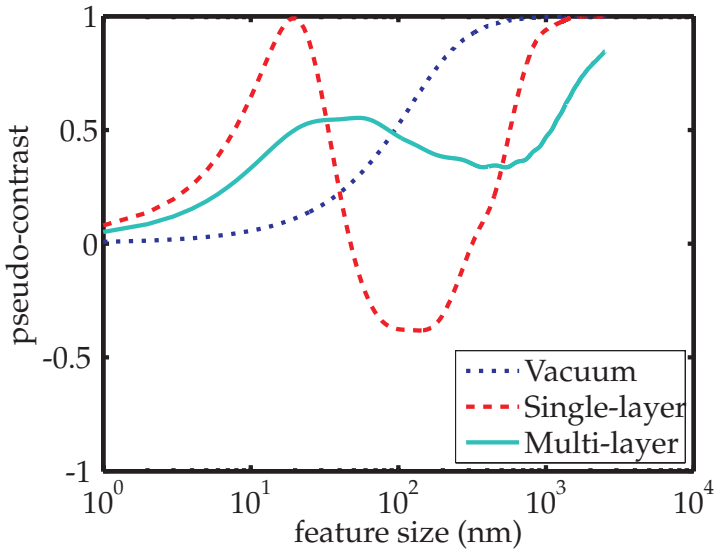

(a)

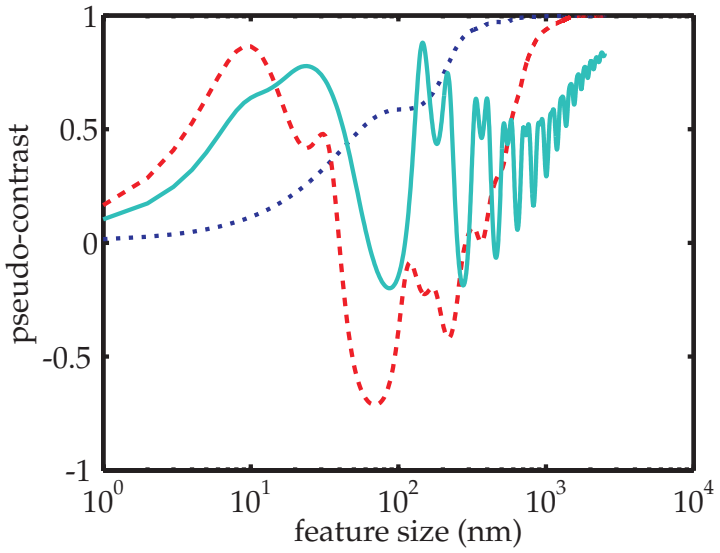

(b)

Figure 4.7: (a) Single and (b) dual dark-slit pseudo-contrast profiles for single layer and multilayer superlenses and an 80 nm vacuum gap.

4.3.2 Correlation Coefficients

While Michelson contrast profiles give a good indication of the relative intensities of extrema in the output profile, they do not show how closely the locations of the output extrema match the locations of the input extrema. In other words, they cannot detect image inversion, displacement or frequency doubling. Modifying the definition

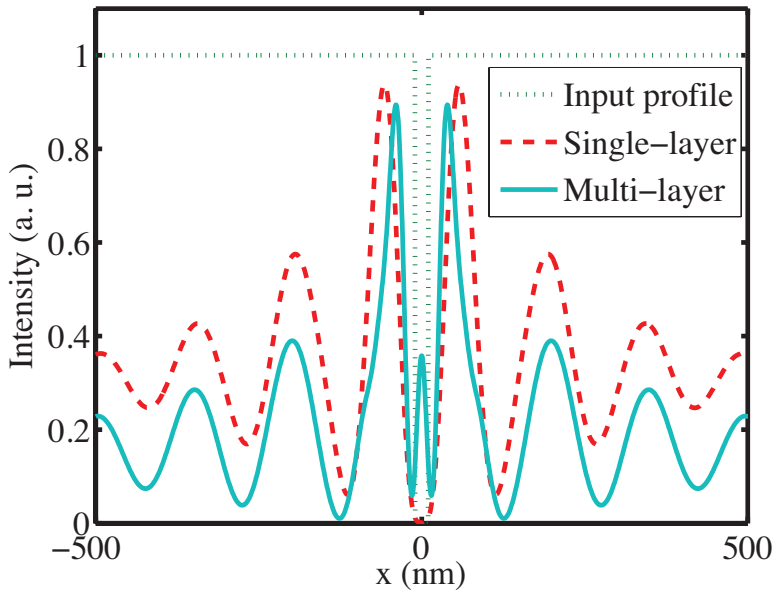

Figure 4.8: Spatial domain output for a 20 nm dark slit (dotted) projected through single layer (dashed) and multilayer (solid) realizable superlenses. The pseudo-contrast is 0.9997 for the single layer lens and 0.4033 for the multilayer lens.

of the Michelson contrast to pseudo contrast as per Eqs. (4.4) and (4.5) is a suitable workaround for relatively simple, non-periodic profiles, but is not practical for complex source images. Even for a single bright slit on an otherwise dark background, the fact that the profile does not have a DC offset means that the contrast profiles become meaningless. Furthermore, the pseudo-contrast profiles are very sensitive to high frequency oscillations in the output intensity profiles, which can lead to inaccuracies that are especially noticeable at low spatial frequencies. This is illustrated in Fig. 4.9(a), which shows the variation in the pseudo-contrast profile for dark line pair images as their line width and spacing are varied. Whilst the pseudo-contrast figure of merit is high and positive for line widths less than 25 nm, above this oscillations caused by ringing in the image are seen throughout the profile. An example of this is shown in Fig. 4.9(b). This demonstrates the need for a more robust figure of merit, preferably one that also takes into account the similarity of the input and output profiles.

One such metric is the correlation coefficient of each input profile and its corresponding output profile for a given lens. Although, strictly speaking, the application of correlation coefficients is limited to continuous, independent, normally distributed random variables [146], they are still useful as a description of the level of distortion introduced to the output profile by a lens. The correlation coefficient, $r_{s,i}$, for an input

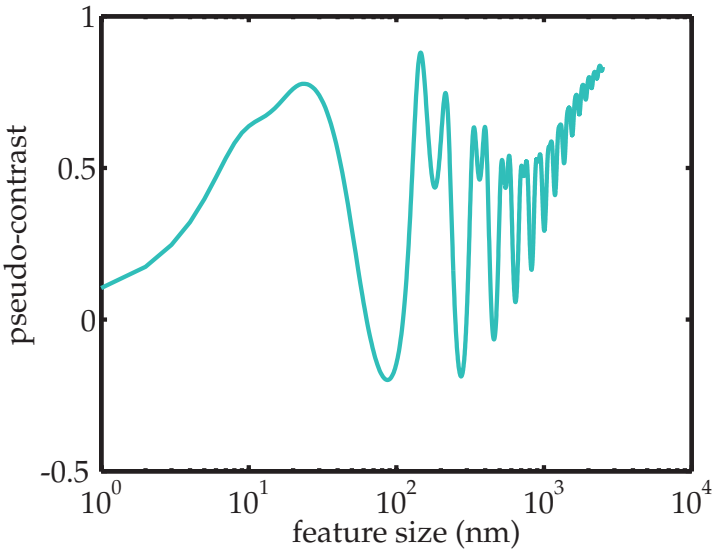

(a)

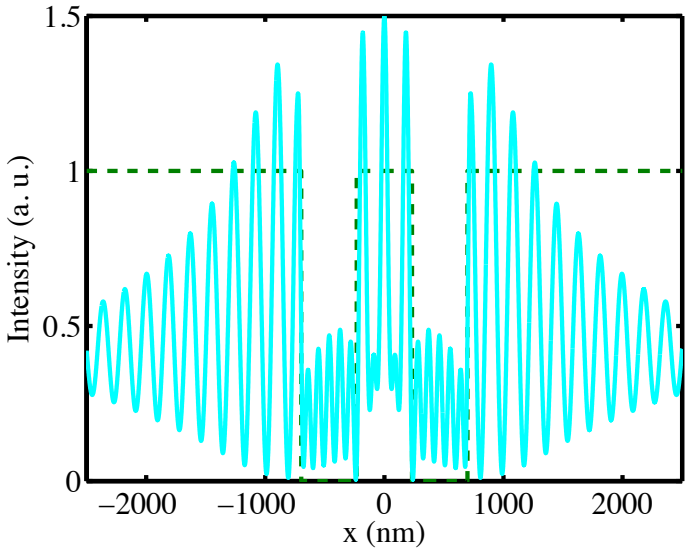

(b)

Figure 4.9: (a) Pseudo-contrast profile for a dual dark-slit pattern exposed to a multi-Ag layered realizable superlens. Note prevalent ripples between 100 nm and 1 μm. (b) Input (dashed) and output (solid) intensity profiles for a 465 nm dual dark-slit pattern imaged through such a lens.

profile, s, and its output profile, i, can be defined as [147]:

$$r_{s,i} = \frac{cov_{s,i}}{\theta_s \theta_i}, \tag{4.7}$$

where θ_s and θ_i are the standard deviations of the intensities of the input and output profiles, respectively, and $cov_{s,i}$ is their covariance.

The correlation coefficients for the bright and dark profiles described in Fig. 4.2 are shown in Fig. 4.10. They highlight an important design consideration, namely, that an image with low distortion, which has a relatively smooth, regular transfer function, is not the same as an image with suitably high luminosity, which is characterised by a large area under the transfer function. Although the two are not mutually exclusive, the former often needs to be diminished to improve the latter. Fig. 4.10(b) and Fig. 4.10(d) provide examples of this difference, where the images produced by the proximity lens have higher correlation coefficients and less distortion than those produced by the superlenses down to very low feature sizes, but are not very useful due to their extremely low intensities. Nevertheless, the insights offered by these correlation functions are an improvement on the contrast and pseudo-contrast profiles, which could not be used on patterns with small or no DC component.

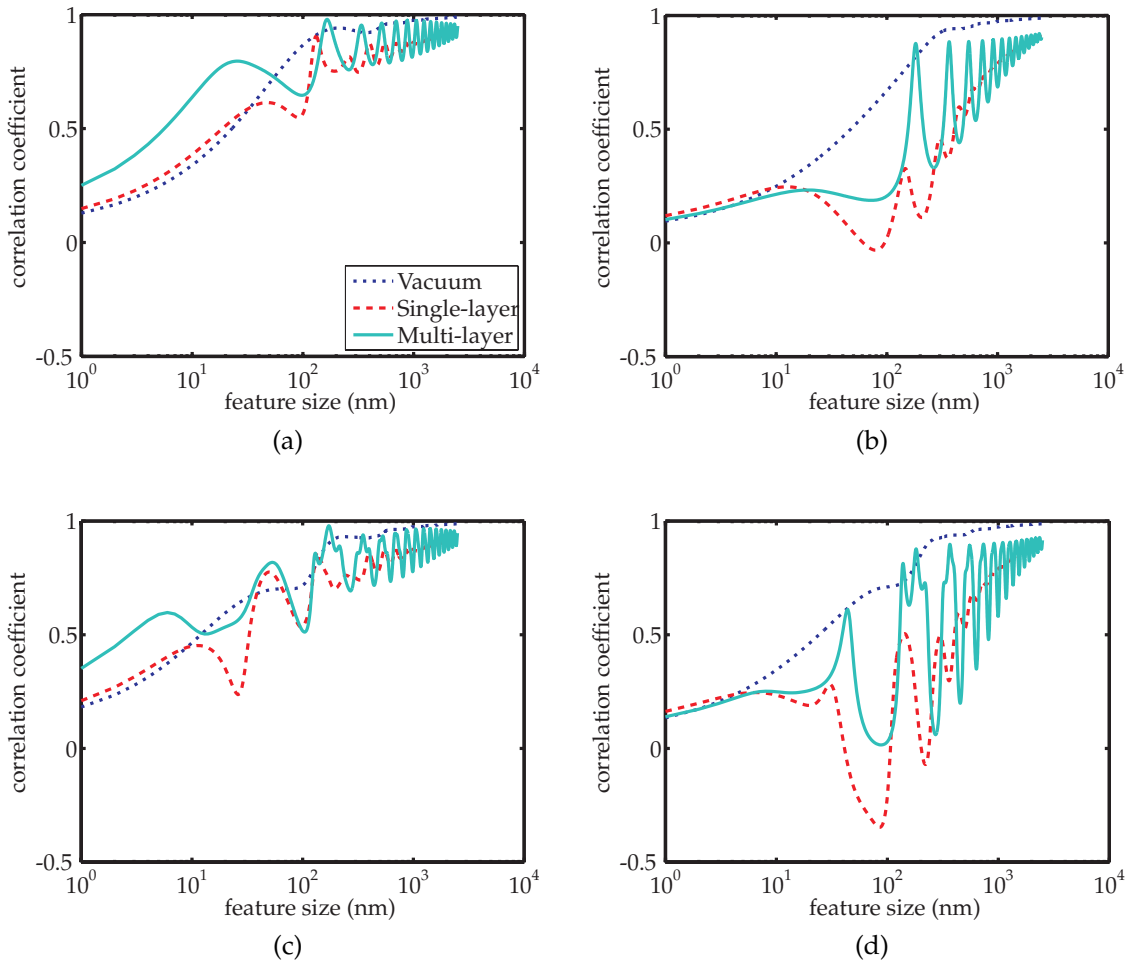

Figure 4.10: (a) Single bright slit, (b) single dark slit, (c) dual bright slit, and (d) dual dark slit correlation coefficient profiles for single layer and multilayer superlenses and an 80 nm vacuum gap.

4.4 Case Study: Thick Silver Superlens

A 2005 paper on imaging through a relatively thick, 120 nm layer of Ag [21] led to a published comment by Durant et al. [148] that included a figure of the analytical transfer function for such a slab of metal, sandwiched between layers of PMMA. A copy of this figure is shown in Fig. 4.11. All of the displayed transmission coefficients were below 0.1, which led the authors to believe that the 120 nm design was irrelevant to the search for a realisable superlens [20]. Furthermore, the thickness of the Ag slab meant that the imaging plane was not within the near field of the object plane, which at first glance precluded the possibility of superresolution [20].

What the authors did not notice was that the coefficients for the DC and peak evanescent wavenumbers were remarkably close, a coincidence that later analysis would identify as a key component required by super-resolving systems [32, 63]. Armed with this new information, the behaviour of a similar slab of Ag is studied here, in terms of the metrics described in Sections 4.2 and 4.3, in order to reassess the potential of sub-wavelength imaging with relatively thick metal slabs. Furthermore, the parameter space surrounding a three layer, PMMA:Ag:SiO_2 superlens stack is explored, with the goal of optimising the lens dimensions for imaging applications.

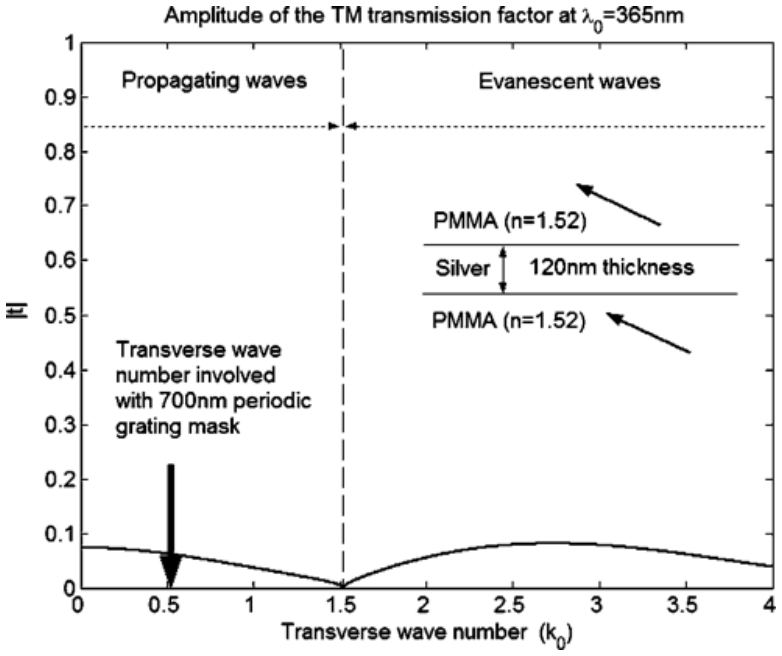

Figure 4.11: Amplitude transfer function calculated by Durant et al. for a 120 nm Ag slab suspended in PMMA [148].

4.4.1 Imaging Through 120 nm of Silver

Durant et al. [148] presented the transfer function of a 120 nm thick Ag slab, surrounded on both sides by PMMA. The index of refraction of the PMMA was given as 1.52 and the wavelength of operation, λ_0, was specified as 365 nm. The transmission of the lens was less than 0.1 over the entire range of wavenumbers shown in the graph, i.e. k_0 between 0 and 4, but the peak evanescent coefficient of ∼0.08 at k_0 = 2.7 was roughly equal to the DC transmission coefficient, giving very high bandwidth of 4.4 $\mu\mathrm{m}^{-1}$ or 1.61 k_0. Assuming that the low overall transmission coefficients could be compensated by longer exposure times, these data suggest that the lens could achieve good resolution and contrast for input patterns with fundamental frequencies between 2.0 and 4.0 k_0, that is, for periods between 90 nm and 180 nm. This would be a significant achievement, given that these periods are below the free-space diffraction limit for the 365 nm wavelength source.

In order to test this theory of sub-wavelength resolution from a 120 nm thick layer of silver, the transfer function for a superlens stack similar to the one shown in Fig. 4.11 is reproduced in Fig. 4.12. To model practical conditions more closely, 10 nm layers of PMMA are appended on each face of the Ag slab. The relative permittivity of Ag is taken to be $-2.7 + 0.23i$ [129], whereas Durant et al. used $\epsilon_{Ag,r} = -2.564 + 0.6i$ [149]. This change is made in order to keep consistency with the rest of the analysis presented in this thesis; furthermore, any difference that results is expected to be small given that both references use experimental data as the basis for their values. Both the horizontal and vertical axes also differ between Figs. 4.11 and 4.12. In Fig. 4.11, the horizontal axis is in units of k_0, equivalent to $\frac{\lambda_0}{\lambda}$, and the vertical axis displays $|t|$. However, Fig. 4.12 has $\frac{k_x}{2\pi}$, or $\frac{1}{\lambda}$ on its horizontal axis and transmitted intensity, $|t|^2$ on its vertical axis, in conformity with the other transfer functions presented in this thesis. Despite these superficial differences, it is clear that the two figures display very similar transfer functions.

Applying the metrics described in Sections 4.2 and 4.3 to the 10:120:10 nm PMMA:Ag:-PMMA lens stack reveals bandwidth of $5.8\ \mu\mathrm{m}^{-1}$ with peak evanescent wavenumber of $8.15\ \mu\mathrm{m}^{-1}$. Similarly, the contrast, pseudo-contrast and correlation metrics return good results for feature sizes down to about 150 nm, as shown in Fig. 4.13, where the input patterns given in Fig. 4.2 have been applied to the superlens. These metrics suggest that a 120 nm slab of Ag may well be able to image below the diffraction limit.

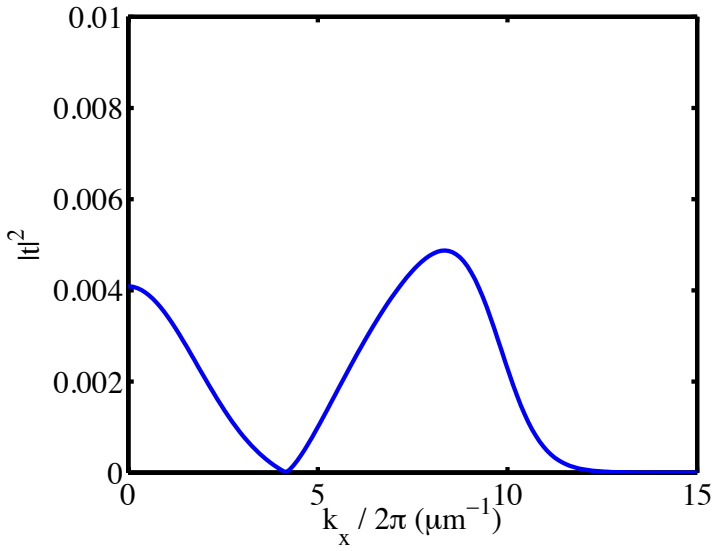

Figure 4.12: Transfer function for a 10:120:10 nm PMMA:Ag:PMMA lens stack, as predicted by TMM.

This conclusion is supported by Fig. 4.14, which shows the expected output profile for the lens described in Fig. 4.12 when exposed to a periodic, square wave input pattern with period of 100 nm. The waveform is clearly resolved and has extremely high Michelson contrast of 0.997. These results appear to contradict the comments made by Durant et al. and are a compelling argument for further research.

4.4.2 Lens Stack Analysis

Durant et al.'s work [148] dismissed the possibility of successful imaging through a 120 nm Ag slab because of the low transmission coefficients involved. However, analysis based on the metrics described in this chapter suggests that sub-wavelength resolution through such a slab may well be possible, as shown Fig. 4.14. Hence, the performance of a family of silver superlenses of increasing thickness is investigated here, with the aim of identifying suitable designs for sub-resolution experiments that may have been overlooked in the past.

Firstly, transfer functions for a family of PMMA:Ag:SiO_2 lens stacks are calculated in Fig. 4.15. The thickness of the PMMA and SiO_2 layers is set at 10 nm, while the Ag thickness is swept between 10 nm and 120 nm in 10 nm steps. SiO_2 relative permittivity

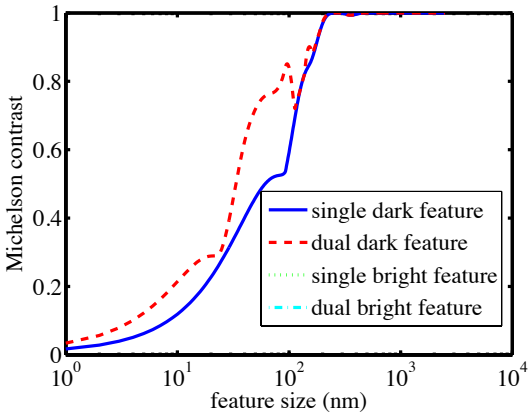

(a)

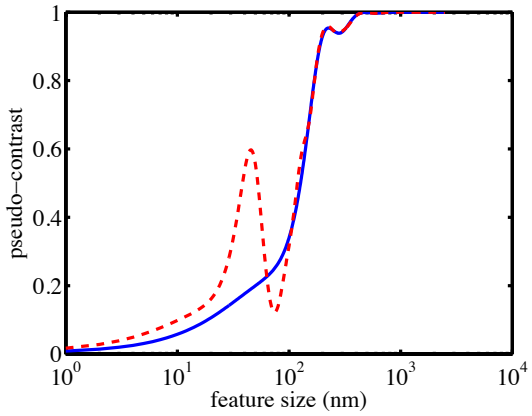

(b)

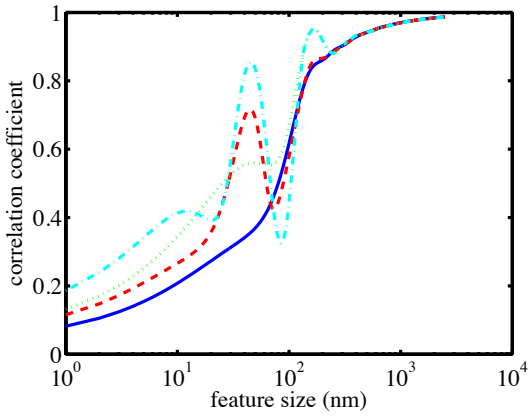

(c)

Figure 4.13: Object-lens metrics for a 10:120:10 nm PMMA:Ag:PMMA lens stack exposed to the family of input profiles shown in Fig. 4.2.

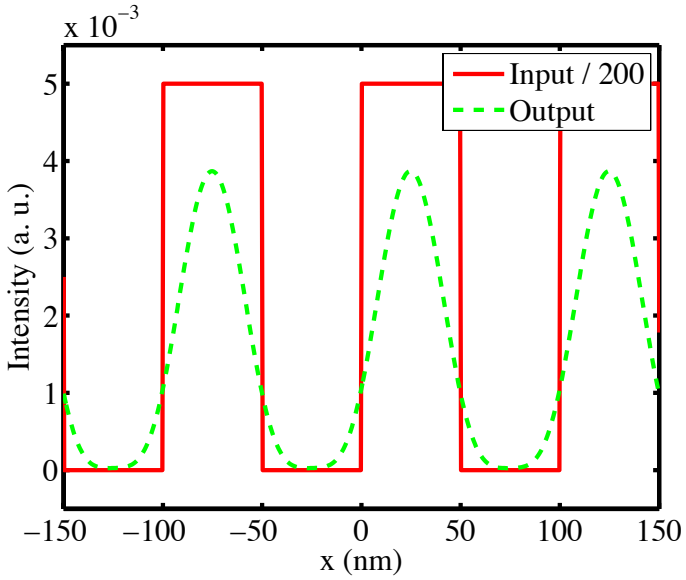

Figure 4.14: TMM output for the lens described in Fig. 4.12, exposed to a 100 nm period square wave.

is set to 2.368 [128] and the composition of the lens stacks is chosen according to the experimental designs of Melville et al. [21].

The various transfer functions shown in Fig. 4.15 can be characterised in terms of their bandwidth [150], which can be graphed on a single plot, shown in Fig. 4.16. This reveals highest bandwidth for stacks with total thickness greater than 100 nm; examining the corresponding curves in Fig. 4.15 shows a close match between the DC and peak evanescent transmission coefficients for these particular designs. Analysing more lens stack families, where both the thickness of the spacer layers and the thickness of the Ag are swept from 10 nm to 120 nm in 10 nm steps, yields the series of bandwidth curves shown in Fig. 4.17.

The effect of the dielectric spacer thickness on bandwidth was also studied, with the results shown in Fig. 4.17. These data show a peak in bandwidth for lens stacks with total width between 120 and 140 nm. For example, the TF of a 20:90:20 nm PMMA:Ag:SiO_2 stack, shown in Fig. 4.18, displays good transmission beyond $\frac{k_x}{2\pi} = 10\ \mu m^{-1}$, i.e. for spatial periods as low as 100 nm. The image produced by a square mask with 100 nm period imaged through such a lens stack is shown in Fig. 4.19. These new results suggest that sub-wavelength resolution may well be possible from a variety of thick Ag films, provided the low overall transmission of the films, which is around -20 dB, can be compensated by longer exposure times.

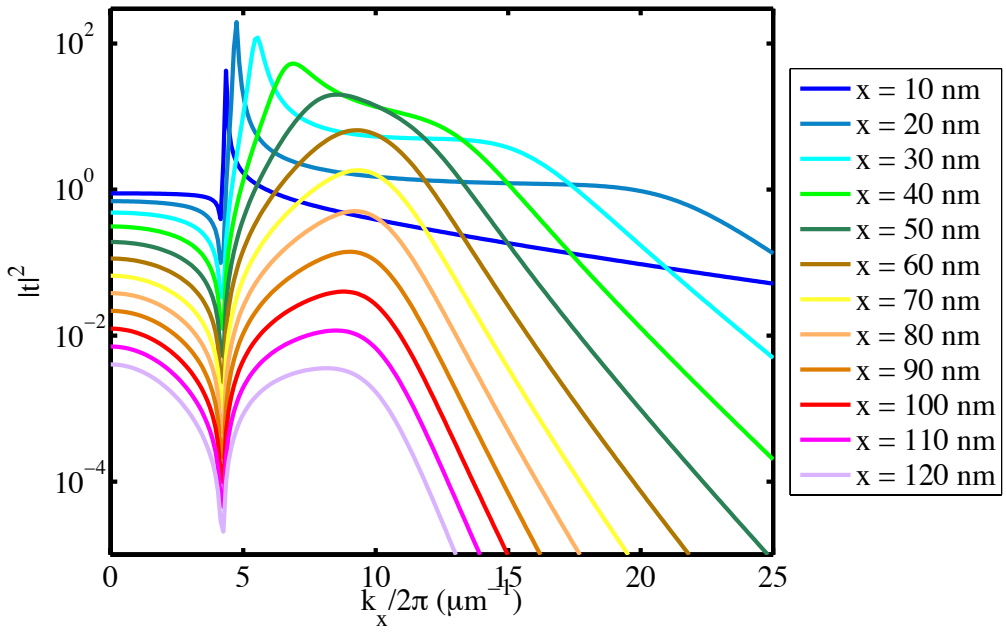

Figure 4.15: Transfer functions for 10:x:10 nm PMMA:Ag:SiO_2 lens stacks, where x = [10, 20, ... 120] nm.

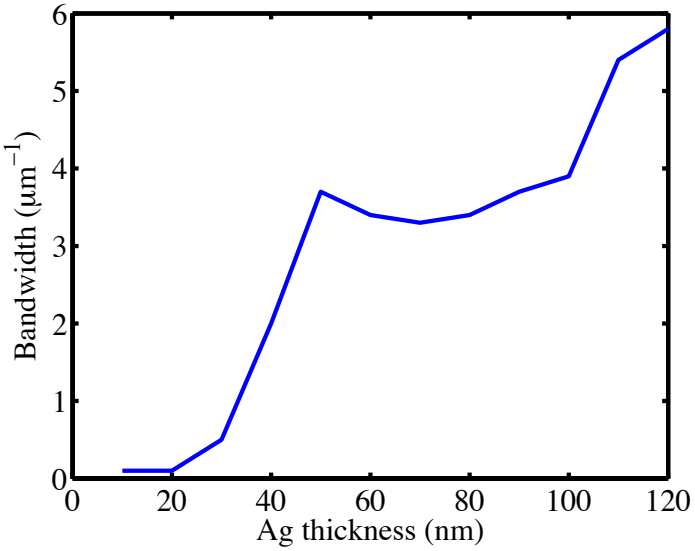

Figure 4.16: Bandwidth curve for the 10:x:10 nm PMMA:Ag:SiO_2 family of lens stacks shown in Fig. 4.15. The values of x are marked on the horizontal axis.

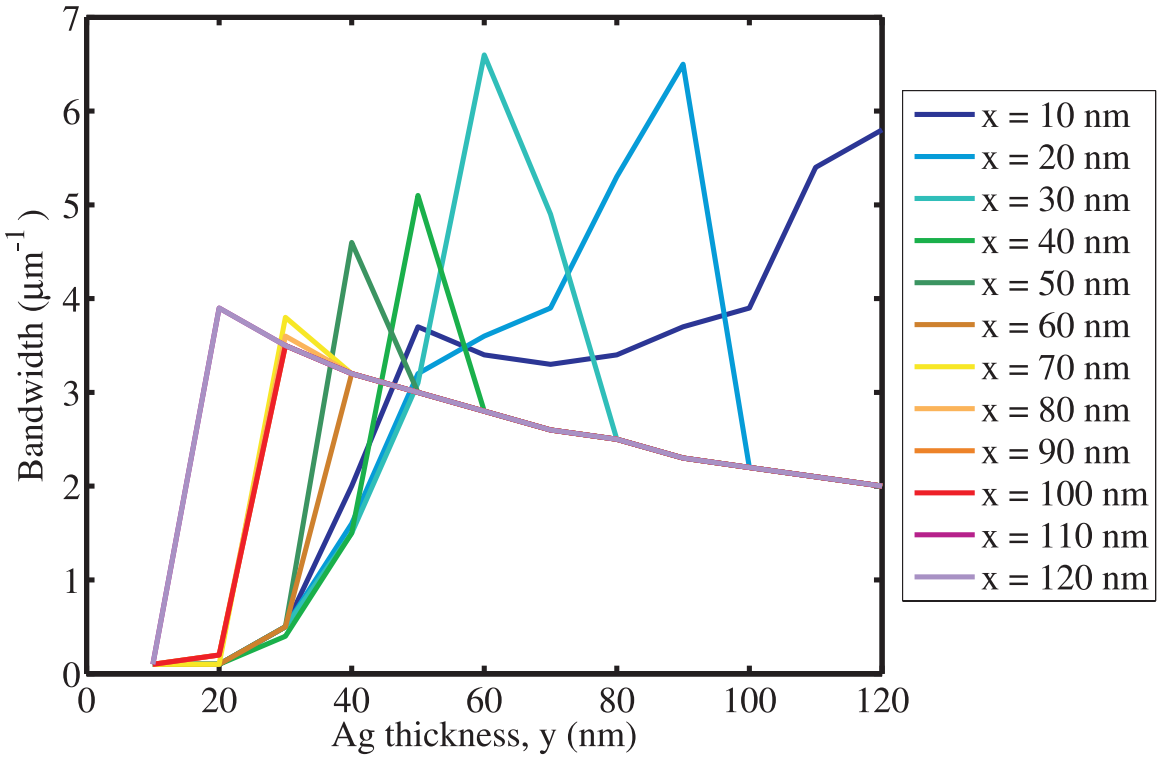

Figure 4.17: Bandwidth curves for x:y:x PMMA:Ag:SiO_2 lens stacks. Each line represents a value of x between 10 nm and 120 nm, varying in 10 nm increments. The values of y, which also vary between 10 nm and 120 nm in 10 nm steps, are represented by the values on the horizontal axis.

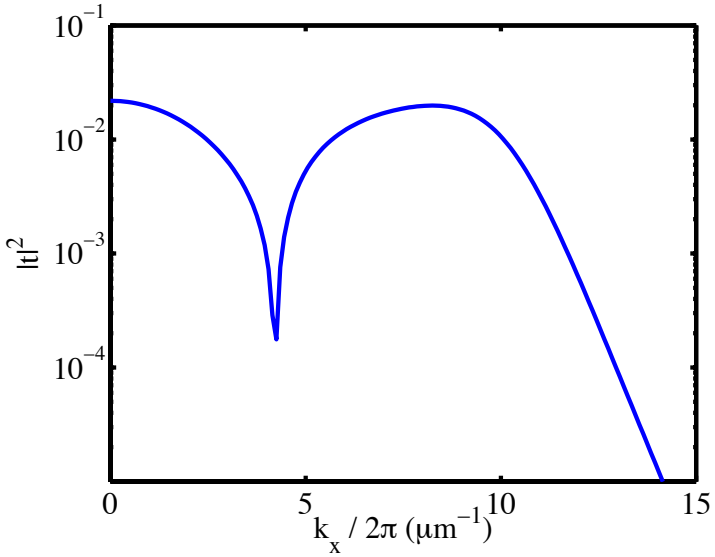

Figure 4.18: TF for a 20:90:20 nm PMMA:Ag:SiO_2 lens stack.

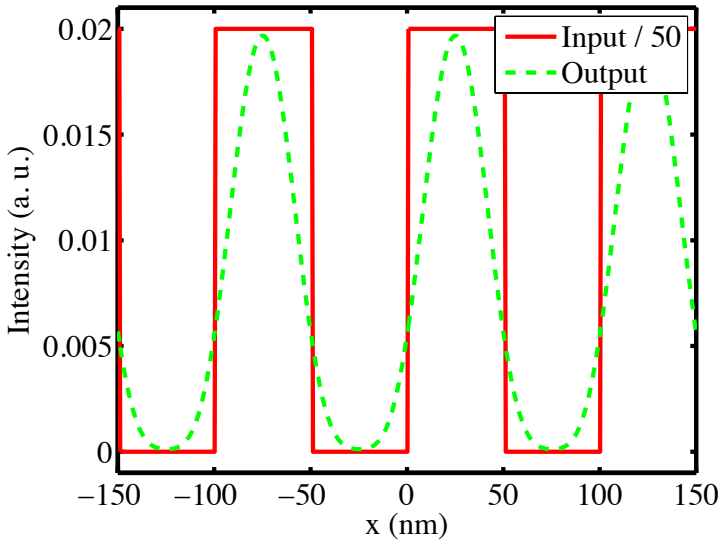

Figure 4.19: TMM output for the lens described in Fig. 4.18, exposed to a 100 nm period square wave.

4.4.3 Mask-Lens Interactions

Although a 120 nm thick Ag slab may well be able to break the diffraction limit in the simplified, isolated environment implied by TMM analysis, practical experiments with such a slab showed that resolution degraded below 0.5 μm [21], approximately an order of magnitude above the predicted resolution for such a system. This discrepancy arose because TMM does not consider the near-field interactions that exist between a mask and the superlens structure. In reality, the superlens structure will always be in intimate proximity with a mask, so that evanescent information, which is normally confined to the near-field of the mask, can be coupled into the superlens and transmitted to the image plane. The consequence of this is that the mask will affect the performance of the superlens. To assess the significance and nature of mask effects full-field FEM analysis has been performed on representative structures. An example is shown in Fig. 4.20, where the input and output electric field intensity profiles are calculated via FEM for a 10:120:10 nm PMMA:Ag:PMMA superlens stack in intimate contact with a 100 nm period, 50 nm thick W grating.

The FEM profiles presented in Fig. 4.20 are drastically different to those calculated by TMM and shown in Fig. 4.14, even though they describe similar situations. For example, the FEM output profiles have much lower contrast of 0.24, compared to ~1.00

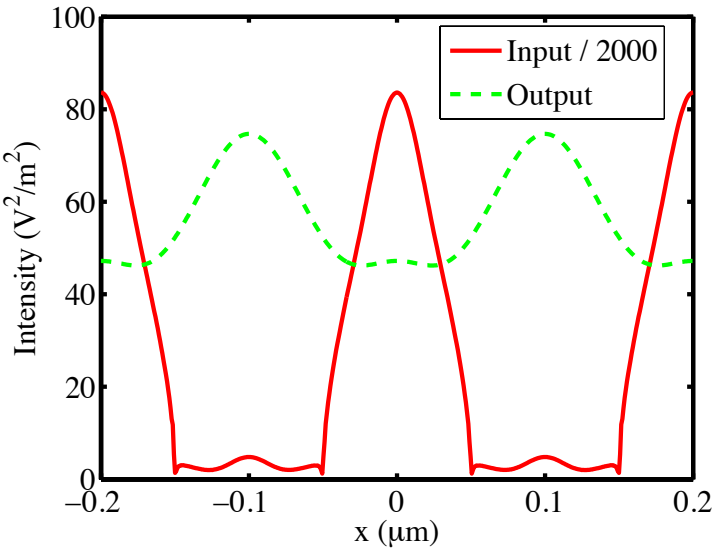

Figure 4.20: Finite element models of the object (dashed) and image (solid) electric field intensity profiles for a 50 nm thick, 100 nm period W mask in intimate contact with a 10:120:10 nm PMMA:Ag:PMMA superlens stack.

for TMM. Estimates of the attenuation between input and output profiles for different models also differ greatly, with FEM predicting an order of magnitude greater reduction in output intensity than TMM. Further differences are quantified by the metrics shown in Table 4.3. The reason for these differences is best explained by comparing the transfer function of a 10:120:10 nm PMMA:Ag:PMMA superlens with and without a mask present, as has been done in Fig. 4.21. The evanescent coefficients of the transfer function are more strongly attenuated when a mask is present, leading to much reduced performance and poor characteristic values.

Table 4.3: Lens-object characterisation metrics for a 10:120:10 nm PMMA:Ag:PMMA superlens stack, both isolated in PMMA and in near-field proximity to a 50 nm thick W mask.

Condition	**Contrast**	**Pseudo-Contrast**	**Correlation Coefficient**
No Mask	0.9973	0.2372	0.8699
W Mask	0.2355	-0.2254	-0.7615

Although these results cast doubt on the suitability of a thick Ag slab for real lensing applications, they do not contradict the earlier conclusion that lensing through an isolated, 120 nm thick layer of Ag should be possible. Instead, they suggest that mask-

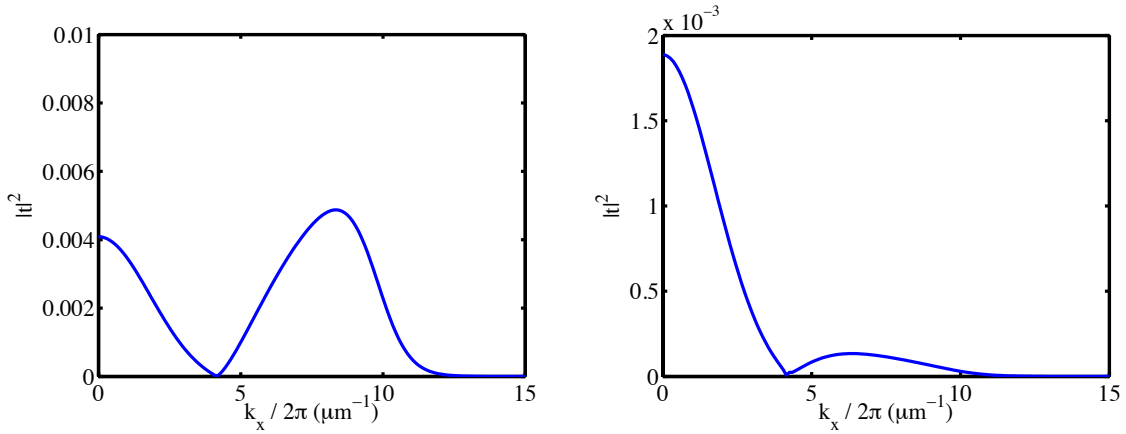

Figure 4.21: Transfer functions for two 10:120:10 nm PMMA:Ag:PMMA superlens stacks, one isolated in PMMA (a) and the other in contact with a 50 nm thick W mask (b). The transfer function in (b) is calculated according to the methods described in Chapter 5.

lens interactions are an important part of evanescent lithography that deserve close attention. Hence, this phenomenon is explored in detail in Chapter 5.

4.5 Summary

New developments in the area of super-resolution imaging have given rise to a need for practical, quantifiable image quality measures that are applicable to a wide range of images. As a result, techniques to measure both lens-specific and object-lens metrics were investigated and applied to several superlenses exposed to one-dimensional luminous intensity profiles. The resulting characteristics each highlighted different features of the images, with the transfer function analysis confirming that increasing the number of layers in a superlens increased the transmission coefficients at high spatial frequency. This is explained by the way sub-wavelength information travels through the system: evanescent mode propagation is dependant on SPR, which occurs at the interface between left-handed and right-handed media, such as at the boundary between Ag and PMMA or SiO_2. Increasing the number of interfaces in a superlens improves the transmission of evanescent modes; conversely, decreasing the number of interfaces or increasing the distance between interfaces decreases evanescent transmission, since evanescent modes decay as they travel away from their source. The im-

proved transfer functions due to laminated superlenses then become intuitive, since the number of interfaces are increased while the total thickness of the superlens is kept constant.

What the transfer function analysis fails to identify is that high image fidelity depends on balanced propagation of sub- and super-wavelength wavenumbers, which typically gets worse in multilayered designs. This is because SPR becomes stronger as the number of layers increases, which leads to a sharper resonant peak in the transfer function with narrower bandwidth and higher Q factor. The ability of a superlens to transmit both propagating and evanescent modes is thus summarised by the BW and Λ_{peak} FOMs, which are able to predict the versatility of lenses for use with objects of different fundamental spatial frequencies.

The lens-object analyses carried out for a series of aperiodic object profiles reveals frequency doubling and image inversion behaviour in both superlens designs examined. Pseudo-contrast profiles were used to predict these phenomena occurring in objects with significant DC offset, while correlation coefficient profiles were able to identify the same features regardless of the type of object waveform used. Additionally, analysis of the correlation coefficient profiles revealed that the least distorted images are not always the most useful ones, especially when practical lithography applications are considered.

Lastly, lens-specific metrics were applied in a case study to reassess the possibility of super-resolution imaging through relatively thick layers of Ag. This analysis returned favourable results for superlens designs up to 140 nm thick, suggesting that reducing lens layer thicknesses is not always a foolproof method of improving performance. However, in order to implement the thick designs proposed here, three important factors need to be taken into consideration. The first relates to the assumption, made throughout this case study, that low transmission through a lens stack can be compensated by increased exposure times in the lithography process. This would rely on a stable illumination source and very low parasitic exposure in order to keep the noise floor in the exposed resist as low as possible. The second consideration relates to the modelling technique used in this chapter. The lens stacks discussed here have been simulated by perfectly smoothly layers, which are not achievable in practice. Since roughness has been shown to degrade the performance of superlenses [28, 117], more analysis would be required to confirm that the sub-wavelength resolution mile-

stone could be achieved by thick and rough lens stacks. Finally and most importantly, near-field mask-lens interactions, which can have a significant effect on lens performance [150], have not been considered in this chapter, nor by other authors who have published results based on TMM [7, 22, 26, 27, 63, 75, 120, 143]. This major deficiency is addressed in Chapter 5, which describes techniques to incorporate near-field mask-lens interactions into regular TMM models. The examples from this case study are revisited in Section 5.7, where more comprehensive results, which include such mask-lens effects, are presented and discussed.

Chapter 5

An Improved Transfer-Matrix Model for Optical Superlenses*

With the aid of the tools described in Chapter 4, the design of superlenses can now be optimised through software modelling; for example, by applying the TMM technique described in Section 3.2. However, since TMM is analytical in nature, care should be taken to check the accuracy of its results and predictions. Early experimental results [22, 23, 28, 151] have already confirmed some of the qualitative predictions of this technique, i.e. that superlenses are able to break the diffraction limit, but many of the quantitative predictions made about superlens performance using TMM have yet to be verified.

This chapter aims to address the quantitative accuracy of analytical superlens models by comparing the results predicted by TMM [30, 63, 140, 152] to rigorous, fully-coupled solutions of Maxwell's equations obtained via FEM [153]. Significant quantitative differences are found between TMM analysis and FEM results, examples of which have already been shown in Section 4.4.3. The cause of these differences can be attributed to near-field mask-superlens interactions that are not accounted for in the simplified models normally used in TMM studies. A modified transfer matrix model (M-TMM) that can treat such mask-superlens interactions approximately is pro-

*Aspects of the work presented in this chapter were published as: C. P. Moore, R. J. Blaikie, and M. D. Arnold, "An improved transfer-matrix model for optical superlenses," *Optics Express*, vol. 17, no. 16, pp. 14260–14269, July 2009 (7 citations as at 17 May 2011, according to Google Scholar and ISI Web of Knowledge.)

posed, and M-TMM- and FEM-generated data sets are compared to quantify the improved accuracy that results.

5.1 Method

As discussed in Chapters 3 and 4, the imaging behaviour of superlenses can be conveniently described by their spatial-frequency transfer function (TF), examples of which are shown in Fig. 5.1. Such TFs have been calculated and reported regularly using analytical TMM techniques [26, 30, 63, 141] but usually for an isolated superlens, rather than for a complete near-field-coupled mask-lens-detector system. The transfer functions in Fig. 5.1 have been calculated using a full-vector simulation model based on Maxwell's equations, which includes the near-field mask-lens interactions for a 40 nm thick tungsten mask, typically used in experiments [22, 28]. This model was implemented using the FEM-based COMSOL Multiphysics engine [122] and was independently verified by CAMFR [123] simulations [32]. The deconvolution method used to extract the TF from such FEM and/or CAMFR spatial domain simulations is described in Section 3.3.3.

The FEM-calculated transfer function for an 80 nm thick silver superlens, made up of 40 nm of silver symmetrically placed between silica dielectric spacers and illuminated at a wavelength of 365 nm, is shown in Fig. 5.1. The resonant peak at $\sim$9 μm^{-1} in the characteristic curve is representative of the surface plasmon (SP)-enhanced behaviour of the evanescent fields in such systems but, as will be shown in Section 5.2, the size and position of this feature does not agree well with conventional TMM results. The transfer function for an 80 nm pure-dielectric gap (dashed line) is also shown to draw attention to the much higher transmission by the superlens of evanescent wave numbers. The full details of the systems used in this example, and the example of a triple-layer lens presented later, are given in Table 5.1.

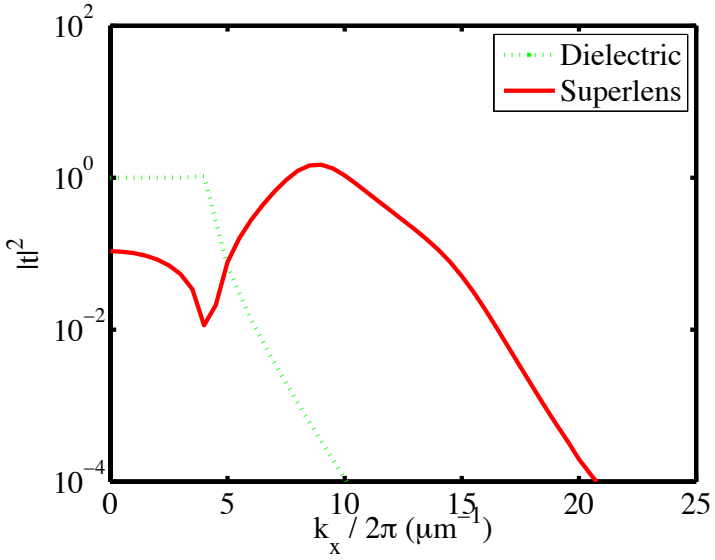

Figure 5.1: Spatial-frequency TFs for the dielectric gap (dashed) and superlens (solid) described in Table 5.1. Both curves are generated from full-vector FEM simulations.

Table 5.1: Materials and dimensions of systems studied. Illumination wavelength is 365 nm and a 40 nm thick tungsten mask layer ($\epsilon_{rW} = -1.497 + 7.690i$) has been used in all cases.

Lens	**Materials and Dimensions (nm)**							**Properties**
Dielectric gap	SiO_2 80							$\epsilon_{rSiO_2} = 2.368$ [128]
Single-layer superlens	SiO_2 20	Ag 40	SiO_2 20					$\epsilon_{rAg} = -2.7 + 0.23i$ [129] $\epsilon_{rSiO_2} = 2.368$
Multilayer superlens	SiO_2 6.7	Ag 13.3	SiO_2 13.3	Ag 13.3	SiO_2 13.3	Ag 13.3	SiO_2 6.7	$\epsilon_{rAg} = -2.7 + 0.23i$ $\epsilon_{rSiO_2} = 2.368$

5.2 Analytical Model

Calculating transfer functions using full vector electromagnetic simulations requires specialised software and careful setup of the numerical models [150]. Analytical approaches are therefore valuable to simplify the characterisation of many-layered superlenses, and a TMM technique has been widely used in the literature [26, 30, 63, 154]. This technique calculates transmission and reflection coefficients between material interfaces in the superlens stack and is computationally economical compared to full-

vector simulations. The compromise required is that spatial variation along an interface is not normally incorporated and perfectly smooth material boundaries have to be assumed. Rigorous incorporation of mask-lens interactions is technically possible for periodic mask objects by calculating their diffraction patterns [155–159] but the resulting analysis becomes object-specific and requires discretisation of the system, so the attractive simplicity of 'standard' TMM is lost.

Similarly, mask-lens interactions can be included by modelling the mask with an effective medium approximation (EMA) technique. This method was pursued by Maldovan et al. [138], who explored the inclusion of EMAs in T-matrix simulations and presented calculated parameters that led to favourable comparisons with FEM models. They expanded on earlier works [160, 161] to derive an EMA that was suitable for use with finitely periodic composites containing arbitrarily-shaped, two-dimensional particles. Unfortunately, their calculations relied on detailed knowledge of the local electric fields around such particles, which normally requires the use of automated numerical methods, such as FEM. Like the rigorous diffraction calculations, this removes much of the speed and agility of the TMM technique. Given this lack of a viable alternative, a straightforward modification to the system model used for TMM analysis is described here that can provide improved accuracy with little additional complexity.

A TMM-calculated transfer function for the isolated single-layer superlens described in Table 5.1 is shown in Fig. 5.2 alongside a similar FEM-based curve, demonstrating the effect of mask-lens interaction. Three features are of interest in Fig. 5.2: firstly, the TMM estimate of the zero-frequency or 'DC' coefficient is larger by a factor of three compared to the FEM estimate. Secondly, the peak transmission, caused by SP field enhancement, is predicted by TMM to be almost a factor of 10 larger than the value calculated FEM. Thirdly, the wave-number at which this peak transmission occurs is underestimated by the TMM analysis at 7.0 $\mu\mathrm{m}^{-1}$, compared with 9.0 $\mu\mathrm{m}^{-1}$ from the FEM technique. The actual values for these metrics are listed in Table 5.2.

Table 5.2: Characteristic metrics for the TMM and FEM transfer functions shown in Fig. 5.2.

Metric	**TMM**	**FEM**
DC coefficient	0.3172×	0.1084×
Peak transmission coefficient	12.04×	1.485×
Peak transmission wavenumber	$7.0 \pm 0.2\ \mu\mathrm{m}^{-1}$	$9.0 \pm 0.5\ \mu\mathrm{m}^{-1}$

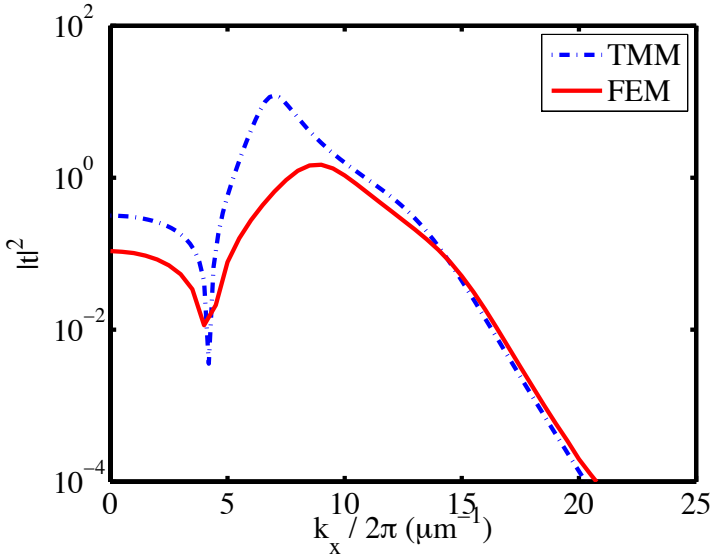

Figure 5.2: TMM (dashed) and FEM (solid) generated transfer functions for the single Ag-layer superlens described in Table 5.1.

The effects of these differences can be seen in Fig. 5.3, where both techniques are used to calculate spatial image profiles for a double slit, sub-wavelength mask [27]. The image profile generated using the TMM-derived transfer function without accounting for mask-lens interaction is clearly in error, with the peak intensities in the image being a factor of three higher than those predicted from the full-field FEM simulations. So, whilst the TMM analysis using a simple isolated-superlens model can be used to determine the qualitative features in superlens imaging, it will typically over-estimate image intensity. Note that this phenomena was seen most dramatically in the analysis of the 140 nm thick superlens performed in Section 4.4.3.

5.3 Modified Transfer-Matrix Model

Although TMM, which is an exact analytical technique, rigorously models electromagnetic behaviour within a superlens stack, the simple isolated-system model that is normally used neglects the interactions that occur between a mask and the outer-most interface of the lens, which Figs. 5.2 and 5.3 showed to be of considerable importance. The reason for this omission is that the spatially-variant features of the mask are orthogonal to the one-dimensional plane that the TMM simulation occupies, and thus

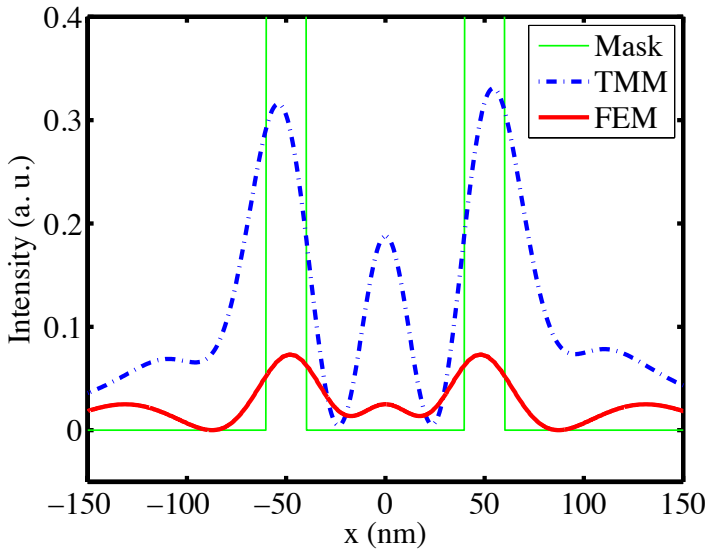

Figure 5.3: Output profiles predicted by TMM (dashed) and FEM (solid) for a unit intensity, sub-wavelength double-slit mask (dotted) with 20 nm wide apertures on a 100 nm centre-to-centre spacing, imaged through a single-Ag layer superlens.

cannot be represented in the simulation. Hence, a modification to the model is necessary to account for mask features and their resulting effects on lens performance.

One such modification, described here, relies on the assumption that any features in the mask are likely to be very small compared to the wavelength, given that the application under consideration is super-resolution imaging. This means that reflection from a dark mask with narrow apertures can be approximated by a single, solid slab, constructed of identical material to the mask. Similarly, if the mask contains only small dark features, then it can be approximated by its host medium and mask-lens interactions can be ignored. Since the analysis for the mostly-light case reduces trivially to that shown in Section 5.2, consideration is given here to the mostly-dark case. The essential argument is that reflections from masks with sub-wavelength spacings cause minimal scattering outside zeroth-order, and hence the amplitude and phase of the reflection from mostly-dark masks is typically independent of the apertures. In this chapter the accuracy of this assumption is tested for mostly-dark masks, by comparing representative results from analyses using the M-TMM technique with full-field simulation results.

The M-TMM technique involves a simple extension of TMM, with the inclusion of first-order mask-superlens reflections. Using TMM, or any other suitable analytical

method, a spatial-frequency-dependent reflection function, r_M, can be calculated for the slab-equivalent of the mask; an example of such a reflection function for a 40 nm thick tungsten slab is shown in Fig. 5.4. Once calculated, r_M is used in combination with the TMM-derived reflection function of the isolated superlens stack, r_L, to calculate the effect that the mask-lens interactions have on the overall transfer function of the super-resolving system.

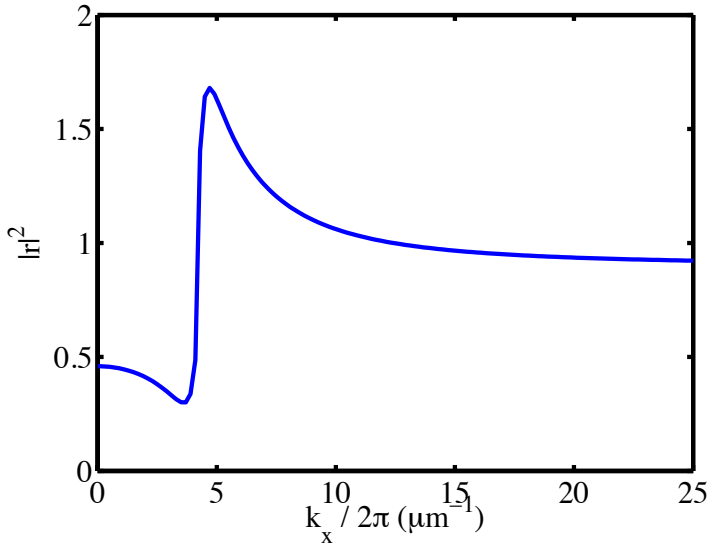

Figure 5.4: Spatial frequency reflection function for a 40 nm thick W slab, $\epsilon_r = 1.497 - 7.69i$.

Fig. 5.5 illustrates the M-TMM calculation. Without considering the mask, an incident signal, ip, is transmitted through the isolated superlens stack according to the TMM-generated transfer function, t, to give an output, $op = ip \times t$. A proportion of ip is also reflected by the lens, giving $ip \times r_L$. When the mask is included in the calculations, $ip \times r_L$ is re-reflected according to r_M, and appears at the object plane as $ip \times r_L \times r_M$, with r_M including the round-trip phase of $exp(-2ik_x d)$ between the lens and the mask. The field on the other side of the superlens stack then becomes $op = ip \times t + ip \times r_L \times r_M \times t$. Just as before, a fraction of this is reflected off the lens and re-reflected off the mask, creating an additional term at the image plane. This series continues ad infinitum, with its sum given by [141, 152]

$$op = \frac{ip \times t}{1 - r_L \times r_M}. \tag{5.1}$$

This allows us to determine a modified transfer funciton, t', which includes the infinite sum of reflections between the mask and lens, that can be calculated as

$$t' = \frac{op}{ip} = \frac{t}{1 - r_L \times r_M}. \tag{5.2}$$

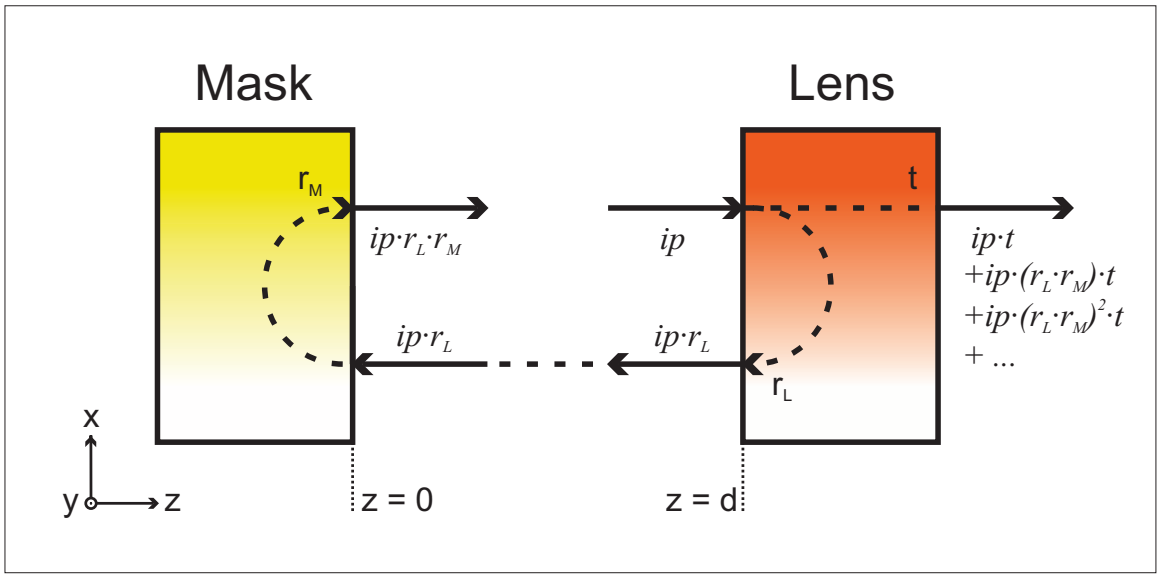

Figure 5.5: Recursive mask-lens interactions.

The different TFs produced by TMM, M-TMM and the FEM simulation are shown in Fig. 5.6 for the single-Ag layer superlens whose parameters are presented in Table 5.1. The M-TMM TF is clearly a better match to the FEM data than the TF obtained from TMM with an isolated-lens model, so the simple first-order assumptions that were made have good validity. Agreement is not perfect, and the differences are quantified here. Firstly, unlike the simple transfer-matrix model, M-TMM predicts a peak in transmission at the same wave number ($8.8 \pm 0.2\ \mu\text{m}^{-1}$) as the FEM simulation ($9.0 \pm 0.5\ \mu\text{m}^{-1}$). Predicted peak transmission from M-TMM differs substantially from the FEM result ($0.6838\times$ compared to $1.485\times$); however, it is still a much better estimate than that obtained using the simple system model ($12.04\times$). The zero-frequency (DC) transmission coefficient from M-TMM is higher than the FEM result ($0.1727\times$ compared to $0.1084\times$), but is better than the figure of $0.3172\times$ for the simple system model. These differences between M-TMM and FEM tend to shrink as the resolution of the FEM data is increased.

A comparison of image profiles calculated by FEM and M-TMM is shown in Fig. 5.7 for the same double-slit object used for Fig. 5.3. In this case the quantitative agreement

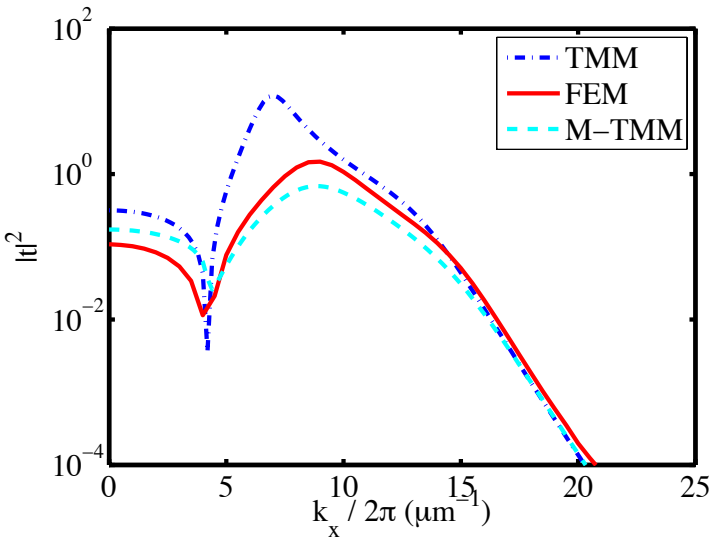

Figure 5.6: M-TMM (dotted), TMM (dashed) and FEM (solid) transfer functions for the single Ag-layer superlens described in Table 5.1.

between the results is very good, again highlighting the fact that the simple, first-order M-TMM accounts for the most significant aspects of mask-lens interactions for imaging sub-wavelength features transmitted through an otherwise-opaque planar screen.

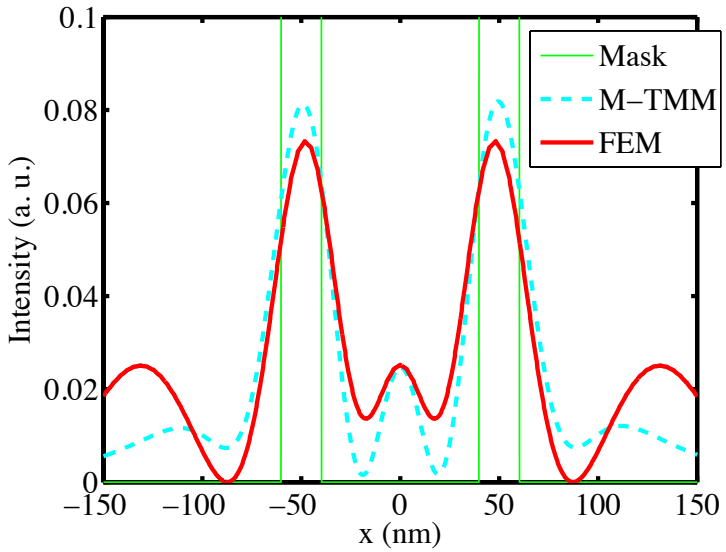

Figure 5.7: Output profiles predicted by M-TMM (dashed) and FEM (solid) for a unit intensity, sub-wavelength double-slit mask (dotted) with 20 nm wide apertures on a 100 nm centre-to-centre spacing.

5.4 Effects of the Detector Layer

Given that the superlens performance is influenced significantly by mask-lens interactions, it is also natural to consider the effects of near-field interactions with the imaging layer beneath the superlens. So far, the medium beneath the superlens was considered to be lossless silica or equivalent dielectric but, in practice, the imaging layer must have some loss and may also be mismatched from its surroundings. The case of severe mismatch is not considered here in detail, as photoresists generally have refractive indices $n \approx 1.7$, close to that of silica. Nevertheless, severe mismatch may be expected if imaging was to take place in another setting, for example with a scanning near-field optical microscope (SNOM). However, the variations of SNOM image collection or how they might be accounted for by further modifications to the TMM models are not considered here.

The effects that were studied in detail were those resulting from using photolithographic imaging layers, such as those already used in optical superlensing experiments [22, 23]. The resulting conclusion was that these do not affect the quantitative imaging results significantly. Fig. 5.8 shows line traces of the intensity at the imaging plane for the single-layer superlens and the two-slit mask object, with three different imaging layers considered: a lossless medium perfectly index-matched to SiO_2, $\epsilon = 2.368$ (solid); AZ Ultra-i 123 photoresist [162] in its unexposed state, having $\epsilon = 2.729 + 0.024\mathrm{i}$ (dashed); and the same resist in its fully-bleached state, with $\epsilon = 2.729 + 0.001\mathrm{i}$ (dotted). There is a relatively modest, $\sim$20% reduction in the peak intensities for the cases where an absorbing photoresist is modelled, which is mainly due to the mismatch with the silica layer. However, most significantly, the bleached or unbleached state of the resist was not found to affect results. This is not surprising, given the small imaginary components of the various permittivity values of the resist.

The case where a non-uniform lateral absorbance profile is present in the resist layer has also been studied, in order to represent the situation near the end of the image capture process where the image has been recorded in this layer and some diffraction from this non-uniform absorbance profile might be expected. No discernible effect is observed on the modelled intensity profile either, since any diffraction will be very weak due to the small imaginary component of the resist permittivity. Hence the effects of the detector layer for photolithographic near-field imaging are not significant, apart from a relatively minor intensity drop due to simple dielectric mismatch and

loss; this is straightforward to account for in any TMM model by incorporating an additional dielectric/photoresist interface if this level of accuracy is required.

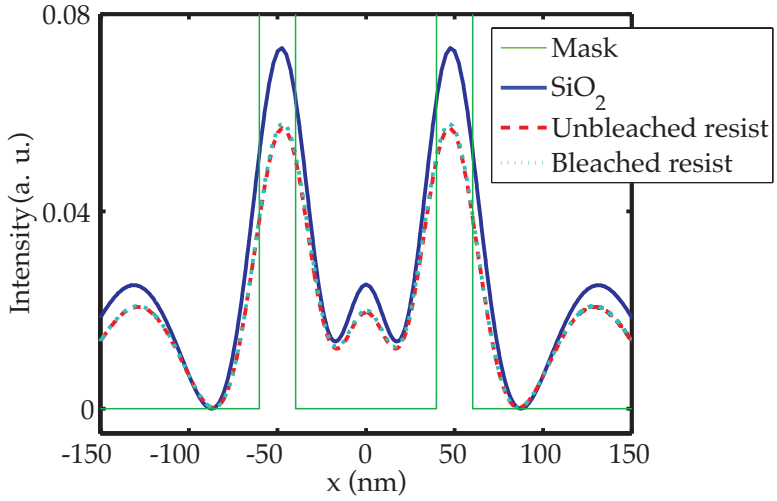

Figure 5.8: FEM modelling results for a unit intensity, sub-wavelength double-slit mask (hairline) imaged through a single-Ag layer superlens with different detector-layer media: lossless SiO_2, ϵ_r = 2.368 (solid); AZ ultra-i 123 photoresist [162] in its unexposed state, $\epsilon_r = 2.729 + 0.024\imath$ (dashed); and the same resist in its fully-bleached state, $\epsilon_r = 2.729 + 0.001\imath$ (dotted).

5.5 Comparison of Processing Requirements for Different Models

Although data produced by the M-TMM model is in much better quantitative agreement with equivalent FEM results than data from TMM, the cost of this improved performance should be considered. The strongest advantage that TMM holds over FEM is the speed with which it produces results; in fact, a case could be made that some quantitative uncertainty in the results is tolerable provided they can be updated quickly and the qualities that they display are sound. Thus it is relevant to consider the processing requirements of M-TMM and to compare these against those of FEM and TMM, so that an informed decision may be made when a modelling technique is to be chosen.

Table 5.3 lists the processing time taken by different modelling techniques to generate TFs and input and output spatial profiles for a 20:40:20 nm PVA:Ag:PVA superlens

exposed to a W mask. The mask is mostly dark, punctuated by only a single 10 nm wide feature, as shown in Fig. 5.9. Details of the different models are as follows: The FEM model domain has dimensions of $500\,\mathrm{nm} \times 10\,\mu\mathrm{m}$; this is covered by a mesh of 119504 elements, affording 239605 degrees of freedom (DOF). Similarly, the TMM and M-TMM models calculate spatial profiles 10 μm in length; the transfer functions produced by all three techniques have a spatial frequency resolution of 0.1 $\mu\mathrm{m}^{-1}$ and a maximum range of $512\,\mu\mathrm{m}^{-1}$. Note that for TMM and M-TMM, the first results produced are TFs, with input and output spatial profiles calculated from these results and thus requiring slightly longer processing time. The FEM process works in the opposite direction, with TFs only calculated once the input and output spatial profiles are known.

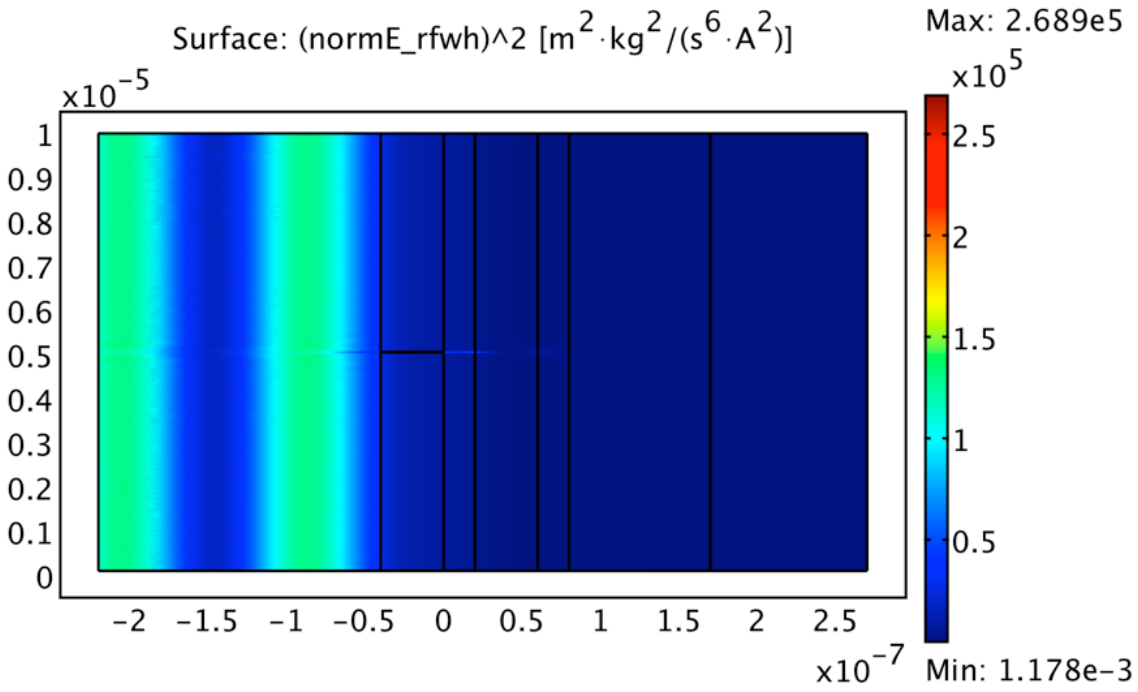

Figure 5.9: Superlens simulation domain modelled by various methods in Table 5.3.

The times listed in Table 5.3 are the cumulative solution processing times reported by each technique for the relevant results, averaged over six runs. The time required to build the model meshes is not included in these measurements. All processing is done in Matlab R2010a [121], with the exception of the FEM spatial profiles, which are calculated first in COMSOL 3.5a [122] and then exported to Matlab for further processing. Code is run on an Intel Core 2 Duo T7500 processor, running at 2.2 GHz with 4 Gb of DDR2 RAM. The operating system is Mac OS X version 10.6.8 "Snow Leopard."

Table 5.3: Comparison of model processing times for superlens simulation.

Output	**Model**		
	TMM	**M-TMM**	**FEM**
Transfer function	5.062 s	6.981 s	20.323 s
Spatial profiles	5.584 s	7.934 s	18.778 s

The speed advantages of TMM over FEM are clear in Table 5.3, with the FEM model taking an average of four times longer to produce a TF than the TMM technique. Similarly, the TMM technique is faster to produce spatial output profiles, although the advantage here is only a factor of three. Yet the biggest revelation contained in Table 5.3 is the minuscule increase in processing time required by M-TMM over TMM. For less than two additional seconds of processing time, the results returned by M-TMM are vastly superior to those of TMM. M-TMM is also faster than FEM, taking less than half the processing time that FEM does to produce comparable results. The advantages of M-TMM become even more apparent when the size of the mesh over the FEM model is increased to reduce noise in the results. Fig. 5.10 shows the relationship between processing time and mesh size for the FEM model illustrated in Fig. 5.9.

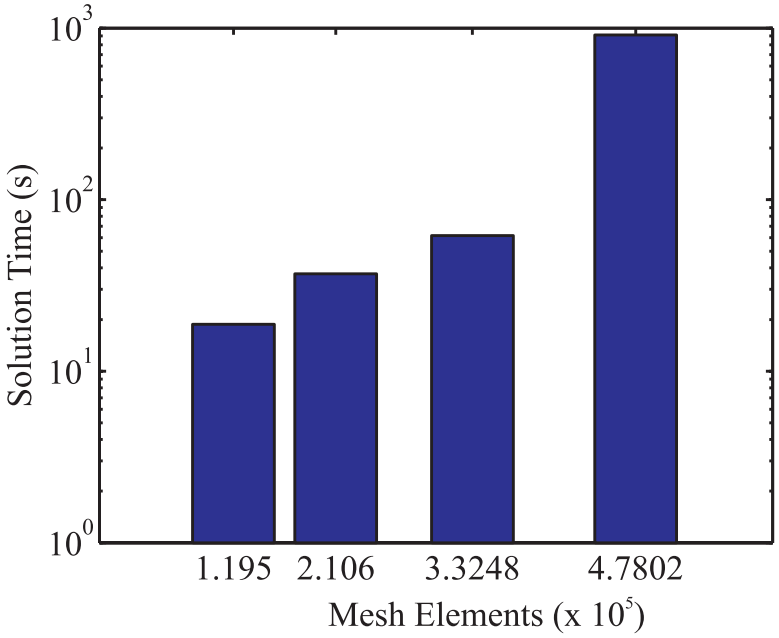

Figure 5.10: Performance characteristics of the FEM solution to the model domain shown in Fig. 5.9. Solution times are the average of six consecutive runs and do not include the time required to generate the model meshes.

FEM processing time increases approximately linearly with mesh element count up to a certain threshold, where the software runs out of available memory and begins to write data out to the hard drive. This phenomena is illustrated in Fig. 5.10, where the processing time for a mesh with $\sim 480,000$ elements is fifteen times greater than the processing time for a mesh with $\sim 330,000$ elements, even though the first mesh is only 50% larger than the second. Although this paging out behaviour can dramatically increase the time required to run a simulation, it is preferable to the alternative, where no paging is used and simulations are terminated arbitrarily when no more free memory is available. This was the default behavior in COMSOL versions prior to 3.5a and it limited the practical maximum mesh size in simulations to about 200,000 elements. (Improvements in algorithmic efficiency and full support for 64 bit hardware architectures in COMSOL version 3.5a explain the lack of paging out for the 330 k element mesh described in Fig. 5.10.)

In contrast to FEM, M-TMM never approaches the memory limits of a modern personal computer; instead, the bottleneck in the M-TMM code is processor speed. Fortunately, there are three options available for improving TMM and M-TMM performance further, should the need arise. Firstly, the analytical simulation parameters described in this section are intentionally over-specified, so as to provide a direct comparison between the TMM, M-TMM and FEM modelling techniques. The maximum range of the Matlab-based models can be safely reduced by an order of magnitude to around $50\ \mu\mathrm{m}^{-1}$, without any practical reduction in usefulness of the model and with an order of magnitude decrease in processing time. Secondly, the Matlab code can be compiled in order to increase the speed of execution at the expense of slower code development. Lastly, Matlab can be run on distributed computing architectures to harness the power of multiple processor cores at once. Although COMSOL can technically also be parallelised, the benefits are not as pronounced given the high memory requirements of the software.

In conclusion, the additional processing time required by M-TMM over TMM is negligible in light of the improved results that it offers. Both techniques produce results faster than FEM, making M-TMM the preferred technique for modelling superlenses. The fact that M-TMM can be sped up further by the use of compilation and other software optimizations only serves to strengthen these findings.

5.6 Multilayer Superlens Performance Example

Modified TMM analysis has also been applied to a triple-layer superlens with the same total thickness as the single-layer example, whose parameters are also described in Table 5.1. Accurate characterisation of such a lens is of special interest, given the attention that multi-layered lenses have received in the literature [25, 27, 63, 77]. As seen in Fig. 5.11, the characteristic differences observed between transfer functions calculated using FEM and a simple TMM model for a single-layer isolated superlens are also present for the multi-layer equivalents: zero-frequency performance varies greatly between techniques and discrepancies remain in the estimates of both the peak transmission and peak wave number. Once again, M-TMM is closer to the FEM-generated results, particularly for the position of the SP peak. The spatial profiles shown in Fig. 5.12 confirm this conclusion, as do the high correlation coefficients [30] between FEM- and M-TMM-generated transfer functions, shown in Table 5.4.

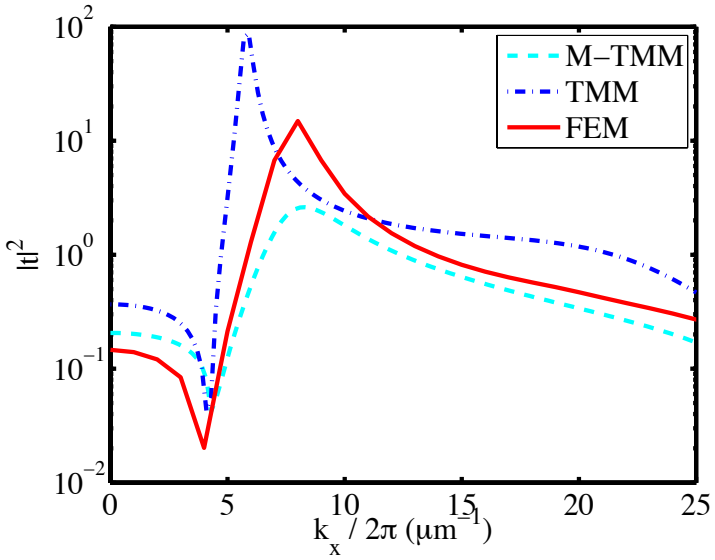

Figure 5.11: M-TMM (dotted), TMM (dashed) and FEM (solid) transfer functions for the multilayer superlens described in Table 5.1.

5.7 Thick Superlenses Revisited

Given the differences between the improvements that M-TMM affords overs TMM, it is worth returning to the example of a thick Ag superlens examined in Section 4.4.

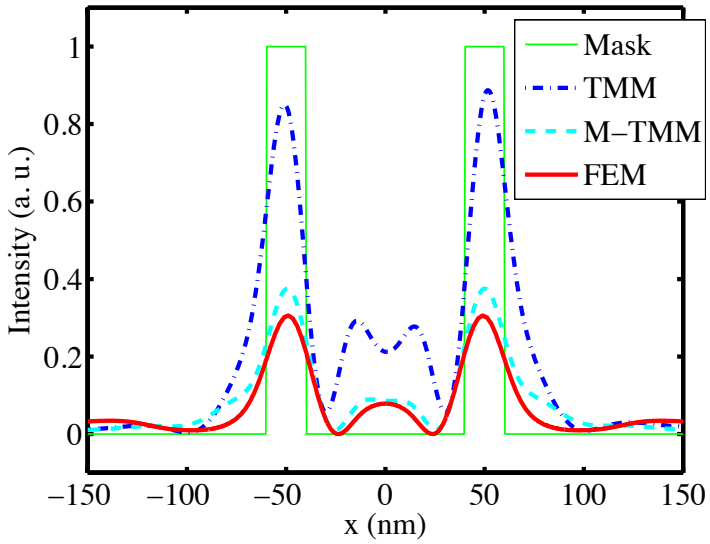

Figure 5.12: Output profiles predicted by TMM (dotted), M-TMM (dashed) and FEM (solid) for a unit intensity, sub-wavelength double-slit mask (hairline) with 20 nm wide apertures on a 100 nm centre-to-centre spacing.

Table 5.4: Superlens characterisation metrics.

Parameter	Single-Ag layer superlens			Multi-Ag layer superlens		
	Simple TMM	Modified TMM	FEM	Simple TMM	Modified TMM	FEM
DC tx	0.3172	0.1727	0.1084	0.3671	0.2060	0.1465
Peak tx	12.04	0.6838	1.485	87.41	2.612	14.88
Peak wave-number (μm^{-1})	7.0 ± 0.1	8.8 ± 0.1	9.0 ± 0.2	5.9 ± 0.1	8.3 ± 0.1	8.0 ± 0.5
Correlation to FEM	0.2380	0.9894	1.000	-0.0411	0.8356	1.000

Analysis with the TMM technique concluded that an isolated, 120 nm thick slab of Ag would be able to reproduce evanescent features, provided the very low transmission through the metal was not washed out by noise in the source of illumination. Results for the more practical situation where a 120 nm thick Ag slab was in close proximity to a photomask were less positive, suggesting much stronger attenuation of evanescent components than in the associated propagating part of the spatial frequency spectrum.

Hence the analysis presented in Section 4.4 is reproduced below using M-TMM, starting first with Fig. 5.13, which shows the TFs for a family of PMMA:Ag:SiO_2 super-

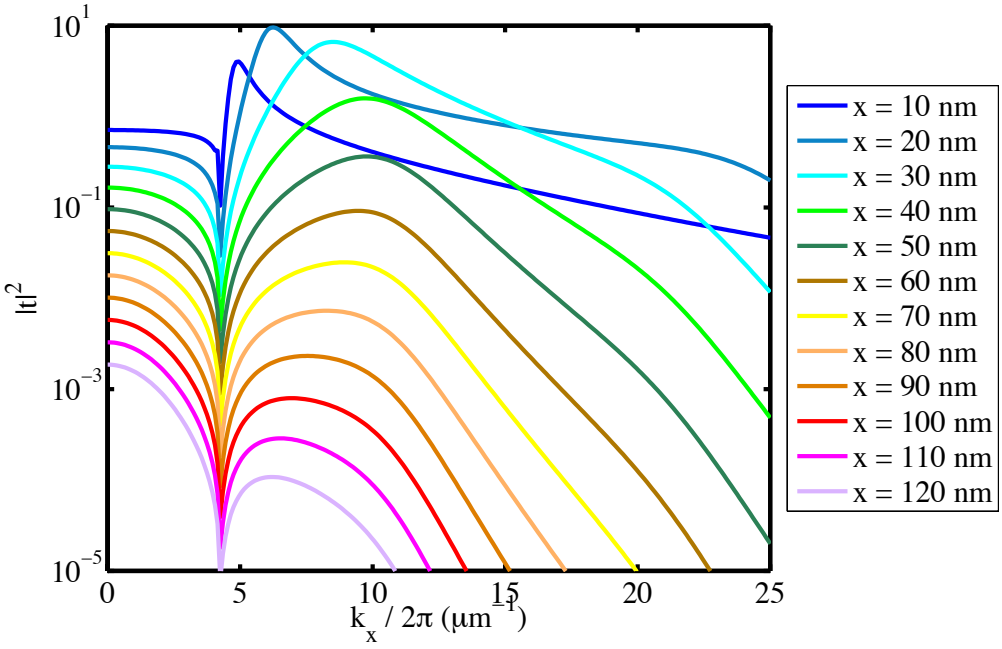

Figure 5.13: Transfer functions calculated via M-TMM for 10:x:10 nm PMMA:Ag:SiO_2 lens stacks in contact with a 50 nm W mask, where x = [10, 20, ... 120] nm.

lenses in intimate contact with a 50 nm thick W mask. The thickness of the PMMA and SiO_2 layers is set at 10 nm, while the Ag thickness is swept between 10 nm and 120 nm in 10 nm steps. The corresponding BW curve for these TFs is shown in Fig. 5.14, with the original TMM-calculated curve from Section 4.4 included for comparison.

The side-by-side analysis shown in Fig. 5.14 reveals some interesting results: firstly, BW is no longer at a peak for a Ag thickness of 120 nm, instead, optimum bandwidth is observed for Ag thicknesses between 60 nm and 70 nm. Secondly, the maximum BW achievable from this family of superlenses has increased, from around 5.8 μm^{-1} to just under 7 μm^{-1}. This trend is present again in Fig. 5.15, which shows the BW curves for the family of superlenses where the thicknesses of both the Ag layer and the surrounding dielectric layers are varied between 10 nm and 120 nm. The peak in BW seen in Fig. 5.14 is repeated here for multiple spacer layers up to 30 nm thick. Taking a 30:60:30 nm PMMA:Ag:SiO_2 stack as an example and studying its transfer function, shown in Fig. 5.16, reveals good transmission beyond $\frac{k_x}{2\pi} = 10\ \mu m^{-1}$, i.e. for spatial periods as low as 100 nm. The image produced by a square wave with 100 nm period imaged through such a lens stack is shown in Fig. 5.17. This sustained bandwidth performance around the 30:60:30 nm thickness window suggests that designs fabricated with these nominal dimensions will be highly resilient to uniform variations

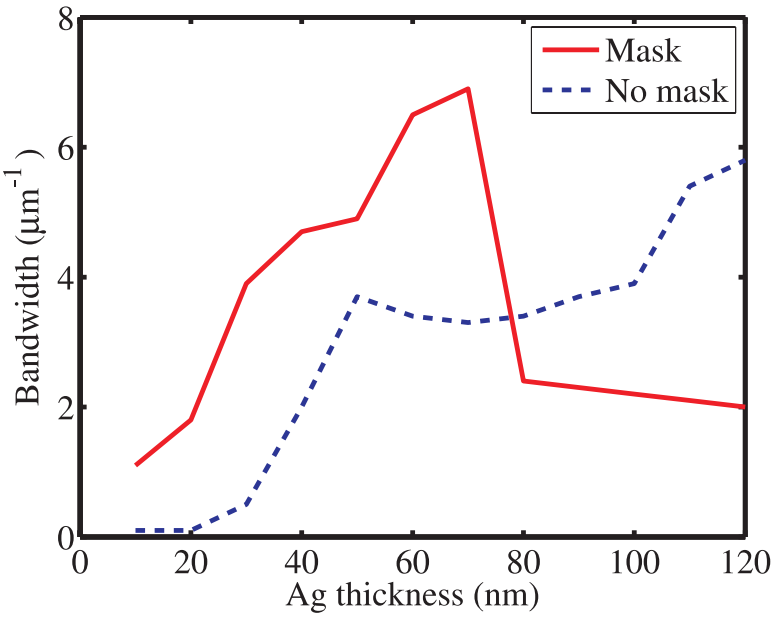

Figure 5.14: Bandwidth curve for the 10:x:10 nm PMMA:Ag:SiO_2 family of lens stacks shown in Fig. 5.13, calculated with (solid) and without (dashed) consideration of a 50 nm W mask placed in contact with the superlens stack. The values of x are marked on the horizontal axis.

in individual layer thickness, making them much easier to fabricate in the laboratory. Furthermore, this robustness was not apparent from the TMM results presented earlier in Section 4.4 and is confirmation that near-field interactions between a mask and superlens can have a strong effect on both the design and performance of the superlens.

5.7.1 Multilayered Superlens Stacks

Although sub-wavelength resolution from a lens stack with a total thickness of more than 120 nm would be a considerable achievement, a desire exists to increase the overall lens thickness even further, to the point where the total Ag thickness is of the order of 120 nm or beyond. Hence, three different lens stacks in contact with 50 nm W masks are analysed via M-TMM in Fig. 5.18, each with total Ag thickness of 120 nm but with different numbers of layers. The first stack is a five layer, 30:60:60:60:30 nm PMMA:Ag:SiO_2:Ag:SiO_2 arrangement. The second stack has seven layers in all, including three Ag layers, each 40 nm thick. The last stack has nine layers with four of those made up of Ag, 30 nm thick. Like the first stack, the first layer in each stack is

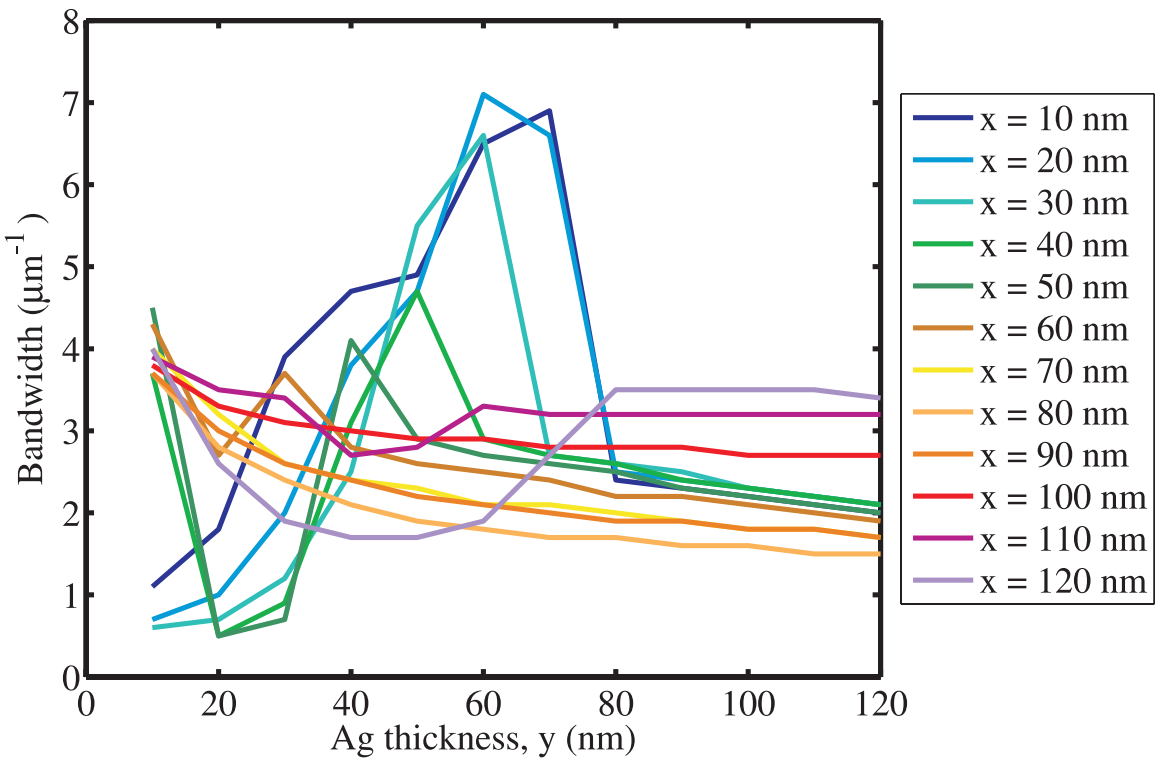

Figure 5.15: Bandwidth curves for x:y:x PMMA:Ag:SiO_2 lens stacks. Each line represents a value of x between 10 nm and 120 nm, varying in 10 nm increments. The values of y, which also vary between 10 nm and 120 nm in 10 nm steps, are represented by the values on the horizontal axis. The effects of a 50 nm thick W mask, placed in contact with the superlens stack, are included in these results.

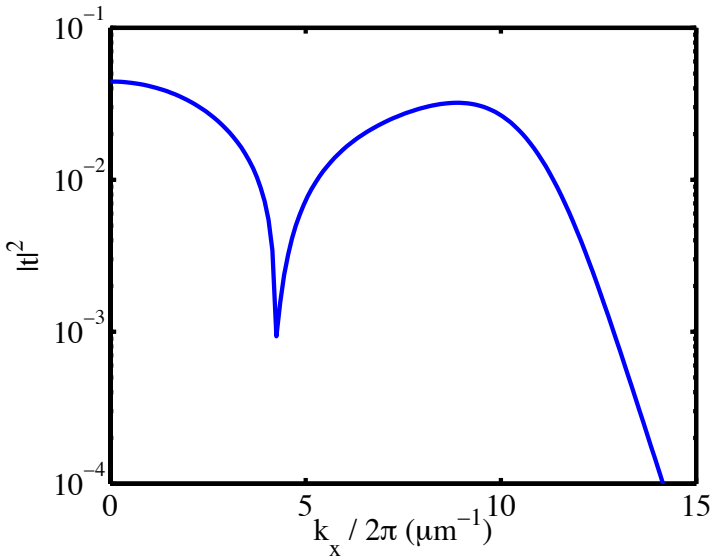

Figure 5.16: Transfer function for a 30:60:30 nm PMMA:Ag:SiO_2 lens stack in contact with a 50 nm thick W mask, calculated via M-TMM.

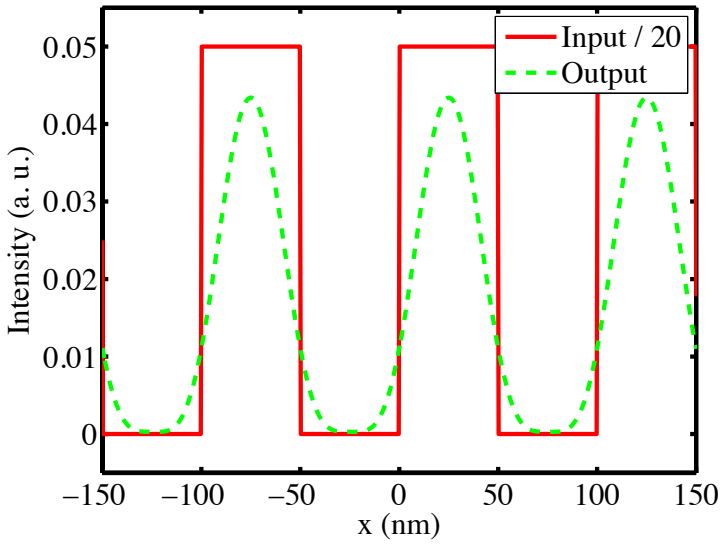

Figure 5.17: M-TMM output for the lens described in Fig. 5.16, exposed to a 100 nm period square wave.

PMMA, half as thick as the neighbouring Ag layer. The remaining spacers between the Ag layers are SiO_2, with thickness equal to that of the Ag layers. Only the last layer is different; it is half as thick as the other layers, in accordance with the Veselago ratio [36]. Note that all three lens stacks have total thickness of 240 nm.

Interestingly, the high transmission predicted for Ag layers approximately 60 nm thick is not preserved when such layers are stacked. Nevertheless, similar performance to that of a 30:60:30 nm lens stack can be achieved by a 240 nm thick stack made up of three 40 nm Ag layers. Such a design raises the possibility of sub-wavelength imaging at almost a quarter of a micron, provided the component films could be grown with adequate precision.

5.8 Summary

The numerical results presented in Table 5.4, together with the transfer functions shown in Figs. 5.6 and 5.11 and the spatial profiles presented in Figs. 5.7 and 5.12 show that results found using a simple, isolated-superlens model in TMM analyses are not quantitatively good approximations of full-wave vector analyses or of real-world performance. The artefacts in these results are addressed to a large extent by the proposed

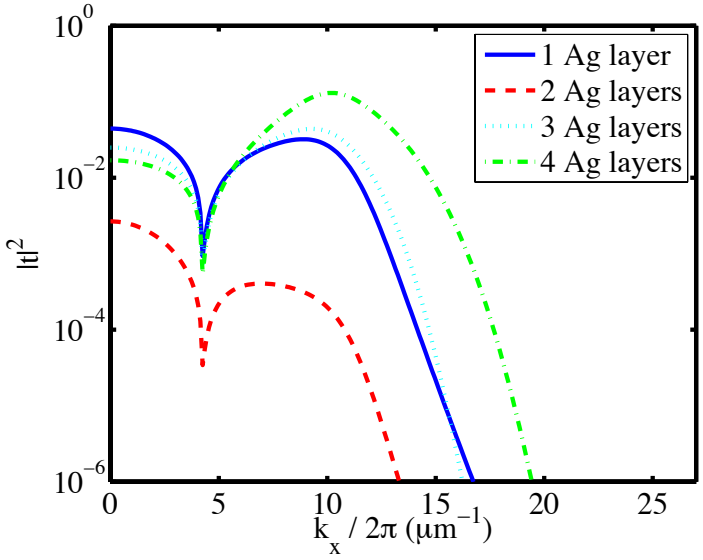

Figure 5.18: Transfer functions for double, triple and quadruple Ag-layer superlens stacks with Ag layer thickness of 60 nm, 40 nm and 30 nm, respectively, giving a total of 120 nm of Ag in each lens stack. The Ag layers are separated by SiO_2, with PMMA and SiO_2 at the start and end of each stack. The thickness of the dielectric layers was set according to the Veselago ratio of 1:2: . . . :2:1. The TF for a single Ag-layer, 30:60:30 nm PMMA:Ag:SiO_2 superlens, first shown in Fig. 5.16, is also displayed. All curves are calculated via M-TMM, which assumes a 50 nm thick solid W mask in contact with each superlens.

modified transfer-matrix model, which provides better estimates of peak wave number and overall transfer function shape. This is the case regardless of the number of layers in the superlens under consideration.

Furthermore, the M-TMM model was used to find a resilient, single-Ag layer superlens design. This consisted of a layer of Ag between 60 nm and 70 nm, sandwiched between a layer of PMMA and one of SiO_2, both with matching thickness between 10 nm and 30 nm. Many-layered lens stacks were also investigated and similar performance was observed for a multi-layered 240 nm thick lens stack as for the 120 nm thick single-layer design described above.

Chapter 6

Experimental Method and Techniques*

To continue the theme of lens model validation, sustained efforts were made to fabricate and characterise planar metallo-dielectric superlens systems. The body of this experimental work was divided into three areas: firstly, the fabrication of masks to provide input stimuli to near-field lenses; secondly, the development of a thin-film photoresist stack used to accurately capture the output intensity profiles from such lenses; thirdly and most importantly, the fabrication of the lenses themselves. The construction of these three fundamental components of an imaging system, as well as their operation and the equipment used to fabricate them are documented in this chapter.

6.1 Mask Fabrication

Three techniques were investigated in order to construct masks for near-field imaging experiments. These were electron beam lithography (EBL), interference lithography (IL) and maskless laser patterning (MLP). Each technique relied on some means of patterning a layer of resist, before etching that pattern into an underlying metal layer.

*Aspects of this chapter will be presented as: C. P. Moore and R. J. Blaikie, "Flexible PDMS Support Layers for the Evanescent Characterization of Near-Field Lithography Systems," at the 55th International Conference on Electron, Ion, and Photon Beam Technology and Nanofabrication (EIPBN 2011) in Las Vegas, Nevada, United States of America, 31 May – 3 June, 2011.

The particular steps required for each method, as well as the key differences between the techniques and the merits of the resulting masks are discussed in this section.

6.1.1 Electron Beam Lithography

The first technique attempted was EBL, which relied on a Raith 150 e-beam lithography system to pattern an electron resist and an Oxford Instruments Plasmalab 80 Plus reactive ion etching (RIE) system to dry etch the resist features into an underlying layer of tungsten (W), using the process outlined in Fig. 6.1. The technique allowed for intricate, high resolution patterns and was therefore attractive for sub-wavelength experiments. Unfortunately, each mask required many hours to write and the resulting patterned area was only 1 mm^2 to 2 mm^2 in size. For these reasons the technique described here was used only for a small number of samples, before other methods were investigated.

The construction process for EBL began with the deposition of a 40 nm W film onto a glass coverslip, using an Edwards Auto 500 sputtering system. Next, a thin film of poly (methyl methacrylate) (PMMA), approximately 130 nm thick, was spun onto the tungsten. The polymer was administered as a 4% (w/w) solution of high molecular weight (HMW) PMMA dissolved in xylene, which was spun using a Laurell 150 mm spin coater. After an oven bake of 185°C for 30 minutes the sample was placed in a Raith 150 EBL system to be patterned.

After patterning, the PMMA was developed at room temperature in a methyl isobutyl ketone (MIBK) solution. The mask features, shown in Fig. 6.2, were then transferred to the underlying tungsten layer via RIE, performed using an Oxford Instruments Plasmalab 80 Plus dry etching system. Once the tungsten was etched, the PMMA layer was dissolved with acetone, leaving a positive photolithography mask. Scanning electron micrographs of the final mask pattern are shown in Fig. 6.3, with the full details of each individual step in the EBL mask fabrication process given in Table 6.1.

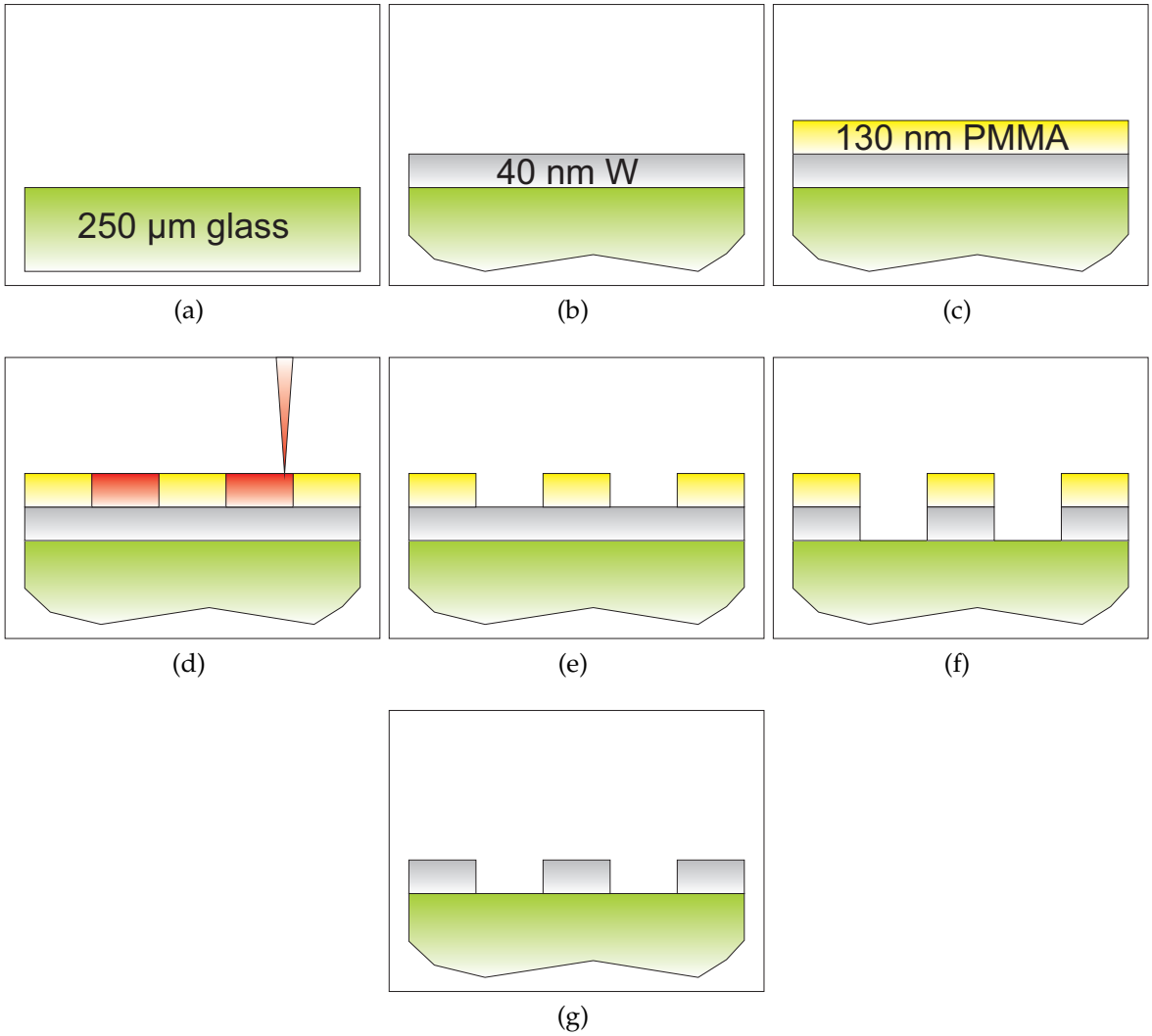

Figure 6.1: Electron beam lithogrpahy mask construction schematic. Starting with a bare substrate (a), a metal film is sputtered (b) before resist is spun on (c). After exposure (d) and development (e) of the resist, the metal is etched (f) and the resist is dissolved (g). Note that illustrations are not to scale.

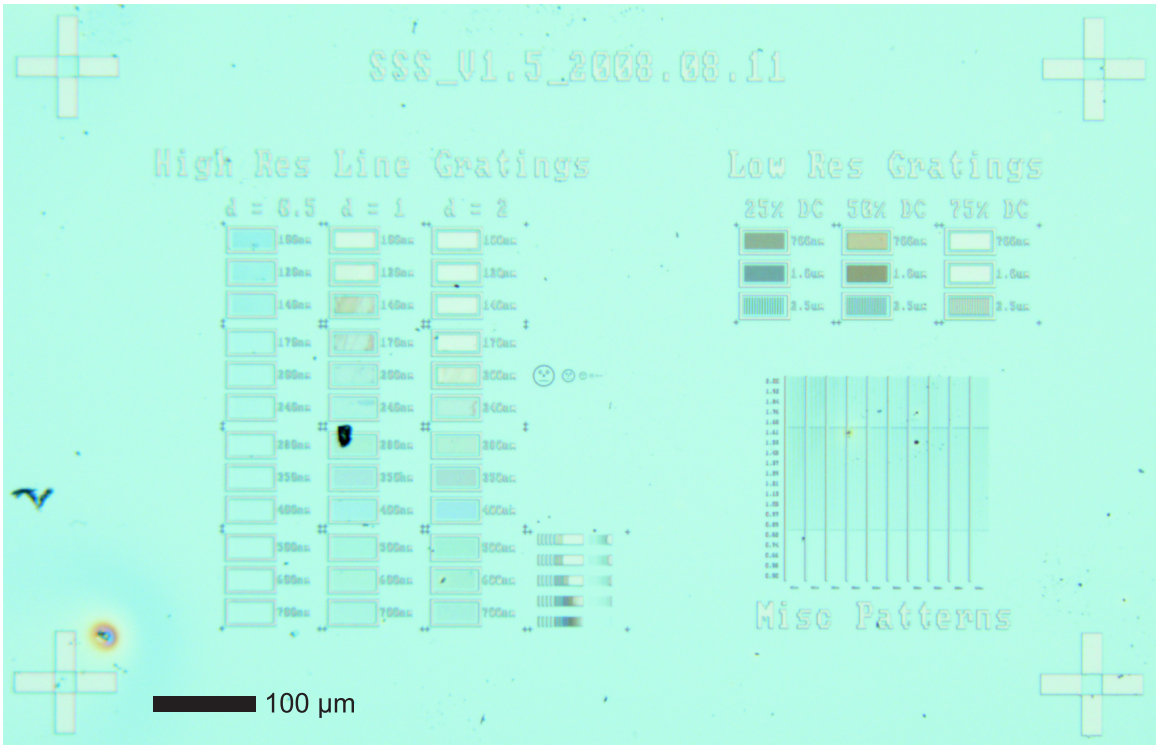

Figure 6.2: Optical micrograph of EBL mask pattern in PMMA.

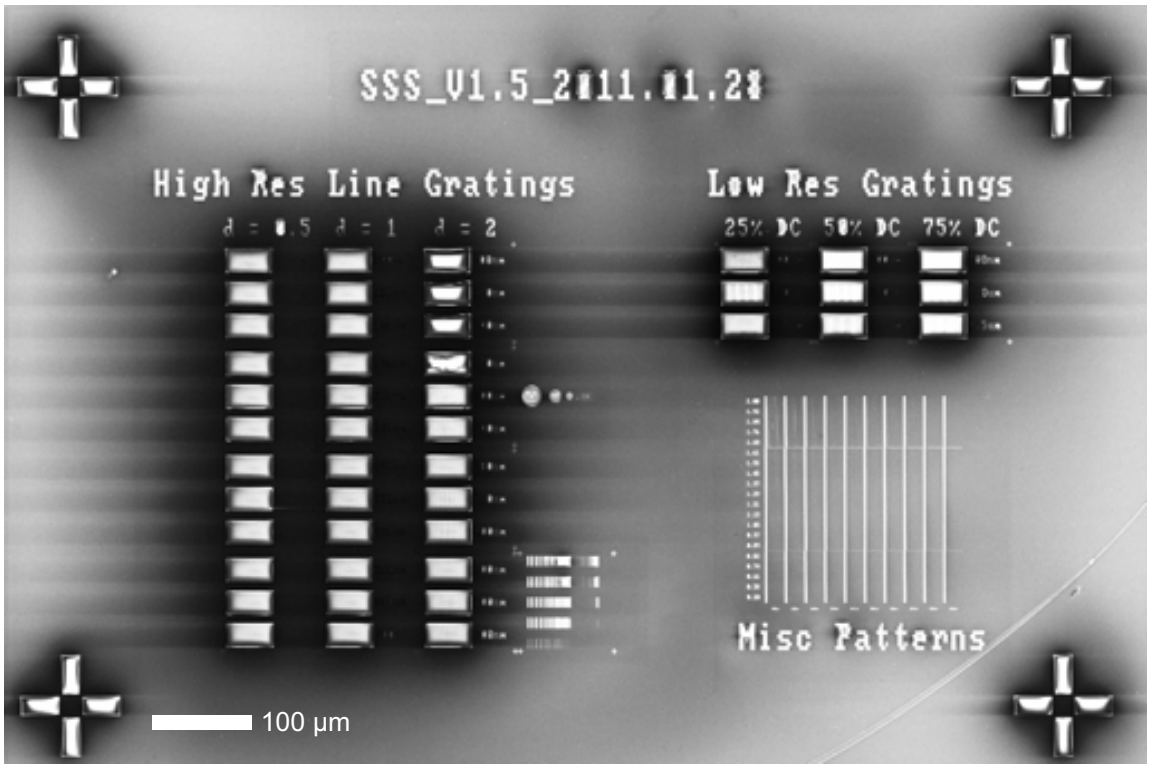

(a)

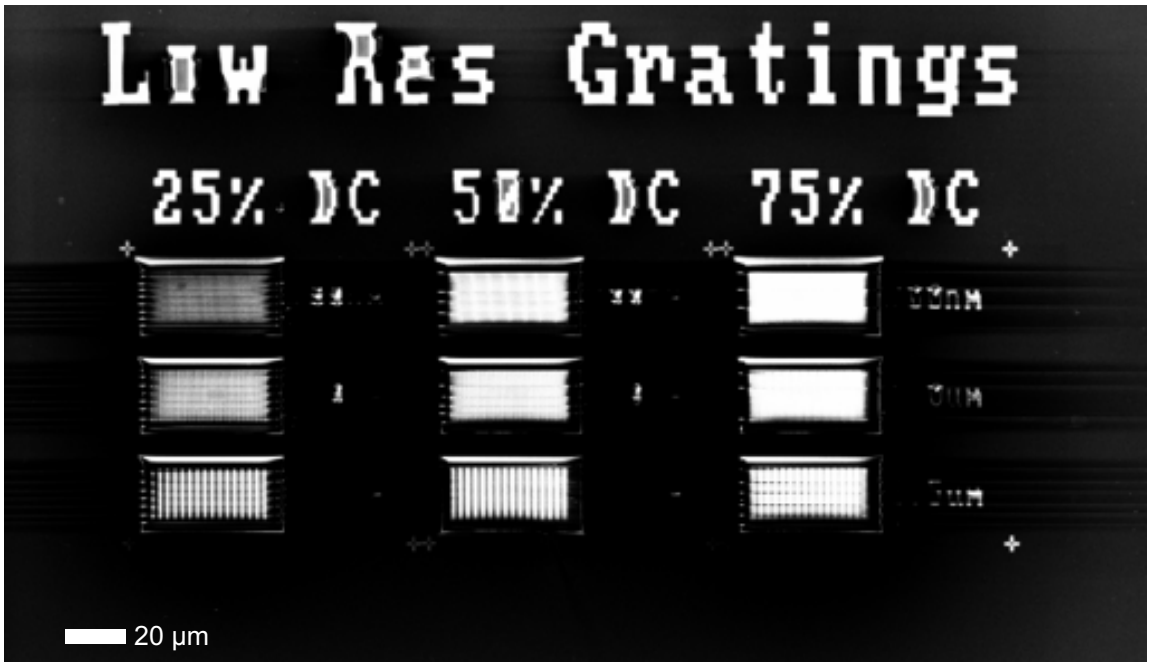

(b)

Figure 6.3: Scanning electron micrographs of EBL mask pattern etched into W (a), with detail of the top right section of the mask shown in (b). Dark regions around features, text distortions and horizontal banding across figure are due to charging of the exposed areas of the non-conductive substrate.

Table 6.1: Electron beam lithography mask recipe.

	Ingredients		
	Substrate	22 mm $\times$ 22 mm $\times$ 250 μm glass coverslips	
	Mask metal	99.95 % pure W sputtering target	
	Resist	4 % (w/w) HMW PMMA in xylene	
	Developer	1:3 (v/v) MIBK:IPA	
	Step	**Equipment**	**Parameters**
1	Sputter W	Edwards Auto 500	300 W DC, Base pressure $\leqslant 7 \times 10^{-5}$ mBar, Ar @ 10 sccm
2	Spin resist	Laurell WS-400B-6NPP-Lite Spin Coater	4000 rpm, 60 s
3	Bake resist	Sanyo Drying Oven	185°C, 30 min
4	Expose resist	Raith 150	Dose: area = $150\ \mu\mathrm{C/cm^2}$, line = 600 pC/cm, dot = 300 fC/dot
5	Develop resist		30 s immersion
6	Rinse		IPA
7	Etch W	Oxford Instruments Plasmalab 80 Plus	NiCr electrode, $\mathrm{SF_6}$ @ 80 sccm, 40°C, 150 mTorr
8	Dissolve resist		Acetone, followed by methanol and IPA

6.1.2 Interference Lithography

In an attempt to reduce the long write times demanded by EBL, a Lloyd's mirror and 325 nm laser were used to write periodic interference patterns into tungsten masks. The IL process, illustrated in Fig. 6.4, began with W deposited onto glass to a nominal thickness of 40 nm, using an Edwards Auto 500 sputterer. The W was then covered with ∼140 nm of Microchemicals AZ Barli-II, an anti-reflective coating (ARC) that reduced reflections and standing waves at the metal surface. The last layer in the stack was a 500 nm film of Microchemicals AZ 1518, a UV-sensitive positive photoresist. Propylene glycol monomethyl ether acetate (PGMEA) was used to dilute the photoresist and limit layer thickness, which in turn reduced the aspect ratio of developed features and eased the criteria that subsequent etch processes had to meet.

Once the mask stack was complete, a Lloyd's mirror was used to pattern the photoresist. The Lloyd's mirror comprised a sample holder and a planar aluminium mirror, both fixed to a rotation stage and placed perpendicular to each other, as shown in Fig. 6.5. A 50 mW Kimmon helium-cadmium (He-Cd) laser operating at 325 nm with a TE polarised output beam was used to illuminate the sample and the mirror, which resulted in an interference patterning forming in the plane of the sample. After exposure, the resist was developed in dilute Microchemicals AZ MIF 326 developer. Undiluted, the concentration of the active ingredient in MIF 326, tetramethyl ammonium hydroxide (TMAH), was 2.38%; however, the solution was further diluted 2:1 with de-ionised water (DIW) to reduce the development rate. This was necessary to limit the dark development rate of the resist, which would otherwise reduce the contrast of the developed patterns.

Once developed, samples were etched using RIE, which proved to be one of the most complicated steps in the mask fabrication process. The ARC layer needed to be removed in steps without damaging the underlying layers, resulting in a three part etch that was difficult to monitor. The first step, shown in Fig. 6.6a, involved etching the ARC with oxygen (O_2), according to the pattern in the resist. Next, the resist pattern was transferred down into the W layer using SF_6 as the etchant, as shown in Fig. 6.6b. This step also partially removed the resist above the ARC. Lastly, the remaining ARC was completely removed with another O_2 etch, shown in Fig. 6.6c. The particulars of these etch steps, together with the rest of the IL process, are documented in Table 6.2.

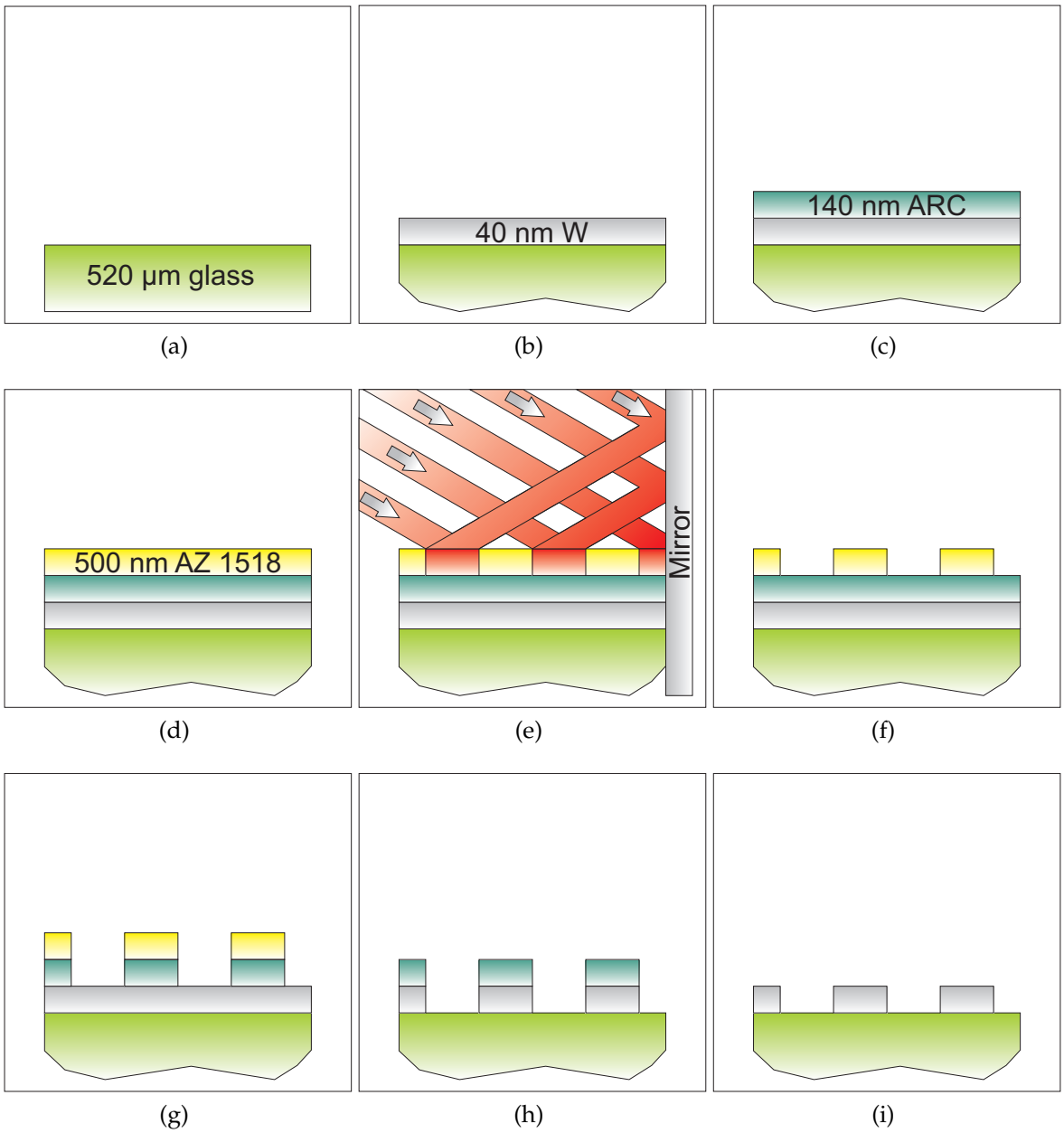

Figure 6.4: Interference lithography mask construction schematic. Starting with a bare substrate (a), a metal film is sputtered (b) before ARC (c) and resist (d) are spun on. After exposure (e) and development (f) of the resist, the ARC (g) and metal (h) are etched. Any remaining resist is collaterally removed during the metal etch. Finally, the remaining ARC is etched away completely (i). Note that illustrations are not to scale.

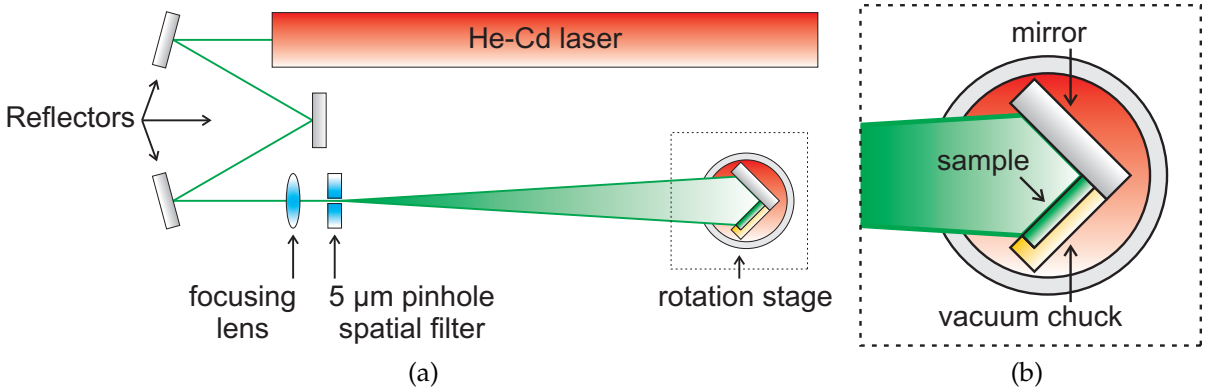

Figure 6.5: Lloyd's mirror IL setup (a), with detail of the rotation stage (b).

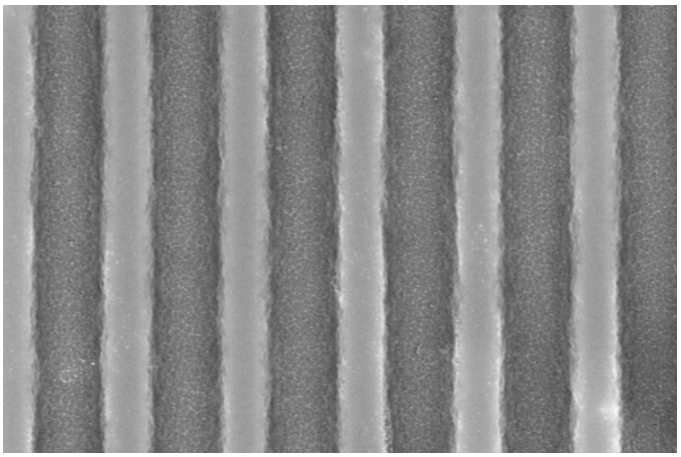

(a)

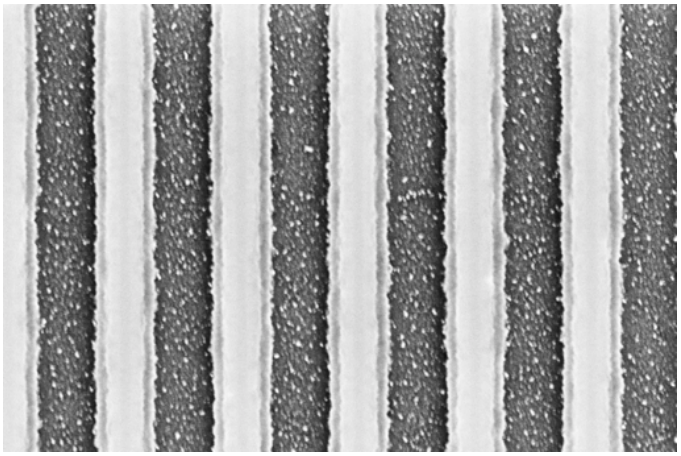

(b)

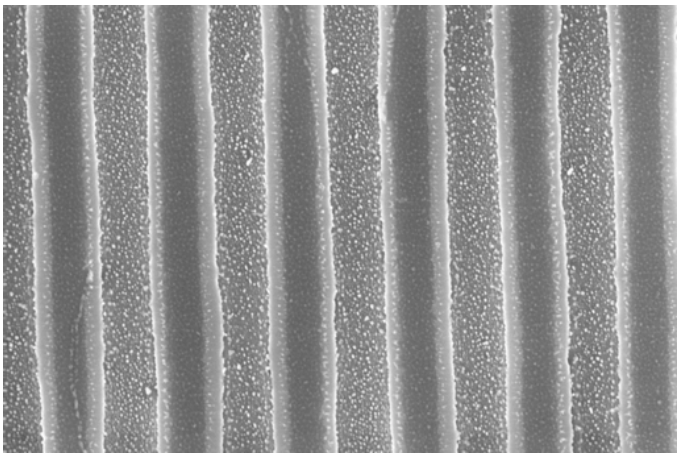

(c)

Figure 6.6: SEM images of different steps in the IL etch process. (a) Resist and ARC pillars on a W substrate after an O_2 etch. (b) Resist, ARC and W pillars on a quartz substrate after O_2 and SF_6 etches. (c) Etched W pillars on a quartz substrate. Nominal period for each pattern is 1 μm.

Table 6.2: Interference lithography mask recipe.

	Ingredients		
	Substrate	10 mm × 10 mm × 520 μm quartz wafer	
	Mask metal	99.95% pure tungsten sputtering target	
	Anti-reflective coating	AZ Barli-II	
	Photoresist	1:1 (v/v) AZ 1518:PGMEA	
	Developer	2:1 (v/v) AZ MIF 326:DIW	
	Step	**Equipment**	**Parameters**
1	Sputter W	Edwards Auto 500	300 W DC, base pressure $\leqslant 7 \times 10^{-5}$ mBar, Ar @ 10 sccm
2	Spin ARC	Headway Research PWM32 Spin Coater	3000 rpm, 30 s
3	Bake ARC	Stuart Scientific Hotplate SH1D	200°C, 30 s
4	Spin resist	Headway Research PWM32 Spinner	3000 rpm, 30 s
5	Bake resist	Stuart Scientific Hotplate SH1D	115°C, 60 s
6	Expose resist	325 nm He-Cd laser	dose = 400 mJ/cm^2, θ = 9.35°, p = 1 μm
7	Develop resist		60 s immersion
8	Rinse		DIW
9	Etch ARC	Oxford Instruments Plasmalab 80 Plus	NiCr electrode, 100 W, 173 K, 8 mTorr, O_2 @ 5 sccm, 150 s
10	Etch W & resist	Oxford Instruments Plasmalab 80 Plus	NiCr electrode, 200 W, 313 K, 150 mTorr, SF_6 @ 80 sccm, 14 s
11	Rinse		Acetone
12	Rinse		Methanol
13	Rinse		IPA
14	Clear ARC	Oxford Instruments Plasmalab 80 Plus	NiCr electrode, 100W, 173 K, 8 mTorr, O_2 @ 5 sccm, 150 s

6.1.2.1 Interference lithography calculations

One of the advantages of the IL system was that the period of the interference pattern, p, was well-defined and easily changed, as shown in Fig. 6.7. This was because p was dependent only on the wavelength of the laser, λ, and the angle of the sample normal relative to the incoming beam, θ:

$$p = \frac{\lambda}{2\sin\theta}. \tag{6.1}$$

With λ fixed at 325 nm, p could be altered by placing the sample on a rotation stage and controlling θ. Increasing θ gave smaller p down to half of the wavelength of the laser, while decreasing θ so that the sample saw more of the incoming beam led to periods greater than the wavelength of the laser. For example, a period of 1 μm required θ of $\sin^{-1}\left(\frac{\lambda}{2p}\right) = 9.35°$, given λ of 325 nm.

The second parameter crucial to the correct operation of the IL system was the dose administered during exposure, d. In order to calculate d, it was first necessary to find the irradiance, i.e. the power density, of the interference pattern, $I_{pattern}$, which was dependent on the irradiance of the laser immediately in front of the rotation stage, I_{laser}. This was indirectly measured using a Thor Labs S120VC 200 – 1100 nm power sensor, connected to a matching PM100A meter. The calculations required to find $I_{pattern}$ and d from the power meter readings, P_{sensor}, are given below using typical values for P_{sensor} and θ. Terms used in these calculations are illustrated in the schematic shown in Fig. 6.7.

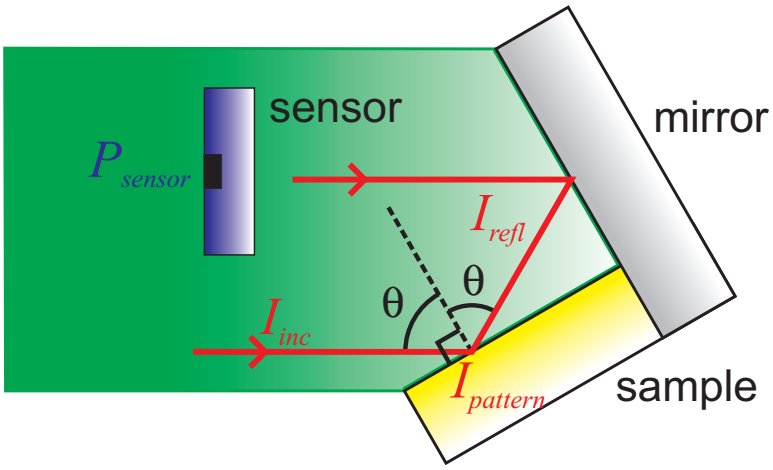

Figure 6.7: Terms used in IL dose calculations. All irradiance and power measurements are RMS, unless otherwise noted.

Placing the S120VC power sensor immediately in front of the rotation stage and facing the laser beam, P_{sensor} was measured to be ~0.200 mW. Given that the diameter of the input aperture of the sensor was 9.5 mm [163], its surface area, A, was given by

$$\begin{aligned} A &= \pi \times \left(\frac{diameter}{2}\right)^2 \\ &= 0.709\ cm^2. \end{aligned} \tag{6.2}$$

Hence the irradiance at the sensor, I_{sensor}, was

$$\begin{aligned} I_{sensor} &= P_{sensor}/A \\ &= 0.200\ mW/0.709\ cm^2 \\ &= 0.282\ mW/cm^2 \end{aligned} \tag{6.3}$$

and the irradiance of the beams directly incident on the sample, I_{inc}, was

$$\begin{aligned} I_{inc} &= I_{sensor} \times \cos\theta \\ &= 0.278\ mW/cm^2, \end{aligned} \tag{6.4}$$

where θ was 9.35° for $p = 1\mu m$, according to Eq. (6.1). Similarly, the irradiance of the beams reflected onto the sample by the mirror, I_{refl}, was

$$I_{refl} = I_{sensor} \times \cos\theta \times R_{mirror}, \tag{6.5}$$

where R_{mirror} was the reflection coefficient of the mirror at 325 nm wavelength, given as 0.93 [164]. This gave I_{refl} = 0.259 mW/cm^2, giving a peak interference pattern irradiance of

$$\begin{aligned} I_{pattern} &= \left(\sqrt{I_{inc}} + \sqrt{I_{refl}}\right)^2 \\ &= 1.074\ mW/cm^2. \end{aligned} \tag{6.6}$$

Given $I_{pattern}$, peak dose, d, was found by integrating over the time period of the exposure, t:

$$\begin{aligned} d &= \int_0^t I_{pattern} dt' \\ &= I_{pattern} \times t. \end{aligned} \tag{6.7}$$

Typically, d between 250 and 400 mJ/cm^2 was used, requiring exposure times of the order of five minutes.

6.1.2.2 Interference lithography challenges

Several problems were encountered with the IL process and with the etch steps, in particular. In early trials, the resist was not completely removed during the second etch, resulting in ARC ridges along the W pillars after the third and final etch, as shown in Fig. 6.8. These unintended features made intimate contact between the metal and a planar surface impossible, rendering the mask unsuitable for its intended purpose.

After attempting to remove the ARC peaks with plasma ashing and successively stronger O_2 plasma etches, the problem was finally solved by removing the samples from the RIE after the SF_6 etch and rinsing them sequentially in acetone, methanol and IPA. The acetone removed any remaining resist and the methanol and IPA removed any acetone residue. Micrographs of the samples before and after the solvent rinse are shown in Fig. 6.9. After rinsing, the samples were returned to the RIE for their final O_2 etch.

A second side effect of the IL process was the roughening of the quartz substrate as a result of the SF_6 etch. Nanometre scale patterning was found on the substrates of all samples that were etched with SF_6, as shown in Fig. 6.10. These were likely islands of SiO_2, given their bright, insulating appearance in the scanning electron microscope (SEM) and the previous documentation of such a phenomenon in the literature [165]. Despite their prominence in SEM images, it is unlikely that these features would have a significant effect on the performance of a near field imaging system, given that their individual sizes were all well below the diffraction limit and their physical location was removed $\sim$40 nm from the object plane.

6.1.3 Maskless Laser Patterning

The third mask fabrication technique studied was maskless laser patterning (MLP), performed using a Heidelberg Instruments μPG 101 laser pattern generator and illustrated in Fig. 6.11. Patterns were designed in Tanner Tools' L-Edit software, before

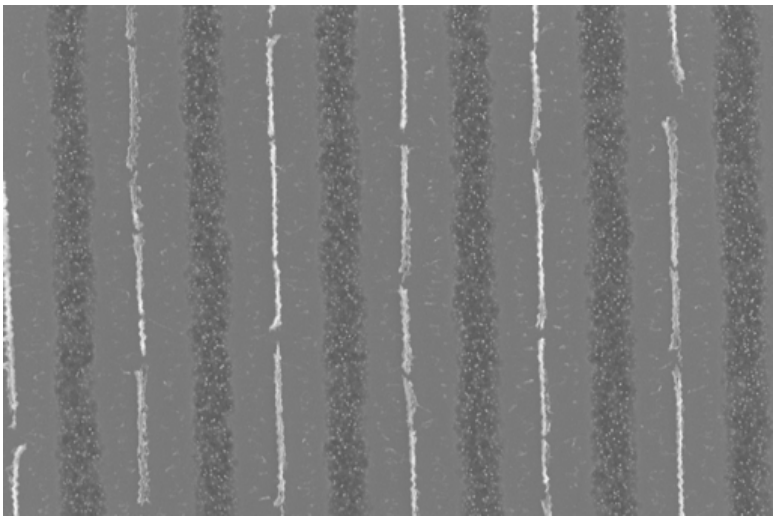

Figure 6.8: SEM micrograph of ARC plateaux affixed to W pillars on a quartz substrate. Nominal period is 1 μm.

being written into 4" (100 mm) square, 0.090" (2.3 mm) thick pre-coated chrome-on-glass blanks from Nanofilm, Inc. Following writing, the blanks were developed in undiluted AZ MIF 326 developer, before being wet etched in a nitric acid-based solution. Finally, the remaining resist was removed by a solvent rinse and mild scrubbing with a cotton bud, giving smooth, ~110 nm high features. Details of each stage in this process are given in Table 6.3, with optical micrographs taken after the development, etching and cleaning steps shown in Fig. 6.12.

This technique gave good results for feature sizes down to 3 μm, with low line edge roughness and steep sidewalls, as shown in Fig. 6.12d. Although resolution was low relative to the other methods studied, the results and analysis presented in Chapter 7 emphasised the need for good feature quality rather than small feature size. MLP was well suited for such requirements, as shown in Fig. 6.13, hence it was used for much of the experimental work presented in this thesis.

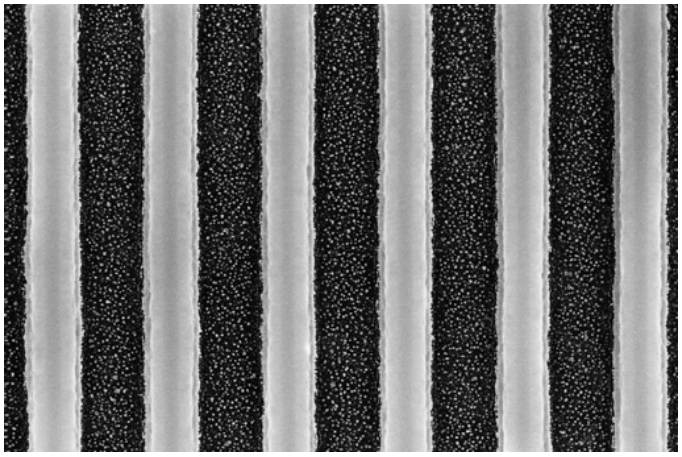

(a)

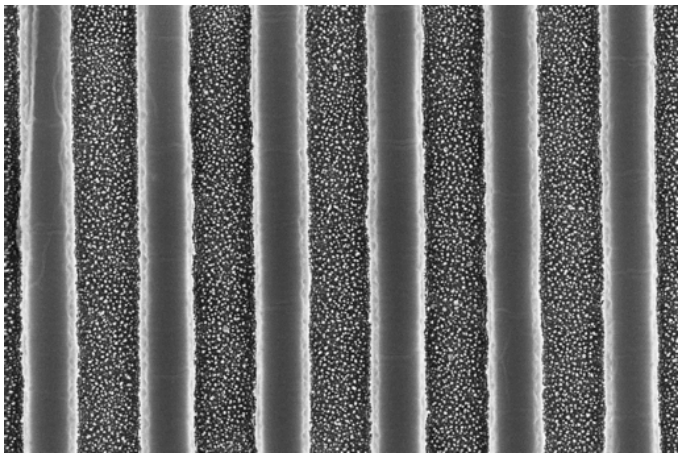

(b)

Figure 6.9: SEM micrograph of resist, ARC and W layers on a quartz substrate (a). The resist is removed after a solvent rinse (b). Nominal period is 1 μm.

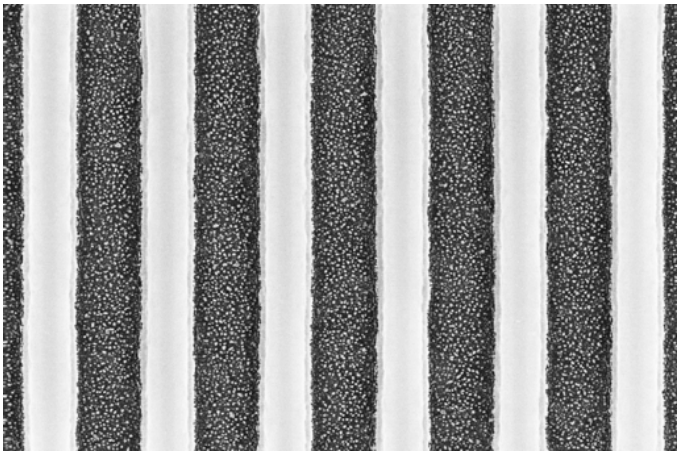

Figure 6.10: SEM micrograph of resist, ARC and W features on a quartz substrate. Bright dots are SiO_2 on the quartz. Nominal period is 1 μm.

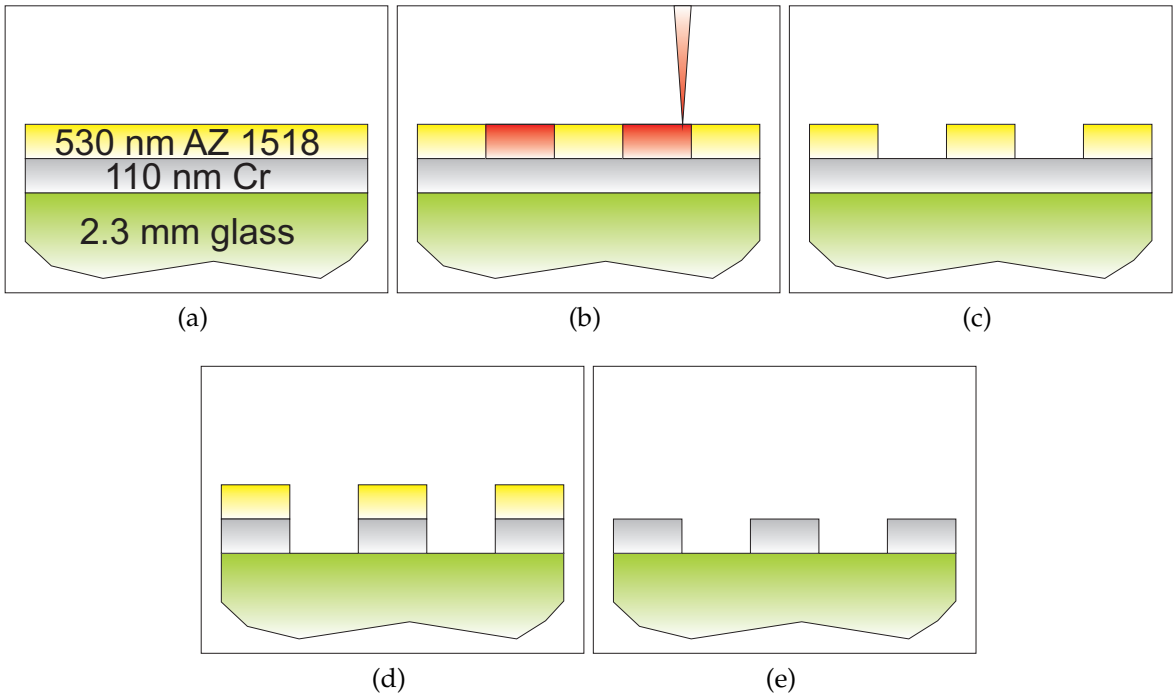

Figure 6.11: Maskless laser patterning mask construction schematic. Starting with a pre-coated metal-resist substrate (a), the resist is written (b) and developed (c). The metal is then etched (d) before the remaining resist is dissolved away (e). Note that illustrations are not to scale.

Table 6.3: Maskless laser patterning mask recipe.

	Ingredients		
	Substrate	4″ × 4″ × 0.090″ (101.6 mm × 101.6 mm × 2.3 mm) pre-coated mask blanks: AZ 1518 resist on chrome (Cr) on soda lime glass	
	Developer	AZ MIF 326	
	Etch	nitric-acid based chrome etch	
	Step	**Equipment**	**Parameters**
1	Write resist	Heidelberg Instruments μPG 101 Laser Pattern Generator	8 mW laser power @ 25% dose
2	Develop resist		45 s immersion
3	Rinse		DIW
4	Etch Cr		60 s immersion
5	Rinse		DIW
6	Dissolve resist		Acetone, in conjunction with mild scrubbing by cotton bud
7	Rinse		Methanol
8	Rinse		IPA

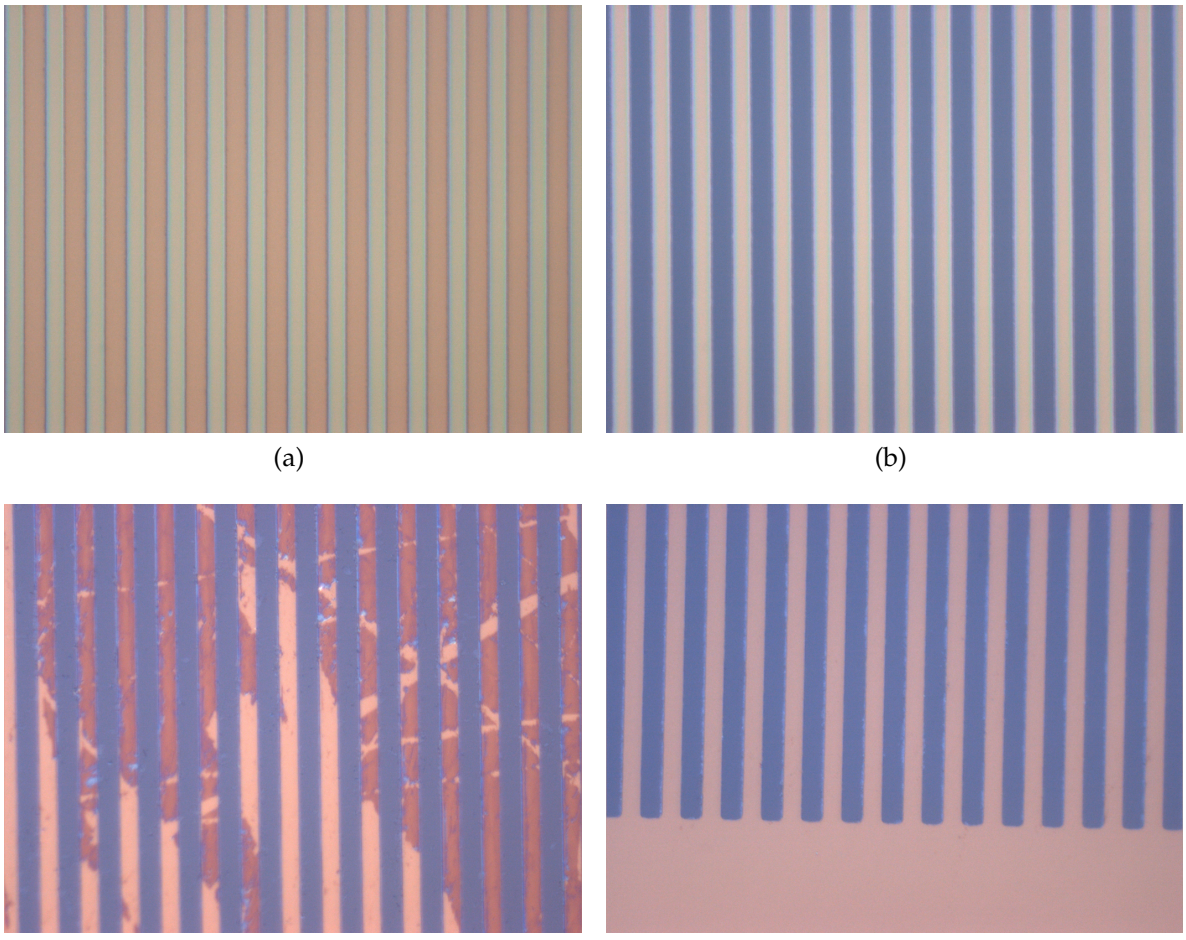

(a) (b)

(c) (d)

Figure 6.12: Optical micrographs of intermediate steps in the MLP process. (a) Post development. Narrow, bright features are resist pillars; darker troughs are Cr. (b) Post etching. Dark troughs are substrate glass, brighter features are Cr pillars, topped by peaks of resist. (c) Post rinse, without scrubbing. Colour variation on bright Cr pillars is due to thin 'skins' of resist. (d) Post rinse with scrubbing. Bright Cr pillars on dark glass substrate. No resist skins remain, indicating scrub has been effective. Nominal period for each pattern is 10 μm.

6.2 Resist Stack Development

Once a suitable mask fabrication technique was developed, the imaging layers required for contact lithography were investigated. It was important that the layers were capable of attaining intimate contact to the mask and lens layers above them, while also capturing very high resolution features. These attributes had not been easy

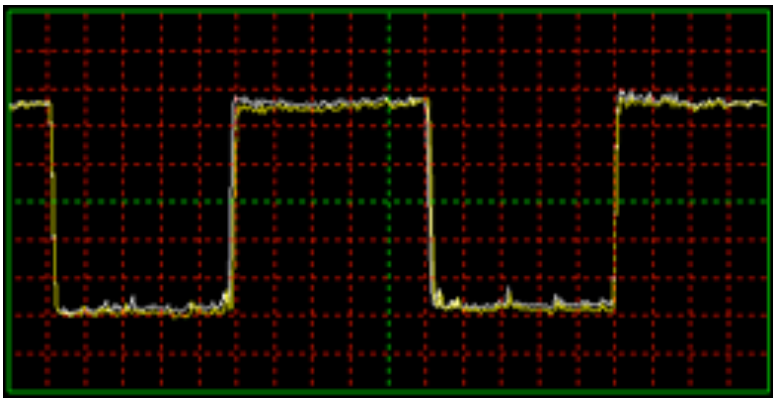

Figure 6.13: AFM height profile of a chrome-on-glass mask generated by MLP, showing regular features with steep sidewalls. Horizontal scale is 1 μm/division, vertical scale is 20 nm/division.

to attain in the past and several methods were proposed to achieve optimum performance.

Firstly, the problem of contact: earlier accounts in the literature relied on conformable metal masks made on SiN substrates [57] or 200 μm thick microscope coverslips [21] to mold intimately to rigid resist layers. Unfortunately, these methods proved to be fragile, as dust particles caught between mask and resist led to frequent mask breakages. Another method avoided such breakages by constructing the mask and lens layers directly on top of the resist [23]; however, the number of applications for this method were limited as it did not allow for separation of the resist layer from the mask after exposure. A third technique proposed flexible PDMS membranes as phase masks for near-field exposures [55, 56, 166]. The mechanical properties of these PDMS masks gave excellent contact; however, their translucency at optical and UV wavelengths made them unsuitable as amplitude masks. So, instead of including PDMS in the mask stack, a layer approximately 1.5 mm thick was incorporated into the resist stack as a suspension layer, as shown in Fig. 6.14. This layer absorbed deformation stress caused by rigid masks, guaranteeing contact across large areas of the sample, shown in Fig. 6.15, and effectively eliminated mask breakages for the experiments reported in this thesis.

A second requirement on the resist stack was that it had to be sensitive to very small, sub-wavelength features, in order to capture the intensity variations that were only present in the near-field. To this end, undiluted AZ 1518 resist was used as the imaging medium, spun to a thickness of $\sim$2.2 μm. Initially, diluted resist was used to reduce

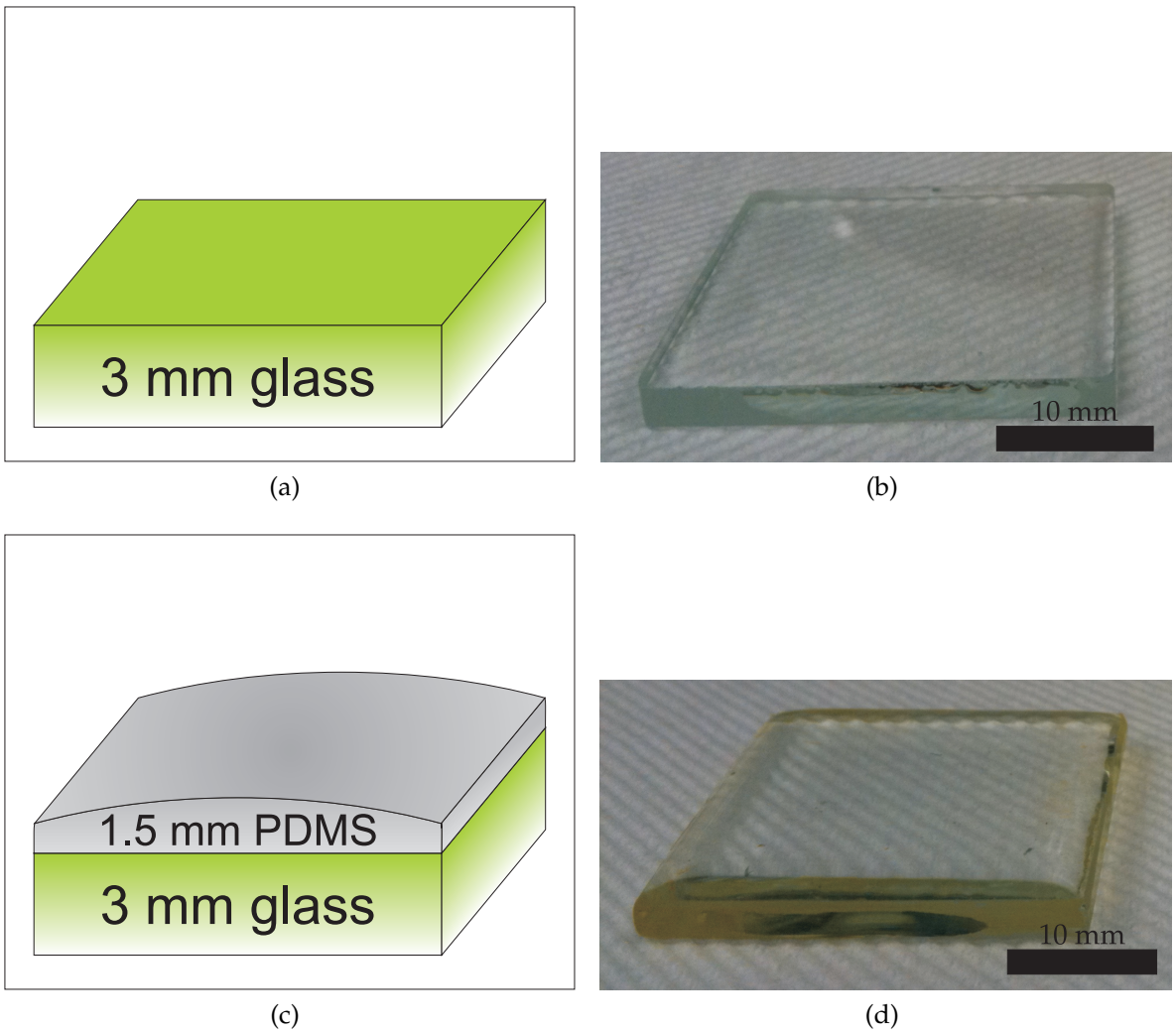

Figure 6.14: Schematics (a, c) and photographs (b, d) of resist stack layers used for near-field imaging experiments. 30 mm square substrate wafers (a and b), covered by cured PDMS (c and d).

the thickness of the film and thus the aspect ratio of features captured in the resist. The concentration was changed to full-strength once the aim of the experiments changed from imaging through the resist to imaging partially into the resist. This meant that total resist thickness was no longer a factor and allowed for higher resolution in the resist as the density of photochromic molecules was higher in straight resist than in diluted solutions. Furthermore, optimum resolution was preserved by including a layer of AZ Barli II ARC between the resist and PDMS layers. This mitigated reflections and standing waves between different layers in the resist stack, thus ensuring that the image in the resist was due only to the mask and lens.

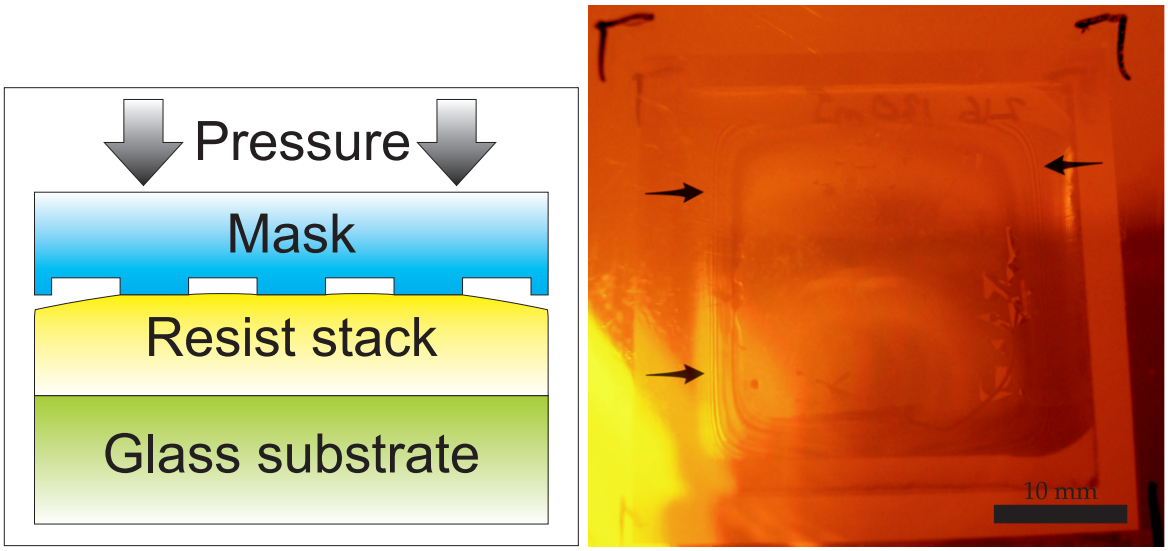

(a) (b)

Figure 6.15: Annotated schematic showing side-on view (a) and photograph showing top-down view (b) of a Cr mask and a PDMS-based resist stack in intimate contact. Interference fringes around the perimeter of the 30 mm $\times$ 30 mm sample, shown by arrows in (b), indicate good contact in the centre of the sample.

With these requirements of contact and resolution in mind, the resist stack was fabricated as follows: firstly, Dow Corning Sylgard 184 PDMS was mixed 10:1 with curing agent and placed in a vacuum desiccator for 30 minutes to allow bubbles to dissipate. The PDMS mixture was then poured onto a 30 mm square glass substrate and cured on a hot plate. Special care had to be taken to ensure that the substrate was both clean and dry before this step, as any solvent residue left on the substrate would prevent the PDMS from curing.

After baking, the stack was placed in an Emitech K1050x Plasma Asher and ashed in an O_2 plasma. This was done to desorb moisture from the surface of the PDMS, increasing its hydrophobicity and hence the adhesion of the ARC layer, which was applied immediately after ashing. Spun on to a thickness of 140 nm, the AZ Barli II ARC was then baked in an oven. This was preferrable to a hotplate, as the relative thickness of the glass substrate limited heat transfer to the ARC from below. After baking, a 2.2 μm layer of AZ 1518 resist was spun on and similarly baked in an oven. This step completed the resist stack fabrication process, which is summarised schematically in Fig. 6.16, with the details of each step listed in Table 6.4.

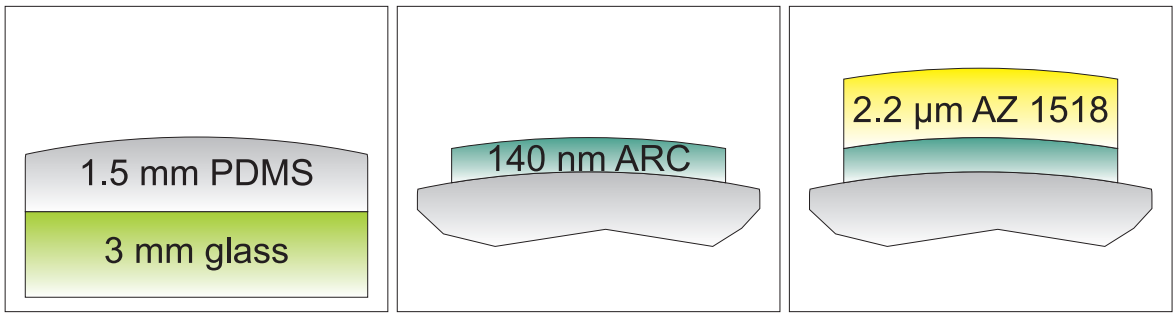

Figure 6.16: Resist stack construction schematic. PDMS is poured onto a substrate (a), before ARC (b) and resist (c) are spun on. Note that illustrations are not to scale.

Table 6.4: Resist stack recipe.

	Ingredients		
	Substrate	30 mm $\times$ 30 mm $\times$ 3 mm glass slides.	
	Suspension medium	Dow Corning Sylgard 184 Silicone Elastomer (PDMS).	
	Anti-reflective coating	AZ Barli II.	
	Photoresist	AZ 1518.	
	Step	**Equipment**	**Parameters**
1	Mix PDMS		10:1 polymer:curing agent.
2	De-gas PDMS	Vacuum desiccator	30 min.
3	Pour PDMS		$\sim$25 mm dia. blob onto substrate.
4	Bake PDMS	Stuart Scientific Hotplate SH1D	65°C, 60 min.
5	Ash PDMS	Emitech K1050x Plasma Asher	100 W, 30 s, Base pressure $\leqslant 7 \times 10^{-1}$ mBar , O_2 @ 9×10^{-1} mBar.
6	Spin ARC	Laurell WS-400B-6NPP-Lite Spin Coater	3000 rpm, 30 s.
7	Bake ARC	Sanyo Drying Oven	185°C, 45 s.
8	Spin resist	Laurell WS-400B-6NPP-Lite Spin Coater	3000 rpm, 30 s.
9	Bake resist	Contherm Digital Series Oven	95°C, 5 min.

6.3 Lens Fabrication

The mask and resist structures described in Sections 6.1 and 6.2 were, on their own, sufficient to form a complete contact lithography system, such as ENFOL [18, 167]. ENFOL required no lens and no further fabrication steps, yet was still capable of beating the diffraction limit [18, 19, 29]. In contrast, superlenses relied on the deposition of Ag films between the mask and resist, which prolonged the fabrication process. The potential payoff was even better resolution, since superlenses were able to enhance evanescent modes, rather than just limit their decay.

Superlenses were fabricated by spinning a layer of poly (vinyl alcohol) (PVA), typically ~20 nm thick, on top of the resist stacks described in Section 6.2. Following this, an Ag film twice the thickness of the PVA layer was evaporated onto the lens stack, as shown in Fig. 6.17. For multi-Ag layered superlenses, a SiO_2 film was then evaporated onto the Ag layer, before more Ag:SiO_2 layer pairs were added. The lens stack was then terminated with a PVA layer, of similar thickness to the first layer.

Initially, SiO_2 was used for the final lens layer, as it was tough enough to protect the top-most Ag layer from oxidation and scratches. Unfortunately, this same toughness greatly hindered removal of the superlens from the resist stack, which was a necessary step after exposure, as described in Section 6.4.3. For this reason PVA, which was readily water soluble, became the material of choice for terminating the lens stack. The details of the PVA deposition, as well as the other fabrication step in the lens fabrication process, are listed in Table 6.5.

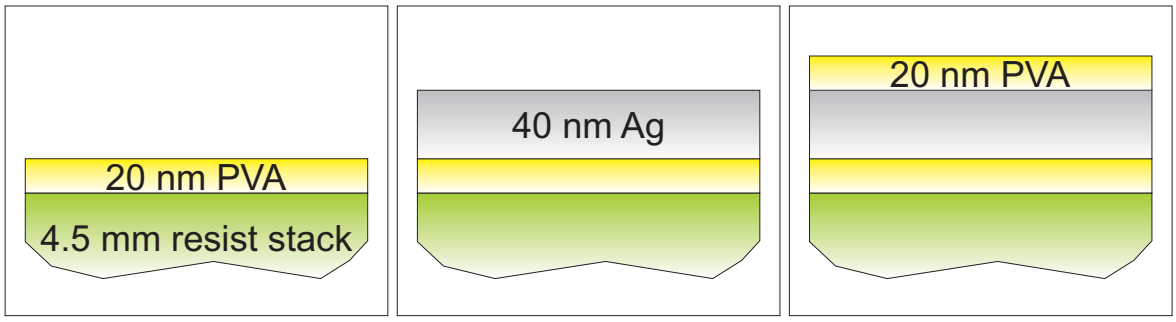

Figure 6.17: Single Ag-layer superlens construction schematic. PVA is spun onto a resist stack (a), before Ag is evaporated (b). Finally, a second layer of PVA is spun on (c). Note that illustrations are not to scale.

Table 6.5: Superlens fabrication recipe.

	Ingredients		
	Substrate	30 mm $\times$ 30 mm $\times$ 4.5 mm resist stack, described in Section 6.2	
	Spacer layers	PVA powder, 87-90% hydrolysed, dissolved 1:150 (w/w) in DIW	
		SiO_x powder	
	Active layer	99.99% pure Ag evaporation target	
	Step	**Equipment**	**Parameters**
1	Spin PVA	Laurell WS-400B-6NPP-Lite Spin Coater	3000 rpm, 30 s
2	Evaporate Ag	Balzers evaporation system:	Base pressure $\leqslant 8 \times 10^{-7}$ Torr,
		BSV 603 evaporation controller,	power = 2.0 (on dial)
		BSP 102 automatic pumping unit controller,	
		Sigma instruments SQM-160 Rate/Thickness monitor	
3	Evaporate SiO_2	Balzers evaporation system	Base pressure $\leqslant 8 \times 10^{-7}$ Torr,
	(optional steps)		power = 2.0 (on dial)
4..n		Repeat steps 2 and 3 as required	
n+1	Spin PVA	Laurell WS-400B-6NPP-Lite Spin Coater	3000 rpm, 30 s

6.4 Exposure and Development

Once all fabrication steps were completed, the exposure and development process was begun, as shown in Fig. 6.18. This involved holding the mask and resist-lens structure in intimate contact, using a 4" (10 cm) square fluoroware slide holder, normally used for storing masks. This was done to ensure intimate contact, as the resist stack was too heavy to be secured to the mask by vacuum alone. Two pieces of sticking tape were used on the sides of the holder to keep it closed and to increase the area of the sample in contact with the mask. A photograph of this arrangement is shown in Fig. 6.19.

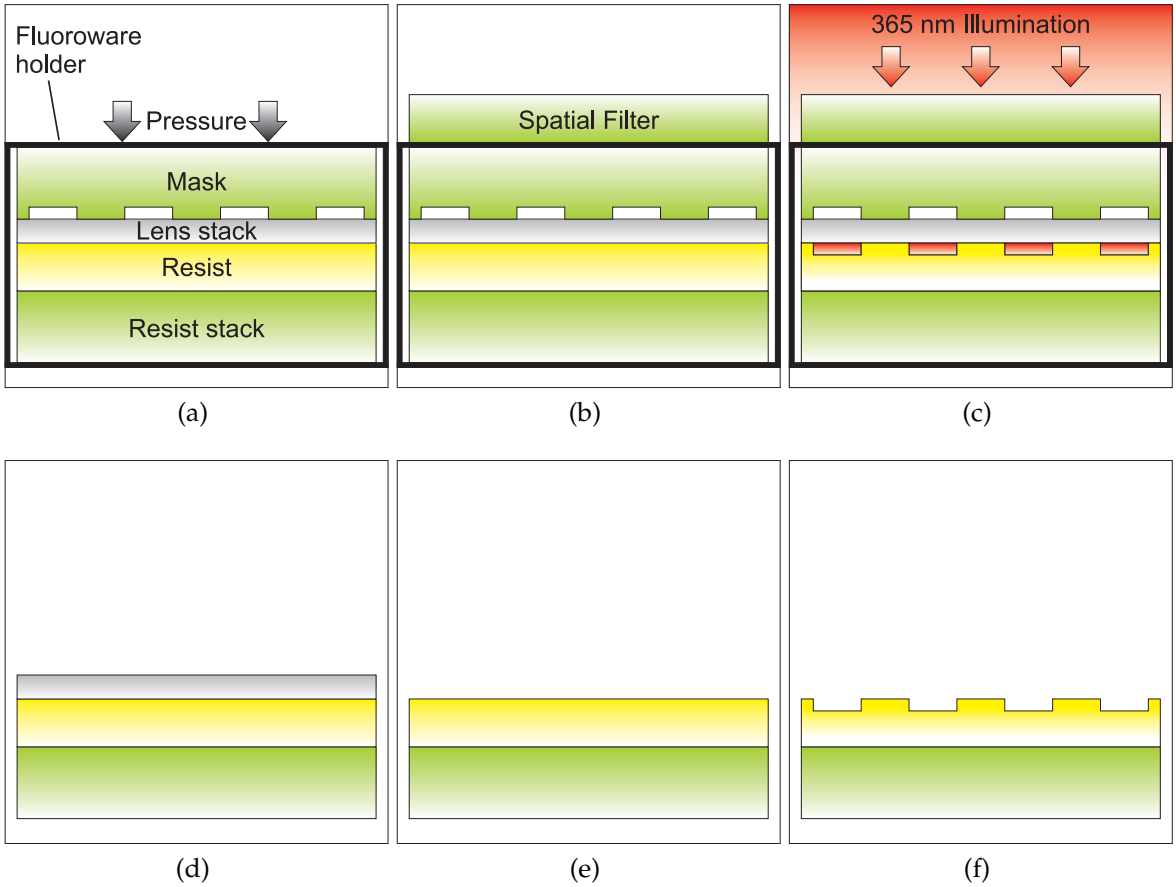

Figure 6.18: Super resolution exposure and development process schematic for super-lenses. First the mask, lens and resist stack are sandwiched together in a fluoroware container (a), onto which a spatial filter is mounted (b). The resist is then exposed (c), after which contact is broken and the mask is removed from the lens-resist stack (d). The lens is then removed (e) so that the resist can be developed (f). The process is identical for ENFOL experiments; however, the lens removal step (e) is not necessary. Note that illustrations are not to scale.

After the fluoroware container was secured, a 365 nm wavelength spatial filter was placed on top of it, covering the entire resist-lens structure. Irradiance through the fluoroware holder and the spatial filter was measured at various wavelengths, in order to determine the effects of these components on the light reaching the resist. These data are presented in Fig. 6.20; they indicate an attenuation at 365 nm of 2.21 dB through the filter alone, 3.17 dB through the holder alone and a combined loss of 5.15 dB through both. This loss was compensated by increasing exposure times by a factor of 3.3.

Once mounted, the whole ensemble was placed in a Karl Süss MA6 mask aligner, which was operated in flood exposure mode. After exposure, the filter and holder were removed from the aligner and the fluoroware container was opened. The resist stack was separated from the mask and developed in a 4:3 solution of AZ MIF 326 and DIW, before being rinsed in DIW. If a superlens was used, the metal and spacer layers of the lens were removed before development, using immersion in DIW and mild agitation with a cotton bud. The details of each step are listed in Table 6.6, with an atomic force microscope (AFM) micrograph of a developed resist pattern imaged through a superlens shown in Fig. 6.21.

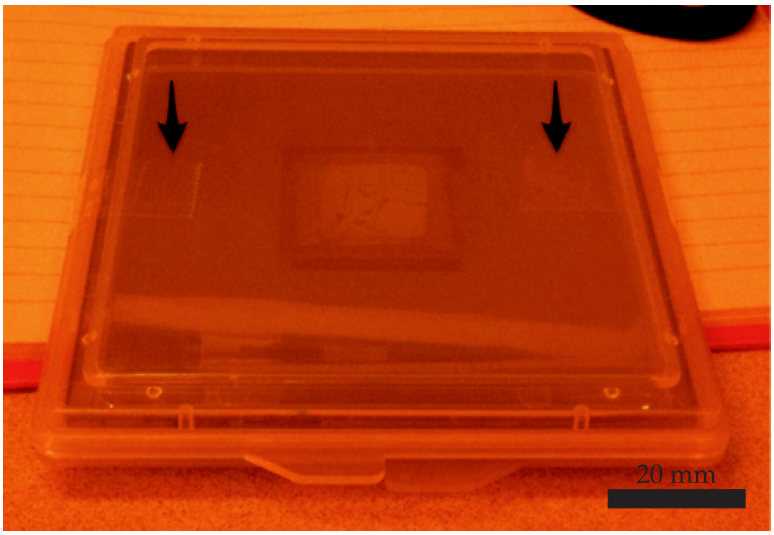

Figure 6.19: Annotated photograph of mask and resist-lens structure (centre) held in intimate contact by a 4" fluoroware container. Arrows indicate pieces of sticking tape on the sides of the container.

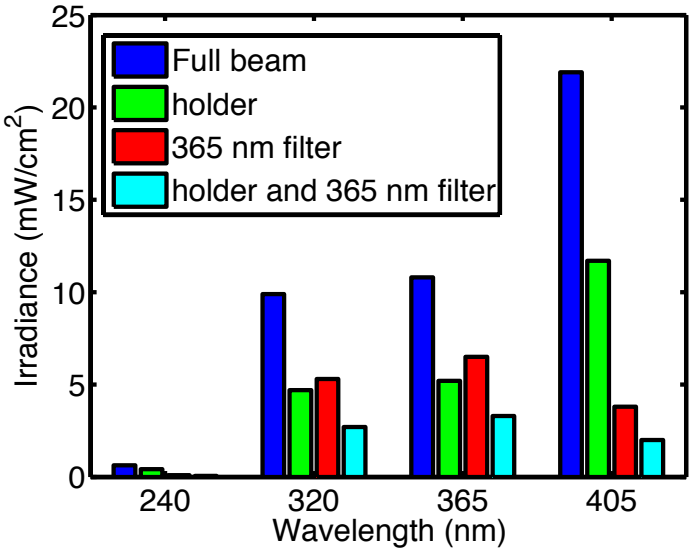

Figure 6.20: MA6 mask aligner irradiance measurements at selected UV wavelengths and through different media.

Table 6.6: Exposure and development recipe.

	Ingredients		
	Resist stack	2.2 μm AZ 1518 resist on top of AZ Barli II ARC and PDMS suspension layer, all on 30 mm $\times$ 30 mm $\times$ 3 mm glass substrate	
	Lens stack	40 nm Ag layer sandwiched between 20 nm PVA spacer layers, all mounted on resist stack	
	Mask	MLP-written 2.3 mm thick Cr-on-glass mask or IL-written 520 μm thick W-on-quartz mask	
	Mask holder	4″ (10 mm) square fluoroware container	
	Spatial filter	Thor Labs 365 nm wavelength 2″ (5 cm) square filter	
	Developer	4:3 AZ MIF 326:DIW	
	Step	**Equipment**	**Parameters**
1	Assemble components		Lock resist-lens stack and mask in mask holder Secure sides with sticking tape Place 365 nm filter on top of mask holder
2	Expose resist	Karl Süss MA6 mask aligner	365 nm, 350 W bulb; flood exposure mode; 30 mJ – 100 mJ dose for ENFOL, 80 mJ – 150 mJ dose for superlenses
3	Remove lens stack, if present		DIW & cotton bud
4	Develop resist		15 s immersion
5	Rinse		DIW

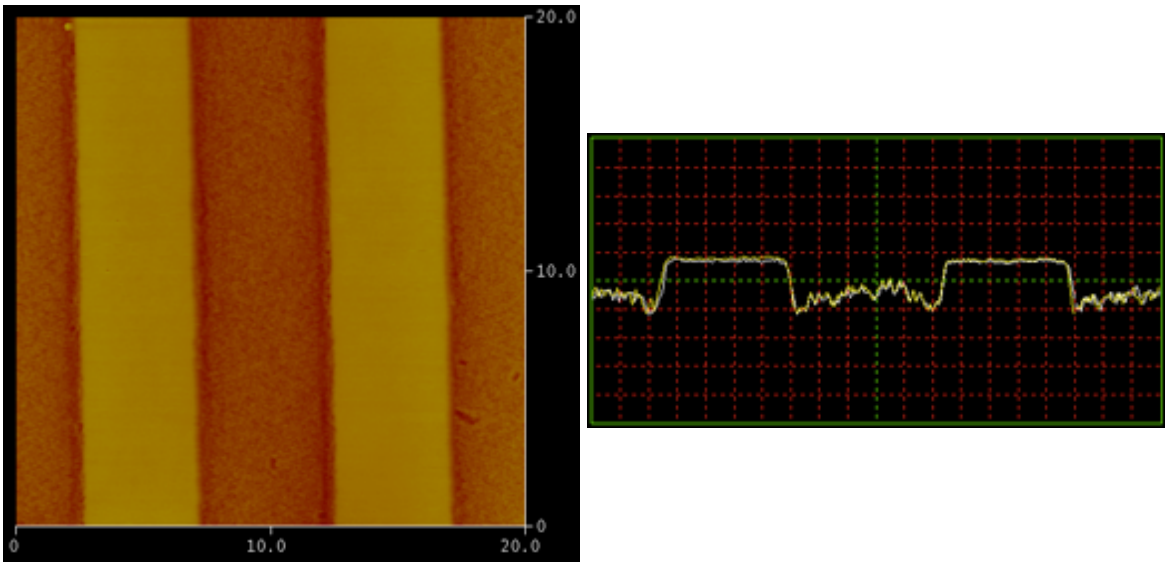

(a) (b)

Figure 6.21: AFM micrographs of developed resist features exposed through a 20:40:20 nm PVA:Ag:PVA superlens. Height plane view (a) and single line height profile (b). Flat peaks in (b) indicate intimate contact between mask and lens. Axes units are in μm for (a) while horizontal scale of (b) is 1 μm/division and vertical scale is 10 nm/division.

Once constructed, the success of the near-field imaging systems hinged on their ability to capture shallow evanescent profiles in the resist, without disturbing or corrupting them. Factors that threatened their correct operation included parasitic exposure of the resist before development, which could potentially contaminate the weak near-field profiles that were sought. An incorrect development protocol could also erode fine details at the top of the resist or pattern features too deeply into the resist, beyond the near-field of the mask or lens. Lastly, care had to be taken when removing superlens structures from the resist stack, so as not to damage the imaging layer. The remainder of this chapter deals with the management and mitigation of these hazards.

6.4.1 Parasitic Exposure

Parasitic exposure of the resist was limited by performing the majority of fabrication and processing under yellow light, in a dedicated room fitted with tinted glass windows and devoid of uncontrolled low-visible and UV wavelength sources. Wafers for ENFOL experiments were kept in this 'yellow' room from the time resist was spun on

until after development, eliminating any concern about parasitic exposure for these types of samples.

For superlenses, it was necessary to remove the samples from the yellow room to evaporate the Ag and SiO_2 layers onto the lens stack. To minimise contamination, the samples were mounted onto a holder inside the yellow room and then completely covered in aluminium foil. The sample holder was then placed in the evaporator and the dome of the evaporator was lowered, with the foil around the samples only removed once the holder was well covered by the dome. The fluorescent lights above the evaporator were turned off while the dome was open. Following evaporation, the dome was lifted and the samples were re-covered with foil as quickly as possible.

A second suspected source of parasitic exposure for the superlens samples, other than the ambient light around the evaporator, was the radiation given off by the Ag and silicon monoxide (SiO) targets as they was heated to boiling point during deposition. Radiation emissions became visible if the target was allowed to evaporate completely, as shown in Fig. 6.22. For this reason targets were not evaporated fully before being replaced; in cases where the targets did inadvertently evaporate to the point of glowing visibly the exposed samples were binned.

Regarding samples exposed under normal conditions, the peak wavelength, λ_{peak}, emitted by Ag at its boiling point, $T = 2212^{\circ}$C [168], was calculated using Wien's displacement law:

$$\lambda_{peak} = \frac{b}{T} \tag{6.8}$$

$$= 1.17\ \mu m, \tag{6.9}$$

where b is Wien's displacement constant, equal to 2.898 $\times$ 10^{-3} m·K. This wavelength is well beyond the visible spectrum and even further beyond the maximum wavelength that AZ 1518 resist is sensitive to, around ~450 nm; in addition, deposition times were short, often lasting less than a minute. Similarly, the boiling point of SiO_2 is 2230°C, giving a nearly identical peak emission wavelength. For these reasons contamination during the evaporation process was discounted as a threat to the fabrication process.

6.4.2 Development Rates

Dark development of the photoresist used in evanescent experiments was a significant concern, as near-field patterns were at risk of being eroded before ever being examined under a microscope. Several trials were performed with varying developer concentrations and times in order to gauge the rate at which the unexposed resist was developing. AZ 1518 photoresist, diluted 1:1 with DIW, was spun onto quartz substrates and baked in an oven at 95°C for 5 min. The samples were then developed and the thickness of each resist layer was measured and compared to readings taken before development. The data for these trials are shown in Table 6.7. Height values are averaged and listed uncertainties are for one standard deviation.

Figure 6.22: Photograph of an almost extinct Ag target emitting radiation during evaporation, seen through a tinted view port. Bright object is an Ag pellet; also visible are aluminium foil, used for protecting the interior of the evaporator, and a part of the target shutter (top right). Photograph was taken moments before the pellet completely evaporated.

Table 6.7: Averaged results for dark development trials of AZ 1518 photoresist.

Dev. conc. (MIF 326:DIW)	Dev. time (s)	Pre-dev. height (nm)	Post-dev. height (nm)	Depth dev'd (nm)	Dev. rate (nm/s)
2:1	60	538.0 ± 5.7	516.3 ± 5.0	21.7 ± 10.7	0.36 ± 0.18
4:3	30	482.8 ± 9.1	489.5 ± 7.6	-6.7 ± 16.7	-0.22 ± 0.56
4:3	15	476.0 ± 7.2	475.0 ± 4.7	1.0 ± 11.9	0.07 ± 0.79

The aim of the dark development rate experiments was to minimise the height difference between readings before and after development; or in other words, to minimise the dark development rate of the resist. The data in Table 6.7 show that this aim was met when the developer was diluted 4:3 with DIW. Similar trials on unexposed superlens samples also confirmed the earlier conclusion that the resist was not being exposed during thin film deposition.

While the peaks in the resist pattern were preserved by nullifying the dark development rate, the resist troughs due to evanescent modes had to be protected by limiting the bright development time and rate. Evanescent modes only have significant amplitudes within λ / 10 of their source; for 365 nm wavelength, this range was $\sim$35 nm. Hence any process that developed features deeper than $\sim$35 nm into the resist were likely to 'drown out' the evanescent intensity profile.

To quantify the rate of development for exposed features a bright development rate trial was performed on AZ 1518 resist that had been baked at 95°C for 5 min. and exposed to a 70 mJ/cm^2 dose of 365 nm wavelength radiation. The results of this trial, summarised in Table 6.8, showed that a 15 s development time was sufficient to clear $\sim$35 nm of fully exposed resist, which was in the right range to observe near-field patterns without drowning them out. In this way both the bright and dark development rates for AZ 1518 resist were quantified and suitable parameters for near-field experiments were identified.

Table 6.8: Averaged results for bright development trial of AZ 1518 photoresist.

Exposure mJ/cm^2	Dev. conc. (MIF 326:DIW)	Dev. time (s)	Pre-dev. height (nm)	Post-dev. height (nm)	Depth dev'd (nm)
70	4:3	15	476.0 ± 7.2	440.8 ± 5.3	35.2 ± 12.5

6.4.3 Superlens Processing

Removing the lens stack from the resist without causing damage proved to be a challenging problem. The first attempt to do this involved rinsing the resist-lens stack in de-ionised water (DIW), with minimal agitation. This left most of the Ag and bottom PVA layers intact on the resist and, in some cases, led to patterning of the Ag layer by the resist after development. This phenomenon is illustrated in Fig. 6.23.

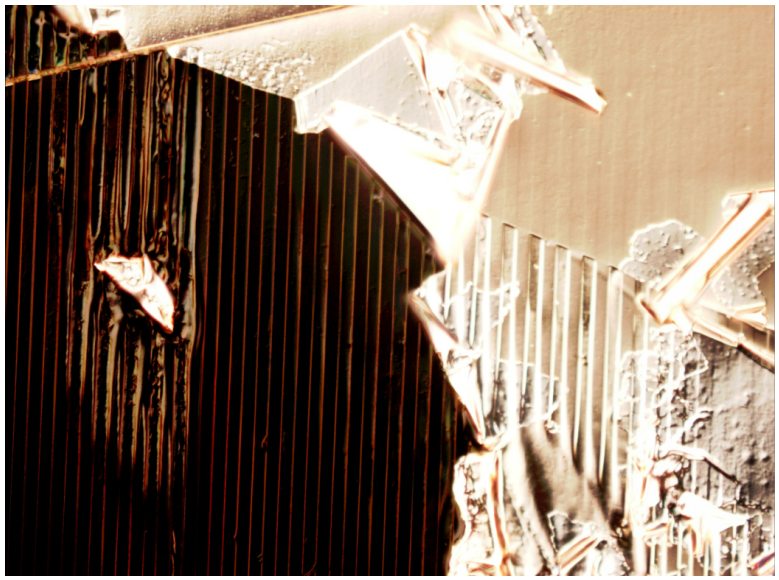

Figure 6.23: Optical micrograph of periodic resist features (left) partially covered by Ag (right and top). Some Ag patterning has occurred after development of the underlying resist (bottom right). Nominal period is 10 μm.

Following the failure caused by a lack of agitation, samples were submerged in DIW and placed in a Unisonics FXP12MH ultrasonic cleaner for 60 s. This step successfully removed the Ag and PVA layers but took the resist and ARC layers as well. This was not entirely unexpected, given the poor adhesion of ARC to untreated PDMS already encountered during the fabrication of the resist stack.

The third attempt to benignly remove the lens stack from the resist involved the use of Cyantek Corp. Cr-7 etchant to improve Ag removal. As before, samples were immersed in DIW; they were then dipped in Cr-7 for 5 s before being rinsed again in DIW. This process removed all visible traces of the Ag layer; however, rough artefacts were left behind that significantly affected the profile of the developed resist. The detrimental effects of the Cr-7 are shown in Fig. 6.24, where a sample processed with the etchant is noticeably rougher than a sample processed only with DIW.

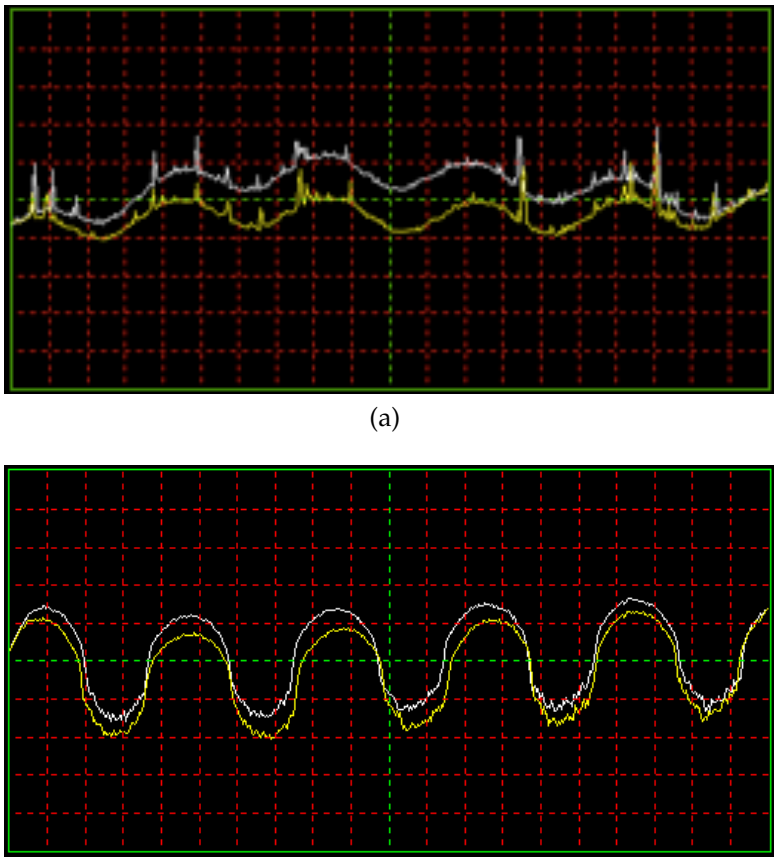

(a)

(b)

Figure 6.24: AFM micrographs of developed resist features exposed through a 40 nm Ag superlens. The sample processed with Cr-7 and DIW (a) has much greater roughness than the sample processed with DIW alone (b). Horizontal scale is 1 μm/division, vertical scale is 10 nm/division.

Finally, Cr-7 was abandoned in favour of DIW alone, with a cotton bud used to provide the mild agitation necessary to remove the PVA and Ag from the resist. The DIW was changed after each sample to prevent redeposition of Ag particles onto wafers. Similarly, each cotton bud was used only once, as extended use led to deposition of cotton particles on the photoresist. This method effectively removed the entire superlens from the sample without roughening the stack, allowing access to the image profile captured in the resist.

6.5 Summary

The mask, resist and superlens fabrication techniques discussed in this chapter can be used together to construct each of the key components required to form a complete near-field imaging system, namely, an object, a lens and an image. The object of the system is formed by UV light travelling through the mask, an image of which is focussed or transmitted by a superlens into a resist stack, where it is captured and preserved for future analysis. Although such superlens-centric systems have been constructed successfully in the past, the robustness, durability and ease of construction of the system described here are much greater than of those reported elsewhere in the literature [18, 22–24, 58]. The main reason for this improvement is the inclusion of a PDMS layer in the resist stack, described in Section 6.2.

With the infrastructure to perform ENFOL and PLL experiments, the way is now clear to explore in detail the real world performance of designs that have so far been studied only via simulation and analytical calculations. Of special interest is the correlation between the experimental results available from this system and the transfer functions described in Chapter 5. This is the goal of the work presented in Chapter 7, which covers the processing and interpretation of image data captured in resist stacks.

Chapter 7

Experimental Characterisation and Comparison to Modelled Results

As a result of the work described in Chapter 4, there are now several computational tools that can be used to understand the predicted behaviour of superlenses. There is also a robust technique that allows superlenses to be fabricated more reliably and predictably than in the past. Given this favourable position, the next challenge lies in increasing the information yield from practical experiments so that the artificial models can be reconciled with the behaviour observed on the test bench.

Previously, super-resolution experiments [18, 22–24, 58] have focused almost exclusively on the minimum half-pitch that a system can successfully resolve. While this is an important metric for initial proofs of concept, it provides only a limited description of the capabilities of a lens, especially when compared to the insights that can be gained from studying the lens transfer function and other imaging metrics. The work in this chapter attempts to build on the analytical characterisation techniques derived in Chapter 4 to give a more extensive description of superlens behaviour, based as much as possible on experimental observation. Specifically, experiments are described that attempt to experimentally measure the transfer function of a superlens.

7.1 Analysis in Three Dimensions

Usually, the goal of positive tone lithography is to transfer two-dimensional features into photoresist so that the top of the developed resist becomes an accurate and faithful reproduction of the mask, shown in Fig. 7.1a. Variation in the depth of the exposed and developed resist, i.e. in the third dimension, is either disregarded or minimised through the use of non-linear or chemically amplified resists, as shown in Fig. 7.1b. This leads to a high contrast, step-like dose-depth curve for the resist, illustrated in Fig. 7.2. However, if the development of the resist can be retarted by means of diluted developer solutions or a reduced exposure dose, then the lithography process can be restricted to the linear or near-linear region of the dose-depth curve, opening up the possibility of greyscale pattern transfer, shown in Fig. 7.1c. Furthermore, this will allow the opportunity to do three-dimensional analysis of resist patterns, where the intensity of light is mapped to the depth of the exposed resist profile.

With this new capability it becomes feasible to experimentally determine the Green's function for a superlens, $h(x, y)$, simply by deconvolving the electric field intensity profiles on either side of the superlens when it is exposed to an appropriately shaped impulse mask:

$$\begin{aligned} img(x, y) &= h(x, y) * obj(x, y) \\ \therefore h(x, y) &= img(x, y) * obj(x, y)^{-1}. \end{aligned} \tag{7.1}$$

Here $obj(x, y)$ is the electric field intensity profile at the exit plane of a mask, captured in photoresist via ENFOL. Similarly, $img(x, y)$ is the profile at the exit plane of the superlens, when the superlens is placed in intimate contact with the mask, and $*$ is the convolution operator.

In order to allow direct comparison with TMM results, the Green's function is normally expressed in the spatial frequency domain as a transfer function, $H(k_x, k_y)$:

$$H(k_x, k_y) = \mathcal{F}\{h(x, y)\}. \tag{7.2}$$

If the mask and superlens intensity profiles are also expressed in the spatial frequency domain, then the deconvolution in Eq. (7.1) becomes a division operation and the anal-

ysis is simplified:

$$\begin{aligned} IMG(k_x, k_y) &= \mathcal{F}\{obj(x, y)\}, \\ OBJ(k_x, k_y) &= \mathcal{F}\{obj(x, y)\}, \\ H(k_x, k_y) &= IMG(k_x, k_y)/OBJ(k_x, k_y). \end{aligned} \tag{7.3}$$

Lastly, $H(k_x, k_y)$ can be approximated by $H(k_x)$, provided the mask pattern is symmetrical in both the x- and y-directions. This process of acquiring $H(k_x)$ from experimental measurements is illustrated in Fig. 7.3.

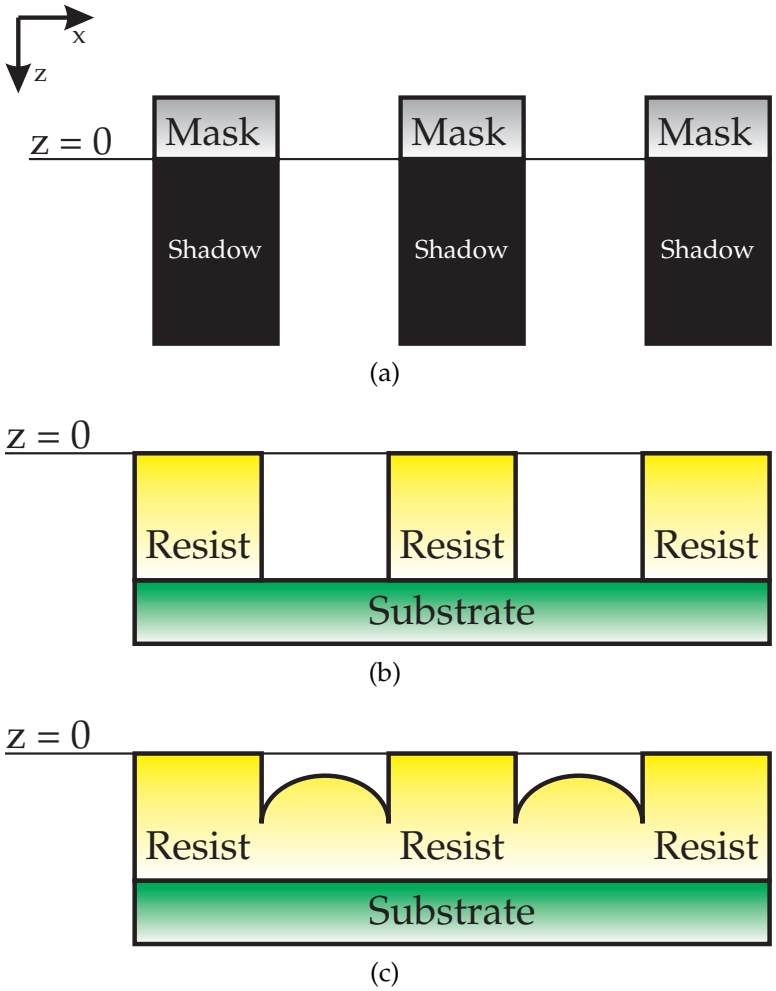

Figure 7.1: Cross section schematics of mask features (a), imaged into an ideal, non-linear photoresist optimised for two-dimensional lithography (b) and a less conventional, three-dimensional resist with a linear response (c).

This approach of measuring profiles on either side of a superlens is pursued here, in order to provide experimental data for comparison with the modelled results presented in Chapters 3, 4 and 5. The work is divided into three parts: firstly, masks need to be designed to provide superlenses with stimuli across a range of spatial frequencies, since the maximum possible quality of any reconstructed transfer function will be determined by the density and distribution of spatial frequency components in the input spectrum. In other words, the shape and size of features on a mask both play a role in determining the quality of TFs that can be found using the mask.

Once appropriate masks are available, ENFOL and PLL experiments need to be performed to capture the input and output field profiles in photoresist. The depth of features within the photoresist is particularly important here, since features that are too deep will not preserve evanescent spatial frequency components and features that are too shallow will have significantly more noise. The protocols described in Chapter 6 are used to manage this delicate relationship.

Lastly, the spatial domain profiles captured in resist films need to be conditioned and converted to the spatial frequency domain, so that TFs can be recovered. This involves 'flattening' and averaging the data, so that individual spatial frequency components

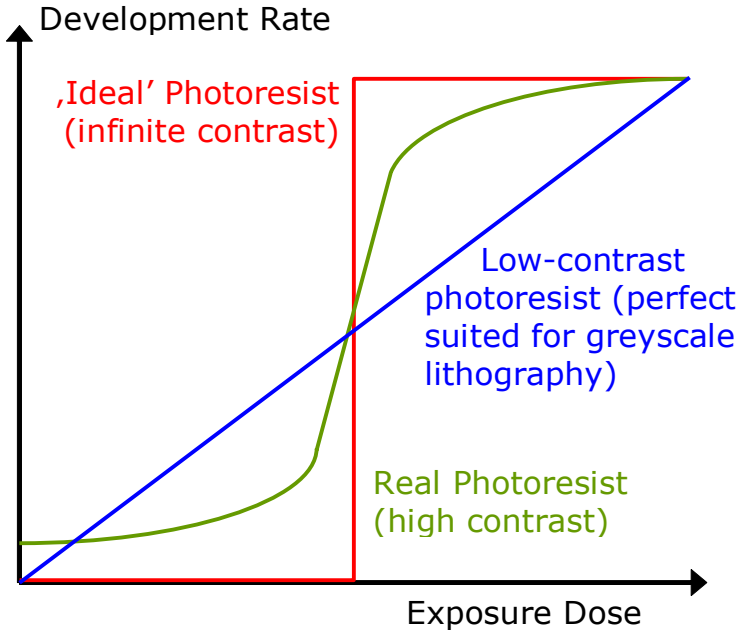

Figure 7.2: Typical exposure dose vs. depth curves for ideal, real and low-contrast photoresists [169]

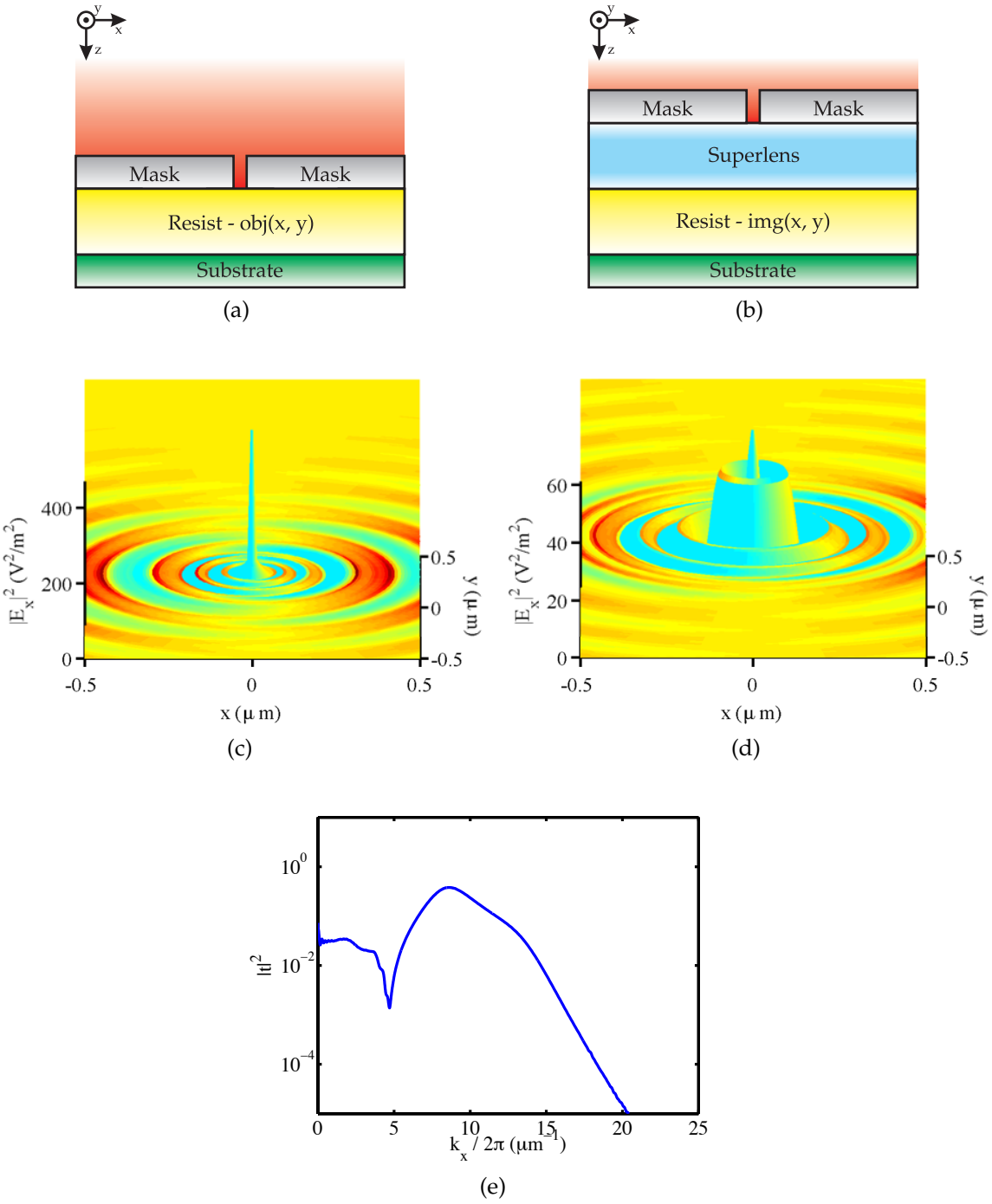

Figure 7.3: Technique used to measure transfer functions. Electric field intensity profiles are captured for an impulse mask, both before (a) and after (b) a superlens is placed in contact with the mask. The resulting object and image profiles, as calculated by finite element modelling, are shown in false colour in (c) and (d), respectively. Deconvolving the resist profiles from each other and applying a Fourier transform allows the calculation of the transfer function of the superlens (e).

are accurately measured without unwanted noise. The details of this step, as well as the ones before it and the results that they produced are all documented in the remainder of this chapter.

7.2 Mask Design and Implementation

Several mask designs were considered before a final pattern was selected and fabricated. The main constraints on the mask patterns were two-fold: firstly, they were required to generate high spatial frequency content, in order to effectively stimulate the superlenses that they would be paired with. Secondly, the electric field intensity profiles produced by the masks had to be well defined and mathematically convenient, in order to allow efficient retrieval of lens transfer functions. The steps taken to design and implement masks that were suitable for the retrieval of superlens transfer functions are discussed in the following sections.

7.2.1 Design Iterations

The design of a mask for the measurement of transfer functions started with a single, minimally dimensioned point-like feature patterned into the mask, shown in Fig. 7.4. This was the simplest design that would lead to an impulse-like intensity profile at the exit plane of the mask, which could be used to extract the transfer function of a lens. This was also the design that required the least amount of processing to extract the Green's function from the resist image profile, since the two would be identical to the degree that the mask intensity profile matched an impulse profile. Only a Fourier transform of the image profile would be necessary to retrieve the transfer function of the system. The only limit on the quality of the reconstructed transfer function would be the diameter of the mask features, w:

$$k_{max} = \frac{1}{w}, \tag{7.4}$$

where k_{max} is the highest wavenumber for which a transmission coefficient can be calculated with some degree of certainty.

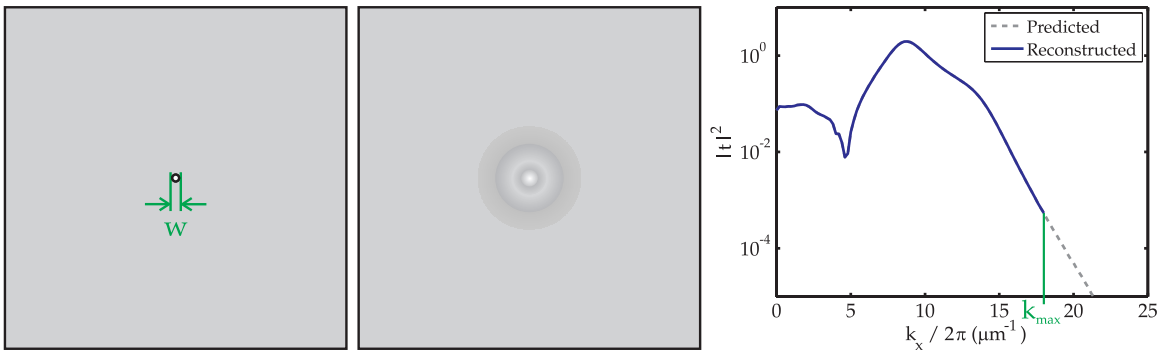

(a) (b) (c)

Figure 7.4: Schematic of a mask with a single, point-like feature (a) that can provide a near perfect impulse to a lens. The resulting image profile (b) is a close approximation of the Green's function of the lens. Applying a Fourier transform to (b) yields the transfer function of the lens (c). The range of the transfer function, k_{max} is only limited by the size of the mask feature, w, with smaller features producing better results.

Unfortunately, this design had the worst durability and was the most difficult to characterise of all of the designs considered. The solitary feature on the mask meant that contamination of the mask at only one point was enough to render the mask useless. A blocked or obstructed point feature would destroy the impulse intensity profile at the mask, ruining the profiles captured beyond the lens. The single feature, with diameter of only a few tens of nanometres, would also be nearly impossible to locate on a mask with millimetre dimensions.

For these reasons the second iteration of the mask design featured a matrix of point-like features, as shown in Fig. 7.5. The abundance of features on this design meant that it had higher durability that the first version of the mask, since contamination of a single feature would not forfeit the entire mask. The price for this added redundancy was that a deconvolution became necessary to extract the Green's function, and hence the transfer function, from the image profile. Furthermore, the quality of the reconstructed transfer function was now limited not just by the size of the features, w, but also by the distance between adjacent features, d. The gap between samples in the spatial frequency domain, Δk, would be given by the reciprocal of d:

$$\Delta k = \frac{1}{d}. \tag{7.5}$$

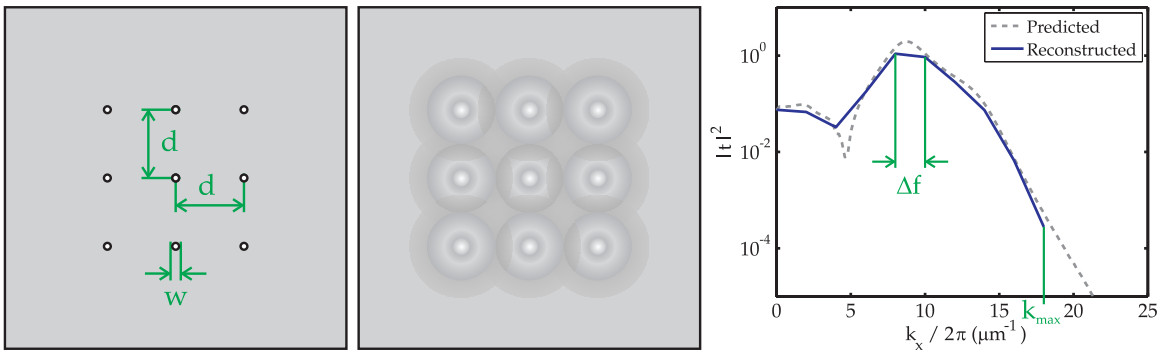

(a) (b) (c)

Figure 7.5: Schematic of a mask with a matrix of isolated, point-like features (a). Like the mask shown in Fig. 7.4a, this design allows the retrieval of the Green's function of a lens from an image of the mask (b); however, deconvolution of the object and image profiles needs to be performed to extract this data. The quality of the resultant transfer function (c) is determined by the properties of the mask: large separation between mask features, d, leads to small sample size, Δf. Furthermore, small mask feature size, w, results in transfer coefficients at a higher maximum spatial frequency, k_{max}.

Although arrays of points were an improvement over a single feature, the incredibly small patterns would still be difficult to find under a microscope. For this reason a third design was considered, one where matrices of single point features were replaced with arrays of low-width lines, resulting in a periodic grating with extremely low duty cycle, as shown in Fig. 7.6. This new design sacrificed isotropic features for ease of measurement and characterisation: samples only needed to be centred in one dimension under a microscope in order to capture a useful profile image. This design also changed the signal processing requirements again, as the two-dimensional Fourier transform that had been necessary to go between the Green's function and transfer function was replaced by an averaging function followed by a one-dimensional Fourier transform.

The fourth and final version of the mask design featured a 50% duty cycle line grating, shown in Fig. 7.7a, instead of the high duty cycle, minimal width line grating used in the third iteration. This change was made to facilitate accurate imaging of the mask, which was performed via AFM. Atomic force microscopy relies on a sharp imaging tip, which is drawn over the surface of a sample to map the contours of that sample. When samples have very small, narrow features, such as those in the third proposed

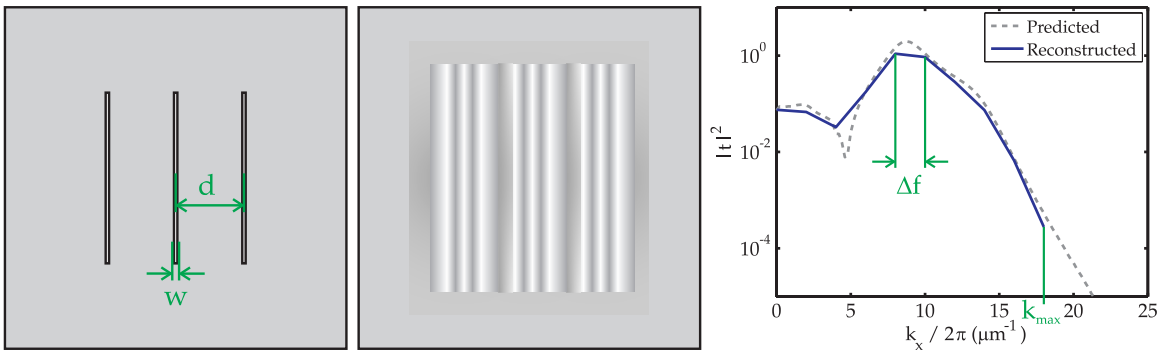

(a) (b) (c)

Figure 7.6: Schematic of a mask with an array of low-width lines (a). The mask allows a one-dimensional reconstruction of a Green's function when imaged by a lens (b), provided an appropriate deconvolution is performed. The quality of the reconstructed transfer function, which is now anisotropic with respect to the orientation of the line features, is controlled by the parameters identified in Fig. 7.5. The duty cycle of the mask is given by w/d.

mask, the tip may not be able to fully penetrate those features and will therefore return inaccurate results, as shown in Fig. 7.8.

Using the dimensions defined in Fig. 7.8, it is possible to calculate the minimum allowable feature width, w_{min}, for a given tip at a given feature depth, h_{max}. w_{min} is made up of the base tip width, w_{tip}, as well as the width of the tip for a given height, w_1, such that

$$w_{min} = w_{tip} + 2 \times w_1. \tag{7.6}$$

Similarly, h_{max} is given by

$$h_{max} = h_{tip} + h_1. \tag{7.7}$$

w_{tip} and h_{tip} are given by the radius of curvature of the tip, r_c, according to the relationships

$$w_{tip} = 2 \times r_c \cos\left(\theta_{cone}\right) \tag{7.8}$$

and

$$h_{tip} = r_c \times \left(1 - \sin\left(\theta_{cone}\right)\right), \tag{7.9}$$

where θ_{cone} is the half cone angle of the tip. Rearranging Eq. (7.7) allows h_1 to be found, which leads to an explicit expression for w_1:

$$h_1 = h_{max} - h_{tip}, \tag{7.10}$$

$$w_1 = h_1 \tan \theta_{cone}. \tag{7.11}$$

For the Mikromasch NSC-11 [170] and Budget Sensors Tap300Al-G [171] probes used for AFM imaging in this thesis, r_c was quoted as less than 10 nm and θ_{cone} was given as 20° for the NSC-11 tips and between 20° and 30° for the Tap300Al-G variety. Assuming

$$r_c = 10\ nm \tag{7.12}$$

and

$$\theta_{cone} = 20^\circ, \tag{7.13}$$

the minimum feature sizes that could be imaged successfully for a given mask depth were found to be

$$w_{min}\left(h_{max} = 50\ nm\right) = 50\ nm \tag{7.14}$$

and

$$w_{min}\left(h_{max} = 110\ nm\right) = 94\ nm. \tag{7.15}$$

This means that features less than 50 nm wide on a 50 nm deep mask will appear shallower than they are to the AFM. If the depth of the mask features is increased to 110 nm, then the minimum feature width for accurate imaging increases to 94 nm. The values of h_{max} are chosen here to correspond to the actual feature heights of the masks measured in Section 7.2.2. Given these calculations, feature width was set to at least ten times w_{min}, in order to minimise artefacts caused by the AFM measurement technique.

One of the consequences of changing to a 50% duty cycle grating is that it was no longer possible to retrieve transmission coefficients for every spatial frequency of interest; instead, only spatial frequencies that coincided with odd multiples of the fundamental spatial frequency of the mask can be predicted, as shown in Fig. 7.7b. In effect, Δf is no longer determined by $1/d$, but by $2/d$. Nevertheless, this approach represents a feasible method of experimentally measuring superlens performance, which has not been possible in the past.

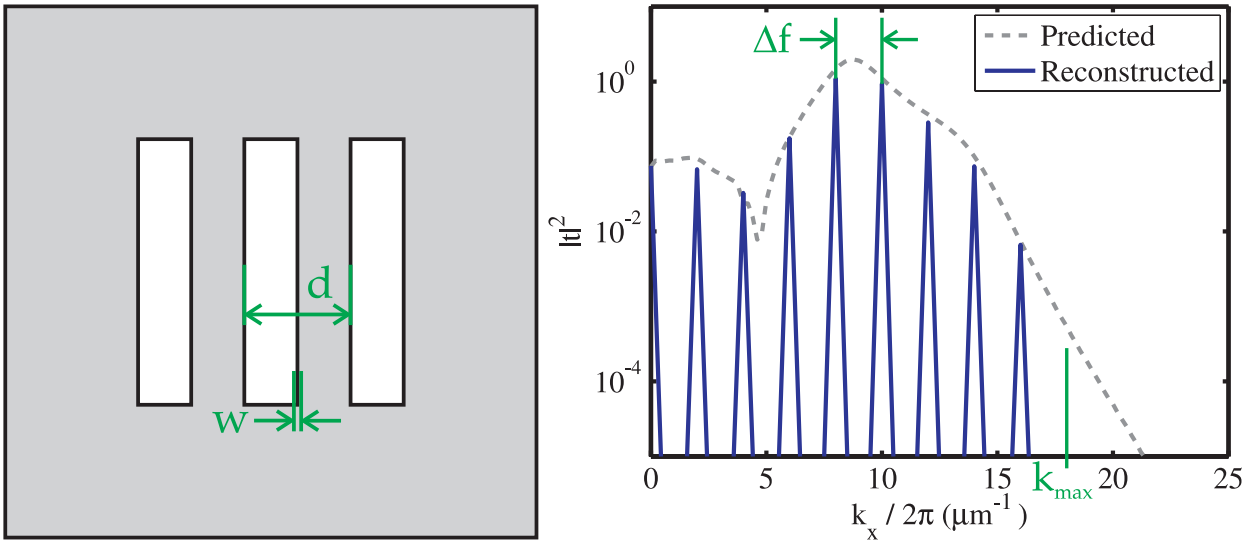

Figure 7.7: Schematic of a mask with 50% duty cycle line grating (a). The grating period, d, determines the resolution of features in the spatial frequency domain (b), according to the relationship $\Delta f = 2/d$, with the highest calculable spatial frequency component of those features determined by the inverse of the step width, $1/w$.

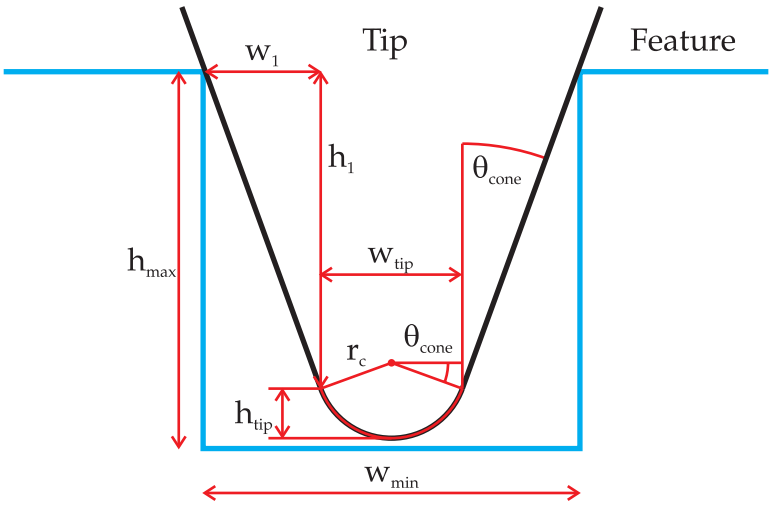

Figure 7.8: AFM tip geometry and minimum imageable feature size.

7.2.2 Implementation

The design shown in Fig. 7.7a was used to pattern experimental masks with periodic, 50% duty cycle line gratings, as shown in Figs. 7.9 and 7.10. The higher duty cycle meant that the construction requirements for this design were less complicated than for the low-width design shown in Fig. 7.6a, allowing MLP to be used in place of more sophisticated, high resolution techniques. Two separate versions of this mask design were fabricated, one with 110 nm high, 10 μm period Cr features, fabricated via MLP and shown in Fig. 7.9; the other with a shorter, 1 μm period, shown in Fig. 7.10. Since the minimum half-pitch resolution of MLP was between 2 and 3 μm, IL was used to generate the 1 μm wide gratings, resulting in ~50 nm high W features.

7.3 Characterisation Experiments

Using the line grating masks described in Section 7.2.2, ENFOL and PLL experiments were performed according to the protocols laid out in Chapter 6. Exposure doses were varied between 60 mJ/cm^2 and 90 mJ/cm^2 for the ENFOL experiments and 100 mJ/cm^2 and 150 mJ/cm^2 for the PLL experiments. The differences between doses was to account for the increased attenuation in the 20:40:20 nm PMMA:Ag:PMMA

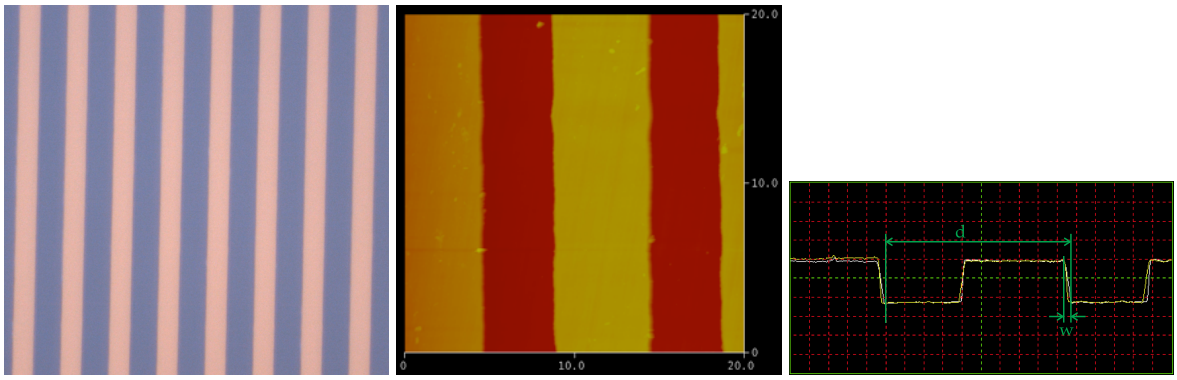

(a) (b) (c)

Figure 7.9: Optical microscopy (a) and AFM micrograph (b) of an MLP mask patterned with a 10 μm period, 50% duty cycle line grating. An AFM linescan of the fabricated mask (c), showing step transition width, w, of the order of 300 nm. Nominal period for each image is 10 μm. Horizontal scale in (c) is 2 μm/division, vertical scale is 50 nm/division.

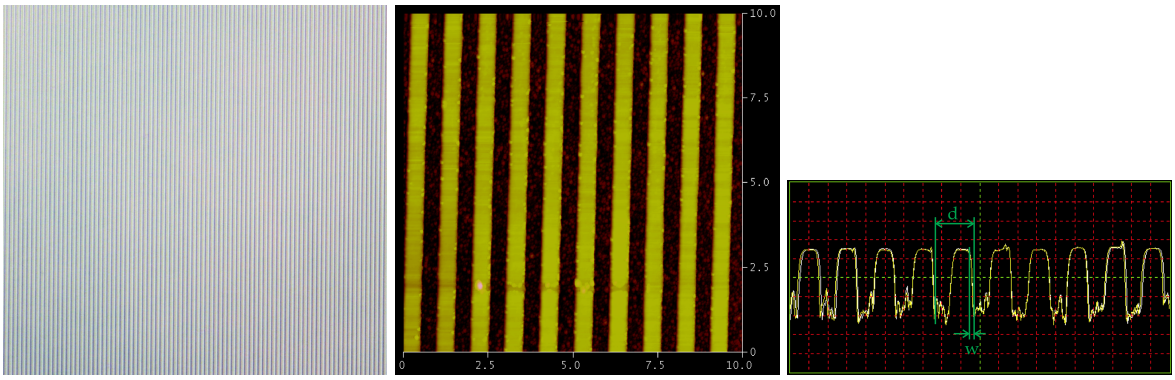

(a) (b) (c)

Figure 7.10: Optical microscopy (a) and AFM micrograph (b) of an IL mask patterned with a 1 μm period, 50% duty cycle line grating. An AFM linescan of the fabricated mask (c), showing step transition width, w, of the order of 100 nm. Nominal period for each image is 1 μm. Horizontal scale in (c) is 500 nm/division, vertical scale is 20 nm/division.

superlens experiments compared to the ENFOL trials. Resist films for both sets of experiments were developed for 15 s in a 4:3 solution of AZ MIF 326 and DIW. The resulting evanescent images were successfully captured for masks with both 10 μm period and 1 μm period gratings, as shown in Figs. 7.11 and 7.12.

The best results in this series of experiments were observed for the 10 μm period grating, which produced profiles with flat, smooth peaks and concave troughs for the PLL experiments, shown in Fig. 7.12b. The flat peaks indicate that there is good contact between the mask, lens and resist, while the concave shape of the exposed features is a symptom of enhanced evanescent modes excited via surface plasmon resonance (SPR); these modes cause ringing around the edges of mask features and are a prerequisite for superresolution in superlenses [20]. In contrast, the ENFOL images of the 10 μm mask only showed convex features, as indicated by Fig. 7.11b. This variation in the shape of exposed features between ENFOL and PLL experiments strengthens the argument that SPR is being observed, since no enhancement of evanescent modes is expected in ENFOL experiments. Lastly, the averaged depth profiles of the data in Figs. 7.11a and 7.12a, presented here in Fig. 7.13, are in excellent agreement with FEM simulations of the expected electric field intensities at the relevant imaging planes, shown in Fig. 7.14, confirming the validity of the features being observed.

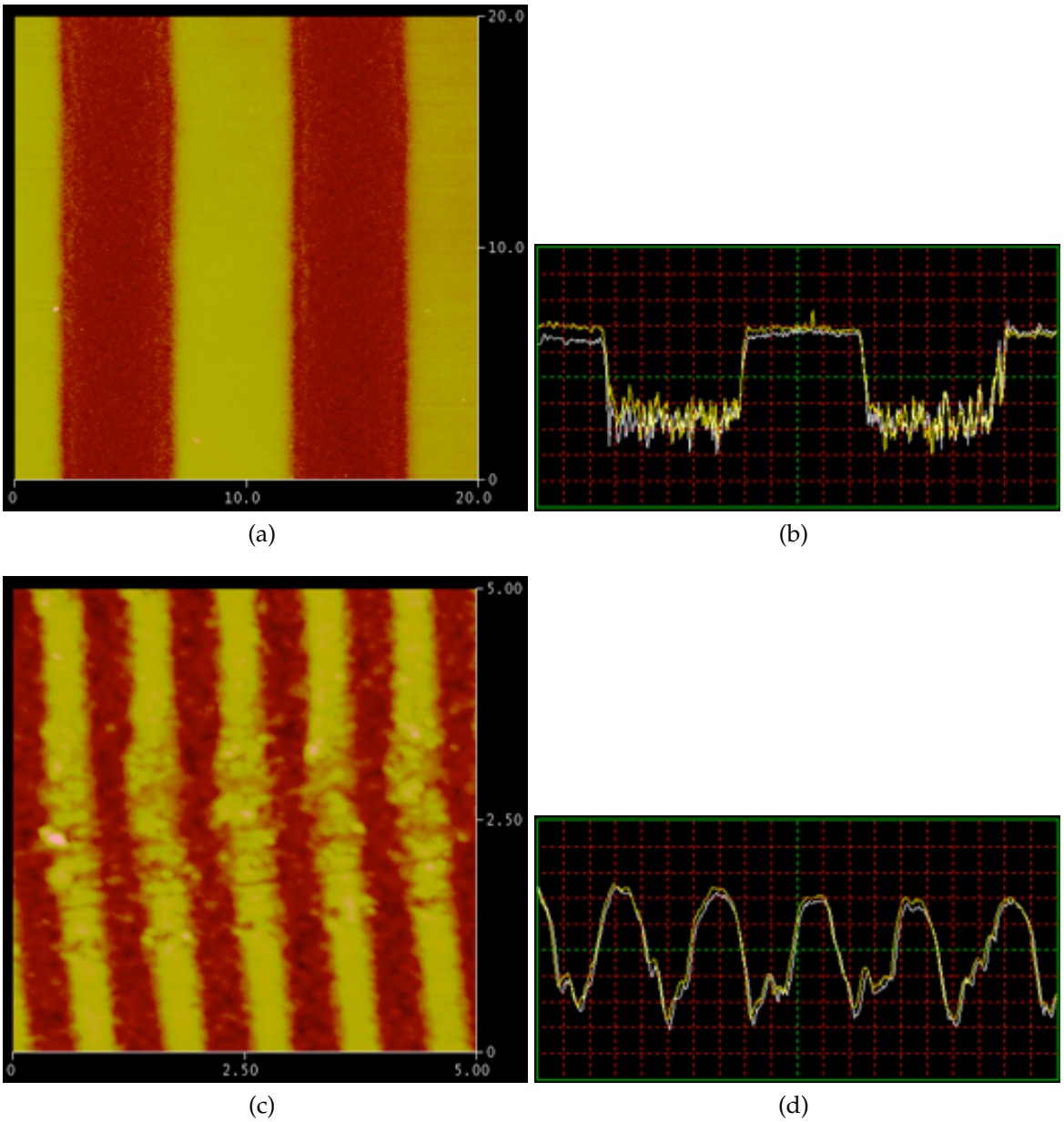

Figure 7.11: AFM micrographs of resist films imaged via ENFOL with a 10 μm period grating (a, b) and a 1 μm period grating (c-d). Plane view micrographs are shown on the left, with the corresponding single profile images shown on the right. Horizontal scales in (b) and (d) are 1 μm/division and 250 nm/division, respectively, with vertical scale of 5 nm/division.

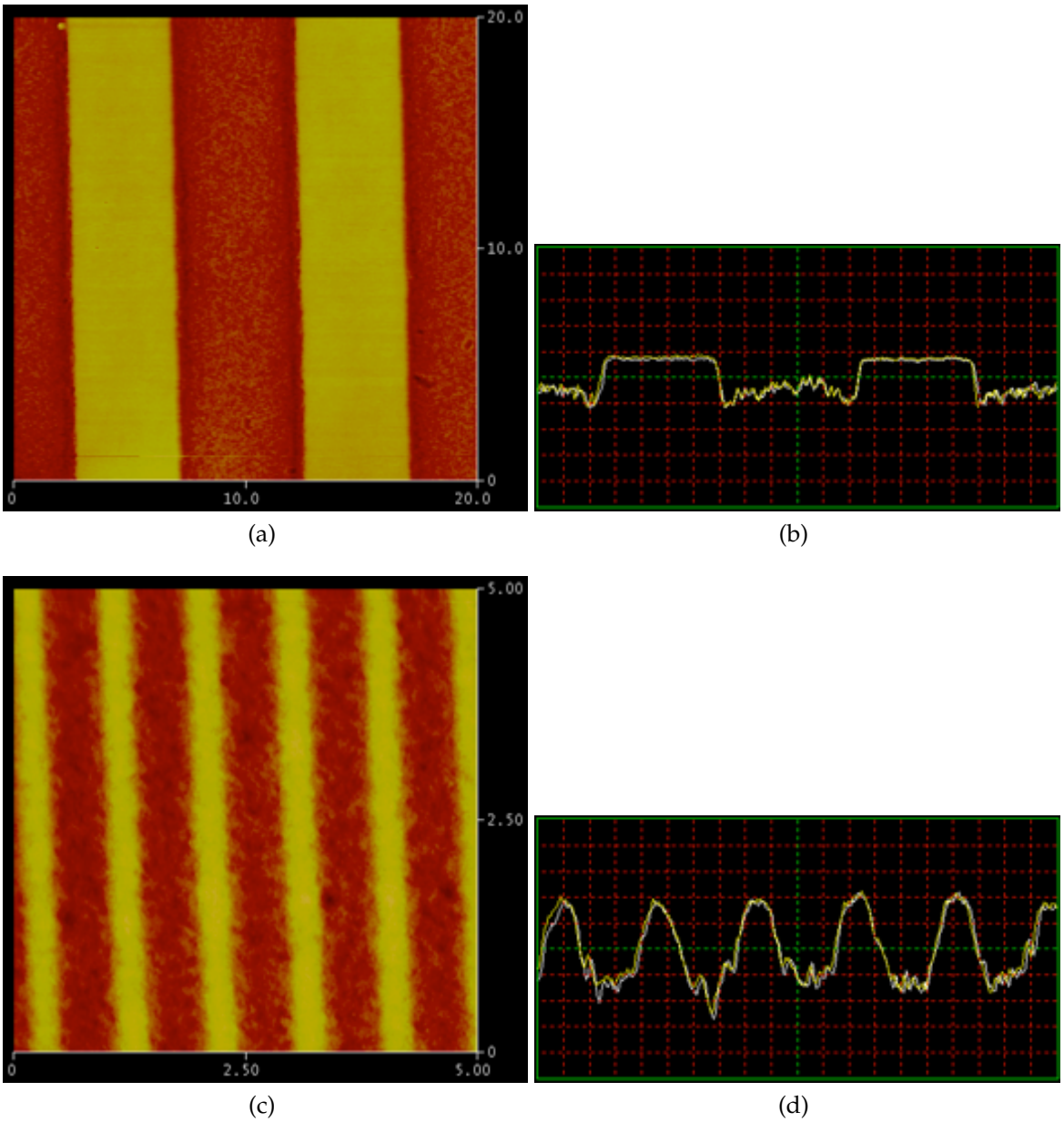

Figure 7.12: AFM micrographs of resist films imaged via a 20:40:20 nm PVA:Ag:PVA superlens with a 10 μm period grating (a, b) and a 1 μm period grating (c-d). Plane view micrographs are shown on the left, with the corresponding single profile images shown on the right. Horizontal scales in (b) and (d) are 1 μm/division and 250 nm/-division, respectively, with vertical scale of 10 nm/division and 2 nm/division.

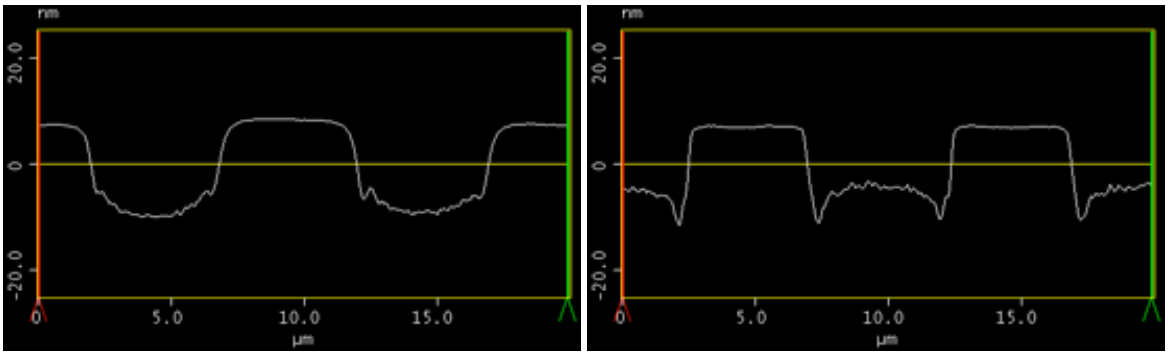

(a) (b)

Figure 7.13: Averaged depth profiles for ENFOL (a) and PLL (b), calculated from the AFM plane measurements shown in Figs. 7.11a and 7.12a.

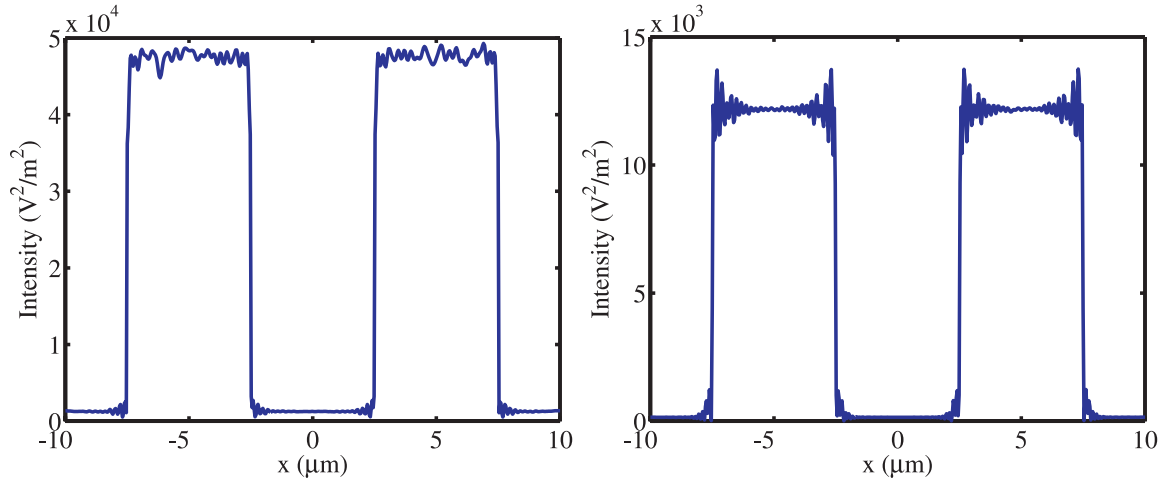

(a) (b)

Figure 7.14: FEM electric field intensity profiles calculated 10 nm beyond the imaging planes in ENFOL (a) and PLL (b) experiments. Higher field intensities in these simulations correspond to deeper feature depths in experiments.

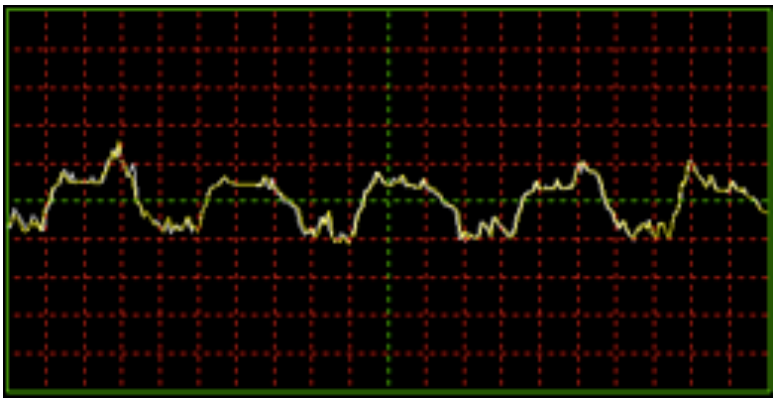

Figure 7.15: AFM depth profile of an AZ 1518 resist film patterned with a 1 μm period grating. Although the fundamental period is well resolved, the peaks and troughs of the pattern are not smooth and the transition regions between peak and trough are irregular. Horizontal scale is 250 nm/division, vertical scale is 50 nm/division.

The data captured from experiments that used a 1 μm period grating as a mask were less convincing; in particular, these profiles, shown in Figs. 7.12d and 7.11d, lacked the smooth peaks and well defined troughs that characterised the 10 μm patterns. The reason for this reduction in feature quality is thought to be due to the AZ 1518 photoresist, which is not well-suited to patterning sub-micron features at high fidelity, as shown in Fig. 7.15. The problem may also be exacerbated by the intentionally slow development scheme described in Section 6.4. Unfortunately the chosen development parameters were necessary to capture evanescent profiles in the resist, so there was little scope to alter them. Despite these imperfections, the profiles captured from the 1 μm masks were still useful in determining some superlens transmission coefficients, as described in Section 7.4.

7.4 Data Processing

Once resist depth data were measured by AFM they were exported to Matlab for processing and presentation in the spatial frequency domain. The individual steps involved in this method are presented graphically in Fig. 7.16 and the relevant Matlab code can be found in Appendix B. A brief description of each operation is included below.

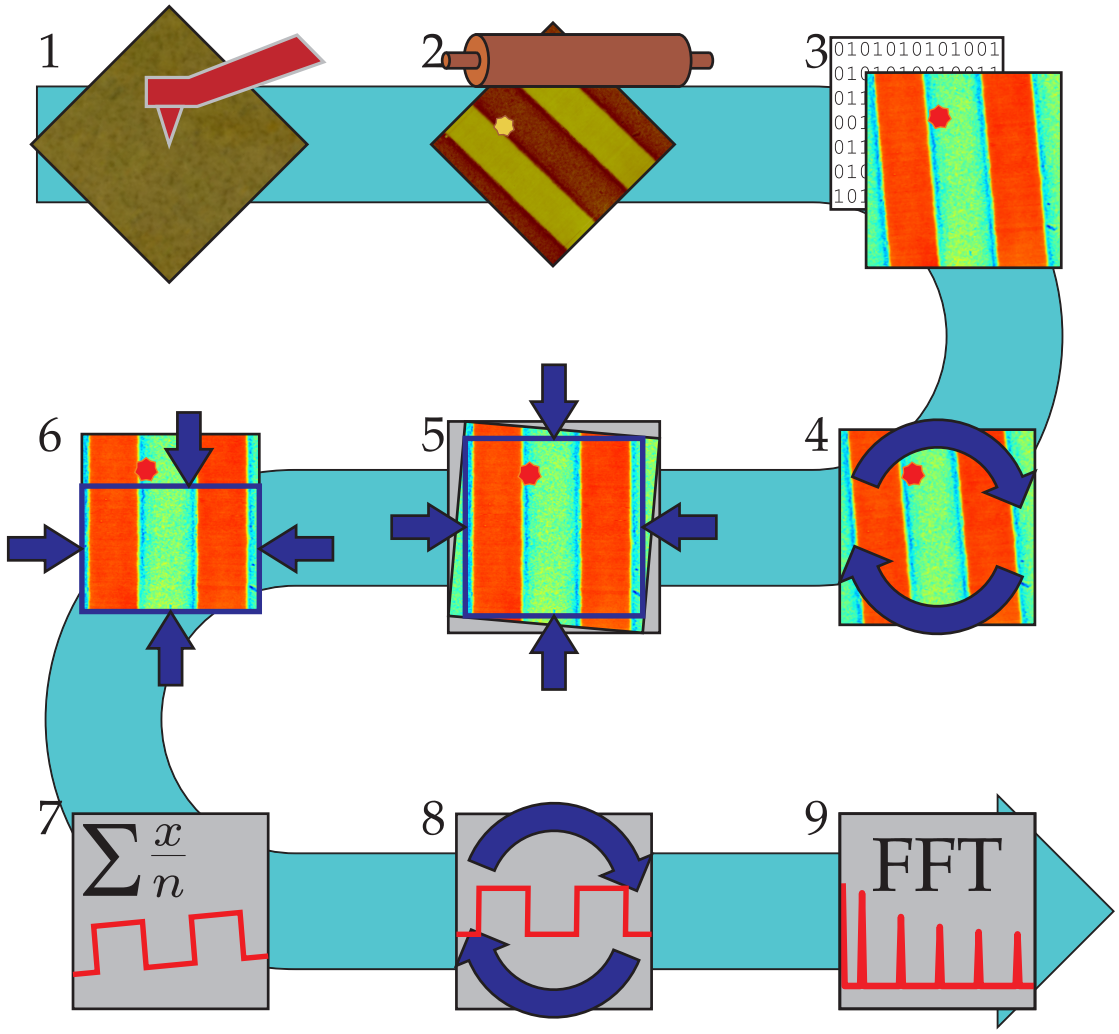

Figure 7.16: Schematic of the data capture and processing steps used to calculate the spatial frequency spectra of patterns in exposed photoresist. 1. AFM scan of resist surface. 2. Flatten data to remove line offsets. 3. Export to Matlab. 4. Rotate about z-axis to improve alignment. 5. Crop to remove void edge data resulting from rotation. 6. Optional second crop to avoid areas of contaminated or corrupt data. 7. Average to remove noise. 8. Rotate about y-axis. 9. Fourier transform to give normalised spatial frequency spectrum.

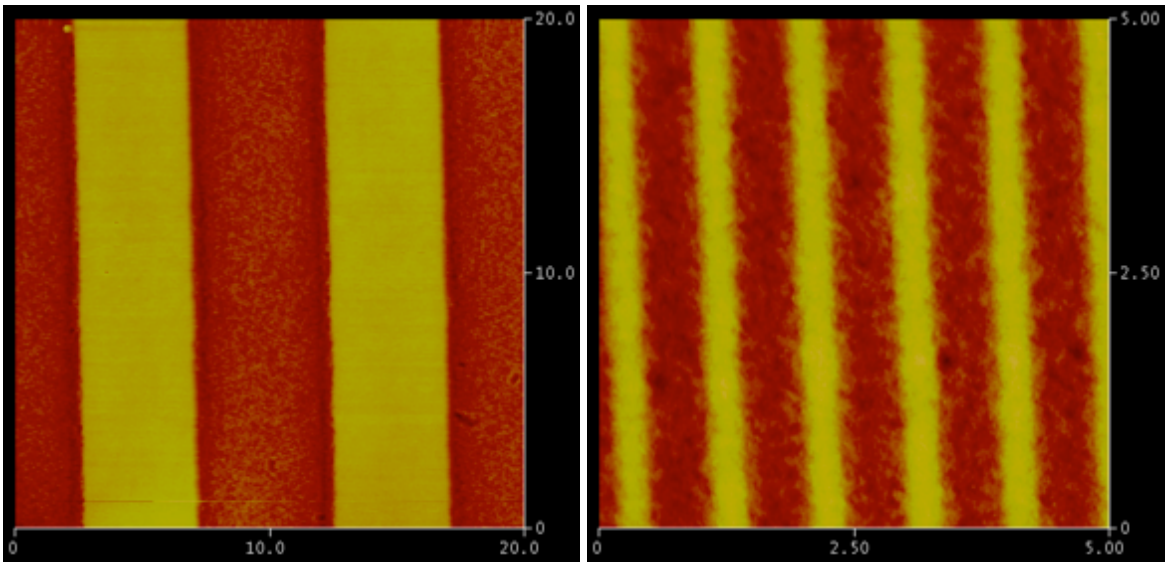

(a) (b)

Figure 7.17: Resist depth images captured via AFM for 10 μm period (a) and 1 μm period (b) gratings. Axes units are in μm.

7.4.1 Resist Profile Spectra

Developed resist samples were measured via AFM and were stored as 20 μm $\times$ 20 μm images for the 10 μm period patterns and 5 μm $\times$ 5 μm images for the 1 μm period patterns, as shown in Fig. 7.17. Regardless of pattern period, each image was made up of 512 $\times$ 512 pixels, giving lateral resolution of 39 nm/pixel for the 20 μm images and 9.8 nm/pixel for the 5 μm images. In the vertical direction the range of motion of the AFM head was limited to a maximum of 2 μm; this allowed a minimum measurable change in depth of 0.01458 nm, corresponding to approximately 17 bits of useful data for each pixel. This resolution was far beyond the expected vertical resolution of the photoresist.

Once image capture was complete a flatten operation, performed via the AFM control software [172], was executed in order to remove spurious offsets from individual lines of data, as shown in Fig. 7.18. The data were then exported to Matlab, where they were rotated so that the feature edges in the image were parallel to the columns of the matrix, as shown in Fig. 7.19. This operation was performed by rotating the image over a range of angles until the standard deviation of each of the columns in the image

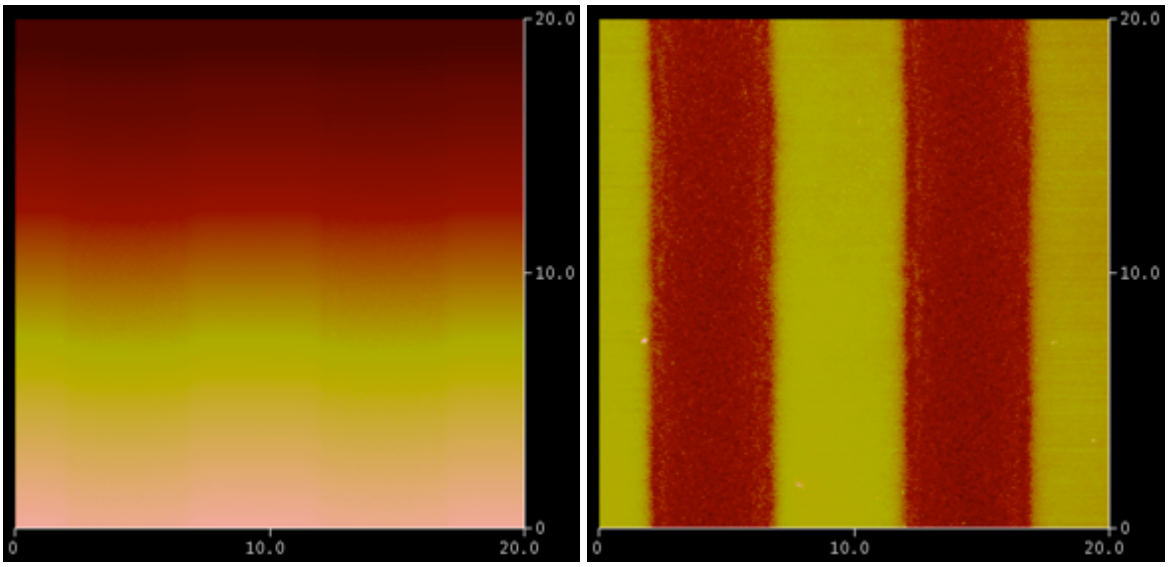

(a) (b)

Figure 7.18: Resist depth data captured via AFM both before (a) and after (b) a first order flatten operation was executed to remove spurious offsets from individual line scans. Axes units are in μm.

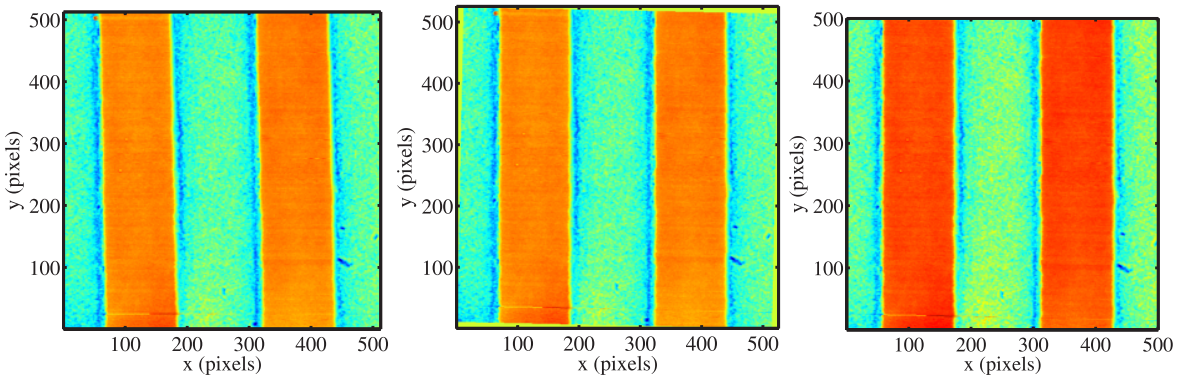

(a) (b) (c)

Figure 7.19: False colour resist depth data captured via AFM, both before (a) and after (b) rotation to align the predominant features in the image with the edges of that image. The resulting triangular areas of blank data around the perimeter of (b) are removed via a crop operation (c).

matrix was minimised. This step was necessary in order to correctly measure the size of features in the image.

After rotation the data were cropped to remove blank areas in the image, shown in Figs. 7.19b and 7.19c. A second crop was ocassionally necessary to remove un-

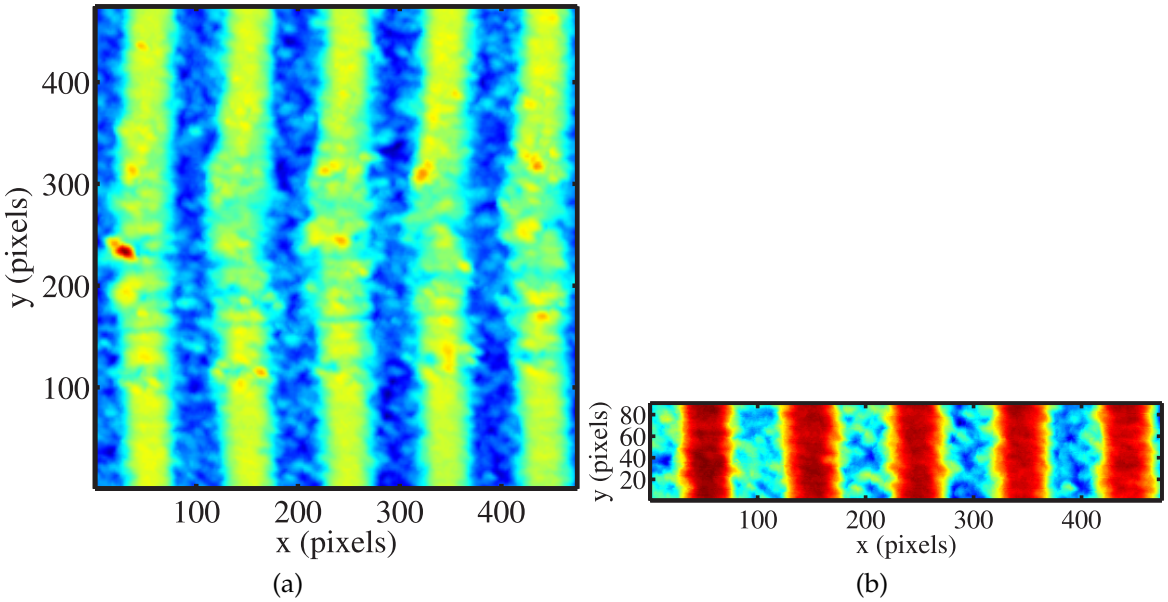

Figure 7.20: False colour resist depth data captured via AFM, showing an area of strong distortion in the pattern of the resist (a). This distortion, which may be caused by contamination on the mask or an area of poorly cured PDMS under the resist, is removed by means of a crop operation (b). This increases the clarity of the patterns present in the data at the expense of reducing the number of data lines that can be averaged to remove noise.

wanted, corrupt or incorrectly patterned areas of the image, as shown in Fig. 7.20. From this point the average of each column of data was calculated again in order to eliminate noise; the result was a vector or 1D line profile of the patterns present in the resist, as shown in Fig. 7.21. If necessary, the line profile vector could be re-flattened about its centre, as shown in Fig. 7.21b, so that the period of features would be correctly translated to the spatial frequency domain. The data was now in a similar form to the individual AFM line profiles shown in Figs. 7.12 and 7.11, albeit with much less noise present. Lastly, the line profile vector was converted to the spatial frequency domain via DFT, to give the normalised spectrum of the resist depth profile, shown in Fig. 7.22. Similar spectra based on the AFM micrographs shown in Figs. 7.11 and 7.12 are presented in Figs. 7.23 and 7.24, with the technique used to extract transfer functions from these data described in Section 7.4.2.

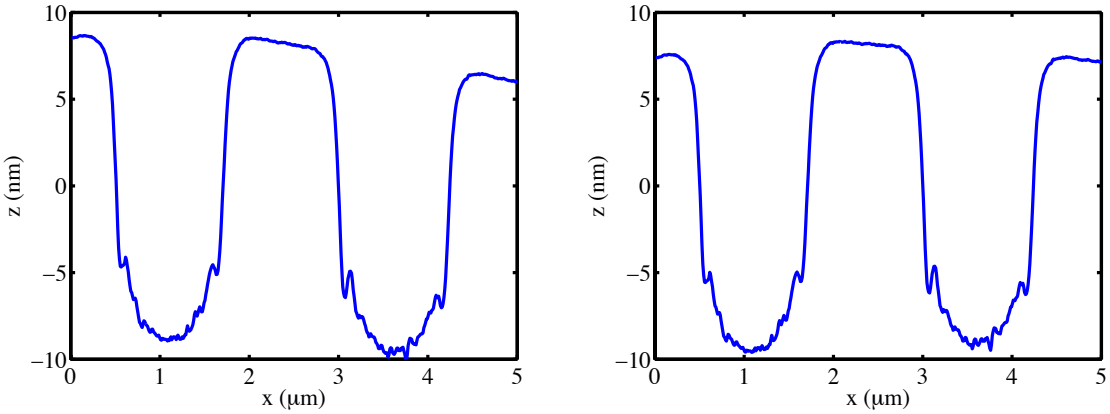

Figure 7.21: Averaged resist depth profile calculated from AFM data (a). This profile may be 'flattened' or rotated around its horizontal and vertical centre point (b) to facilitate accurate representation of the profile in the spatial frequency domain.

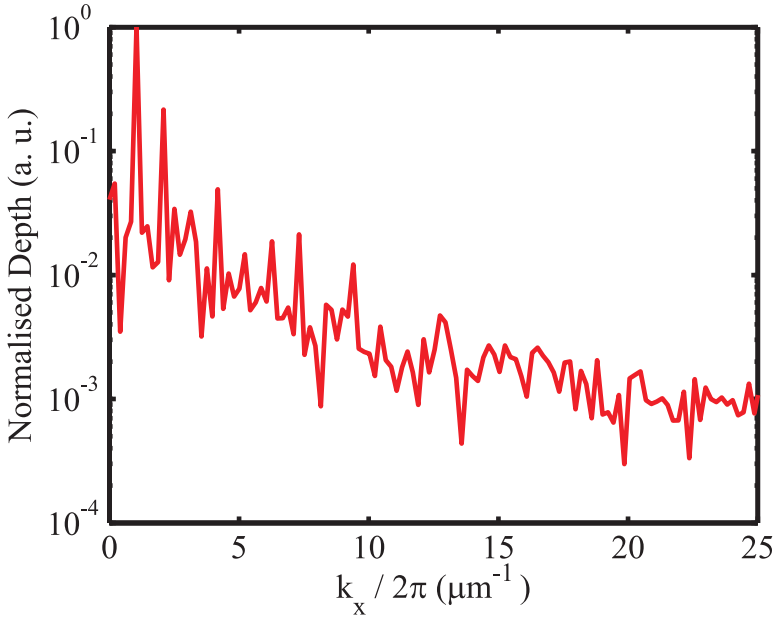

Figure 7.22: Normalised depth spectrum of the averaged line profile shown in Fig. 7.21b.

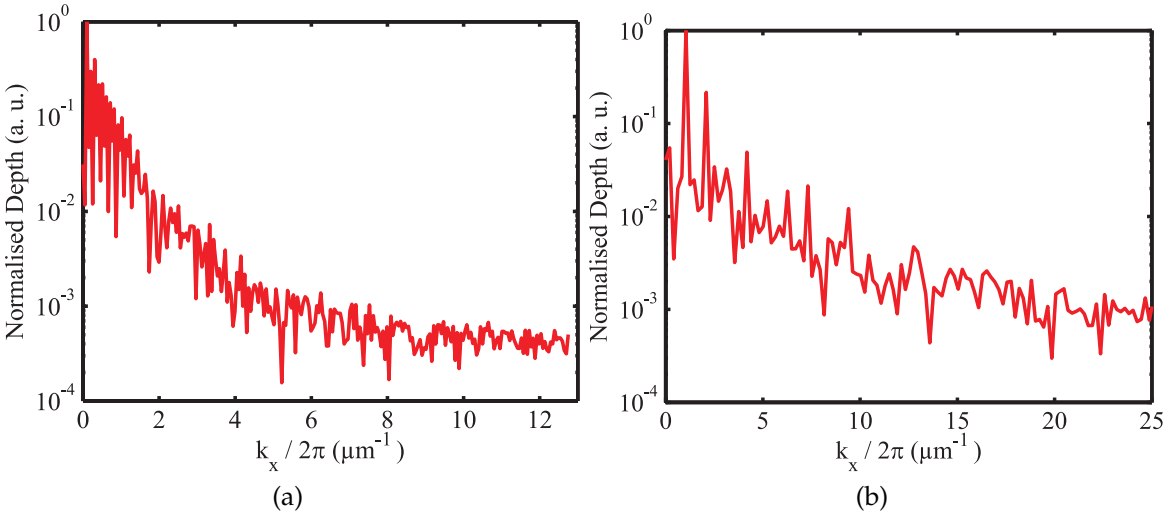

Figure 7.23: Normalised spatial frequency spectra of resist films imaged via a 20:40:-20 nm PVA:Ag:PVA superlens with a 10 μm period mask (a) and a 1 μm period mask (b).

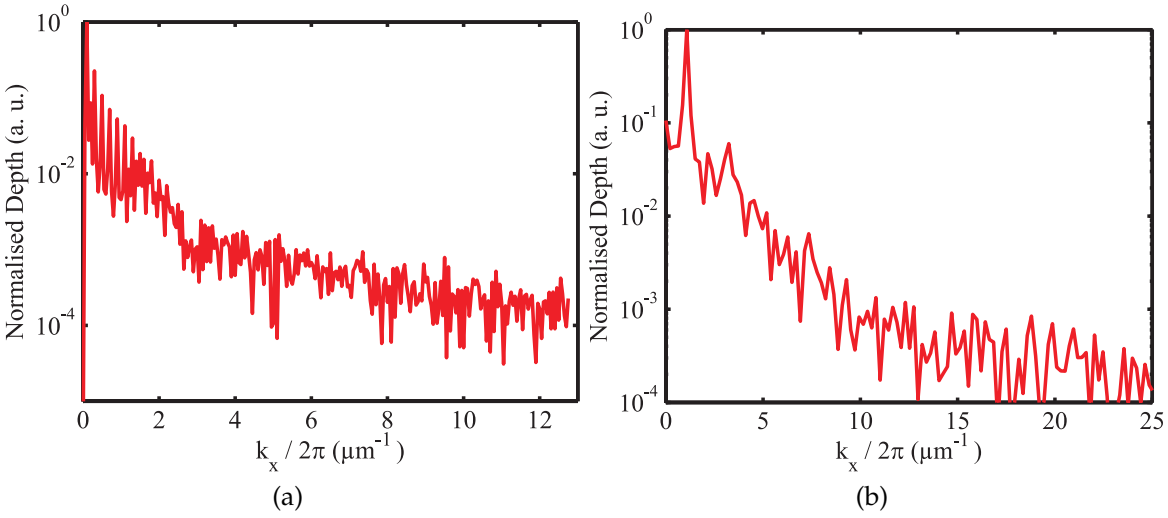

Figure 7.24: Normalised spatial frequency spectra of resist films imaged via ENFOL with a 10 μm period mask (a) and a 1 μm period mask (b).

7.4.2 Transfer Function Calculation

There are two possible methods of finding TFs using the data provided in Section 7.4.1. Firstly, TFs can be calculated by dividing the spectra obtained from PLL experiments with those obtained from ENFOL, provided the same mask is used for each set of experiments. This method is feasible because the input electrical field used to stimulate the superlens in the PLL experiments, $IP(k)_{PLL}$, is the same as the output field captured in the photoresist in ENFOL experiments, $OP(k)_{ENFOL}$. Hence the transfer function of the superlens, $H(k)_{PLL}$, can be determined experimentally according to

$$\begin{aligned} H(k)_{PLL} &= \frac{OP(k)_{PLL}}{IP(k)_{PLL}} \\ &= \frac{OP(k)_{PLL}}{OP(k)_{ENFOL}}, \end{aligned} \tag{7.16}$$

where $OP(k)_{PLL}$ is the output PLL spectrum. The beauty of this technique is that any distortion in the measured profiles that stems from the response of the photoresist will be cancelled out, since it will affect both the ENFOL and PLL profiles equally.

Another option for extracting TFs from spectral data is to use the depth spectra of masks as the input data, $IP(k)_{mask}$. Transfer functions for both superlenses and ENFOL structures can then be determined by taking the ratio of the output spectra to the $IP(k)_{mask}$. This method has the advantage that the mask spectra, shown in Fig. 7.25, generally have lower noise than resist-based spectra; however, a greater degree of approximation is necessary since the intensity profile of the mask is assumed to be directly proportional to the inverse of its depth profile.

Regardless of which method is used to extract TFs, care has to be taken to ensure that the data captured are valid. The spectra of the mask patterns implemented in Section 7.2.2 are characterised by nulls between harmonic spatial frequencies; these nulls limit the spatial frequencies at which transmission coefficients can be retrieved. For a $20\ \mu\mathrm{m} \times 20\ \mu\mathrm{m}$ image of a 10 μm period mask, harmonics appear at 0.1 $\mu\mathrm{m}^{-1}$, 0.3 $\mu\mathrm{m}^{-1}$, 0.5 $\mu\mathrm{m}^{-1}$, 0.7 $\mu\mathrm{m}^{-1}$ etc., up to a theoretical maximum of 12.7 $\mu\mathrm{m}^{-1}$, which is determined by the number and size of the data pixels captured via AFM. The harmonics are more spread out for a $5\ \mu\mathrm{m} \times 5\ \mu\mathrm{m}$ image of a 1 μm period mask, occurring at 1 $\mu\mathrm{m}^{-1}$, 3 $\mu\mathrm{m}^{-1}$, 5 $\mu\mathrm{m}^{-1}$, 7 $\mu\mathrm{m}^{-1}$ etc, up to a theoretical maximum of 51 $\mu\mathrm{m}^{-1}$.

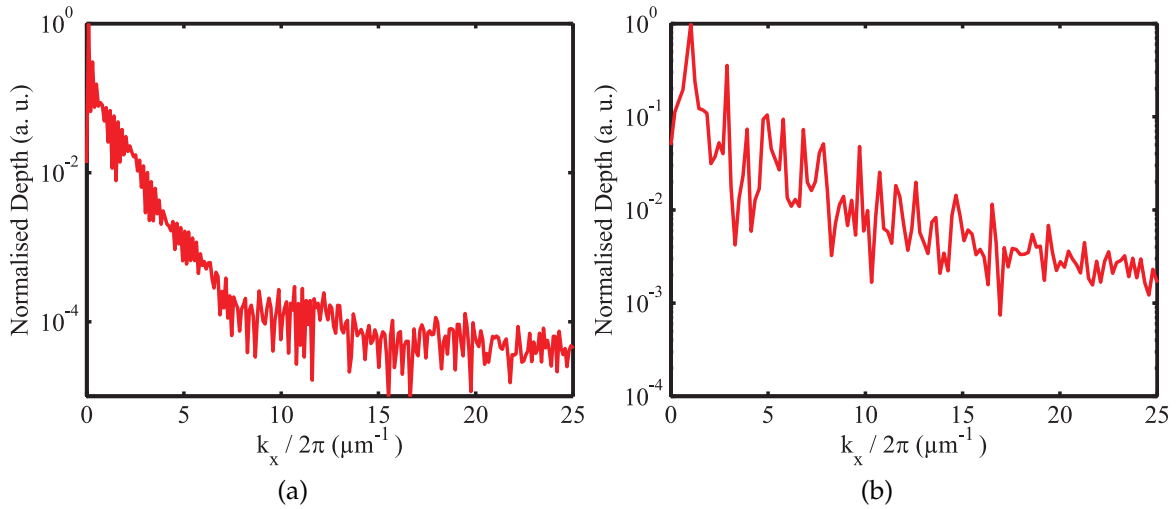

Figure 7.25: Normalised spatial frequency spectra of a 10 μm period MLP mask (a) and a 1 μm period IL mask (b).

An additional constraint on the validity of captured data was that the location of the harmonics was not exact, due to rounding in the DFT algorithm and drift in the AFM, which varied between scans. For most 5 μm scans, the deviation from nominal values was found to be between 4% and 7%. This meant that harmonic coefficients had to be identified manually, rather than relying exclusively on their expected location.

7.4.2.1 Spectral Intensity Scaling

Once valid data are isolated and the ratio of spectral coefficients is calculated, a further step is necessary to make the derived TF a quantitative estimate of the performance of a superlens. This step involves correcting the scaling of the transmission coefficients, since the mask, ENFOL and PLL spectra that they are based on are all normalised during the data acquisition process. If left uncorrected, comparing their relative intensities would have only qualitative significance, hence an additional scaling factor must be applied to remedy this loss of quantitative certainty.

Initially, the appropriate value of scaling coefficient was sought from experimental data. Light intensity readings were taken with and without a superlens obstructing the beam path of a 365 nm wavelength light source. The DC or zero-frequency transmission coefficient of the superlens was then calculated by taking the ratio of the two intensity readings; this value gave the scaling coefficient required to make the

reconstructed superlens TF a quantitative measurement. This experiment is shown in Fig. 7.26, with corresponding results shown in Table 7.1. These results indicate that transmission through the superlens for very low spatial frequencies is 59.8%, which corresponds to a DC transmission coefficient of about 0.6.

There are two problems with this method: firstly, the reconstructed superlens TF is assumed to be normalised by its DC transmission coefficient. In reality, the data is normalised by the coefficient of the lowest reconstructed wavenumber, which is 0.1 $\mu\mathrm{m}^{-1}$ for a 10 $\mu\mathrm{m}$ period mask and 1 $\mu\mathrm{m}^{-1}$ for a 1 $\mu\mathrm{m}$ period mask. For the 1 $\mu\mathrm{m}$ period mask, this implies an assumption that the transfer function of the superlens is constant between DC and 1 $\mu\mathrm{m}^{-1}$. Unfortunately, we know from the modelling work presented in Chapters 4 and 5 that this is not the case.

The second difficulty created by this method is that the readings taken by the light intensity meter represent not only the DC transmission of the superlens, but also the transmission of the superlens for all other propagating wavenumbers. Although the measurements were conducted without a mask between the superlens and the light source, dust particles, contaminants on the superlens and noise in the light source were all potential sources of propagating spatial frequency modes, which could skew the readings of the light meter. This concern, together with the assumption of constant transmission for low spatial frequencies, gave cause for an alternative method of normalisation to be used.

An alternative means of finding the appropriate scaling coefficient for reconstructed TFs involves matching the transmission coefficient of the lowest reconstructed wavenumber to the equivalent coefficient from a modelled TF. The lowest reconstructed wavenumber is chosen as this corresponds to the fundamental spatial frequency of the mask that was used to produce the TF. The coefficient at this wavenumber therefore has the best signal-to-noise ratio (SNR) of all reconstructed coefficients and is likely to provide the most reliable normalisation.

Based on a M-TMM model of a 20:40:20 nm PVA:Ag:PVA superlens exposed to a 110 nm thick NiCr slab, the TFs produced by the 10 $\mu\mathrm{m}$ period masks were scaled to have transmission of 0.147$\times$ at a spatial frequency of 0.1 $\mu\mathrm{m}^{-1}$. Similarly, the TFs produced by 1 $\mu\mathrm{m}$ period masks were scaled to have transmission of 0.0997$\times$ at a spatial frequency of 1 $\mu\mathrm{m}^{-1}$. The M-TMM model used in this case was for a 20:40:20 nm PVA:Ag:PVA superlens exposed to a 50 nm thick W slab. Corresponding models for

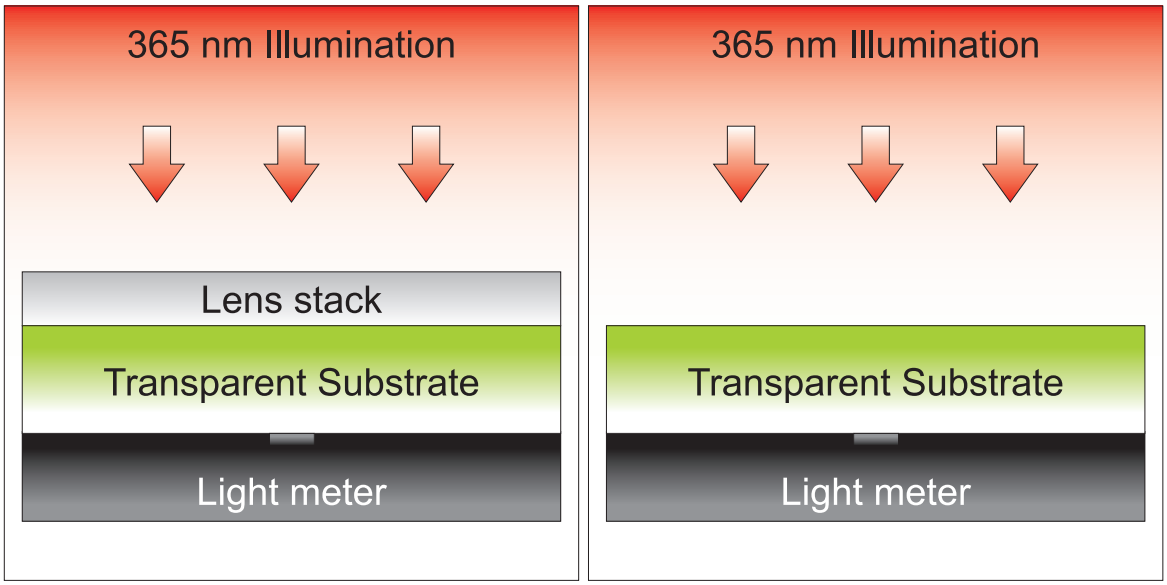

(a) (b)

Figure 7.26: Superlens DC transmission coefficient measurement experiment. A 20:40:20 nm PVA:Ag:PVA superlens stack and a transparent quartz substrate are exposed to 365 nm light in a Karl Süss MA6 mask aligner. The power transmitted by the lens and substrate assembly is measured by a Süss MicroTec Model 1000 intensity meter (a), with the measurement compared to the power transmitted by only the substrate (b) to give a measure of the DC or low spatial frequency attenuation of the superlens.

Table 7.1: DC transmission coefficient measurement results for a 20:40:20 nm PVA:Ag:PVA superlens on a 520 μm quartz substrate.

	Component	**Transmitted Intensity (mW/cm^2)**	**Transmission coefficient, t**
(1)	MA6 Mask Aligner	9.5	1.000
(2)	Substrate	8.95	0.942
(3)	Superlens and substrate	5.35	0.563
(4)	Superlens alone: (3) / (2)		0.598

ENFOL exposures predicted constant transmission of 1.0 for wavenumbers below the diffraction limit.

7.4.3 Uncertainty of Reconstructed Transmission Coefficients

To calculate the uncertainties in the experimentally derived TFs it is necessary to consider both the standard deviation in the amplitude of the coefficients and the uncertainty in their location along the spatial frequency axis. The amplitude standard deviation is due to noise in the AFM scans, which is caused both by the AFM itself and also by the quality of the photoresist. In contrast, horizontal variation is due to drift in the AFM, which will elongate or compress the measured spectra, as well as rounding errors introduced by the limited resolution of the FFT. Methods of quantifying these uncertainties are discussed in Sections 7.4.3.1 and 7.4.3.2, before they are applied to experimental data in Section 7.4.4.

7.4.3.1 Vertical Uncertainty

To find the variance of a TF coefficient, it is first necessary to know the variances of the spectra that the coefficient is derived from. Similarly, to know the variances of the spectra, it is necessary to know the variances of their respective spatial domain data. Using the surface profiles shown in Figs. 7.10c, 7.11d and 7.12d as examples, the variances of the height data in the y direction, σ^2_{plane}, have average values of $928\ \mathrm{nm}^2$, $70.9\ \mathrm{nm}^2$ and $7.08\ \mathrm{nm}^2$, respectively. The variances, $\sigma^2_{spectrum}$, of the corresponding spectra, shown in Figs. 7.25b, 7.24b and 7.23b, are given by [173]:

$$\sigma^2_{spectrum} = \frac{\sigma^2_{plane}}{c_n^2 \times N}, \tag{7.17}$$

where c_n is the scaling coefficient used to normalise the spectrum and N is the number of elements in the spectrum. For Figs. 7.25b, 7.24b and 7.23b, $\sigma^2_{spectrum}$ was $6.25 \times 10^{-3}\ \mathrm{nm}^2$, $4.47 \times 10^{-3}\ \mathrm{nm}^2$ and $4.36 \times 10^{-3}\ \mathrm{nm}^2$, respectively. Next, the variance of the transfer function coefficients, σ^2_H, can be calculated from the variances of its constituent spectra, σ^2_Y and σ^2_X, since the transfer function, H, is essentially a ratio of two spectra, Ψ_Y and Ψ_X:

$$H = \frac{\Psi_Y}{\Psi_X}. \tag{7.18}$$

Accordingly, σ_H^2 is given by [174]:

$$\sigma_H^2 = \sigma^2\left(\frac{\Psi_Y}{\Psi_X}\right) = \frac{Y_i^2}{X_i^2}\left[\frac{\sigma_X^2}{X_i^2} - \frac{\sigma_{XY}}{X_iY_i} + \frac{\sigma_Y^2}{Y_i^2}\right], \tag{7.19}$$

where X_i and Y_i are the i^{th} coefficient of Ψ_X and Ψ_Y, respectively, and σ_{XY} is the covariance of Ψ_X and Ψ_Y, derived from the covariance of their two corresponding profiles, according to Eq. (7.17).

Finding the covariance of the profiles is not a trivial matter, since the phase of the patterns in the profiles is random, dependent only on the location of the AFM head relative to the sample at the time of scanning. To eliminate the effects of this random phase in the source data, a section, $x_{section}$, of the object profile, $x_{profile}$, shown in Fig. 7.27a, is swept across the image profile, $y_{profile}$, shown in Fig. 7.27b, and the correlation coefficient of the overlapping data, ρ, is calculated at each point in $y_{profile}$, according to Eq. (7.20):

$$\rho = \frac{\sigma_{section,overlap}}{\sigma_{section}\sigma_{overlap}}, \tag{7.20}$$

where $\sigma_{section,overlap}$ is the covariance of $x_{section}$ and the part of $y_{profile}$ that it covers; $\sigma_{section}$ is the standard deviation of $x_{section}$ and $\sigma_{overlap}$ is the standard deviation of the part of $y_{profile}$ that is covered by $x_{section}$. The size of $x_{section}$ is chosen to include at least one half period of the pattern in $x_{profile}$.

Once the maximum ρ is found for a given section of $x_{profile}$, the location of $x_{section}$ in $x_{profile}$ is incremented and the correlation measurement process is completed again. In this way both $x_{profile}$ and $y_{profile}$ are swept to find the maximum possible correlation coefficient between the two profiles, ρ_{max}. This process of recovering the correlation coefficient is illustrated in Fig. 7.27 and the code used to implement it is listed in Appendix C.

Given ρ_{max}, the covariance of the profiles, $\sigma_{x_{profile},y_{profile}}$, is found by multiplying by $\sigma_{x_{profile}}$ and $\sigma_{y_{profile}}$:

$$\sigma_{x_{profile},y_{profile}} = \rho_{max} \times \sigma_{x_{profile}}\sigma_{y_{profile}}. \tag{7.21}$$

In a similar way to Eq. (7.17), the covariance of the spectra is thus given by

$$\sigma_{XY} = \frac{\sigma_{x_{profile},y_{profile}}}{c_{n,x}c_{n,y} \times \sqrt{N_xN_y}}, \tag{7.22}$$

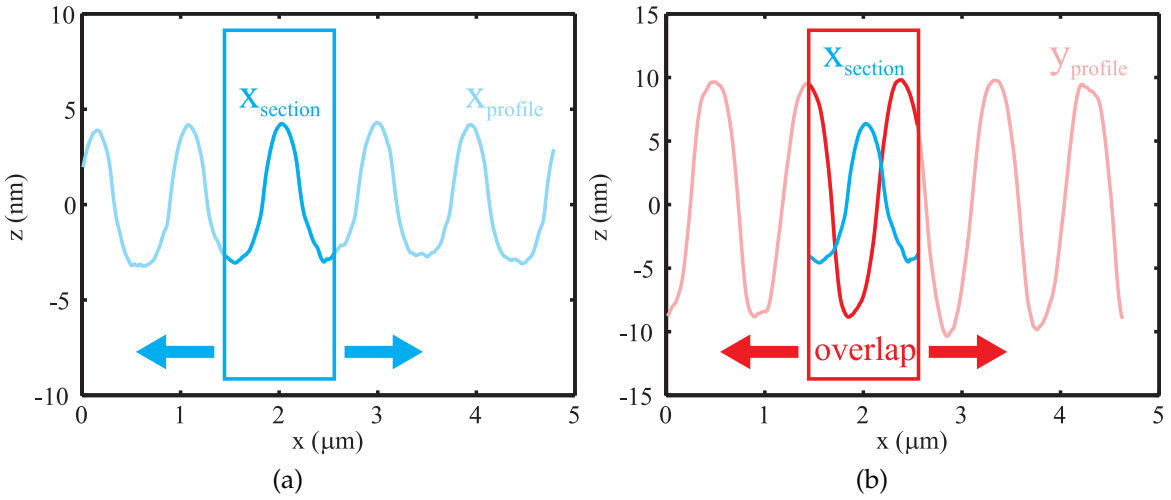

Figure 7.27: Correlation coefficient measurement process. (a) A section, $x_{section}$, is taken from an AFM object profile, $x_{profile}$, and is shifted across the length of (b) a similar image profile, $y_{profile}$. The correlation coefficient, ρ, of the overlapping data is recorded for each position of $x_{section}$. Once $x_{section}$ has covered the entire $y_{profile}$, a new section is chosen from $x_{profile}$ and the measurement process is repeated until all parts of the object and image profiles have been compared against each other. The correlation coefficient of the two profiles, $x_{profile}$ and $y_{profile}$, is approximated as the maximum correlation coefficient, ρ_{max}, observed between $x_{section}$ and $y_{profile}$.

where $c_{n,x}$ and $c_{n,y}$ are the coefficients used to normalise Ψ_X and Ψ_Y, and N_x and N_y are the number of elements in $x_{profile}$ and $y_{profile}$, respectively.

Finally, σ_H^2 is divided by $\frac{1}{c_s^2}$, where c_s is the scaling coefficient used to match the measured and predicted transmission coefficients at $1\ \mu\mathrm{m}^{-1}$, described in Section 7.4.2.1. The square root of this value then yields the standard deviations of the TF coefficients, σ_H, which are shown as vertical lines in the experimental TFs described in Section 7.4.4.

7.4.3.2 Horizontal Uncertainty

Despite the appropriate scaling of reconstructed transmission coefficients, there are two significant sources of horizontal uncertainty that affect the reconstructed TFs: firstly, mechanical drift of the AFM head during measurements causes compression or elongation in the spatial frequency domain. This effect increases with wavenumber, making the location of high wavenumber coefficients less certain than the location

of coefficients at lower wavenumbers. For the AFM scans shown in Figs. 7.23, 7.24 and 7.25, drift affected coefficient locations by up to 0.05 $\mu\mathrm{m}^{-1}/\mu\mathrm{m}^{-1}$.

The second source of uncertainty is rounding error in the location of spectral peaks, due to the finite resolution of the DFT used during data processing. This phenomenon is equally likely to affect low wavenumbers as it is to affect high wavenumbers; adding an uncertainty of up to $\pm 0.08\ \mu\mathrm{m}^{-1}$, depending on the exact number of data points used in the transform. The net effect of these two types of uncertainty was that wavenumber coefficients differed from their expected locations by between 0.9% and 8%, with the greatest uncertainty of $\pm 0.83\ \mu\mathrm{m}^{-1}$ occurring for the data shown in Fig. 7.24b at a nominal wavenumber of 13 $\mu\mathrm{m}^{-1}$. For TF coefficients, which were calculated as the ratio of two spectra, the horizontal uncertainties were estimated by taking the larger of the two uncertainties from the coefficients' constituent spectra.

7.4.4 Measured Transfer Functions

Using the spectral comparison and normalisation technique described in Section 7.4.2, the ENFOL and PLL spatial frequency spectra shown in Figs. 7.23 and 7.24 are combined to give an experimental TF for the 20:40:20 nm PVA:Ag:PVA superlens described in Section 7.3. These results are shown in Fig. 7.28, along with the relevant uncertainty data. Further results obtained by comparing ENFOL and PLL data to the mask spectra shown in Fig. 7.25 are presented in Figs. 7.29 and 7.30.

Vertical error bars for each of the data points in these figures represent ± 1 standard deviation, whereas the error bars in the horizontal direction describe the maximum spatial frequency deviation present in each coefficient's constituent data points. Due to the restriction of using logarithmic plots to display these data, the lower vertical bound on some data points cannot be displayed, particularly if the expected magnitude of the coefficient is less than its standard deviation. An analysis on the quality and accuracy of each of these results follows in Section 7.5.

7.5 Discussion and Comparison to Modelled Results

The first feature that should be noted when studying the experimentally measured TFs shown in Figs. 7.28, 7.29 and 7.30 is that the data derived from the 10 μm period masks are not ideal for the type of analysis attempted here. The reasons for this are two-fold: firstly, the harmonics in the 10 μm spectra are clustered very close together, with only 0.2 $\mu\mathrm{m}^{-1}$ separating adjacent peaks. This has the effect of drowning out any trend in the TF data, due to the large noise levels in each measurement. Secondly, all of the spatial frequency transmission coordinates that can be measured are in the propagating part of the spectrum, below the free-space diffraction limit of $\sim 2.74\ \mu\mathrm{m}^{-1}$. This makes the data useless for analysing superresolving systems, which by definition operate beyond the diffraction limit. For these reasons the TFs derived from 10 μm period masks are disregarded for the remainder of this chapter.

The second important feature of the measured TFs is that their range is unexpectedly small, reaching only to 13 $\mu\mathrm{m}^{-1}$ for the curves derived from 1 μm period masks. This range is much smaller than the theoretical maximum range of 51 $\mu\mathrm{m}^{-1}$, quoted in Section 7.4.2. The reason for this is the finite noise floor in the exposed photoresist films, which prevents the accurate measurement of spectral components below a certain threshold. In practical terms, the magnitude of the measured coefficient at

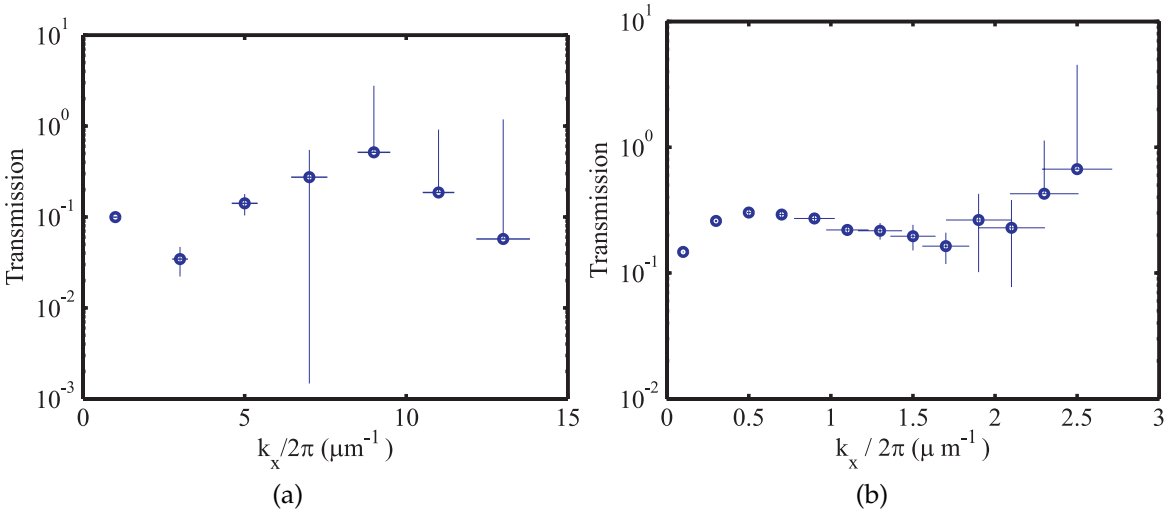

Figure 7.28: Experimentally derived transfer functions for a 20:40:20 nm PVA:Ag:PVA superlens exposed to a 1 μm period mask (a) and 10 μm period mask (b). The TFs are based on the PLL and ENFOL spectra shown in Figs. 7.23 and 7.24, respectively.

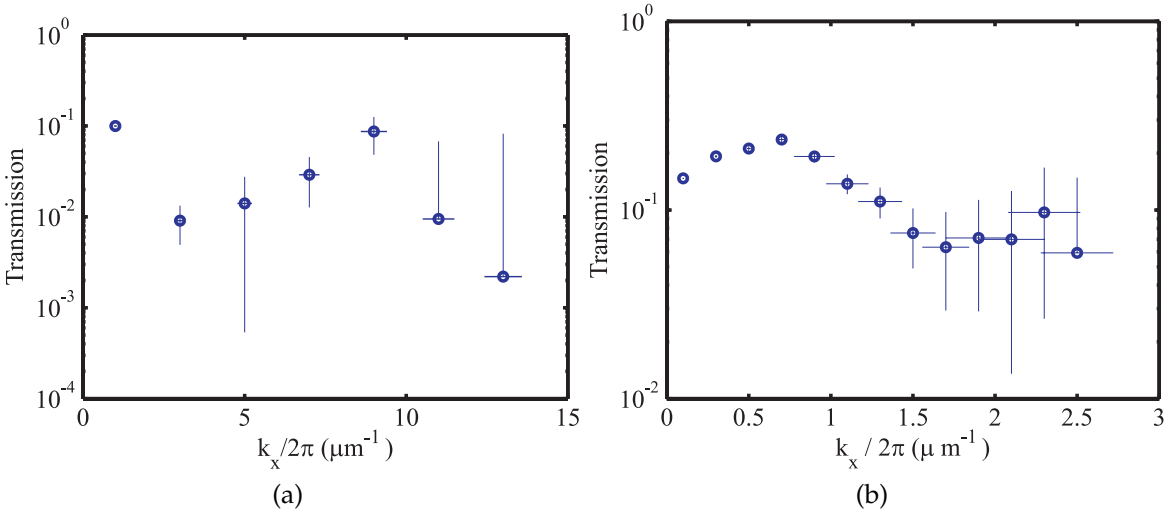

Figure 7.29: Experimentally derived transfer functions for a 20:40:20 nm PVA:Ag:PVA superlens exposed to a 1 μm period mask (a) and 10 μm period mask (b). The TFs are based on the PLL and mask depth spectra shown in Figs. 7.23 and 7.25, respectively.

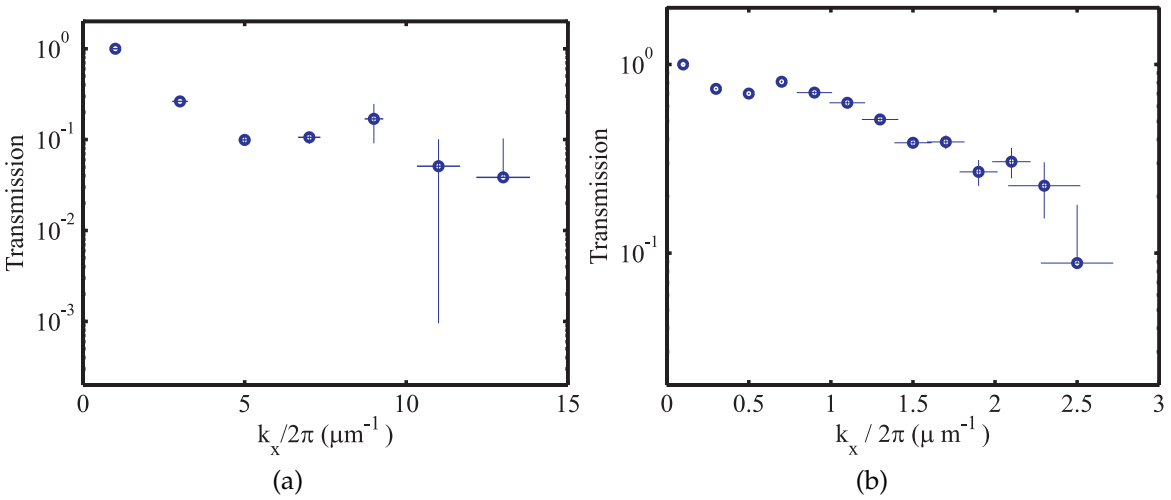

Figure 7.30: Experimentally derived transfer functions for an ENFOL system comprising AZ 1518 photoresist in contact with a 1 μm period mask (a) and 10 μm period mask (b). The TFs are based on the ENFOL and mask depth spectra shown in Figs. 7.24 and 7.25, respectively.

15 $\mu\mathrm{m}^{-1}$ in the spectrum shown in Fig. 7.23b would have to be a factor of $10\times$ smaller than the equivalent coefficient in Fig. 7.24b in order for the experimental data to match the M-TMM model. At 17 $\mu\mathrm{m}^{-1}$, a net difference of two orders of magnitude would be necessary to match the model; at 19 $\mu\mathrm{m}^{-1}$, the difference would need to be three orders of magnitude. Instead, the amplitudes of the measured coefficients are consistently of the same order of magnitude at similar wavenumbers, indicating that the noise floor is indeed limiting the validity of this analysis beyond 13 $\mu\mathrm{m}^{-1}$.

Although increasing the exposure dose and development time could lower the noise floor, this would decrease the sensitivity of the photoresist to the evanescent part of the spatial frequency spectrum and would increase distortion in the z-direction. Alternatively, an improved photoresist could be used for these experiments; however, the triple requirements of i-line sensitivity, nanometer scale resolution and near linear dose response mean that such a resist is unlikely to become available in the short term. The effect of the photoresist sensitivity can be seen in the ENFOL TF shown in Fig. 7.30a, which essentially plots the sensitivity of the photoresist for different wavenumbers. The strong attenuation of the photoresist response function for wavenumbers above 1 $\mu\mathrm{m}^{-1}$ indicates the extent to which the photoresist and its corresponding exposure and development conditions are limiting the efficacy of the analysis presented here.

Despite these disadvantages, the TFs based on 1 μm period data shown in Figs. 7.28, 7.29 and 7.30 can still shed new light on superlens behaviour when they are compared to modelled TFs, derived via TMM, M-TMM and FEM. Such comparisons are made in Fig. 7.31 for the PLL TFs and in Fig. 7.32 for the ENFOL TFs. The PLL models are based on a 20:40:20 nm PVA:Ag:PVA superlens, considered without a mask in the TMM model, with a solid W mask, $\epsilon_{r,W} = 1.497 - 7.69i$, in the M-TMM model, and with a single 10 nm feature W:air mask in the FEM simulation. The two experimental data curves in Fig. 7.31 are taken from the TFs shown in Figs. 7.28a and 7.29a. The first experimental curve, labelled 'PLL / Mask' in Fig. 7.31, is based on the ratio of the PLL output spectrum shown in Fig. 7.23b to the mask depth spectrum of Fig. 7.25b. The second experimental curve is labelled 'PLL / ENFOL', and is based on the PLL output spectrum shown in Fig. 7.23b divided by the ENFOL spectrum of Fig. 7.24b.

Similarly, the ENFOL data shown in Fig. 7.32 are based on a 20 nm thick layer of unexposed AZ 1518 photoresist, $\epsilon_{r,AZ1518} = 2.933 - 0.1226i$, with no mask considered for

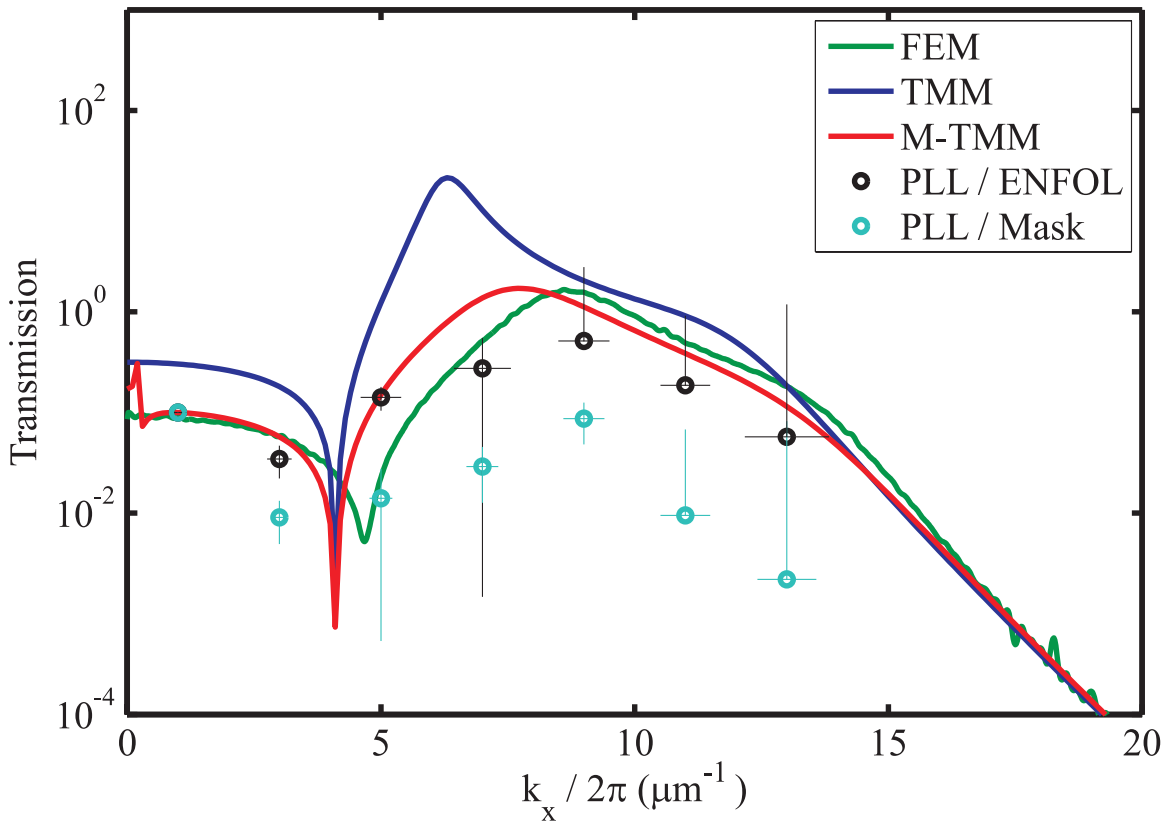

Figure 7.31: Transfer functions for a 20:40:20 nm PVA:Ag:PVA superlens, calculated from TMM (blue), M-TMM (red) and FEM (green) simulations. Also shown are experimental TFs for the same superlens, measured with respect to a mask depth profile (cyan) and an ENFOL profile (black).

the TMM model, a solid W mask in the M-TMM model, and a single 10 nm feature W:air mask in the FEM simulation. Note that in this case, there is no difference in the TFs predicted by TMM and M-TMM. The 20 nm thickness in the models is chosen to match the average depth of the ENFOL line spectra shown in Fig. 7.11. The experimental data, labelled 'ENFOL / Mask' in Fig. 7.32, is based on the ratio of the ENFOL output spectrum shown in Fig. 7.24b to the 1 μm period mask depth spectrum of Fig. 7.25b.

The comparison in Fig. 7.31 reveals that the measured 'PLL / ENFOL' TF is in good quantitative agreement with the predictions made by M-TMM at nominal wavenumbers up to 5 μm^{-1}. In particular, the coefficients at 5 μm^{-1} are beyond the diffraction limit of 365 nm wavelength light, which indicates that this analysis is useful in both the propagating and evanescent parts of the spectrum. In contrast, coefficients between 5 μm^{-1} and 13 μm^{-1} are slightly attenuated relative to the M-TMM and FEM

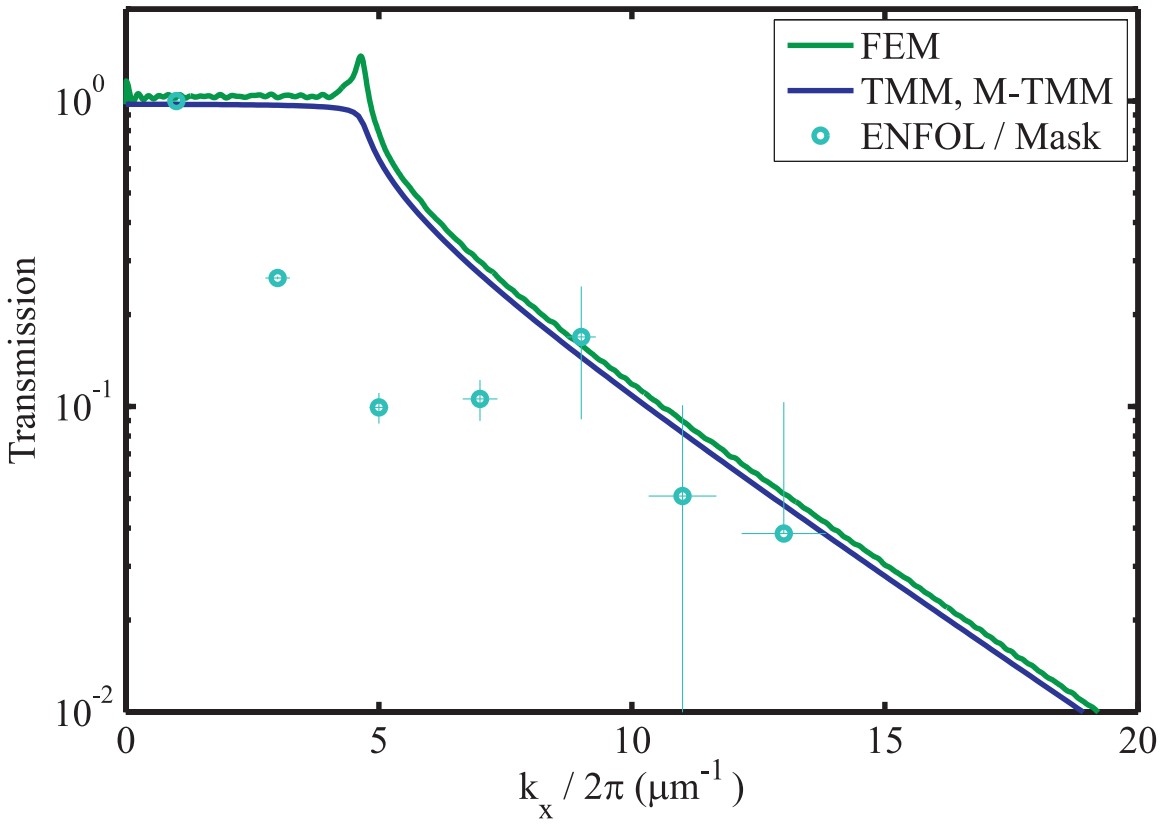

Figure 7.32: Transfer functions for an ENFOL lithography system, calculated from TMM and M-TMM (blue), and FEM (green) simulations. Also shown is an experimental TFs for the same system, measured with respect to a mask depth profile (cyan).

models. This is most probably due to the non-zero roughness of the Ag and dielectric layers, which is likely to retard the plasmon resonance and subsequent evanescent enhancement of the superlens [28]. Given this attenuation due to roughness, the rate of decay of transmission for coefficients between 9 $\mu\mathrm{m}^{-1}$ and 13 $\mu\mathrm{m}^{-1}$ is consistent with that predicted by both M-TMM and FEM, once the lower peak transmission is taken into account. This suggests that the material property parameters used in these models and given earlier in Chapters 3 and 5 are valid; it also validates the M-TMM model and confirms its superiority over TMM as a technique for modelling practical superlens lithography experiments.

Lastly, the 'PLL / Mask' curve shown in Fig. 7.31 has considerably lower transmission coefficients than the similar 'PLL / ENFOL' curve. The reason for this is that the response of the photoresist, which decreases with increasing spatial frequency, is inherently included in the PLL spectrum but not in the mask spectrum. This same underestimation of transmission coefficients is seen in the experimental 'ENFOL / Mask' curve shown in Fig. 7.32. This confirms that the response of the photoresist plays a significant role in these experiments and that TF coefficients calculated from a mixture of resist and mask spectra need to be compensated to correctly report transmission.

7.6 Summary

Protocols laid out in Chapter 6 were used in this chapter to perform nanolithography experiments. The resulting measurements of photoresist films showed effects of plasmon resonance, which is a prerequisite for superresolution. This validated the methods described in Chapter 6 as suitable for their intended purpose.

Analyses of experimental data were also performed in the spatial frequency domain, where two different mask designs were used to find the TFs for PLL and ENFOL systems. Although the larger, 10 μm period grating mask was found to be a poor choice for characterisation in the spatial frequency domain, the smaller, 1 μm period grating mask gave results that revealed the desired TFs for both PLL and ENFOL systems. These TFs compared favourably to modelled data, even confirming the improved accuracy of the M-TMM technique over the TMM technique.

Although the results presented in this chapter were all generally positive, it should be noted that the conclusions presented here are based on only a limited number of experimental samples; this means that they should be treated as preliminary results until further evidence is provided to confirm their validity. The reason for this small ensemble of results is that further data gathering was hindered by a series of large earthquakes that hit Christchurch between September 2010 and February 2011 [175], culminating in the closure of the nanofabrication facilities at the University of Canterbury for two weeks in September 2010 and six weeks in early 2011. Although this disruption meant that more definitive data could not be generated before the submission deadline of this thesis, the full validation of the methods presented here is nevertheless expected in the fullness of time.

Chapter 8

Conclusion

The results presented in this thesis include a comprehensive set of performance metrics for the characterisation of imaging systems, with particular emphasis on behaviour in the evanescent regime. The calculation of these metrics was based on analytical techniques, which were validated against full-field vector simulations to ensure accuracy. A series of experiments were also performed to measure the transfer functions of selected ENFOL and PLL imaging systems from AFM micrographs. This was a novel approach that, to the best of the author's knowledge, had not been attempted in the past. The experimental results showed good agreement with theoretical data and added further validation to the analytical methods that were used to calculate performance metrics. A summary of these findings is given in this chapter, before a brief discussion of possible future applications and challenges faced by silver-based superlenses.

8.1 Analytical Characterisation of Near-Field Imaging Systems

Transfer matrix modelling (TMM) was used to calculate transfer functions (TFs) for a number of different planar imaging technologies, including evanescent near-field optical lithography (ENFOL) and a range of different planar lensing lithography (PLL)-based systems. From these TFs a set of metrics were derived, which characterised the

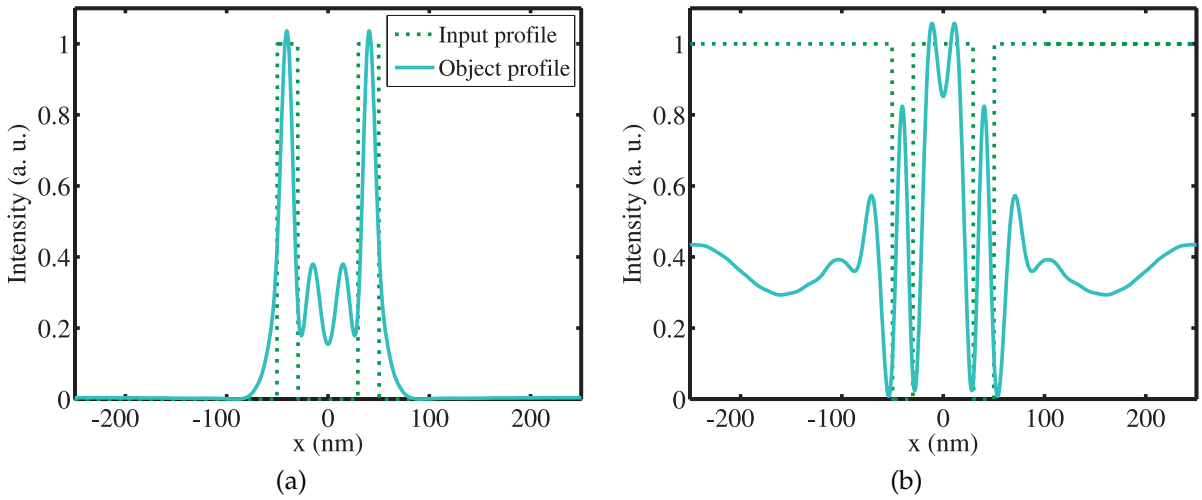

Figure 8.1: Input (dotted) and output (solid) profiles for an 80 nm thick superlens composed of eight 5 nm Ag layers, first shown in Fig. 4.1, exposed to a mostly dark (a) and mostly bright (b) mask comprising two 20 nm features with 100 nm centre-to-centre spacing.

performance of a system both in general terms and for specific input profiles. The more specific metrics, called object-lens metrics, assessed the suitability of imaging systems for a given application and revealed that superlenses, in particular, have highly variable performance, which depends strongly on the type of object profile that is being imaged. An example of this variability in performance for relatively similar input profiles is shown in Fig. 8.1, where two objects with identical spectral content but different DC components produce vastly different output profiles.

One of the causes of this variability in performance was a mismatch between DC or low spatial frequency transmission in the propagating domain and the evanescent enhancement seen beyond the diffraction limit. The relationship between these two properties was best expressed by the bandwidth metric, which returned higher values when the propagating transmission of a system was closely matched to peak transmission in the evanescent domain. The benefit of the bandwidth metric was that it could be calculated without consideration of any input profile, making it a lens-specific metric with wide application.

The characterisation results calculated with TMM were compared to full field vector simulations carried out via FEM. These FEM simulations showed only qualitative agreement with the TMM data, with higher peak transmission spatial frequencies and

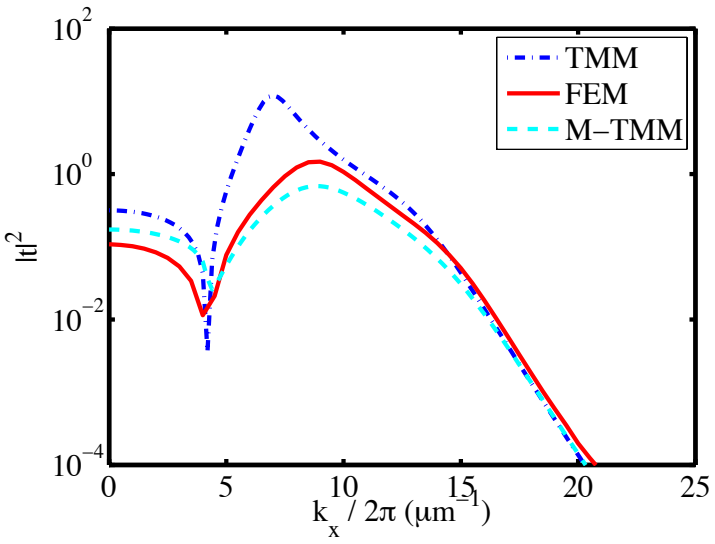

Figure 8.2: Transfer functions calculated from TMM (dot-dashed), M-TMM (dashed) and FEM (solid) simulations for a 20:40:20 nm SiO_2:Ag:SiO_2 superlens exposed to a 50 nm thick W mask, patterned with a 1 μm period, 50% duty cycle grating. The M-TMM curve, which approximates the mask with a solid W slab, provides a better match to the full-vector FEM solution than the TMM curve does.

lower peak transmission coefficients predicted by FEM. the reason for this was that the TMM technique does not take account of near-field interactions between a superlens and the mask that is supplying it with an object profile. The severity of this shortcoming was lessened by a modification to the TMM technique, known as M-TMM, which incorporated the mask into the TMM calculations by approximating it as a solid slab. An example of the improved TFs calculated by M-TMM is shown in Fig. 8.2, with TMM- and FEM-generated TFs included for comparison. In theory, the results returned by M-TMM would be most accurate for masks with very high duty cycle, where the approximation of the mask to a solid slab was the most realistic. However, improved results were seen from M-TMM over TMM even for masks with 50% duty cycle, as shown in Fig. 8.3, suggesting that M-TMM is an important improvement over TMM that is applicable in a wide range of applications.

Lastly, TMM and M-TMM were used to explore the effects of increased layer thickness and repeated laminated structures in superlens designs; data from both techniques confirmed that performance does not always increase as layer thicknesses shrink, nor as the number of laminations increases. For instance, for a PMMA:Ag:SiO_2 superlens modelled via M-TMM, optimum results were found for Ag thicknesses between 50 nm

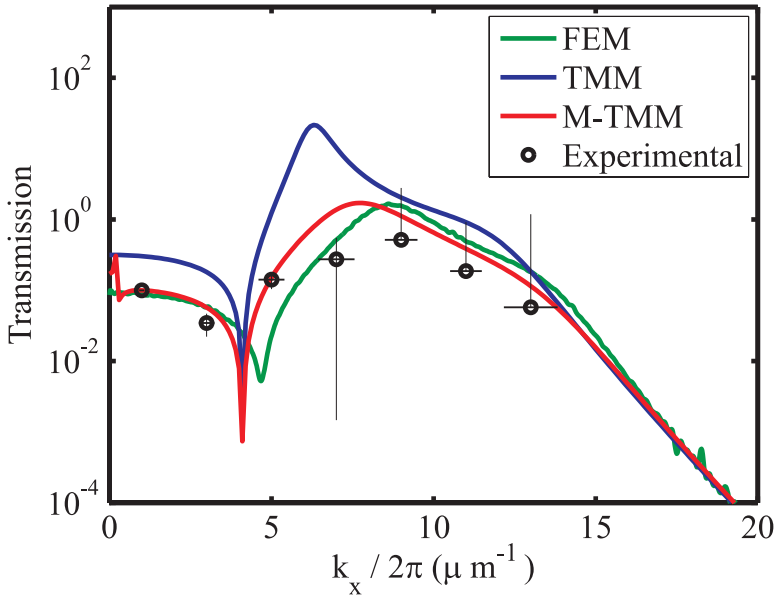

Figure 8.3: Transfer functions calculated from TMM (dotted), M-TMM (dashed) and FEM (solid) simulations and from experimental data (dot-dashed) for a 20:40:20 nm PVA:Ag:PVA superlens exposed to a 50 nm thick W mask, patterned with a 1 μm period, 50% duty cycle grating. The M-TMM curve, which approximates the mask with a solid W slab, provides a better match to the experimental results and full-vector FEM solution than the TMM curve does, even though the duty cycle of the mask is only 50%.

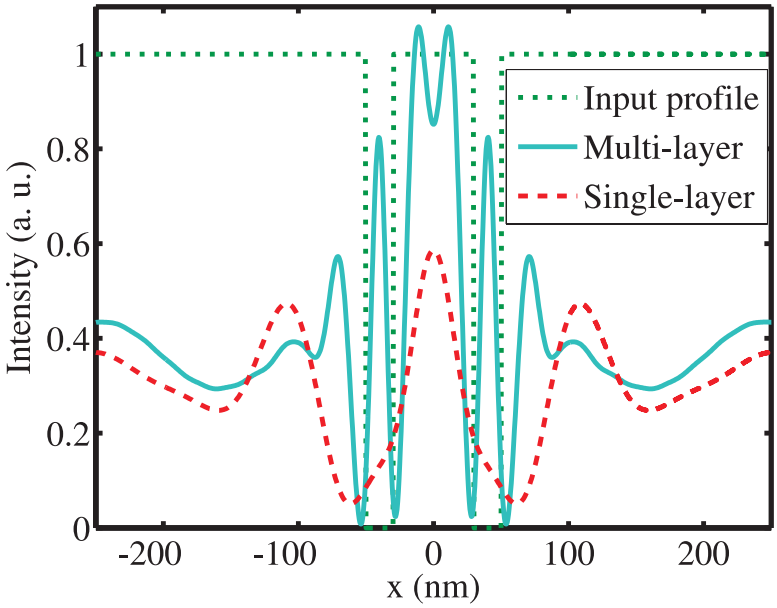

Figure 8.4: Output profiles for single-Ag layer (dashed) and multi-Ag layer (solid) superlenses exposed to a mostly bright mask (dotted) composed of two 20 nm features with 100 nm centre-to-centre spacing. This figure is reproduced from Fig. 4.1b.

and 70 nm, with individual dielectric thicknesses set from 10 nm to 30 nm, rather than at lower Ag thicknesses of 30 nm or less. Similarly, changing from a single-Ag layer design to a laminated, multi-Ag layered design did not always improve performance, as shown in Fig. 8.4.

8.2 Experimental Characterisation of Near-Field Imaging Systems

The accuracy of the TMM, M-TMM and FEM models was tested experimentally by developing a system to directly measure the TFs of PLL and ENFOL systems. Averaged line profiles were taken from AFM data, which were then converted to the spatial frequency domain and combined to give practical transfer functions for the systems under consideration. Although the recovered TFs were somewhat noisy and of limited resolution, the trends that they contained were strong enough to provide good qualitative and quantative agreement with modelled data.

One of the important innovations that allowed the determination of these results was the addition of a flexible layer of PDMS in the resist stack, between the substrate and ARC layer. This polymer absorbed strain introduced between the mask, superlens and resist and eliminated the incidence of broken masks, which was an obstacle experienced in previous PLL and ENFOL experiments [7]. A further improvement was the use of large period, micron-scale grating masks to facilitate the measurement of TFs from ENFOL and PLL systems. By measuring step responses rather than impulse responses, the manufacturing constraints on the masks were greatly reduced and a greater amount of time was allowed for the optimisation of the exposure and development protocols, which were essential to capture sub-wavelength features in the resist stacks.

The resulting TFs, which were derived from experimental data produced with these masks, were consistent with the FEM and M-TMM TFs. A small degree of attenuation was noted in the experimental TFs at evanescent wavenumbers; this was likely due to the surface roughness of the Ag and dielectric films, which was already known to limit superlens performance [28]. Nevertheless, the experimental data provided convincing affirmation for the use of M-TMM over TMM, which was one of the goals of the experimental work undertaken in this thesis.

Despite the success of the experimental data in confirming the accuracy and usefulness of M-TMM and FEM over TMM, there were several factors that limited the efficacy of the practical results. Firstly, the response of the AZ 1518 photoresist was identified as a limiting factor in the performance that is achievable from near-field experiments. An example of the effect that the photoresist response has on experimental results is shown in Figs. 8.5a and 8.5b, where the measured TFs of separate ENFOL and PLL systems have much greater attenuation than expected. The attenuation in these figures is due to the way the TFs were calculated: the image profiles, which were captured in AZ 1518 photoresist and were thus affected by the spatial frequency response of the resist, were compared to object profiles taken directly from a W mask, which were not distorted by the resist. When the response of the resist is included in both the image and object profiles, as was done in Fig. 8.5c, the resulting TF has much less attenuation and resembles theoretical results much more closely.

Secondly, only a handful of transmission coefficients were able to be measured for each imaging system. This was due to the spacing of the harmonics in the spectra of the

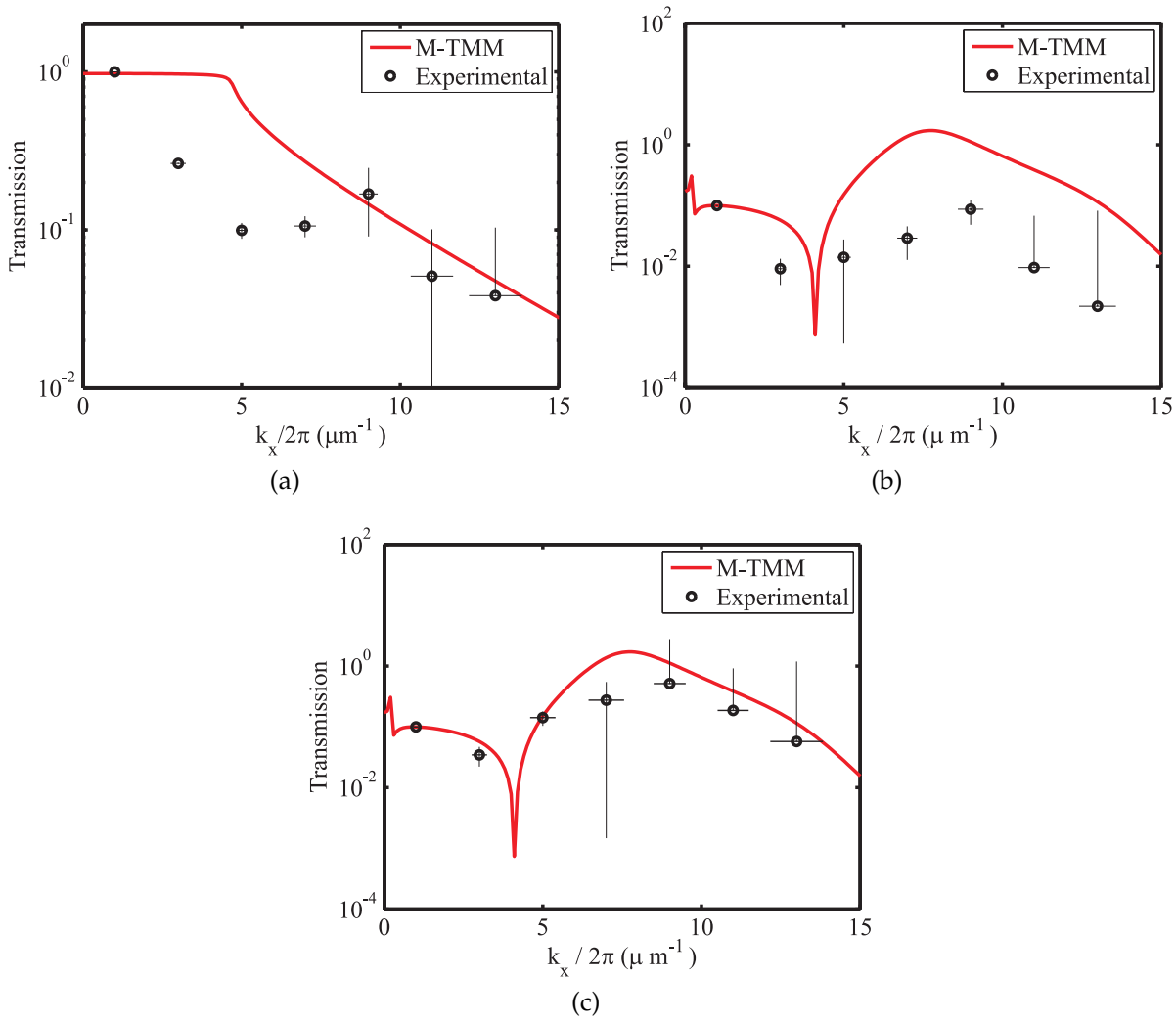

Figure 8.5: Transfer functions measured from experimental data (solid) and predicted by M-TMM (dashed) for an ENFOL process with image plane situated 20 nm into the photoresist layer (a) and a 20:40:20 nm PVA:Ag:PVA superlens (b, c). The measured TFs in (a) and (b) are attenuated relative to the predicted curves, due to the non-ideal response of the photoresist. This distortion is not present when the ratio of the PLL and ENFOL spectra is calculated, as the effects of the resist in both profiles cancel each other out.

1 μm period masks. These occurred only at whole wavenumbers, which meant that fine detail around the conventional diffraction limit was lost from the reconstructed TFs. Although 10 μm period masks that had more closely spaced harmonics were used in initial experiments, these proved to have too limited a range in the spatial frequency domain and were not suitable for capturing sub-wavelength transmission coefficients. No doubt a similar mask design, based perhaps on a 2 μm or 3 μm period grating, will yield more expansive results in the future.

8.3 Outlook

Despite the limitations discussed in the previous section, the experimental results presented in this thesis shed new light on the behaviour of practical sub-wavelength imaging systems and are an improvement over the information that was previously available about such systems. Similarly, the analytical and simulation data have revealed trends and characteristics that were not previously evident. Given this new data and the increased understanding that they offer on the subject of superlensing and near-field lithography, the question arises as to possible uses of superlenses in the commercial integrated circuit manufacturing industry. Although the future is notoriously hard to predict for such an innovative and fast-moving sector of the global economy, three points stand out as issues that will need to be addressed before superlenses can take a place in the ITRS.

The first of these points to note is that techniques like PLL and ENFOL, by their nature, require contact or near contact between different components in the imaging stack. This results in increased mask contamination and wear, which is incredibly unattractive to the semiconductor industry and makes ENFOL and, by extension, PLL, unlikely candidates for wide-scale adoption. An interesting example relating to this fact stems from 2006, when a group from Canon inc. showed that the ENFOL process could be optimised to produce 32 nm half pitch features from 365 nm wavelength light [19, 29], a result which would give a truly impressive 17 nm feature size if scaled down to 193 nm wavelength or even 14 nm if scaled to 157 nm. Despite the fact that these minimum feature sizes are well within the requirements of the 22 nm node that is currently in use today [4], they generated little commercial interest and the techniques used to fabricate them were not put to commercial use.

The second point worthy of discussion is the wavelength at which PLL operates. PLL, or any other technology relying on silver-based superlenses, is likely to use wavelengths at or above 365 nm, since this is the commercially available wavelength that is closest to the wavelength where the magnitude of the relative permittivity of Ag is in the range of lithographically useful dielectrics such as PMMA, SiO_2, PVA and most commercial photoresists. Even with the best reported results of $\lambda/12$ [24], this relatively large wavelength means that minimum feature sizes are of the order of 30 nm, which is above the current industry standard of 22 nm. If superlenses were to be used for commercial applications that required sub-30 nm features, it is highly likely that an alternative material to Ag would have to be found. One possible replacement is aluminium (Al), which displays favourable properties around 193 nm wavelength [176], coinciding with the primary wavelength emitted by ArF excimer lasers. Despite this shorter operating wavelength, Al has much greater absorbance than Ag and further work is required before it can be acclaimed as a worthy replacement for the noble metal.

Thirdly, any practical uses for Ag superlens systems are likely to be held back by the requirement for ultra-high resolution resists that are sensitive at 365 nm. Unfortunately, the resists that were developed when 365 nm was used as an industry standard wavelength were not designed for low-nanometre feature sizes, hence there is considerable degradation of such resists at higher spatial frequencies. Future improvements to Ag superlens performance will no doubt hinge on the introduction of novel, high resolution photoresists that are sensitive at 365 nm. One interesting development in this area is the use of UV-curable glues as high-resolution i-line photoresists [23, 24]. Although subwavelength patterns have been recorded in such media, it remains to be seen whether these features can be successfully transferred from the glue into subsequent layers, as is necessary for a fully functional thin film fabrication process.

In terms of other research opportunities and applications outside of commercial lithography, exciting possibilities include adapting superlenses for use with near-field scanning microscopy [177]. This novel microscopy technique relies on sampling the near-field of an object with an optical probe to achieve sub-wavelength resolution. The evanescent enhancement provided by Ag superlenses may well be beneficial in this setting, allowing even greater resolution from fixed wavelengths.

A second possible application for superlenses involves imaging sub-wavelength, periodic features from super-wavelength scale mask patterns. A similar concept was shown using an ENFOL-style process [56, 166], where sub-100 nm features were successfully imaged from the near-field intensity variations produced by micron-scale phase masks. Given the process described in Chapter 6 for capturing evanescent intensity variations in photoresist, this application would appear to be a natural progression for the work described in this thesis.

8.4 Summary

Only time will tell if superlenses are to play a large part in the evolution of technology in the twenty-first century. In terms of scientific discoveries, they were a brilliant solution [20] to a challenge that had stumped scientists for more than 30 years [36]. Their practical implementation by two independent groups in 2005 [22, 23] was a tour de force in wrestling cutting-edge performance from i-line lithographic tools that had long before passed from the attention of the most prominent academic and industrial circles. The results presented in this thesis complement these initial experimental works by providing a detailed characterisation of superlens behaviour, uncovering along the way features that were not immediately noted in the excitement following Pendry's initial proposal. Regardless of whether superlenses ever play a practical part in the battle to shrink feature sizes and increase component densities, the quirks of their unorthodox behaviour are now better known than ever before.

Appendices

Appendix A

Transfer Matrix Model Implementation

The source code used to implement the transfer matrix modelling (TMM) technique is presented here, for ease of reference and to aid future validation of the results presented in this thesis. The code was written as a series of script ($.m$) files, interpreted by Matlab. Generated figures were saved manually in encapsulated postscript format and were converted to portable document format either via CorelDRAW or with Mac OS X's pstopdf command line tool.

The main script file, $TMM.m$, contains code that governs the scale and scope of the TMM simulations, as shown in Listing A.1. The file can be divided roughly into four parts: firstly, the definition of constants that determine which simulations are run and under what conditions. Secondly, the construction of the T-matrices themselves, which are handled through calls to $addMedium.m$ and $addInterfaces.m$, shown in Listings A.2 and A.3. Thirdly, input profiles are constructed using any one of $addSource.m$, $addSquare.m$ or $addDelta.m$, shown in Listings A.4, A.5 and A.6. These input profiles are processed through the T-matrices, the results of which are used by $getStats.m$, shown in Listing A.7, to calculate characterisation metrics. Lastly, $TMM.m$ generates figures of the calculated metrics by calling the $plot$ family of functions, given in Listings A.8 to A.16.

Listing A.1: TMM.m

```
1 % TMM.m
2 % T-Matrix script file
3 % by C. P. Moore
4 % 10-10-2007
5 %
6 % DEPENDENCIES
7 % Generate lens stacks:
8 % addMedium.m
```

```
% addInterfaces.m
%
% Generate mask data:
% addSource.m, addSquare.m, addDelta.m
%
% Characterise lenses:
% getStats.m
%
% Display results:
% plotContrast.m, plotPC.m, plotError.m, plotCC.m, plotRF.m, plotTF.m,
% plotPF.m, plotTF_prime.m, plotPF_prime.m
% publishPlot.m
%

tic % Start timer - useful for identifying slow sections of code.

% clear all;
% close all;
% clc;

% #DEFINEs
% Define global constants.  Repeat the 'global constName' command in any
% file that uses the constants. (eg. getStats.m)
global constants;
constants.TRUE  = 1;
constants.FALSE = 0;
constants.SMALL_NUM = 1e-9;    % Non-zero value used to prevent truncation
                               % of trailing zeroes in arrays.
constants.NM_PER_M = 1e9;

%%%%%%%%%%%%%%%%%%%%%%%%%%%  CONTROL PARAMETERS.  %%%%%%%%%%%%%%%%%%%%%%%%%%%%


%%%%%%%%%%%%%%%%%%  DATA PARAMETERS.  TRUE = 1, FALSE = 0.   %%%%%%%%%%%%%%%%%%
% Generate Data:
constants.DATA  = constants.TRUE;
% Save Data:
constants.SAVE = ~constants.TRUE;

% Number of times to iterate through lens-generation code:
constants.BATCHES = 1;

% Lenses:
constants.LENSES = constants.TRUE;
constants.LENS1  = constants.TRUE;
constants.LENS2  = ~constants.TRUE;
constants.LENS3  = ~constants.TRUE;

% Lens labels:  No spaces allowed, as these double as the filenames for
% saving the raw data.
constants.LENS1_label = 'Experimental';
constants.LENS2_label = 'Single-layer';
constants.LENS3_label = 'Multi-layer';

% Local data path:
constants.PATH = 'Data/'; % Include trailing slash

% Use optimised (t') input profiles?
constants.REFLECT = constants.TRUE;
% Mask-reflection data path:
constants.REFLECT_PATH = 'Data/r_Mask/512/';
constants.REFLECT_MODEL = 'r_W';
% constants.REFLECT_MODEL = 'r_NiCr';

% Input profiles:
constants.INPUT = ~constants.TRUE;
constants.SD    = ~constants.TRUE;    % Single dark slit
constants.SB    = ~constants.TRUE;    % Single bright slit
constants.DD    = ~constants.TRUE;    % Dual dark slit
constants.DB    = ~constants.TRUE;    % Dual bright slit
constants.PP    = ~constants.TRUE;    % Periodic pattern
constants.RAMAKRISHNA_IP = ~constants.TRUE; % Two slits, 20 nm wide, 80 nm
                                            % apart.

```

```
% Results for constants.SPATIAL slit width (nm) are shown in the spatial
% domain.
% Enter constants.FALSE to bypass.
constants.SPATIAL   = 100; % 75; % 135;

% Model parameters:
%%%  NB:The following constants must all be > 0:  %%%
constants.MIN_PERIODS        = 5;    % Minimum number of complete periods
                                     % to simulate.
constants.PATTERN_PERIOD_MIN =  1;    % nm
constants.PATTERN_PERIOD_MAX =  2500; % nm
constants.lambda = 365;       % (nm) Wavelength of exposing radiation.
constants.LAMBDA_MIN = 10000;  % (nm).  Size of input pattern.
                               % Increase to increase resolution in TF'ns.
                               % Decrease to increase speed.

% Ag permittivity values:
constants.MELVILLE      = constants.TRUE;
constants.RAMAKRISHNA   = ~constants.TRUE;
constants.PENDRY        = ~constants.TRUE;
constants.PERFECT       = ~constants.TRUE;

%%%%%%%%%%%%%%%%%%%%%%%%%% DISPLAY PARAMETERS %%%%%%%%%%%%%%%%%%%%%%%%%%%%%
% Display results:
% Note: indentation of constants denotes relative order in program flow.
constants.DISPLAY = constants.TRUE;
constants.K0_PLOTS = ~constants.TRUE;      % Display TF'ns with k0 scale,
                                           % cf. k_x/2pi.
    constants.RF        = ~constants.TRUE;
    constants.RF_PRIME  = ~constants.TRUE; % r' = r_L * r_M *
                                           % e^(2 * i * k_z * d);
    constants.TF        = constants.TRUE;  % Magnitude transfer function
    constants.PF        = ~constants.TRUE; % Phase transfer function
    constants.TF_PRIME  = constants.TRUE; % Modified magnitude TF:
                                           % abs(t / (1 - r')).
    constants.PF_PRIME  = ~constants.TRUE; % Modified phase TF:
                                           % arg(t / (1 - r')).

    % Statistics:
    constants.STATS = ~constants.TRUE;
        constants.CONTRAST  = constants.TRUE;
        constants.PC        = constants.TRUE;
        constants.ERROR     = constants.TRUE;
        constants.CC        = constants.TRUE;

%%%%%%%%%%%%%%%%%%%%%%%%%  END OF CODE PARAMETERS.  %%%%%%%%%%%%%%%%%%%%%%%%%

% k0 and ks both relate to wave-number values.
constData.k0 = 2 * pi / constants.lambda;
constData.ks = 2 * pi * 1e6 * 1e-9;  % x-scale is: kx / 2 * pi (1/um), wave units
% are in nm.

% constants.LAMBDA = Sample length (nm). Affects spatial-domain resolution.
% constants.N = # Data points used in FFT. Affects frequency-domain res'n.
% Seems to work best for constants.N = 2 * constants.LAMBDA, regardless of
% the size of constants.LAMBDA (above, say, 10K?)
if (constants.SB || constants.SD),
    % Single-slit values:
    constants.LAMBDA = 20000;
elseif (constants.DD || constants.DB || constants.RAMAKRISHNA_IP),
    % Dual-slit values:
    constants.LAMBDA = 30000;
elseif constants.PP,
    % Periodic pattern values:
    constants.LAMBDA = constants.MIN_PERIODS * constants.PATTERN_PERIOD_MAX;
else
    constants.LAMBDA = constants.LAMBDA_MIN;
end
% Check that constants.LAMBDA is of sufficient size to give good resolution
% in TF'ns.
if constants.LAMBDA < constants.LAMBDA_MIN,
    constants.LAMBDA = constants.LAMBDA_MIN;
end
constants.N = 1024; % * 2; % + 1;
```

```
157
158 % Define transfer function parameters:
159 MAX_K = (constants.N / 2 - 1) * 2 * pi / constants.LAMBDA;
160 MIN_K = -(constants.N / 2) * 2 * pi / constants.LAMBDA;
161 constData.RESOLUTION = 2 * pi / constants.LAMBDA;
162 constData.kx = MIN_K:constData.RESOLUTION:MAX_K;
163
164 % Define size of TF array:
165 constData.t = zeros(1, constants.N);
166 % Initialise statistics structure:
167 constData.statistics.Mcontrast = 0;
168
169 % Choose material permittivity values:
170 if constants.MELVILLE,
171     eAg = -2.7 + 0.23i;
172 elseif constants.RAMAKRISHNA,
173     eAg = -1 + 0.4i;
174 elseif constants.PENDRY,
175     h = 6.63 * 10^-34;
176     e_charge = 1.6 * 10^-19;
177     c = 3.0 * 10^8;
178     f = c / constants.lambda;
179     E = h * f;
180     omega = E / e_charge;              % (omega in eV).
181     eAg = 5.7 - 9^2 * omega^-2 + 0.4i; % (-1.2830 + 0.4i @ 365nm.
182                                        % Similar to Ramakrishna).
183 elseif constants.PERFECT,
184     eAg = -1;
185 end;
186 eAgM = -2.7 + 0.23i;
187 eAgSim = -1.05 + 0.001i;
188 eAgPalik = -2.564 + 0.6i;
189 % ePMMA = 2.3013 + 0.0014i;
190 ePMMA = 2.3104;
191 eSiO2 = 2.368;
192 eResist = 2.79;
193 eVacuum = 1;
194 eW = 1.497 + 7.69i;
195 eSi = 34.387 + 37.73i;
196 eNiCr = -2.923 + 8.495i;
197 e123lossless = 2.7291;
198 e123exp = 2.7291 + 0.0033i;
199 e123unexp = 2.7285 + 0.0793i;
200 e1518exp = 2.888 + 0.0197i;
201 e1518unexp = 2.933 + 0.1226i;
202 ePVA = 2.25; % 1.819;
203 % Lee et al.'s values at 11um:
204 eSiO2_11 = 3.71 + 0.16i;
205 eSiC_11 = -3.71 + 0.23i;
206
207 %%%%%%%%%%%%%%%%%%%%%%%%%%%%%%%%   Create Lenses   %%%%%%%%%%%%%%%%%%%%%%%%%%%%%%%%
208 if constants.DATA,
209     if constants.LENSES,
210         % Load mask reflection profile:
211         if constants.REFLECT,
212             load(strcat(constants.REFLECT_PATH, constants.REFLECT_MODEL, '.mat'));
213             constData.r_Mask = eval(constants.REFLECT_MODEL);
214         end
215
216         for batch_ctr = 1:constants.BATCHES,
217             status = strcat('Generating lens # ', int2str(batch_ctr));
218             disp(status);
219
220             if constants.LENS1,
221                 % Initialise variables:
222                 lens1Data = constData;
223                 lens1Data.label = constants.LENS1_label;
224                 lens1.num_layers = 0;
225                 % Generate superlens stacks:
226 %                 lens1 = addMedium(e1518unexp, 1, 0, lens1);
227 %                 lens1 = addMedium(e1518unexp, 1, 20, lens1);
228 %                 lens1 = addMedium(e1518unexp, 1, 0, lens1);
229
230                 lens1 = addMedium(ePVA, 1,   0,     lens1);
```

```
231                 lens1 = addMedium(ePVA, 1,  20,     lens1);
232                 lens1 = addMedium(eAg,  1,  40,     lens1);
233                 lens1 = addMedium(ePVA, 1,  20,     lens1);
234                 lens1 = addMedium(ePVA, 1,   0,     lens1);
235 %                 lens1 = addMedium(e1518unexp, 1,   20,     lens1);
236 %                 lens1 = addMedium(e1518unexp, 1,   0,     lens1);
237                 lens1Data = addInterfaces(lens1, lens1Data);
238                 % Measure bandwidth:
239             end
240             if constants.LENS2,
241                 lens2Data = constData;
242                 lens2Data.label = constants.LENS2_label;
243                 lens2.num_layers = 0;
244                 lens2 = addMedium(ePMMA, 1,   0,     lens2);
245                 lens2 = addMedium(ePMMA, 1,  20,     lens2);
246                 lens2 = addMedium(eAg,   1,  40,     lens2);
247                 lens2 = addMedium(eSiO2, 1,  10,     lens2);
248                 lens2 = addMedium(eSiO2, 1,   0,     lens2);
249                 lens2Data = addInterfaces(lens2, lens2Data);
250             end
251             if constants.LENS3,
252                 lens3Data = constData;
253                 lens3Data.label = constants.LENS3_label;
254                 lens3.num_layers = 0;
255                 lens3 = addMedium(ePMMA, 1,   0,     lens3);
256                 lens3 = addMedium(ePMMA, 1, 2.5,     lens3);
257                 lens3 = addMedium(eAg,   1,   5,     lens3);
258                 lens3 = addMedium(ePMMA, 1,   5,     lens3);
259                 lens3 = addMedium(eAg,   1,   5,     lens3);
260                 lens3 = addMedium(ePMMA, 1,   5,     lens3);
261                 lens3 = addMedium(eAg,   1,   5,     lens3);
262                 lens3 = addMedium(ePMMA, 1,   5,     lens3);
263                 lens3 = addMedium(eAg,   1,   5,     lens3);
264                 lens3 = addMedium(ePMMA, 1,   5,     lens3);
265                 lens3 = addMedium(eAg,   1,   5,     lens3);
266                 lens3 = addMedium(ePMMA, 1,   5,     lens3);
267                 lens3 = addMedium(eAg,   1,   5,     lens3);
268                 lens3 = addMedium(ePMMA, 1,   5,     lens3);
269                 lens3 = addMedium(eAg,   1,   5,     lens3);
270                 lens3 = addMedium(ePMMA, 1,   5,     lens3);
271                 lens3 = addMedium(eAg,   1,   5,     lens3);
272                 lens3 = addMedium(eSiO2, 1, 2.5,     lens3);
273                 lens3 = addMedium(eSiO2, 1,   0,     lens3);
274                 lens3Data = addInterfaces(lens3, lens3Data);
275             end
276             toc
277         end
278     end
279     %%%%%%%%%%%%%%%%%%%%%%%   Generate Input Pattern   %%%%%%%%%%%%%%%%%%%%%%%
280     % Default parameter values:
281     duty_cycle = 1; % (nm/nm)  Set to 1 for non-periodic patterns.
282     dc_offset = 0;
283     ph_offset = 0;
284     ampl = 1;
285     num_peaks = 1;
286     limit_max = 10;
287     limit_min = -10;
288
289     if (constants.SB || constants.DB || constants.PP),
290         % Bright-slit values:
291         % As per default.
292     elseif (constants.SD || constants.DD),
293         % Dark-slit values:
294         dc_offset = 1;
295         ampl = -1;
296     end
297     if constants.PP,
298         duty_cycle = 0.5;
299         dc_offset = 0.5;
300         ampl = 1;
301         %wave_shape = 'shifted_square';
302         %duty_cycle = 0.25;
303     end
304
```

```
305     %%%%%%%%%%%%%%%%%%%%%%%%%%%%%%%   Main Loop:   %%%%%%%%%%%%%%%%%%%%%%%%%%%%%%%
306     if constants.INPUT,
307         disp('Calculating results and statistics.');
308         for pattern_period = constants.PATTERN_PERIOD_MIN:constants.PATTERN_PERIOD_MAX,
309             samples_per_period = constants.N / constants.LAMBDA * pattern_period;
310             samples_per_nm = constants.N / constants.LAMBDA;
311
312             % Input pattern:
313             if (constants.SB || constants.SD),
314                 ip_TM = addDelta(ampl, dc_offset, num_peaks, constants.N / constants.LAMBDA * pattern_period, constants.N);
315             elseif (constants.DB || constants.DD),
316                 ip_TM = addSource('dualslits', ampl, dc_offset, limit_max, limit_min, pattern_period, duty_cycle, constants.
                        LAMBDA, constants.N);
317 %                 ip_TM = addSource('dualslits', ampl, dc_offset, limit_max, limit_min, pattern_period, duty_cycle, constants
        .N / constants.LAMBDA * pattern_period, constants.N);
318             elseif constants.PP,
319                 ip_TM = addSquare(ampl, dc_offset, ph_offset, constants.N / constants.LAMBDA * pattern_period, constants.N);
320 %                 ip_TM = addSine(ampl, dc_offset, ph_offset, constants.N / constants.LAMBDA * pattern_period, constants.N);
321             elseif constants.RAMAKRISHNA_IP,
322                 disp('RAMA');
323 %                     ip_TM(1, constants.N) = constants.SMALL_NUM;
324 %                     ip_TM(1, (constants.N / 2 - 60 * samples_per_nm):(constants.N / 2 - 40 * samples_per_nm)) = 1;
325 %                     ip_TM(1, (constants.N / 2 + 40 * samples_per_nm):(constants.N / 2 + 60 * samples_per_nm)) = 1;
326 % NB: test_vec replaced with ip_TM!!!!!
327                 disp('Using ip_TM.');
328                 test_vec_gen;
329             end
330
331
332             % Generate output patterns & calculate their statistics:
333             if constants.LENS1,
334                 if constants.REFLECT,
335                 lens1Data.result = ifft(lens1Data.tprime .* fftshift(fft(ip_TM)));
336                 else
337                     lens1Data.result = ifft(lens1Data.t .* fftshift(fft(ip_TM)));
338                 end
339                 if constants.STATS,
340                     lens1Data.statistics = getStats(abs(ip_TM).^2, abs(lens1Data.result).^2, pattern_period, lens1Data.
                            statistics);
341
342                 end
343             end
344             if constants.LENS2,
345                 if constants.REFLECT,
346                     lens2Data.result = ifft(lens2Data.tprime .* fftshift(fft(ip_TM)));
347                 else
348                     lens2Data.result = ifft(lens2Data.t .* fftshift(fft(ip_TM)));
349                 end
350                 if constants.STATS,
351                     lens2Data.statistics = getStats(abs(ip_TM).^2, abs(lens2Data.result).^2, pattern_period, lens2Data.
                            statistics);
352                 end
353             end
354             if constants.LENS3,
355                 if constants.REFLECT,
356                     lens3Data.result = ifft(lens3Data.tprime .* fftshift(fft(ip_TM)));
357                 else
358                     lens3Data.result = ifft(lens3Data.t .* fftshift(fft(ip_TM)));
359                 end
360                 if constants.STATS,
361                     lens3Data.statistics = getStats(abs(ip_TM).^2, abs(lens3Data.result).^2, pattern_period, lens3Data.
                            statistics);
362                 end
363             end
364
365             % Capture input and/or output pattern data at a specific frequency.
366             if (pattern_period == constants.SPATIAL),
367                 constants.SPATIAL_input = ip_TM;
368                 if constants.LENS1,
369                     constants.SPATIAL_output1 = lens1Data.result;
370                     lens1Data.contour_data(batch_ctr, :) = lens1Data.result(1, :);
371                 end
372                 if constants.LENS2,
373                     constants.SPATIAL_output2 = lens2Data.result;
```

```
                    lens2Data.contour_data(batch_ctr, :) = lens2Data.result(1, :);
                end
                if constants.LENS3,
                    constants.SPATIAL_output3 = lens3Data.result;
                    lens3Data.contour_data(batch_ctr, :) = lens3Data.result(1, :);
                end
            end
        end
        toc
    end

    % Save Lens data:
    if constants.SAVE,
        disp('saving data to:');
        disp(constants.PATH);
        mkdir(constants.PATH);
        if constants.INPUT,
            fileName = strcat(constants.PATH, 'testVector', num2str(constants.SPATIAL), '.mat');
            save(fileName, 'ip_TM');
        end
        if constants.LENS1,
            fileName = strcat(constants.PATH, lens1Data.label, '.mat');
            save(fileName, 'lens1Data');
        end
        if constants.LENS2,
            fileName = strcat(constants.PATH, lens2Data.label, '.mat');
            save(fileName, 'lens2Data');
        end
        if constants.LENS3,
            fileName = strcat(constants.PATH, lens3Data.label, '.mat');
            save(fileName, 'lens3Data');
        end
    end
%%%%%%%%%%%%%%%%%%%%%%%%%%%%%%%%%%%%%%%%%%%%%%%%%%%%%%%%%%%%%%%%%%%%%%%%%%%%%%%
% If ~constants.Data, load saved data:
elseif constants.DISPLAY,
    disp('loading data from: ');
    disp(constants.PATH);
    if constants.INPUT,
        fileName = strcat(constants.PATH, 'testVector', num2str(constants.SPATIAL), '.mat');
        load(fileName);
    end
    if constants.LENS1,
        fileName = strcat(constants.PATH, constants.LENS1_label, '.mat');
        load(fileName);
    end
    if constants.LENS2,
        openPath = strcat(constants.PATH, constants.LENS2_label, '.mat');
        load(openPath);
    end
    if constants.LENS3,
        openPath = strcat(constants.PATH, constants.LENS3_label, '.mat');
        load(openPath);
    end
end

%%%%%%%%%%%%%%%%%%%%%%%%%%%%   Display results:   %%%%%%%%%%%%%%%%%%%%%%%%%%%%
%
if constants.DISPLAY,
    if constants.INPUT,
        % Show input pattern
        figure;
        plot((1:length(ip_TM)) * constants.LAMBDA / constants.N, (ip_TM), 'color', [0 .5 0]);
        xlabel('x (nm)', 'FontSize', 18);
        ylabel('intensity (arbitrary units)', 'FontSize', 18);
        title('ip_TM input pattern', 'FontSize', 18);
        publishPlot;
        % axis([4000 6000, 0 1]);
    end

    if constants.STATS && constants.CONTRAST,
        % Show Michelson contrast profiles.
        figure;
        hold on;
```

```
448         if constants.LENS1,
449             plotContrast(lens1Data, 'b');
450         end
451         if constants.LENS2,
452             plotContrast(lens2Data, 'r');
453         end
454         if constants.LENS3,
455             plotContrast(lens3Data, 'c');
456         end
457         legend(lens1Data.label, lens2Data.label, lens3Data.label, 'FontSize', 18, 'Location', 'Best');
458         set(gca,'XScale', 'log');
459         title('Michelson contrast vs. wavelength', 'FontSize', 18);
460         publishPlot;
461     end
462
463     if constants.STATS && constants.PC,
464         % Show pseudo-contrast profiles.
465         figure;
466         hold on;
467         if constants.LENS1,
468             plotPC(lens1Data, 'b');
469         end
470         if constants.LENS2,
471             plotPC(lens2Data, 'r');
472         end
473         if constants.LENS3,
474             plotPC(lens3Data, 'c');
475         end
476         set(gca,'XScale','log');
477         legend(lens1Data.label, lens2Data.label, lens3Data.label, 'FontSize', 18, 'Location', 'Best');
478         title('Pseudo-contrast vs. wavelength', 'FontSize', 18);
479         publishPlot;
480         % axis([1 1e4 1e-4 1]);
481     end
482
483     if constants.STATS && constants.ERROR,
484         % Show error profiles.
485         figure;
486         hold on;
487         if constants.LENS1,
488             plotError(lens1Data, 'b');
489         end
490         if constants.LENS2,
491             plotError(lens2Data, 'r');
492         end
493         if constants.LENS3,
494             plotError(lens3Data, 'c');
495         end
496         set(gca,'XScale','log');
497         set(gca,'YScale','log');
498         legend(lens1Data.label, lens2Data.label, lens3Data.label, 'FontSize', 18, 'Location', 'Best');
499         title('Error between input and output intensities vs. wavelength', 'FontSize', 18);
500         publishPlot;
501         % axis([1 1e4 1e-4 1e1]);
502     end
503
504     if constants.STATS && constants.CC,
505         % Show cross-correlation profiles.
506         figure;
507         hold on;
508         if constants.LENS1,
509             plotCC(lens1Data, 'b');
510         end
511         if constants.LENS2,
512             plotCC(lens2Data, 'r');
513         end
514         if constants.LENS3,
515             plotCC(lens3Data, 'c');
516         end
517         set(gca,'XScale','log');
518         legend(lens1Data.label, lens2Data.label, lens3Data.label, 'FontSize', 18, 'Location', 'Best');
519         title('Correlation coefficient of the input and output intensities vs. wavelength', 'FontSize', 18);
520         publishPlot;
521         % axis([1 1e4 1e-4 1]);
```

```
522     end
523
524     if constants.RF,
525         % Show frequency-domain reflection functions.
526         figure;
527         hold on;
528         if constants.LENS1,
529             plotRF(lens1Data, 'b');
530         end
531         if constants.LENS2,
532             plotRF(lens2Data, 'r');
533         end
534         if constants.LENS3,
535             plotRF(lens3Data, 'c');
536         end
537         set(gca,'YScale','log');
538         legend(lens1Data.label, lens2Data.label, lens3Data.label, 'Location', 'Best');
539         % title('Reflection function(s)', 'FontSize', 18);
540         publishPlot;
541         axis([0 25 0.0001 100]);
542     end
543
544     if constants.TF,
545         % Show frequency-domain transfer functions.
546         figure;
547         hold on;
548         if constants.LENS1,
549             plotTF(lens1Data, 'b');
550         end
551         if constants.LENS2,
552             plotTF(lens2Data, 'r');
553         end
554         if constants.LENS3,
555             plotTF(lens3Data, 'c');
556         end
557         set(gca,'YScale','log');
558 %         legend(lens1Data.label, lens2Data.label, lens3Data.label, 'Location', 'Best');
559         % title('Transfer function(s)', 'FontSize', 18);
560         publishPlot;
561         axis([0 25 0.0001 100]);
562     end
563
564     if constants.PF,
565         figure;
566         hold on;
567         if constants.LENS1,
568             plotPF(lens1Data, 'b');
569         end
570         if constants.LENS2,
571             plotPF(lens2Data, 'r');
572         end
573         if constants.LENS3,
574             plotPF(lens3Data, 'c');
575         end
576         publishPlot;
577         axis([0 25 -pi pi]);
578     end
579
580     if constants.RF_PRIME,
581         figure;
582         hold on;
583         if constants.LENS1,
584             plotRF_PRIME(lens1Data, 'b');
585         end
586         if constants.LENS2,
587             plotRF_PRIME(lens2Data, 'r');
588         end
589         if constants.LENS3,
590             plotRF_PRIME(lens3Data, 'c');
591         end
592         set(gca,'YScale','log');
593         publishPlot;
594         axis([0 25 1e-10 1e2]);
595     end
```

```
596
597     if constants.TF_PRIME && constants.REFLECT,
598         figure;
599         hold on;
600         if constants.LENS1,
601             plotTF_PRIME(lens1Data, 'b');
602         end
603         if constants.LENS2,
604             plotTF_PRIME(lens2Data, 'r');
605         end
606         if constants.LENS3,
607             plotTF_PRIME(lens3Data, 'c');
608         end
609         set(gca,'YScale','log');
610         publishPlot;
611         axis([0 25 0.0001 100]);
612     end
613
614     if constants.PF_PRIME && constants.REFLECT,
615         figure;
616         hold on;
617         if constants.LENS1,
618             plotPF_PRIME(lens1Data, 'b');
619         end
620         if constants.LENS2,
621             plotPF_PRIME(lens2Data, 'r');
622         end
623         if constants.LENS3,
624             plotPF_PRIME(lens3Data, 'c');
625         end
626         publishPlot;
627         axis([0 25 -pi pi]);
628     end
629
630     if constants.SPATIAL && constants.INPUT,
631         % Show  input and output pattern data at a specific frequency.
632         figure;
633         hold on;
634         plot((1:length(constants.SPATIAL_input)) * constants.LAMBDA / constants.N - constants.LAMBDA / 2, abs(constants.
                SPATIAL_input).^2, 'Color', [0 .5 0]); %, ...
635         if constants.LENS1,
636             plot((1:length(constants.SPATIAL_input)) * constants.LAMBDA / constants.N - constants.LAMBDA / 2, abs(constants.
                    SPATIAL_output1).^2, 'b'); %, ...
637         end
638         if constants.LENS2,
639             plot((1:length(constants.SPATIAL_input)) * constants.LAMBDA / constants.N - constants.LAMBDA / 2, abs(constants.
                    SPATIAL_output2).^2, 'r'); %, ...
640         end
641         if constants.LENS3,
642             plot((1:length(constants.SPATIAL_input)) * constants.LAMBDA / constants.N - constants.LAMBDA / 2, abs(constants.
                    SPATIAL_output3).^2, 'c');
643         end
644         xlabel('x (nm)', 'FontSize', 18);
645         ylabel('|t|^2 (arbitrary units)', 'FontSize', 18);
646         legend('Input pattern', lens1Data.label, lens2Data.label, lens3Data.label, 'Location', 'Best');
647         title(strcat('input and output patterns for wavelength = ', num2str(constants.SPATIAL), ' nm'), 'fontsize', 18);
648         publishPlot;
649         axis([(-2 * constants.SPATIAL) (2 * constants.SPATIAL) -5 2]);
650     end
651     toc
652 end
653
654 beep;
655 toc
656 % Colour order:
657 % Blue
658 % Green
659 % Red
660 % Cyan
661 % Purple
662 % Mustard
663 %
```

Listing A.2: addMedium.m

```
function medium = addMedium(epsilon, mu, thickness, medium)
% addMedium.m
% Optical Medium Generation file
% by C. P. Moore
% 22-11-2006
%
% extending TMatrix.m
%
% Usage:
% medium = addMedium(epsilon, mu, thickness, medium)
%
% Inputs:
% epsilon: electrical permittivity of the medium.
% mu: magnetic permeability of the medium.
% th: thickness of the medium, in nm.
%
% Outputs:
% medium: new medium.
%
% In words:
% addMedium creates an optical layer in medium thickness thick (nm), with
% relative electrical permittivity, epsilon,
% and relative magnetic mermeability, mu.
%
medium.num_layers = medium.num_layers + 1;
medium.e(medium.num_layers)  = epsilon;
medium.u(medium.num_layers)  = mu;
medium.th(medium.num_layers) = thickness;
```

Listing A.3: addInterfaces.m

```
function sysParam = addInterfaces(medium, sysParam)
% addInterfaces.m
% Optical Interface Generation file
% by C. P. Moore
% 22-11-2006
%
% Usage:
% addInterfaces(medium, n, MAX_CTR, MAX_N, kx, d, T)
%
% Inputs:
% medium: an array of media, interfaces are created between medium(1)
% and medium(MAX_N).
% MAX_N: Another constant.  Defined in addMedium.m.
% sysParam: Array defined in createSystem.m.  Contains MAX_CTR, kx, d and
% T values.
%
%


% Global constant importation:
global constants;

constants.REVERSE = constants.TRUE;

K_LIMIT = 5000; % 50 % Highest value of K to be simulated.
% MAX_N = length(medium.e);
MAX_N = medium.num_layers;
%buffer = [1 2 3 4 5];

for ctr = 1:(constants.N),
    T = eye(2);
    R = eye(2);
% DEBUG %
%      if abs(sysParam.kx(ctr)) == 1,
%          ctr = ctr + 1;
%      end

    kz = sqrt(medium.e .* medium.u .* (sysParam.k0^2) - sysParam.kx(ctr)^2);  % kz normalised to k0!!

% DEBUG %
```

```
40 %sysParam.kz(ctr, :) = kz(1,:);
41
42     z_disp = medium.th(1);
43     for n = 2:MAX_N,
44         % T(0) Matrix @ (n - 1) : n interface.
45         T011 = medium.e(n) / kz(n) + medium.e(n - 1) / kz(n - 1);
46         T012 = medium.e(n) / kz(n) - medium.e(n - 1) / kz(n - 1);
47         T021 = medium.e(n) / kz(n) - medium.e(n - 1) / kz(n - 1);
48         T022 = medium.e(n) / kz(n) + medium.e(n - 1) / kz(n - 1);
49
50         R011 = medium.e(n - 1) / kz(n - 1) + medium.e(n) / kz(n);
51         R012 = medium.e(n - 1) / kz(n - 1) - medium.e(n) / kz(n);
52         R021 = medium.e(n - 1) / kz(n - 1) - medium.e(n) / kz(n);
53         R022 = medium.e(n - 1) / kz(n - 1) + medium.e(n) / kz(n);
54
55         T0scale = (1 / 2 * kz(n) / medium.e(n));
56         T0 = T0scale * [T011, T012; T021, T022];
57
58         R0scale = (1 / 2 * kz(n - 1) / medium.e(n - 1));
59         R0 = R0scale * [R011, R012; R021, R022];
60
61         % Phase Matrices: refer phase to image plane. Give T-matrix, ie.
62         % T(z = d);
63         Tp = [exp(-1i * kz(n) * z_disp), 0; 0, exp(1i * kz(n) * z_disp)] * T0 * [exp(1i * kz(n - 1) * z_disp), 0; 0, exp(-1i
               * kz(n - 1) * z_disp)];
64         Rp = [exp(-1i * kz(n - 1) * z_disp), 0; 0, exp(1i * kz(n - 1) * z_disp)] * R0 * [exp(1i * kz(n) * z_disp), 0; 0, exp
               (-1i * kz(n) * z_disp)];
65
66         z_disp = z_disp + medium.th(n);
67
68         T = Tp * T;
69         R = R * Rp;
70     end
71
72     % So far, T describes an interfaces at z = d, but calculates the
73     % coefficients for that interface in the z = 0 plane.
74     % Tend gives these coefficients in the z = d plane.
75     %
76     Tend = [exp(1i * kz(n) * z_disp), 0; 0, exp(-1i * kz(n) * z_disp )] * T;
77     % Tend = T;
78     Rend = R * [exp(-1i * kz(n) * z_disp), 0; 0, exp(1i * kz(n) * z_disp)];
79
80     % Transmission coefficients:
81     % [t; 0] = T*[1; r]
82     if ~constants.REVERSE,
83         sysParam.t(1, ctr) = (Tend(1, 1) * Tend(2, 2) - Tend(1, 2) * Tend(2, 1)) / Tend(2, 2);
84     else
85         sysParam.t(1, ctr) = 1 / Rend(1, 1);
86     end
87     if isnan(sysParam.t(1, ctr)) || abs(ctr - constants.N / 2) * sysParam.RESOLUTION / sysParam.ks > K_LIMIT,
88         sysParam.t(1, ctr) = 0;
89     end
90
91 %     sysParam.t2(1, ctr) = (Tbegin(1, 1) * Tbegin(2, 2) - Tbegin(1, 2) * Tbegin(2, 1)) / Tbegin(2, 2);
92 %     if isnan(sysParam.t2(1, ctr)) || abs(ctr - constants.N / 2) * sysParam.RESOLUTION / sysParam.ks > K_LIMIT,
93 %         sysParam.t2(1, ctr) = 0;
94 %     end
95
96     % Reflection phase shift:
97     % r0 = exp(-2 * i * kz(n - 1) * z_disp) * rd
98     % Reflection coefficients:
99     if ~constants.REVERSE,
100        sysParam.r(1, ctr) = -Tend(2, 1) / Tend(2, 2);
101    else
102        sysParam.r(1, ctr) = Rend(2, 1) / Rend(1, 1);
103        % sysParam.r(1, ctr) = exp(-2 * i * kz(1) * z_disp) * -T(2, 1) / T(2, 2);
104    end
105    if isnan(sysParam.r(1, ctr)) || abs(ctr - constants.N / 2) * sysParam.RESOLUTION / sysParam.ks > K_LIMIT,
106        sysParam.r(1, ctr) = 0;
107    end
108
109 %     sysParam.r2(1, ctr) = -Tend(2, 1) / Tend(2, 2);
110 %     if isnan(sysParam.r2(1, ctr)) || abs(ctr - constants.N / 2) * sysParam.RESOLUTION / sysParam.ks > K_LIMIT,
111 %         sysParam.r2(1, ctr) = 0;
```

```
%     end
    if constants.REFLECT,
        sysParam.rprime(1, ctr) = sysParam.r(1, ctr) * sysParam.r_Mask(1, ctr); % * exp(2 * 1i * kz(2) * (medium.th(2) -
             medium.th(1)));
%
        sysParam.tprime(1, ctr) = sysParam.t(1, ctr) / (1 - sysParam.rprime(1, ctr));
%         if abs(sysParam.rprime(1, ctr)) > 1,
%             sysParam.tprime(1, ctr) = 0;
%         end
    end
end
% sysParam.rprime = sysParam.r .* sysParam.r_Mask .* exp(2 * 1i * kz(2) * (medium.th(2) - medium.th(1)));
% sysParam.tprime = sysParam.t ./ (1 - sysParam.rprime);
```

Listing A.4: addSources.m

```
function intensity_vector = addSource(wave_shape, amplitude, dc_offset, limit_max, limit_min, pattern_period, duty_cycle,
     pattern_length, num_samples)
% addSource.m
% Test pattern generation file
% by C. P. Moore
% 08-12-2006
%
% Usage:
% intensity_vector = addSource(wave_shape, amplitude, dc_offset,
% limit_max, limit_min, pattern_period, sample_length, num_samples)
%
% Inputs:
% wave_shape: A string, either 'cosine', 'square' or 'triangle'.
% amplitude: intensity value.
% dc_offset: intensity offset.
% limit_max, limit_min: clipping values.
% pattern_period: (nm).
% pattern_length: (nm).
% num_samples: number of samples in the pattern vector.
%
samples_per_nm = num_samples / pattern_length;
samples_per_period = num_samples / pattern_length * pattern_period;
%

switch lower(wave_shape)
    case 'square',
        % Create square wave template.
        single_period(1 : samples_per_period) = dc_offset;
        single_period(samples_per_period * duty_cycle + 1 : samples_per_period) = amplitude + dc_offset;
        % Prevent truncation of trailing zeroes:
        if numel(single_period) < samples_per_period,
            single_period(samples_per_period) = 1e-4;
        end
        % Clone the template:
        intensity_vector = repmat(single_period, [1 round(num_samples / samples_per_period - 0.5)]);
        % Copy the required fraction of the template into the end of the
        % pattern:
        tail = mod(num_samples, samples_per_period);
        if(tail > 0),
            intensity_vector(num_samples - tail + 1:num_samples) = single_period(1:tail);
        end

    case 'shifted_square',
        ph_offset = 90; % degrees
        shift_amount = (ph_offset / 360) * samples_per_period;

        % Create square wave template.
        single_period(1 : samples_per_period) = dc_offset;
        single_period(samples_per_period - samples_per_period * duty_cycle + 1 : samples_per_period) = amplitude + dc_offset;
        % Phase shift:
        temp = single_period(1:shift_amount);
        single_period(1:num_samples - shift_amount) = intensity_vector(shift_amount + 1:num_samples);
        single_period(num_samples - shift_amount + 1:num_samples) = temp;
        % Prevent truncation of trailing zeroes:
        if numel(single_period) < samples_per_period,
            single_period(samples_per_period) = 1e-4;
```

```
56          end
57
58          % Clone the template:
59          intensity_vector = repmat(single_period, [1 round(num_samples / samples_per_period - 0.5)]);
60          % Copy the required fraction of the template into the end of the
61          % pattern:
62          tail = mod(num_samples, samples_per_period);
63          if(tail > 0),
64              intensity_vector(num_samples - tail + 1:num_samples) = single_period(1:tail);
65          end
66
67      case 'cosine',
68          ctr = 1:num_samples;
69          intensity_vector = amplitude * cos(2 * pi * ctr / samples_per_period) + dc_offset;
70
71      case 'sine',  % More efficient than passing a seldom-used ph_offset variable between functions.  Untested.
72          ph_offset = 90; % degrees
73          ctr = 1:num_samples;
74          intensity_vector = amplitude * cos(2 * pi * ctr / samples_per_period + ph_offset) + dc_offset;
75
76      case 'triangle',
77          % Very, very slow.  Needs to be matricised.
78          CTR1_MAX = 2 * pattern_length / pattern_period;
79          CTR2_MAX = num_samples / (2 * pattern_length  / pattern_period);
80          for ctr1 = 1:CTR1_MAX,
81             for ctr2 = 1:CTR2_MAX,
82                intensity_vector(round((ctr1 - 1) * CTR2_MAX + ctr2)) = amplitude * (mod(ctr1, 2) * ctr2 + mod(ctr1 - 1, 2) * (
                       CTR2_MAX - ctr2)) / CTR2_MAX + dc_offset;
83             end
84          end
85
86      case 'delta',
87          intensity_vector(1:num_samples) = dc_offset;
88          intensity_vector(round((-duty_cycle / 2) * pattern_period * num_samples / pattern_length + num_samples / 2):round((
                duty_cycle / 2) * pattern_period * num_samples / pattern_length + num_samples / 2)) = dc_offset + amplitude;
89
90      case 'dualslits',
91          intensity_vector(1:num_samples) = dc_offset;
92          intensity_vector(round((-3 * duty_cycle / 2) * pattern_period * num_samples / pattern_length + num_samples / 2):round
                ((-duty_cycle / 2) * pattern_period * num_samples / pattern_length + num_samples / 2)) = dc_offset + amplitude;
93          intensity_vector(round((duty_cycle / 2) * pattern_period * num_samples / pattern_length + num_samples / 2):round((3 *
                 duty_cycle / 2) * pattern_period * num_samples / pattern_length + num_samples / 2)) = dc_offset + amplitude;
94      otherwise,
95        ;
96  end
97
98  % Prevent truncation of trailing zeroes:
99  if numel(intensity_vector) < num_samples,
100     intensity_vector(num_samples) = 1e-4;
101 end
102
103 % Clip peaks:
104 for ctr = 1:num_samples,
105     if intensity_vector(num_samples) > limit_max,
106         intensity_vector(num_samples) = limit_max;
107     else
108         if intensity_vector(num_samples) < limit_min,
109             intensity_vector(num_samples) = limit_min;
110         end
111     end
112 end
```

Listing A.5: addSquare.m

```
1  function intensity_vector = addSquare(amplitude, dc_offset, ph_offset, duty_cycle, samples_per_period, num_samples)
2  %
3  % addSquare.m
4  % Square-wave generation file
5  % by C. P. Moore
6  % 22-10-2006
7  %
8  % Usage:
```

```
% intensity_vector = addSquare(amplitude, dc_offset, ph_offset, duty_cycle,
% samples_per_period, num_samples)
%
% Inputs:
% amplitude: zero-to-peak value (au).
% dc_offset: (au).  dc_offset = 0 corresponds to a wave whose minimum is
% zero and maximum is amplitude.
%
% ph_offset: (degrees).
% | ph_offset | Phase characteristics |
% -------------------------------------
% |     0     | -ve   sine            |
% |    90     | -ve cosine            |
% |   180     |       sine            |
% |   270     |     cosine            |
% -------------------------------------
%
% duty_cycle: 0 < duty_cycle <= 1.  duty_cycle = 0.5 corresponds to a
% symmetrical wave.  duty_cycle = 1 corresponds to a d.c. signal
% with amplitude = amplitude + dc_offset.
% samples_per_period: The number of samples in one period of the output
% pattern.
% num_samples: The total number of samples in the entire output pattern.
%

% Global constant importation:
global constants

% Create square wave template.
single_period(1 : samples_per_period) = dc_offset;
single_period(samples_per_period - round(samples_per_period * duty_cycle) + 1 : samples_per_period) = amplitude + dc_offset;
% Phase shift:
shift_amount = round(ph_offset / 360 * samples_per_period);
if(shift_amount) > 0,
    temp = single_period(1:shift_amount);
    single_period(1:samples_per_period - shift_amount) = single_period(shift_amount + 1:samples_per_period);
    single_period(samples_per_period - shift_amount + 1:samples_per_period) = temp;
end

% Prevent truncation of trailing zeroes in template:
if numel(single_period) < samples_per_period,
    single_period(samples_per_period) = constants.SMALL_NUM;
end

% Clone the template:
intensity_vector = repmat(single_period, [1 round(num_samples / samples_per_period - 0.5)]);
% Copy the required fraction of the template into the end of the
% pattern:
tail = mod(num_samples, samples_per_period);
if(tail > 0),
    intensity_vector(num_samples - tail + 1:num_samples) = single_period(1:tail);
end

% Prevent truncation of trailing zeroes in output pattern:
if numel(intensity_vector) < num_samples,
    intensity_vector(num_samples) = constants.SMALL_NUM;
end
```

Listing A.6: addDelta.m

```
function intensity_vector = addDelta(amplitude, dc_offset, num_peaks, samples_per_period, num_samples)
%
% addDelta.m
% Delta-function generation file
% by C. P. Moore
% 22-10-2006
%
% Usage:
% intensity_vector = addDelta(amplitude, dc_offset, num_peaks,
% samples_per_period, num_samples)
%
% Inputs:
```

```
% amplitude: peak-to-peak value (au).
% dc_offset: (au).
% num_peaks: 1 or 2 corresponding to an _n_ or _m_ type waveform, or any
% other arbitrarily large whole, positive number less than num_samples / 2.
% (Let's be realistic here, folks! ;)
% samples_per_peak: The number of samples in one peak of the output
% pattern.
% num_samples: The total number of samples in the entire output pattern.
%

samples_per_peak = samples_per_period; % / 2;
intensity_vector(1:num_samples) = dc_offset;

toggle = true;
for ctr = (num_peaks * 2) - 1 : -2 : 1,
    if ctr * samples_per_peak < num_samples,
        intensity_vector(round(-ctr * samples_per_peak / 2 + num_samples / 2):round(ctr * samples_per_peak / 2 + num_samples
            / 2)) = toggle * dc_offset + amplitude;
        toggle = not(toggle);
    else
        disp('Error generating Delta function input pattern.  Increase N and/or decrease num_peaks to solve this problem.');
        break;
    end
end

% Prevent truncation of trailing zeroes:
if numel(intensity_vector) < num_samples,
    intensity_vector(num_samples) = 1e-4;
end
```

Listing A.7: getStats.m

```
function stats = getStats(src, img, pattern_period, stats);
%
% getStats.m
% function to collate waveform information such as contrast, dc value,
% maximum & minimum values.
%
% Correlation code from
% http://en.wikipedia.org/wiki/Correlation_coefficient on 04-02-2007.
%

% Global constant importation:
global constants

% Single slit case
if constants.CONTRAST,
    stats.Mcontrast(pattern_period) = getContrast(img);
    % Michelson contrast:
    maxm = max(img(:));
    minm = min(img(:));
    stats.Mcontrast(pattern_period) = (maxm - minm) / (maxm + minm);
end
if constants.PC,
    stats.dc(pattern_period) = mean(img(:));
    if (constants.SB | constants.SD),
        % SINGLE SLIT:
        lext = img(round(length(img) / 2));
    else
        % DUAL SLITS:
        if pattern_period < 5,
            disp('Dual slit pseudo-contrast: application specific!! Use with caution.  Conditions: local extrema at N / 2 +
                pattern_period * N / LAMBDA.');
        end
        lext = img(round(constants.N * (1 / 2 + pattern_period / constants.LAMBDA)));
    end
    if (constants.SB | constants.DB),
        % BRIGHT SLIT(S):
        stats.pcontrast(pattern_period) = (lext - stats.dc(pattern_period)) / (stats.dc(pattern_period) + lext);
    else
        stats.pcontrast(pattern_period) = (stats.dc(pattern_period) - lext) / (stats.dc(pattern_period) + lext);
    end
```

```
end

if constants.ERROR,
    % Error: Option 1. make a < 1:
    % a = sum(src .* img) / sum(src.^2);
    % H_raw = sum((a .* src - img).^2); % NB: should be sum[(abc)^2], not [sum(abc)]^2.

    % Option 2. make a > 1:
    a = sum(src .* img) / sum(img.^2);
    H_raw = sum((src - a .* img).^2);

    % Normalise H:
    % H = H_raw ./ var(src);
    % H = H_raw;
    stats.H(pattern_period) = H_raw ./ pattern_period;
    % stats.H(pattern_period) = H_raw ./ sum(a .* src);
%   stats.H(pattern_period) = H_raw ./ length(img);

    stats.a(pattern_period) = a;
end

if constants.CC,
    % Cross-correlation:
    sum_src2 = 0;
    sum_img2 = 0;
    sum_coprod = 0;
    mean_src = src(1);
    mean_img = img(1);
    for i = 2:constants.N,
        sweep = (i - 1) / i;
        delta_src = src(i) - mean_src;
        delta_img = img(i) - mean_img;

        sum_src2 = sum_src2 + (delta_src)^2 * sweep;
        sum_img2 = sum_img2 + (delta_img)^2 * sweep;
        sum_coprod = sum_coprod + delta_src * delta_img * sweep;

        mean_src = mean_src + delta_src / i;
        mean_img = mean_img + delta_img / i;
    end;

    sd_src = sqrt(sum_src2 / constants.N);
    sd_img = sqrt(sum_img2 / constants.N);
    cov_src_img = sum_coprod / constants.N;

    r = cov_src_img / (sd_src * sd_img);

    stats.cc(pattern_period) = r;
end
```

Listing A.8: plotContrast.m

```
function plotContrast(lensData, colour);
%
% plotContrast.m
% Contrast plotting file
% by C. P. Moore
% 17-10-2007
%
% Inputs:
% lensData: a lensXData variable generated by getStats.m.
% colour: a string containing one of the following characters or keywords:
%           b     blue
%           g     green
%           r     red
%           c     cyan
%           m     magenta
%           y     yellow
%           k     black
%

% Global constant importation:
```

```
21 global constants
22
23 if (colour == 'g') | (colour == 'green'),
24     colour = [0 0.5 0];
25 end
26 semilogx(constants.PATTERN_PERIOD_MIN:constants.PATTERN_PERIOD_MAX, lensData.statistics.Mcontrast(constants.
       PATTERN_PERIOD_MIN:constants.PATTERN_PERIOD_MAX), 'color', colour);
27 xlabel('feature size (nm)', 'FontSize', 18);
28 ylabel('Michelson contrast', 'FontSize', 18);
```

Listing A.9: plotPC.m

```
1  function plotPC(lensData, colour);
2  %
3  % plotPC.m
4  % Pseudo-contrast plotting file
5  % by C. P. Moore
6  % 17-10-2007
7  %
8  % Inputs:
9  % lensData: a lensXData variable generated by getStats.m.
10 % colour: a string containing one of the following characters or keywords:
11 %           b     blue
12 %           g     green
13 %           r     red
14 %           c     cyan
15 %           m     magenta
16 %           y     yellow
17 %           k     black
18 %
19
20 % Global constant importation:
21 global constants
22
23 if (colour == 'g') | (colour == 'green'),
24     colour = [0 0.5 0];
25 end
26 semilogx(constants.PATTERN_PERIOD_MIN:constants.PATTERN_PERIOD_MAX, lensData.statistics.pcontrast(constants.
       PATTERN_PERIOD_MIN:constants.PATTERN_PERIOD_MAX), 'color', colour);
27 xlabel('feature size (nm)', 'FontSize', 18);
28 ylabel('pseudo-contrast', 'FontSize', 18);
```

Listing A.10: plotError.m

```
1  function plotError(lensData, colour);
2  %
3  % plotError.m
4  % Error plotting file
5  % by C. P. Moore
6  % 17-10-2007
7  %
8  % Inputs:
9  % lensData: a lensXData variable generated by getStats.m.
10 % colour: a string containing one of the following characters or keywords:
11 %           b     blue
12 %           g     green
13 %           r     red
14 %           c     cyan
15 %           m     magenta
16 %           y     yellow
17 %           k     black
18 %
19
20 % Global constant importation:
21 global constants
22
23 if (colour == 'g') | (colour == 'green'),
24     colour = [0 0.5 0];
25 end
26 loglog(constants.PATTERN_PERIOD_MIN:constants.PATTERN_PERIOD_MAX, lensData.statistics.H(constants.PATTERN_PERIOD_MIN:
       constants.PATTERN_PERIOD_MAX), 'color', colour);
```

```
27 xlabel('feature size (nm)', 'FontSize', 18);
28 ylabel('error (arbitrary units)', 'FontSize', 18);
```

Listing A.11: plotCC.m

```
1  function plotCC(lensData, colour);
2  %
3  % plotCC.m
4  % Correlation coefficient plotting file
5  % by C. P. Moore
6  % 17-10-2007
7  %
8  % Inputs:
9  % lensData: a lensXData variable generated by getStats.m.
10 % colour: a string containing one of the following characters or keywords:
11 %           b     blue
12 %           g     green
13 %           r     red
14 %           c     cyan
15 %           m     magenta
16 %           y     yellow
17 %           k     black
18 %
19
20 % Global constant importation:
21 global constants
22
23 if (colour == 'g') | (colour == 'green'),
24     colour = [0 0.5 0];
25 end
26 semilogx(constants.PATTERN_PERIOD_MIN:constants.PATTERN_PERIOD_MAX, lensData.statistics.cc(constants.PATTERN_PERIOD_MIN:
       constants.PATTERN_PERIOD_MAX), 'color', colour);
27 xlabel('feature size (nm)', 'FontSize', 18);
28 ylabel('correlation coefficient', 'FontSize', 18);
```

Listing A.12: plotRF.m

```
1  function plotRF(lensData, colour);
2  %
3  % plotRF.m
4  % Reflection function plotting file
5  % by C. P. Moore
6  % 11-03-2008
7  %
8  % Inputs:
9  % lensData: a lensXData variable generated by getStats.m.
10 % colour: a string containing one of the following characters or keywords:
11 %           b     blue
12 %           g     green
13 %           r     red
14 %           c     cyan
15 %           m     magenta
16 %           y     yellow
17 %           k     black
18 %
19
20 global constants;
21
22 if strcmp(colour, 'g') || strcmp(colour, 'green'),
23     colour = [0 0.5 0];
24 end
25 if constants.K0_PLOTS,
26     plot(lensData.kx / lensData.k0, abs(lensData.r).^2, 'color', colour);
27     xlabel('k_x/k_0', 'FontSize', 18);
28 else
29     plot(lensData.kx / lensData.ks, abs(lensData.r).^2, 'color', colour);
30     xlabel('k_x/2\pi (\mum^{-1})', 'FontSize', 18);
31 end
32 ylabel('Reflection', 'FontSize', 18);
```

Listing A.13: plotTF.m

```
function plotTF(lensData, colour);
%
% plotTF.m
% Reflection function plotting file
% by C. P. Moore
% 11-03-2008
%
% Inputs:
% lensData: a lensXData variable generated by getStats.m.
% colour: a string containing one of the following characters or keywords:
%           b     blue
%           g     green
%           r     red
%           c     cyan
%           m     magenta
%           y     yellow
%           k     black
%

global constants;

if strcmp(colour, 'g') || strcmp(colour, 'green'),
    colour = [0 0.5 0];
end
if constants.K0_PLOTS,
    semilogy(lensData.kx / lensData.k0, abs(lensData.t).^2, 'color', colour);
%     plot(lensData.kx / lensData.k0, abs(lensData.t), 'color', colour);
    xlabel('k_x / k_0', 'FontSize', 18);
else
    semilogy(lensData.kx / lensData.ks, abs(lensData.t).^2, 'color', colour);
    xlabel('k_x / 2\pi (\mum^{-1})', 'FontSize', 18);
end
ylabel('|t|^2', 'FontSize', 18);
```

Listing A.14: plotPF.m

```
function plotPF(lensData, colour);
%
% plotPF.m
% Phase transfer function plotting file
% by C. P. Moore
% 08-06-2009
%
% Inputs:
% lensData: a lensXData variable generated by getStats.m.
% colour: a string containing one of the following characters or keywords:
%           b     blue
%           g     green
%           r     red
%           c     cyan
%           m     magenta
%           y     yellow
%           k     black
%

global constants;

if strcmp(colour, 'g') || strcmp(colour, 'green'),
    colour = [0 0.5 0];
end
if constants.K0_PLOTS,
    semilogy(lensData.kx / lensData.k0, angle(lensData.t), 'color', colour);
    xlabel('k_x/k_0', 'FontSize', 18);
else
    semilogy(lensData.kx / lensData.ks, angle(lensData.t), 'color', colour);
    xlabel('k_x/2\pi (\mum^{-1})', 'FontSize', 18);
end
ylabel('Phase', 'FontSize', 18);
```

Listing A.15: plotTF_prime.m

```
function plotTF(lensData, colour);
%
% plotTF.m
% Reflection function plotting file
% by C. P. Moore
% 11-03-2008
%
% Inputs:
% lensData: a lensXData variable generated by getStats.m.
% colour: a string containing one of the following characters or keywords:
%           b     blue
%           g     green
%           r     red
%           c     cyan
%           m     magenta
%           y     yellow
%           k     black
%

global constants;

if strcmp(colour, 'g') || strcmp(colour, 'green'),
    colour = [0 0.5 0];
end
if constants.K0_PLOTS,
    semilogy(lensData.kx / lensData.k0, abs(lensData.tprime).^2, 'color', colour);
    xlabel('k_x/k_0', 'FontSize', 18);
else
    semilogy(lensData.kx / lensData.ks, abs(lensData.tprime).^2, 'color', colour);
    xlabel('k_x/2\pi (\mum^{-1})', 'FontSize', 18);
end
ylabel('Transmission', 'FontSize', 18);
title('t'''', 'FontSize', 18);
```

Listing A.16: plotPF_prime.m

```
function plotPF_PRIME(lensData, colour)
%
% plotPF_PRIME.m
% Phase transfer function plotting file
% by C. P. Moore
% 08-06-2009
%
% Inputs:
% lensData: a lensXData variable generated by getStats.m.
% colour: a string containing one of the following characters or keywords:
%           b     blue
%           g     green
%           r     red
%           c     cyan
%           m     magenta
%           y     yellow
%           k     black
%

global constants;

if strcmp(colour, 'g') || strcmp(colour, 'green'),
    colour = [0 0.5 0];
end

if constants.K0_PLOTS,
    plot(lensData.kx / lensData.k0, angle(lensData.tprime), 'color', colour);
    xlabel('k_x/k_0', 'FontSize', 18);
else
    % semilogy(lensData.kx / lensData.ks, phase(lensData.tprime), (2 * pi)), 'color', colour);
    plot(lensData.kx / lensData.ks, angle(lensData.tprime), 'color', colour);
    xlabel('k_x/2\pi (\mum^{-1})', 'FontSize', 18);
end
ylabel('Phase', 'FontSize', 18);
```

```
35 title('P''', 'FontSize', 18);
```

Appendix B

Atomic Force Microscopy Data Processing

The Matlab source code used to implement the image processing steps described in Section 7.4 and Fig. 7.16 is presented in Listing B.1. The code, which is stored in a single file, $getAFM.m$, opens an ASCII file generated by the AFM software and stores the contents of that file in a matrix variable. Various signal conditioning steps are then completed before the averaged cross-section of the data and the corresponding spatial frequency spectrum are returned in a data structure. The particular operations that are performed on the data are governed by a series of flags stored in the k data structure, defined at the top of the file. This structure is conceptually similar to the $constants$ global data structure used in Appendix A.

Listing B.1: getAFM.m

```
1  function [AFMdata, crossSection, stepRespSpectrum, impulseRespSpectrum, x_axis] = getAFM(srcAFM, sizeOfSample_um,
       numAFMsamples, aspectRatio, profile_type) %#ok<FNDEF>
2  % [AFMdata, crossSection, stepRespSpectrum, impulseRespSpectrum, x_axis] = getAFM(srcAFM, sizeOfSample_um, numAFMsamples,
       aspectRatio, profile_type);
3  % getAFM.m
4  %
5  % File to import AFM data.
6  %
7  % Example data used to call getAFM:
8  % srcAFM = '../Import/AFM/S230_1u_20110505/230_1u_plane2.asc';
9  %                          % ASCII file exported from AFM software.
10 % sizeOfSample_um = 5;
11 % numAFMsamples = 512;
12 % aspectRatio = 1;          % Could be 1, 1/2, 1/4, 1/8, ... 1/256.
13 % obj_profile_type = 'W';   % 'W' or 'M', depending if the profile has more
14 %                          troughs (M) or peaks (W).  Used in the
15 %                          flattening algorithm.
16 %
17 % Author: C. P. Moore
18 % 28 December 2009
```

```
% Functionalised on 07 July 2010

% close all;

global k;
k.ROTATE            = k.TRUE;
k.AVERAGE           = k.TRUE;
k.FLATTEN           = k.TRUE; % Broken for scans of more than two periods.
k.AREA_OF_INTEREST  = ~k.TRUE;
k.AFM               = k.TRUE;
k.FEM               = ~k.TRUE;

% k.FIGS              = k.TRUE; % Defined in measureTF.m
  k.RAW_ROT_USE     = k.TRUE;
  k.USE             = ~k.TRUE;
  k.XSEC            = ~k.TRUE;
  k.HYBRID          = k.TRUE;   % Combines k.USE and k.XSEC
  k.SRS             = k.TRUE;
  k.FLAT_SMOOTH     = ~k.TRUE;
  k.SIGMA           = ~k.TRUE;
  k.IRS             = ~k.TRUE;

k.BIG_NUM = 1000;
k.UNITS = 1e-9; % m.
k.XTN = '.mphtxt';
k.NM_PER_UM = 1e3;

% centreX = numAFMsamples / 2;
% centreY = numAFMsamples * aspectRatio / 2;

% 1 of 4: Capture AFM Data
if k.AFM,
    tic
    % open input file:
    [fid, msg] = fopen(srcAFM, 'r');
    if fid == -1,
        % print error message:
        fprintf(2, msg);
        beep;
        error('AFM file not found!');
        return; %#ok<UNRCH>
    end

    % find start of line data:
    ctr = 1;
    % Nanoscope v5.1.2r3: use for old data files (pre-2009)
    % id_str = 'Exported image units';
    % Nanoscope v5.3.1r1:
    % id_str = '\*File list end';
    % id_str = '        ';
    id_str = '\Exported image units: nm';

    % Find start of AFM data:
    while k.TRUE,
        tline = fgetl(fid);
        if (strfind(tline, id_str)),
            break;
        else
            ctr = ctr + 1;
            if ctr > k.BIG_NUM,
                beep;
                fprintf(2, 'Format of AFM file is incorrect or header is exceedingly long (> %d lines).\nExpecting string "%s
                      " directly above start of sample data.\n', k.BIG_NUM, id_str);
                return;
            end
        end
    end

    % Find start of useful AFM data:
    % For aspect ratios != 1:1, first (0.5 - AR / 2) * 512 lines are zeros,
    % or non-data.
    ctr = ctr + round((0.5 - aspectRatio / 2) * 512);

    % import line data into matrix:
```

```
    AFMdata = dlmread(srcAFM, '', [ctr, 0, ctr + aspectRatio * numAFMsamples - 1, numAFMsamples - 1]);

    % Dummy (Ideal) AFMdata:
    % AFMdata = [zeros(1, numAFMsamples / 2), ones(1, numAFMsamples / 2)] -
    % 0.5;
    % AFMdata = repmat(AFMdata, numAFMsamples, 1);

    st = fclose(fid);
    if st == -1,
        % print error message:
        beep;
        fprintf(2, 'Error closing input file.\n');
        return;
    end
    toc

    % 2 of 4: Find rotation in AFM data:
    if k.FIGS && k.RAW_ROT_USE,
        % Show pre-processed image:
        figure;
        subplot(1, 3, 1), imagesc(AFMdata);
        set(gca,'YDir','normal');
        title('raw AFM data');
        xlabel('x (pixels)');
        ylabel('y (pixels)');
        axis image;
        publishPlot;
    end
%     figure;
%     mesh(AFMdata);
%     title('meshed AFM data');
%     % Find 2D spectrum of AFMdata:
%     AFMspectrum = fftshift(fft2(fftshift(AFMdata)));
%     figure;
%     mesh(abs(AFMspectrum));
%     title('meshed AFM spectrum');

    if k.ROTATE,
        step = 0;
        lower_lim = -10; % degrees
        upper_lim = 10;  % degrees
        increment = (upper_lim - lower_lim) / 50;

        % Find angle of rotation:
        num_iterations = 3;
        tolerance = 0.001;
        while (step < num_iterations) && increment >= tolerance,
            rot_angle = lower_lim:increment:upper_lim;
            sigma = zeros(1, length(rot_angle));

            % Rotate AFMdata in increments:
            for ctr = 1:length(rot_angle),
               rotatedAFMdata = imrotate(AFMdata, rot_angle(ctr));
               % Shrink usable area according to rotation.
               % Original sizes:
               % x = size(AFMdata, 2);
               % y = size(AFMdata, 1);
               % Sizes after rotation:
               % x_rot = x * cos(theta) + y * sin(theta);
               % y_rot = x * sin(theta) + y * cos(theta);
               % Useable size:
               % x_use = (x * cos(theta) - y * sin(theta))
               %                         / (cos^2(theta) - sin^2(theta));
               % y_use = (x * sin(theta) - y * cos(theta))
               %                         / (sin^2(theta) - cos^2(theta));
               %
               % Note: x_rot > x > x_use.
               % See Notebook entry on 13 Oct 2010 for derivation.
               % In this implementation,
               x = size(AFMdata, 2);
               y = size(AFMdata, 1);
               x_rot = size(rotatedAFMdata, 2);
               y_rot = size(rotatedAFMdata, 1);
               theta = deg2rad(rot_angle(ctr));
```

```
166             x_use = floor(abs((x * cos(theta) - y * abs(sin(theta)))) / ...
167                 (cos(theta) * cos(theta) - sin(theta) * sin(theta)));
168             y_use = floor(abs((x * abs(sin(theta)) - y * cos(theta))) / ...
169                 (cos(theta) * cos(theta) - sin(theta) * sin(theta)));
170             sampleX = x_use;
171             sampleY = y_use;
172             centreRotatedX = floor(x_rot / 2);
173             centreRotatedY = floor(y_rot / 2);
174             % Check that rotation is not too great:
175             if (sampleX > x) || (sampleY > y),
176                 % Rotated too far - can't get a decent sample.
177                 sigma(ctr) = k.BIG_NUM;
178             else
179                 centrePiece = rotatedAFMdata((centreRotatedY - floor(sampleY / 2) + 1):(centreRotatedY + floor(sampleY /
                        2)), (centreRotatedX - floor(sampleX / 2) + 1):(centreRotatedX + floor(sampleX / 2)));
180                 sigma(ctr) = sum(std(centrePiece)) / sum(size(centrePiece)) / sampleX;
181             end
182         %        [rot_angle(ctr), size(centrePiece), sampleX]
183          end
184
185          [val, loc] = min(sigma);
186          best_angle = lower_lim + (loc - 1) * increment;
187          lower_lim = best_angle - increment / 2;
188          upper_lim = best_angle + increment / 2;
189          increment = increment / 10;
190          step = step + 1;
191          % % DEBUG:
192          % figure;
193          % imagesc(imrotate(AFMdata, best_angle));
194          % set(gca,'YDir','normal');
195          % title(strcat('step=', num2str(step), ' \theta=', num2str(best_angle)));
196      end
197
198      disp(strcat('de-Rotate: Minimum sigma of ', num2str(val), ' at ', num2str(rot_angle(loc)), ' degrees.'));
199      rotatedAFMdata = imrotate(AFMdata, rot_angle(loc));
200      % Shrink usable area according to rotation.
201      theta = deg2rad(rot_angle(loc));
202      x_use = floor(abs((x * cos(theta) - y * abs(sin(theta)))) / ...
203          (cos(theta) * cos(theta) - sin(theta) * sin(theta)));
204      y_use = floor(abs((x * abs(sin(theta)) - y * cos(theta))) / ...
205          (cos(theta) * cos(theta) - sin(theta) * sin(theta)));
206      sampleX = x_use;
207      sampleY = y_use;
208      centreRotatedX = floor(x_rot / 2);
209      centreRotatedY = floor(y_rot / 2);
210      centrePiece = rotatedAFMdata((centreRotatedY - floor(sampleY / 2) + 1):(centreRotatedY + floor(sampleY / 2)), (
             centreRotatedX - floor(sampleX / 2) + 1):(centreRotatedX + floor(sampleX / 2)));
211      disp(strcat('Useable dimensions: ', num2str(size(centrePiece, 2)), '_x_', num2str(size(centrePiece, 1))));
212
213      if k.FIGS && k.RAW_ROT_USE,
214          % Show de-rotated image:
215          subplot(1, 3, 2), imagesc(rotatedAFMdata);
216          set(gca,'YDir','normal');
217          title('de-rotated AFM data');
218          xlabel('x (pixels)');
219          ylabel('y (pixels)');
220          axis image;
221          publishPlot;
222
223          % Show usable image area:
224          subplot(1, 3, 3), imagesc(centrePiece);
225          set(gca,'YDir','normal');
226          title('useable AFM data');
227          xlabel('x (pixels)');
228          ylabel('y (pixels)');
229          axis image;
230          publishPlot;
231      end
232  else % No rotation:
233      centrePiece = AFMdata;
234      loc = 1;
235      clear rot_angle;
236      rot_angle(loc) = 0;
237  end
```

```
238
239     if k.AREA_OF_INTEREST,
240         AOIxCentre = 474 / 2; % pixel #
241         AOIyCentre = 80 / 2; % pixel #
242         AOIxRange = 474; % pixels
243         AOIyRange = 80; % pixels
244
245         % DON'T CHANGE!! Unscratched area for 230_1u_plane2.asc:
246         % AOIxCentre = 474 / 2; % pixel #
247         % AOIyCentre = 80 / 2; % pixel #
248         % AOIxRange = 474; % pixels
249         % AOIyRange = 80; % pixels
250
251         % Note: 1 pixel equals sizeOfSample_um / numAFMsamples
252         AOIxLower = round(AOIxCentre - AOIxRange / 2 + 1);
253         AOIxUpper = round(AOIxCentre + AOIxRange / 2);
254         AOIyLower = round(AOIyCentre - AOIyRange / 2 + 1);
255         AOIyUpper = round(AOIyCentre + AOIyRange / 2);
256         centrePiece = centrePiece(AOIyLower:AOIyUpper, AOIxLower:AOIxUpper);
257     end
258
259     if k.FIGS && k.USE,
260         figure;
261         imagesc([0, sizeOfSample_um * size(centrePiece, 2) / numAFMsamples], [0, sizeOfSample_um * size(centrePiece, 1) /
                numAFMsamples], centrePiece);
262         set(gca,'YDir','normal');
263 %         colormap(gray);
264         colormap(autumn);
265 %         title('useable AFM data');
266         xlabel('x (\mum)');
267         ylabel('y (\mum)');
268         publishPlot;
269     end
270
271     % 3 of 4: Display average cross-section:
272     if k.AVERAGE,
273         rawCrossSection = mean(centrePiece);
274         sdCrossSec = std(centrePiece);
275         if k.FIGS && k.XSEC,
276             figure;
277             plot((1:length(rawCrossSection)) / numAFMsamples * sizeOfSample_um, rawCrossSection);
278             hold on;
279             plot((1:length(rawCrossSection)) / numAFMsamples * sizeOfSample_um, sdCrossSec, 'r');
280             if k.ROTATE,
281                 title('AFM-based cross section (rotated, averaged) w Std. Dev.');
282             else
283                 title('AFM-based cross section (averaged) w Std. Dev.');
284             end
285             xlabel('x (\mum)');
286             ylabel('z (nm)');
287             publishPlot;
288         end
289     else
290         rawCrossSection = centrePiece(numAFMsamples / 2, :);
291         sdCrossSec = std(rawCrossSection);
292         if k.FIGS && k.XSEC,
293             figure;
294             plot((1:length(rawCrossSection)) / numAFMsamples * sizeOfSample_um, rawCrossSection);
295             title('AFM-based cross section (raw)');
296             xlabel('x (\mum)');
297             ylabel('z (nm)');
298             publishPlot;
299         end
300     end
301
302     if k.FIGS && k.HYBRID,
303         figure;
304         subplot('position', [.13 .51 .775 .446]),
305         imagesc([0, sizeOfSample_um * size(centrePiece, 2) / numAFMsamples], [0, sizeOfSample_um * size(centrePiece, 1) /
                numAFMsamples], centrePiece);
306         set(gca,'YDir','normal');
307 %         colormap(gray);
308         colormap(autumn);
309 %         title('useable AFM data');
```

```
310         ylabel('y (\mum)'); %, 'position', [-1.967, 9.763, 1]); % Default: [-1.646, 9.763, 1]
311         set(gca, 'XTick', []);
312         xlims = get(gca, 'XLim');
313         publishPlot;
314
315         subplot('position', [.13 .182 .775 .269]),
316         plot((1:length(rawCrossSection)) / numAFMsamples * sizeOfSample_um, rawCrossSection);
317         hold on;
318         if k.AVERAGE,
319             % Show standard deviation of rawCrossSection:
320             plot((1:length(rawCrossSection)) / numAFMsamples * sizeOfSample_um, sdCrossSec, 'r');
321         end
322         xlabel('x (\mum)');
323         ylabel('z (nm)'); %, 'position', [-1.967, -.177, 1]);
324         set(gca, 'XLim', xlims);
325         publishPlot;
326     end
327
328     %
329     if k.FLATTEN,
330         step = 0;
331         lower_lim = -2.5;
332         upper_lim = 2.5;
333         num_iterations = 10;
334         increment = (upper_lim - lower_lim) / num_iterations;
335         num_pts = length(rawCrossSection);
336         x = [-(num_pts / 2 - 0.5):(num_pts / 2 - 0.5)] .* sizeOfSample_um ./ num_pts .* k.NM_PER_UM;
337
338         % Find angle of rotation:
339         while (step < 5),
340             rot_angle = lower_lim:increment:upper_lim;
341             sd = zeros(1, length(rot_angle));
342
343             % Rotate rawCrossSection in increments:
344             for ctr = 1:length(rot_angle),
345                 crossSection = rawCrossSection + x .* tan(deg2rad(rot_angle(ctr)));
346                 % Find the flat plateau above the global mean:
347                 % First, make parts below the mean zero:
348                 flat_part = crossSection .* (crossSection > mean(crossSection));
349                 % Next, remove zeros:
350                 ctr2 = 1;
351                 while ctr2 < length(flat_part),
352                     if flat_part(ctr2) == 0,
353                         flat_part(ctr2) = [];
354                     else
355                         ctr2 = ctr2 + 1;
356                     end
357                 end
358                 % Find the sample standard deviation of points above the
359                 % mean:
360                 sd(ctr) = std(flat_part);
361             end
362             [val, loc] = min(sd);
363             best_angle = rot_angle(loc);
364             if (best_angle <= lower_lim) || (best_angle >= upper_lim),
365                 beep;
366                 error('Error in flattening algorithm - angles too large!');
367                 % break;
368             end
369
370             disp(strcat('Flatten #', num2str(step), ': Minimum sigma of ', num2str(val), ' at ', num2str(rot_angle(loc)), '
                      degrees.'));
371
372             lower_lim = best_angle - increment;
373             upper_lim = best_angle + increment;
374             increment = increment / num_iterations;
375             step = step + 1;
376         end
377         % Rotate crossSection by best angle:
378         crossSection = rawCrossSection + x .* tan(deg2rad(best_angle));
379
380         if k.FIGS && k.FLAT_SMOOTH,
381             figure;
382             plot((1:length(crossSection)) / numAFMsamples * sizeOfSample_um, crossSection);
```

```
383             hold on;
384             plot((1:length(crossSection)) / numAFMsamples * sizeOfSample_um, sdCrossSec, 'r');
385             title('Flattened Cross Section (fine) w Std. Dev.');
386             xlabel('x (\mum)');
387             ylabel('z (nm)');
388             publishPlot;
389 
390             if k.SIGMA,
391                 figure;
392                 plot(rot_angle, sd);
393                 title('std. dev. vs. rotation angle');
394                 publishPlot;
395             end
396         end
397     else
398         % Don't flatten:
399         crossSection = rawCrossSection;
400     end
401     toc
402 
403 % Display fft of cross-section:
404 stepResp = crossSection;
405 N = size(stepResp, 2);
406 stepRespSpectrum = 1 / N * fft(stepResp, N);
407 stepRespSpectrum = fftshift(stepRespSpectrum);
408 
409 % Normalise stepRespSpectrum so that DC intensity == 1:
410 % stepRespSpectrum = stepRespSpectrum ./ max(stepRespSpectrum);
411 
412 stepRespPSD = abs(stepRespSpectrum);
413 strcat('Normalisation is 1 /_', num2str(max(stepRespPSD)))
414 stepRespPSD = stepRespPSD ./ max(stepRespPSD);
415 
416 x_axis = ((1:N) - N / 2 - 1) * numAFMsamples / N / sizeOfSample_um;
417 if k.FIGS && k.SRS,
418     figure;
419     % Depth ~ Intensity ~ t^2 ~E_x^2. i.e. no need to square stepRespPSD.
420     %  semilogy(x_axis, stepRespPSD.^2, 'r');
421     semilogy(x_axis, stepRespPSD, 'r');
422     title('Normalised Step Response Spectrum of Averaged Data');
423     xlabel('k_x / 2\pi (\mum^{-1})');
424     ylabel('Normalised Depth (a. u.)');
425     axis([0 25 1e-4 1e0])
426     publishPlot;
427 end
428 toc
429 
430 % 4 of 4: Display transfer function:
431 % Given a step-response, the impulse response can be found by
432 % differentiating the step-response data in the spatial domain, and then
433 % using the FFT to transform the differentiated data into the frequency
434 % domain.
435 %
436 % Differentiate the step response: diff = (sr(2:N) - sr(1:N - 1)) / dx
437 stepResp1 = stepResp;
438 stepResp2 = stepResp;
439 % Trim first element from stepResp1:
440 stepResp1(:, [1]) = []; %#ok<*NBRAK>
441 % Trim last element from stepResp2:
442 stepResp2(:, [size(stepResp2, 2)]) = [];
443 % NB: stepResp1,2 are smaller than stepResp by 1 element.
444 
445 % % Calculate spatial x-axis:
446 dx = sizeOfSample_um / numAFMsamples;
447 % tf_x_axis = (0:dx:(dx * N)) - (dx * (N / 2 + 1));
448 
449 % Calculate impulse response in spatial domain:
450 % i.e. differentiate step response:
451 impulseResp = (stepResp1 - stepResp2) / dx;
452 
453 % Find transfer function:
454 % impulseRespSpectrum = 1 / numAFMsamples * fft(impulseResp, N); % * dx; <- Multiplying by dx makes amplitude proportional to
        N.
455 impulseRespSpectrum = 1 / (N - 1) * fft(impulseResp, N - 1); % * dx; <- Multiplying by dx makes amplitude proportional to N.
```

```
456 % Normalise impulseRespSpectrum, so that DC intensity == 1:
457 impulseRespSpectrum = impulseRespSpectrum ./ max(impulseRespSpectrum);
458 impulseRespSpectrum = fftshift(impulseRespSpectrum);
459
460 x_axis1 = ((1:size(impulseResp, 2)) - size(impulseResp, 2) / 2 - 1) / sizeOfSample_um;
461
462 if k.FIGS && k.IRS,
463     figure;
464     semilogy(x_axis1, abs(impulseRespSpectrum), 'g');
465     title('Normalised Impulse Response Spectrum');
466     axis([0 25 1e-8 1]);
467     publishPlot;
468 end
469 toc
```

Appendix C

Correlation Coefficient Estimation for Two Height Profiles with Random Phase Offset

The Matlab source code used to implement the correlation coefficient calculation technique discussed in Section 7.4.3.1 is given in Listing C.1. For input, the code relies on data structures generated by the AFM data processing file discussed in Appendix B. Output is the maximum correlation coefficient between a section of the input profile and the output profile. The offsets to the section in the input profile as well to the part of the output profile that corresponds to the maximum correlation coefficient are also given.

Listing C.1: measureRho.m

```
% measureRho.m
%
% File to calculate correlation coefficient between two AFM profiles.
%
% Author: C. P. Moore
% 05 March 2012
%
% Run measureTF.m (and its child, getAFM.m) first.
% measureTFcorr.m uses crossSection_img and crossSection_obj data from
% measureTF.m.
%
% Output is maximum correlation coefficient, as well as offset data for
% _obj and _img profiles that gives  maximum correlation coefficient.
%

img = crossSection_img;

%% For equal sized mask and PR scans:
obj = crossSection_obj;

```

```
%% For 10 um period mask and 20 um PR scans:
% XS_obj2 =crossSection_obj(2:2:508);
% obj = XS_obj2;

PERIODS_PER_PROFILE = 3; % Nominal number of periods in each crossSection profile. Set to 3 for 10 um Mask data, 5 otherwise.
XS_size = min(length(obj), length(img));
% Sample size is at least one period of data:
sample_size = round(XS_size / (PERIODS_PER_PROFILE - 1));


%% Number of points at which to look for correlation:
scan_size = XS_size - sample_size;

c = zeros(2);
c_max = 0;
c_abs_max = 0;
tic
% Scan along img:
for ctr2 = 1:scan_size,
  % Progress indicator:
  disp(strcat(num2str(ctr2), ' of ', num2str(scan_size)));
  % scan along obj:
  for ctr = 1:scan_size,
%     for ctr = 1:1,
    c = corrcoef(obj(ctr:(ctr + sample_size)), img(ctr2:(ctr2 + sample_size)));
    if c(1, 2) > c_max,
      c_max = c(1, 2);
      k1 = ctr;
      k2 = ctr2;
    end
%     if abs(c(1, 2)) > c_abs_max,
%         c_abs_max = abs(c(1, 2));
%         k1_abs = ctr;
%         k2_abs = ctr2;
%     end
  end
end
toc

c_max
k1
k2

% c_abs_max
% k1_abs
% k2_abs

figure;
hold on;
% Show obj:
plot(obj(k1:(k1 + sample_size)));
% Show img:
plot(img(k2:(k2 + sample_size)), 'r');


% Note: cov = corrcoef(X,Y) = cov(X,Y) / (std(X) * std(Y))
```

Bibliography

[1] D. E. Liddle, "The wider impact of Moore's law," *Solid-State Circuits Newsletter*, vol. 20, no. 3, pp. 28–30, September 2006.

[2] R. P. Feynman, "There's plenty of room at the bottom," *Engineering and Science Magazine*, vol. 23, no. 5, February 1960.

[3] G. E. Moore, "Cramming more components onto integrated circuits," *Electronics*, vol. 38, no. 8, April 1965.

[4] International Technology Roadmap for Semiconductors, http://www.intel.com/technology/silicon/itroadmap.htm, retrieved 25 March 2011.

[5] Wgsimon, transistor Count and Moore's Law - 2008, https://secure.wikimedia.org/wikipedia/en/wiki/File:Transistor_Count_and_Moore%27s_Law_-_2008.svg, retrieved on 25 March 2011.

[6] C. Mack, *Fundamental principles of optical lithography: the science of microfabrication*. John Wiley and Sons, Inc., 2007.

[7] D. O. S. Melville, "Planar lensing lithography: Enhancing the optical near field," Ph.D. dissertation, University of Canterbury, Christchurch, Canterbury, New Zealand, February 2006.

[8] O. Alexandrov, numerical aperture, https://secure.wikimedia.org/wikipedia/en/wiki/File:Numerical_aperture.svg, retrieved on 30 March 2011.

[9] S. H. Zaidi and S. R. J. Brueck, "Multiple-exposure interferometric lithography," *Journal of Vacuum Science and Technology B*, vol. 11, no. 3, pp. 658–666, May 1993.

[10] M. Switkes and M. Rothschild, "Resolution enhancement of 157 nm lithography by liquid immersion," *Journal of Micro/Nanolithography, MEMS and MOEMS*, vol. 1, no. 3, p. 225, May 2002.

[11] T. M. Bloomstein, M. Rothschild, R. R. Kunz, D. E. Hardy, R. B. Goodman, and S. T. Palmacci, "Critical issues in 157 nm lithography," *Journal of Vacuum Science and Technology B*, vol. 16, no. 6, pp. 3154–3157, September 1998.

[12] B. Wu and A. Kumar, "Extreme ultraviolet lithography: a review," *Journal of Vacuum Science and Technology B*, vol. 25, no. 6, p. 1743, October 2007.

[13] G. R. Brewer and J. P. Ballantyne, *Electron-beam technology in microelectronic fabrication*. Academic Press, 1980.

[14] M. Komuro and S. Matsui, *Sub-Half-Micron Lithography for ULSIs*. Cambridge, United Kingdom: Cambridge University Press, 2000, ch. Ion-beam lithography.

[15] S. Y. Chou, P. R. Krauss, and P. J. Renstrom, "Imprint lithography with 25-nanometer resolution," *Science*, vol. 272, no. 5258, pp. 85–87, April 1996.

[16] M. LaPedus, "Nikon tips 193-nm immersion tool, illuminator," EE Times Europe Business News, February 2011. [Online]. Available: http://eetimes.eu/en/nikon-tips-193-nm-immersion-tool-illuminator.html?cmp_id=7&news_id=222906140

[17] ——, "Inside intel's litho strategy at 22-nm," EE Times News & Analysis, March 2010. [Online]. Available: http://www.eetimes.com/electronics-news/4088119/Inside-Intel-s-litho-strategy-at-22-nm

[18] M. M. Alkaisi, R. J. Blaikie, S. J. McNab, R. Cheung, and D. R. S. Cumming, "Sub-diffraction-limited patterning using evanescent near-field optical lithography," *Applied Physics Letters*, vol. 75, no. 22, pp. 3560–3562, November 1999.

[19] T. Ito, T. Yamada, Y. Inao, T. Yamaguchi, N. Mizutani, and R. Kuroda, "Fabrication of half-pitch 32 nm resist patterns using near-field lithography with *a*-si mask," *Applied Physics Letters*, vol. 89, no. 3, p. 033113, July 2006.

[20] J. B. Pendry, "Negative refraction makes a perfect lens," *Physical Review Letters*, vol. 85, no. 18, pp. 3966–3969, October 2000.

[21] D. O. S. Melville, R. J. Blaikie, and C. R. Wolf, "Submicron imaging with a planar silver lens," *Applied Physics Letters*, vol. 84, no. 22, pp. 4403–4405, May 2004.

[22] D. O. S. Melville and R. J. Blaikie, "Super-resolution imaging through a planar silver layer," *Optics Express*, vol. 13, no. 6, pp. 2127–2134, March 2005.

[23] N. Fang, H. Lee, C. Sun, and X. Zhang, "Sub-diffraction-limited optical imaging with a silver superlens," *Science*, vol. 308, pp. 534–537, April 2005.

[24] P. Chaturvedi, W. Wu, V. J. Logeeswaran, Z. Yu, M. S. Islam, S. Y. Wang, R. S. Williams, and N. X. Fang, "A smooth optical superlens," *Applied Physics Letters*, vol. 96, no. 4, p. 043102, January 2010.

[25] S. A. Ramakrishna, J. B. Pendry, M. C. K. Wiltshire, and W. J. Stewart, "Imaging the near field," *Journal of Modern Optics*, vol. 50, no. 1, pp. 1419–1430, June 2003.

[26] D. R. Smith, D. Schurig, M. Rosenbluth, S. Schultz, S. A. Ramakrishna, and J. B. Pendry, "Limitations on sub-diffraction imaging with a negative refractive index slab," *Applied Physics Letters*, vol. 82, p. 1506, 2003.

[27] S. A. Ramakrishna, "Physics of negative refractive index materials," *Reports on Progress in Physics*, vol. 68, pp. 449–521, January 2005.

[28] D. O. S. Melville and R. J. Blaikie, "Experimental comparison of resolution and pattern fidelity in single- and double-layer planar lens lithography," *Journal of the Optical Society of America B: Optical Physics*, vol. 23, no. 3, pp. 461–467, March 2006.

[29] T. Yamaguchi, T. Yamada, A. Terao, T. Ito, Y. Inao, N. Mizutani, and R. Kuroda, "Fabrication of hp 32 nm resist patterns using near-field lithography," *Microelectronic Engineering*, vol. 84, no. 5, pp. 690–693, May 2007, proceedings of the 32nd International Conference on Micro- and Nano-Engineering.

[30] C. P. Moore, M. D. Arnold, P. J. Bones, and R. J. Blaikie, "Image fidelity for single-layer and multi-layer silver superlenses," *Journal of the Optical Society of America A: Optics, Image Science and Vision*, vol. 25, no. 4, pp. 911–918, April 2008.

[31] C. P. Moore, R. J. Blaikie, and M. D. Arnold, "An improved transfer-matrix model for optical superlenses," *Optics Express*, vol. 17, no. 16, pp. 14 260–14 269, July 2009.

[32] C. P. Moore and R. J. Blaikie, "Plasmonic superlenses: theory, practice and recent developments," *Asian Journal of Physics*, vol. 18, no. 1, pp. 7–16, 2009.

[33] K. Iizuka, *Engineering Optics*, 3rd ed. New York, United States of America: Springer, 2008.

[34] O. Alexandrov, snell's law, http://upload.wikimedia.org/wikipedia/commons/3/3f/Snells_law2.svg, retrieved on 5 April 2011.

[35] "Codata value: Speed of light in vacuum," the NIST reference on Constants, Units, and Uncertainty. NIST. http://physics.nist.gov/cgi-bin/cuu/Value?c, retrieved on 4 April 2011.

[36] V. G. Veselago, "The electrodynamics of substances with simultaneously negative values of ϵ and μ," *Soviet Physics Uspekhi*, vol. 10, no. 4, pp. 509–514, 1968.

[37] I. M. Frank, "A conceptual history of the Vavilov-Cherenkov radiation," *Soviet Physics Uspekhi*, vol. 27, no. 5, p. 385, May 1984.

[38] J. B. Pendry, A. J. Holden, D. J. Robbins, and W. J. Stewart, "Magnetism from conductors and enhanced nonlinear phenomena," *IEEE Transactions on Microwave Theory and Techniques*, vol. 47, no. 11, pp. 2075–2084, November 1999.

[39] J. B. Pendry, A. J. Holden, W. J. Stewart, and I. Youngs, "Extremely low frequency plasmons in metallic mesostructures," *Physical Review Letters*, vol. 76, pp. 4773–4776, June 1996.

[40] J. B. Pendry, A. J. Holden, D. J. Robbins, and W. J. Stewart, "Low frequency plasmons in thin-wire structures," *Journal of Physics: Condensed Matter*, vol. 10, no. 22, pp. 4785–4809, March 1998.

[41] R. A. Shelby, D. R. Smith, S. C. Nemat-Nasser, and S. Schultz, "Microwave transmission through a two-dimensional, isotropic, left-handed metamaterial," *Applied Physics Letters*, vol. 78, no. 4, pp. 489–491, January 2001.

[42] D. R. Smith, W. J. Padilla, D. C. Vier, S. C. Nemat-Nasser, and S. Schultz, "Composite medium with simultaneously negative permeability and permittivity," *Physical Review Letters*, vol. 84, pp. 4184–4187, May 2000.

[43] R. A. Shelby, D. R. Smith, and S. Schultz, "Experimental verification of a negative index of refraction," *Science*, vol. 292, no. 5514, pp. 77–79, April 2001.

[44] D. R. Smith, J. B. Pendry, and M. C. K. Wilthsire, "Metamaterials and negative refractive index," *Science*, vol. 305, no. 5685, pp. 788–792, August 2004.

[45] G. W. 't Hooft, "Comment on negative refraction makes a perfect lens," *Physical Review Letters*, vol. 87, no. 24, p. 249701, November 2001.

[46] J. B. Pendry, "Pendry replies:," *Physical Review Letters*, vol. 87, no. 24, p. 249702, November 2001.

[47] J. M. Williams, "Some problems with negative refraction," *Physical Review Letters*, vol. 87, no. 24, p. 249703, November 2001.

[48] J. B. Pendry, "Pendry replies:," *Physical Review Letters*, vol. 87, no. 24, p. 249704, November 2001.

[49] N. Garcia and M. Nieto-Vesperinas, "Left-handed materials do not make a perfect lens," *Physical Review Letters*, vol. 88, no. 20, p. 207403, May 2002.

[50] ——, "Is there an experimental verification of a negative index of refraction yet?" *Optics Letters*, vol. 27, no. 11, pp. 885–887, 2002.

[51] J. B. Pendry, "Comment on left-handed materials do not make a perfect lens," *Physical Review Letters*, vol. 91, no. 9, p. 099701, August 2003.

[52] M. Nieto-Vesperinas and N. Garcia, "Nieto-Vesperinas and Garcia reply:," *Physical Review Letters*, vol. 91, no. 9, p. 099702, August 2003.

[53] M. C. K. Wilthsire, "Bending light the wrong way," *Science*, vol. 292, no. 5514, pp. 60–61, April 2001.

[54] A. Kumar and G. M. Whitesides, "Features of gold having micrometer to centimeter dimensions can be formed through a combination of stamping with an elastomeric stamp and an alkanethiol "ink" followed by chemical etching," *Applied Physics Letters*, vol. 63, no. 14, pp. 2002–2004, October 1993.

[55] J. A. Rogers, K. E. Paul, R. J. Jackman, and G. M. Whitesides, "Using an elastomeric phase mask for sub-100 nm photolithography in the optical near field," *Applied Physics Letters*, vol. 70, no. 20, pp. 2658–2660, May 1997.

[56] J. Aizenberg, J. A. Rogers, K. E. Paul, and G. M. Whitesides, "Imaging the irradiance distribution in the optical near field," *Applied Physics Letters*, vol. 71, no. 26, pp. 3773–3775, December 1997.

[57] M. M. Alkaisi, R. J. Blaikie, and S. J. McNab, "Nanolithography using wet etched silicon nitride phase masks," *Journal of Vacuum Science and Technology B*, vol. 16, no. 6, pp. 3929–3933, November 1998.

[58] J. G. Goodberlet and H. Kavak, "Patterning sub-50 nm features with near-field embedded-amplitude masks," *Applied Physics Letters*, vol. 81, no. 7, pp. 1315–1317, 2002.

[59] T. Ito, M. Ogino, T. Yamanaka, Y. Inao, T. Yamaguchi, N. Mizutani, and R. Kuroda, "Fabrication of sub-100 nm patterns using near-field mask lithography with ultra-thin resist process," *Journal of Photopolymer Science and Technology*, vol. 18, no. 3, pp. 435–441, May 2005.

[60] V. M. Shalaev, "Optical negative-index metamaterials," *Nature Photonics*, vol. 1, no. 1, pp. 41–48, January 2007.

[61] V. G. Veselago and E. E. Narimanov, "The left hand of brightness: past, present and future of negative index materials," *Nature Materials*, vol. 5, no. 10, pp. 759–762, October 2006.

[62] R. Merlin, "Radiationless electromagnetic interference: Evanescent-field lenses and perfect focusing," *Science*, vol. 317, no. 5840, pp. 927–929, August 2007.

[63] D. O. S. Melville and R. J. Blaikie, "Analysis and optimization of multilayer silver superlenses for near-field optical lithography," *Physica B: Condensed Matter*, vol. 394, pp. 197–202, May 2007.

[64] Z. Liu, S. Durant, H. Lee, Y. Pikus, N. Fang, Y. Xiong, C. Sun, and X. Zhang, "Far-field optical superlens," *Nano Letters*, vol. 7, no. 2, pp. 403–408, January 2007.

[65] X. Wei, X. Luo, X. Dong, and C. Du, "Localized surface plasmon nanolithography with ultrahigh resolution," *Optics Express*, vol. 15, no. 21, pp. 14 177–14 183, October 2007.

[66] W. Srituravanich, N. Fang, C. Sun, Q. Luo, and X. Zhang, "Plasmonic nanolithography," *Nano Letters*, vol. 4, no. 6, pp. 1085–1088, June 2004.

[67] P.-Y. Chen and S.-C. Wu, "A periodic porous-nanostructured left-handed material slab at optical frequencies," *Microwave and Optical Technology Letters*, vol. 50, no. 1, pp. 216–220, January 2008.

[68] A. J. Hoffman, L. V. Alekseyev, S. S. Howard, K. J. Franz, D. Wasserman, V. A. Podolskiy, E. E. Narimanov, D. L. Sivco, and C. Gmachl, "Negative refraction in semiconductor metamaterials," *Nature Materials*, vol. 6, no. 12, pp. 946–950, December 2007.

[69] J. Kästel, M. Fleischhauer, S. F. Yelin, and R. L. Walsworth, "Tunable negative refraction without absorption via electromagnetically induced chirality," *Physical Review Letters*, vol. 99, no. 7, p. 073602, 2007.

[70] N. Fang, D. Xi, J. Xu, M. Ambati, W. Srituravanich, C. Sun, and X. Zhang, "Ultrasonic metamaterials with negative modulus," *Nature Materials*, vol. 5, no. 6, pp. 452–456, June 2006.

[71] U. Leonhardt, "Optical conformal mapping," *Science*, vol. 312, no. 5781, pp. 1777–1780, June 2006.

[72] J. B. Pendry, D. Schurig, and D. R. Smith, "Controlling electromagnetic fields," *Science*, vol. 312, no. 5781, pp. 1780–1782, June 2006.

[73] X. Wang, Z. Ren, and K. Kempa, "Unrestricted superlensing in a triangular two dimensional photonic crystal," *Optics Express*, vol. 12, no. 13, pp. 2919–2924, June 2004.

[74] Z. Lu, J. A. Murakowski, C. A. Schuetz, S. Shi, G. J. Schneider, and D. W. Prather, "Three-dimensional subwavelength imaging by a photonic-crystal flat lens using negative refraction at microwave frequencies," *Physical Review Letters*, vol. 95, no. 15, p. 153901, 2005.

[75] C. Luo, S. G. Johnson, J. D. Joannopoulos, and J. B. Pendry, "Subwavelength imaging in photonic crystals," *Physical Review B: Condensed Matter and Material Physics*, vol. 68, no. 4, p. 045115, July 2003.

[76] ——, "All-angle negative refraction without negative effective index," *Physical Review B: Condensed Matter and Material Physics*, vol. 65, no. 20, p. 201104, May 2002.

[77] E. Shamonina, V. A. Kalinin, K. H. Ringhofer, and L. Solymar, "Imaging, compression and poynting vector streamlines for negative permittivity materials," *Electronics Letters*, vol. 37, no. 20, pp. 1243–1244, September 2001.

[78] P. A. Belov and Y. Hao, "Subwavelength imaging at optical frequencies using a transmission device formed by a periodic layered metal-dielectric structure operating in the canalization regime," *Physical Review B: Condensed Matter and Material Physics*, vol. 73, no. 11, p. 113110, March 2006.

[79] L. V. J., N. P. Kobayashi, M. S. Islam, W. Wu, P. Chaturvedi, N. X. Fang, S. Y. Wang, and R. S. Williams, "Ultrasmooth silver thin films deposited with a germanium nucleation layer," *Nano Letters*, vol. 9, no. 1, pp. 178–182, 2009.

[80] M. Tsang and D. Psaltis, "Theory of resonantly enhanced near-field imaging," *Optics Express*, vol. 15, no. 19, pp. 11 959–11 970, September 2007.

[81] S. A. Ramakrishna, J. B. Pendry, D. Schurig, D. R. Smith, and S. Schultz, "The asymmetric lossy near-perfect lens," *Journal of Modern Optics*, vol. 49, no. 10, pp. 1747–1762, August 2002.

[82] J. A. Porto, F. J. García-Vidal, and J. B. Pendry, "Transmission resonances on metallic gratings with very narrow slits," *Physical Review Letters*, vol. 83, no. 14, pp. 2845–2848, October 1999.

[83] T. W. Ebbesen, H. J. Lezec, H. F. Ghaemi, T. Thio, and P. A. Wolff, "Extraordinary optical transmission through sub-wavelength hole arrays," *Nature*, vol. 391, no. 6668, pp. 667–669, February 1998.

[84] T. Xu, C. Du, C. Wang, and X. Luo, "Subwavelength imaging by metallic slab lens with nanoslits," *Applied Physics Letters*, vol. 91, no. 20, p. 201501, 2007.

[85] S. Zhang, W. Fan, N. C. Panoiu, K. J. Malloy, R. M. Osgood, and S. R. Brueck, "Optical negative-index bulk metamaterials consisting of 2D perforated metal-dielectric stacks," *Optics Express*, vol. 14, no. 15, pp. 6778–6787, July 2006.

[86] S. Durant, Z. Liu, N. Fang, and X. Zhang, "Theory of optical imaging beyond the diffraction limit with a far-field superlens," in *Plasmonics: Metallic Nanostructures and their Optical Properties IV. Proceedings of the SPIE.*, ser. Presented at the Society of Photo-Optical Instrumentation Engineers (SPIE) Conference, M. I. Stockman, Ed., vol. 6323, September 2006, p. 63231H.

[87] S. Durant, Z. Liu, J. M. Steele, and X. Zhang, "Theory of the transmission properties of an optical far-field superlens for imaging beyond the diffraction limit," *Journal of the Optical Society of America B: Optical Physics*, vol. 23, no. 11, pp. 2383–2392, November 2006.

[88] T. R. M. Sales and G. M. Morris, "Fundamental limits of optical superresolution," *Optics Letters*, vol. 22, no. 9, pp. 582–584, 1997.

[89] M. G. Blaber, M. D. Arnold, N. Harris, M. J. Ford, and M. B. Cortie, "Plasmon absorption in nanospheres: A comparison of sodium, potassium, aluminium, silver and gold," *Physica B: Condensed Matter*, vol. 394, no. 2, pp. 184–187, May 2007.

[90] J. Liu, K. E. McBean, N. Harris, and M. B. Cortie, "Optical properties of suspensions of gold half-shells," *Materials Science and Engineering B*, vol. 140, no. 3, pp. 195–198, June 2007.

[91] T. Taubner, D. Korobkin, Y. Urzhumov, G. Shvets, and R. Hillenbrand, "Near-field microscopy through a SiC superlens," *Science*, vol. 313, no. 5793, p. 1595, September 2006.

[92] S. Hrabar, Z. Eres, and J. Bartolic, "Capacitively loaded loop as basic element of negative permeability meta-material," *Proceedings of the 32nd European Microwave Conference*, pp. 327–330, October 2002.

[93] E. Shamonina, V. A. Kalinin, K. H. Ringhofer, and L. Solymar, "Magnetoinductive waves in one, two, and three dimensions," *Journal of Applied Physics*, vol. 92, no. 10, pp. 6252–6261, November 2002.

[94] C. R. Simovski and S. He, "Frequency range and explicit expressions for negative permittivity and permeability for an isotropic medium formed by a lattice of perfectly conducting ω particles," *Physics Letters A*, vol. 311, no. 2-3, pp. 254–263, May 2003.

[95] M. Shamonin, E. Shamonina, V. Kalinin, and L. Solymar, "Properties of a metamaterial element: Analytical solutions and numerical simulations for a singly split double ring," *Journal of Applied Physics*, vol. 95, no. 7, pp. 3778–3784, April 2004.

[96] M. Scalora, G. D'Aguanno, M. Bloemer, M. Centini, D. de Ceglia, N. Mattiucci, and Y. S. Kivshar, "Dynamics of short pulses and phase matched second harmonic generation in negative index materials," *Optics Express*, vol. 14, no. 11, pp. 4746–4756, May 2006.

[97] A. Husakou and J. Herrmann, "Steplike transmission of light through a metal-dielectric multilayer structure due to an intensity-dependent sign of the effective dielectric constant," *Physical Review Letters*, vol. 99, no. 12, p. 127402, 2007.

[98] I. I. Smolyaninov, Y.-J. Hung, and C. C. Davis, "Magnifying superlens in the visible frequency range," *Science*, vol. 315, no. 5819, pp. 1699–1701, March 2007.

[99] A. D. Boardman, P. Egan, L. Velasco, and N. King, "Control of planar nonlinear guided waves and spatial solitons with a left-handed medium," *Journal of Optics A: Pure and Applied Optics*, vol. 95, no. 7, pp. 3778–3784, April 2004.

[100] D. Schurig, J. J. Mock, B. J. Justice, S. A. Cummer, J. B. Pendry, A. F. Starr, and D. R. Smith, "Metamaterial electromagnetic cloak at microwave frequencies," *Science*, vol. 314, no. 5801, pp. 977–980, November 2006.

[101] Y. Huang, Y. Feng, and T. Jiang, "Electromagnetic cloaking by layered structure of homogeneous isotropic materials," *Optics Express*, vol. 15, no. 18, pp. 11 133–11 141, September 2007.

[102] K. Guven, E. Saenz, R. Gonzalo, E. Ozbay, and S. Tretyakov, "Electromagnetic cloaking with canonical spiral inclusioins," *New Journal of Physics*, vol. 10, p. 115037, November 2008.

[103] N. A. Zharova, I. V. Shadrivov, and Y. S. Kivshar, "Inside-out electromagnetic cloaking," *Optics Express*, vol. 16, no. 7, pp. 4615–4620, March 2008.

[104] F. Bilotti, S. Tricarico, and L. Vegni, "Electromagnetic cloaking devices for TE and TM polarizations," *New Journal of Physics*, vol. 10, no. 11, p. 115035, November 2008.

[105] A. Greenleaf, Y. Kurylev, M. Lassas, and G. Uhlmann, "Electromagnetic wormholes and virtual magnetic monopoles from metamaterials," *Physical Review Letters*, vol. 99, no. 18, p. 183901, August 2007.

[106] W. Cai, U. K. Chettiar, A. V. Kildishev, and V. M. Shalaev, "Nonmagnetic cloak with minimized scattering," *Applied Physics Letters*, vol. 91, no. 4, p. 111105, September 2007.

[107] M. Fox, "Invisibility device possible, in theory," Reuters, 26 May 2006. [Online]. Available: http://www.abc.net.au/science/articles/2006/05/26/1648328.htm

[108] I. Sample, "Cloaking device makes objects invisible — to infrared light anyway," 18 March 2010. [Online]. Available: http://www.guardian.co.uk/science/2010/mar/18/cloaking-device-objects-invisible-infrared

[109] G. Gbur, "Nonradiating sources and other "invisible" objects," *Progress in Optics*, vol. 45, pp. 273–315, 2003.

[110] S. A. Cummer, B.-I. Popa, D. Schurig, D. R. Smith, and J. Pendry, "Full-wave simulations of electromagnetic cloaking structures," *Physical Review E: Statistical, Nonlinear, and Soft Material Physics*, vol. 74, no. 036621, September 2006.

[111] S. A. Cummer, B.-I. Popa, D. Schurig, D. R. Smith, J. Pendry, M. Rahm, and A. Starr, "Scattering theory derivation of a 3D acoustic cloaking shell," *Physical Review Letters*, vol. 100, p. 024301, January 2008.

[112] T. Ergin, N. Stenger, P. Brenner, J. B. Pendry, and M. Wegener, "Three-dimensional invisibility cloak at optical wavelengths," *Science*, vol. 328, no. 5976, pp. 337–339, April 2010.

[113] H. Kosaka, T. Kawashima, A. Tomita, M. Notomi, T. Tamamura, T. Sato, and S. Kawakami, "Superprism phenomena in photonic crystals," *Physical Review B: Condensed Matter and Material Physics*, vol. 58, no. 16, pp. R10 096–R10 099, October 1998.

[114] M. Notomi, "Theory of light propagation in strongly modulated photonic crystals: Refractionlike behavior in the vicinity of the photonic band gap," *Physical Review B: Condensed Matter and Material Physics*, vol. 62, no. 16, pp. 10 696–10 705, October 2000.

[115] E. Cubukcu, K. Aydin, E. Ozbay, S. Foteinopolou, and C. M. Soukoulis, "Subwavelength resolution in a two-dimensional photonic-crystal-based superlens," *Physical Review Letters*, vol. 91, no. 20, p. 207401, November 2003.

[116] P. A. Belov, C. R. Simovski, and P. Ikonen, "Canalization of subwavelength images by electromagnetic crystals," *Physical Review B: Condensed Matter and Material Physics*, vol. 71, no. 19, p. 193105, May 2005.

[117] M. Schøler and R. J. Blaikie, "Simulations of surface roughness effects in planar superlenses," *Journal of Optics A: Pure and Applied Optics*, vol. 11, no. 10, p. 105503, August 2009.

[118] S. Ramo, J. R. Whinnery, and T. van Duzer, "Plane-wave propagation and reflection," in *Fields and waves in communication electronics*, 3rd ed. John Wiley and Sons, Inc., 1994, pp. 300–309.

[119] W. H. Hayt and J. A. Buck, *Engineering Electromagnetics*, 7th ed. Boston, Massachusetts, United States of America: McGraw-Hill, 2006.

[120] N. Fang and X. Zhang, "Imaging properties of a metamaterial superlens," *Applied Physics Letters*, vol. 82, no. 2, pp. 161–163, January 2003.

[121] Matlab is a registered trademark of The MathWorks, Inc., ©1984–2009.

[122] COMSOL is a registered trademark of COMSOL AB, ©1997–2010.

[123] P. Bienstman, "Rigorous and efficient modelling of wavelength scale photonic components," Ph.D. dissertation, Ghent University, Ghent, Belgium, 2002.

[124] COMSOL Multiphysics RF Module User's Guide, November 2008, ©1998–2008.

[125] M. W. Parker, *Pysics of Optoelectronics*. Boca Raton, Florida, United States of America: CRC Press, 2005.

[126] P. P. Silvester and R. L. Ferrari, *Finite Elements for Electrical Engineers*, 3rd ed. Cambridge, United Kingdom: Cambridge University Press, 1996.

[127] M. N. O. Sadiku, *Numerical techniques in electromagnetics*, 2nd ed. Boca Raton, Florida, United States of America: CRC Press, 2000.

[128] D. R. Lide, *The CRC handbook of chemistry and physics*, 88th ed. Boca Raton London New York Washington, DC: CRC Press, 2008.

[129] P. B. Johnson and R. W. Christy, "Optical constants of the noble metals," *Physical Review B: Condensed Matter and Material Physics*, vol. 6, no. 12, pp. 4370–4379, December 1972.

[130] Optical parameters of photoresists application note, revised 27 January 2010 © MicroChemicals GmbH.
http://www.microchemicals.eu/technical_information/photoresists_optical_parameters.pdf, retrieved on 27 June 2010.

[131] AZ BARLi II Bottom Antireflective Coating data sheet © AZ Electronic Materials.
http://www.az-em.com/PDFs/barli_ll/az_barli_ii.pdf, retrieved on 28 May 2010.

[132] G. Ghosh, "Dispersion-equation coefficients for the refractive index and birefringence of calcite and quartz crystals," *Optics Communications*, vol. 163, pp. 95–102, May 1999.

[133] P. Chaturvedi and N. X. Fang, "Molecular scale imaging with a multilayer superlens," *Material Research Society Symposium Proceedings*, vol. 919, pp. 0919–J04–07, May 2006.

[134] R. Carminati, J. J. Sáenz, J.-J. Greffet, and M. Nieto-Vesperinas, "Reciprocity, unitarity, and time-reversal symmetry of the s matrix of fields containing evanescent components," *Physical Review A*, vol. 62, no. 1, p. 012712, June 2000.

[135] I. Karnadi, A. A. Iskandar, and M.-O. Tjia, "Analysis of Ag-superlens performances using spatial convolution formulation," *Journal of the Optical Society of America A: Optics, Image Science and Vision*, vol. 27, no. 2, pp. 268–275, February 2010.

[136] R. Kotyński, "Fourier optics approach to imaging with sub-wavelength resolution through metal-dielectric multilayers," *Opto-Electronics Review*, vol. 18, no. 4, pp. 366–375, June 2010, arXiv:1006.3669v1 [physics.optics].

[137] G. Li, J. Li, H. L. Tam, C. T. Chan, and K. W. Cheah, "Near field imaging with resonant cavity lens," *Optics Express*, vol. 18, no. 3, pp. 2325–2331, February 2010.

[138] M. Maldovan, M. R. Bockstaller, E. L. Thomas, and W. C. Carter, "Validation of the effective-medium approximation for the dielectric permittivity of oriented nanoparticle-filled materials: effective permittivity for dielectric nanoparticles in multilayer photonic composites," *Journal of Applied Physics B*, vol. 76, no. 8, pp. 877–884, July 2003.

[139] A. Moroz, "A recursive transfer-matrix solution for a dipole radiating inside and outside a stratified sphere," *Annals of Physics*, vol. 315, no. 2, pp. 352–418, 2005.

[140] P. Pereyra, "Resonant tunneling and band mixing in multichannel superlattices," *Physical Review Letters*, vol. 80, no. 12, pp. 2677–2680, March 1998.

[141] P. Pereyra, A. Robledo-Martinez, and M. Morales-Luna, "The effect of complex and negative indices in the transmission of electromagnetic waves through superlattices," *Microelectronics Journal*, vol. 39, no. 3-4, pp. 394 – 397, March 2008, the Sixth International Conference on Low Dimensional Structures and Devices - LDSD'07.

[142] M. Scalora, M. J. Bloemer, A. S. Pethel, J. P. Dowling, C. M. Bowden, and A. S. Manka, "Transparent, metallo-dielectric, one-dimensional, photonic band-gap structures," *Journal of Applied Physics*, vol. 83, no. 5, pp. 2377–2383, 1998.

[143] S. Shi, Z. Zhang, M. He, X. Li, J. Yang, and J. Du, "Analysis of surface-plasmon-polaritons-assisted interference imaging by using silver film with rough surface," *Optics Express*, vol. 18, no. 10, pp. 10 685–10 693, May 2010.

[144] S. J. McNab and R. J. Blaikie, "Contrast in the evanescent near field of $\lambda/20$ period gratings for photolithography," *Applied Optics*, vol. 39, no. 1, pp. 20–25, January 2000.

[145] A. A. Michelson, *Studies in optics*. Chicago, Illinois, United States of America: University of Chicago Press, 1962.

[146] H. Lohninger, *Teach/Me Data Analysis*. Berlin, New York, Tokyo: Springer-Verlag, 1999.

[147] H. Abdi, *Encyclopedia of Measurement and Statistics*. Thousand Oaks, California, United States of America: Sage, 2007, ch. Coefficients of Correlation, Alienation and Determination, pp. 158–162.

[148] S. Durant, N. Fang, and X. Zhang, "Comment on "submicron imaging with a planar silver lens" [Appl. Phys. Lett. 84, 4403 (2004)]," *Applied Physics Letters*, vol. 86, p. 126101, March 2005.

[149] E. D. Palik, Ed., *Handbook of Optical Constants of Solids*, 3rd ed. San Diego, United States of America: Academic Press, 1998.

[150] C. P. Moore, R. J. Blaikie, and M. D. Arnold, "Improved analytical models for single- and multi-layer silver superlenses," *Material Research Society Symposium Proceedings*, vol. 1182, April 2009.

[151] P. Andrew and W. L. Barnes, "Energy transfer across a metal film mediated by surface plasmon polaritons," *Science*, vol. 306, no. 5698, pp. 1002–1005, November 2004.

[152] O. S. Heavens, *Optical properties of thin solid films*. London, United Kingdom: Butterworths Scientific Publications, 1955.

[153] J. Jia, *The finite element method for electromagnetics*. New York, United States of America: John Wiley and Sons, Inc., 1993.

[154] K. Lee, Y. Jung, G. Kang, H. Park, and K. Kim, "Active phase control of a Ag near-field superlens via the index mismatch approach," *Applied Physics Letters*, vol. 94, no. 10, March 2009.

[155] J. B. Pendry and A. MacKinnon, "Calculation of photon dispersion relations," *Physical Review Letters*, vol. 69, no. 19, pp. 2772–2775, November 1992.

[156] L. C. Botten, M. S. Craig, R. C. McPhedran, J. L. Adams, and J. R. Andrewartha, "The dielectric lamellar diffraction grating," *Optica Acta*, vol. 28, no. 3, pp. 413–428, 1981.

[157] ——, "The finitely conducting lamellar diffraction grating," *Optica Acta*, vol. 28, no. 8, pp. 1087–1102, 1981.

[158] L. C. Botten, M. S. Craig, and R. C. McPhedran, "Highly conducting lamellar diffraction gratings," *Journal of Modern Optics*, vol. 28, no. 8, pp. 1087–1102, August 1981.

[159] M. G. Moharam, E. B. Grann, D. A. Pommet, and T. K. Gaylord, "Formulation for stable and efficient implementation of the rigorous coupled-wave analysis of binary gratings," *Journal of the Optical Society of America A: Optics, Image Science and Vision*, vol. 12, no. 5, pp. 1068–1076, May 1995.

[160] J. C. Maxwell-Garnett, "Colours in metal glasses and metal films," *Philosophical Transactions of the Royal Society of London, Series A*, vol. 203, pp. 385–420, June 1904.

[161] K. Busch and C. M. Soukoulis, "Transport properties of random media: A new effective medium theory," *Physical Review Letters*, vol. 75, no. 19, pp. 3442–3445, Nov 1995.

[162] A. Z. Ultra-i™ 123 data sheet © 2005 Rohm and Haas Electronic Materials. http://www.microresist.de/products/room_haas/pdf/ULTRA-i_123_Serie.pdf, retrieved on 18 July 2009.

[163] S120VC Compact Photodiode Power Head with Silicon Detector spec sheet, Rev A 1 October 2008, Thor Labs. http://www.thorlabs.com/Thorcat/18300/18357-S01.pdf, retrieved on 10 December 2010.

[164] Protected and UV-Enhanced Aluminum Mirrors datasheet, updated 23 March 2009 © Thorlabs. http://www.thorlabs.com/catalogpages/v20/681.pdf, retrieved on 29 December 2010.

[165] A. J. Watts, W. J. Varhue, and M. L. Gibson, "SiO_2 deposition as a byproduct of SF_6 plasma in an electron cyclotron resonance reactor," *Thin Solid Films*, vol. 220, no. 1–2, pp. 55–58, November 1992.

[166] J. Aizenberg, J. A. Rogers, K. E. Paul, and G. M. Whitesides, "Imaging profiles of light intensity in the near field: applications to phase-shift lithography," *Applied Optics*, vol. 37, no. 11, pp. 2145–2152, April 1998.

[167] J. G. Goodberlet, "Patterning 100 nm features using deep-ultraviolet contact lithography," *Applied Physics Letters*, vol. 76, no. 6, pp. 667–669, 2000.

[168] Y. Bentor, Chemical Element.com - Silver, http://www.chemicalelements.com/elements/ag.html, retrieved on 2 January 2011.

[169] Greyscale Lithography with Photoresists application note, revised 11 November 2009 © MicroChemicals GmbH. http:/www.microchemicals.eu/technical_information/greyscale_lithography.pdf, retrieved on 10 November 2010.

[170] NSC11 information and ordering webpage, © MikroMasch. http://www.spmtips.com/nsc/n11/, retrieved on 3 May 2011.

[171] AFM probe Model Tap300Al-G datasheet, © Budget Sensors. www.budgetsensors.com/downloads/Tap300Al_Datasheet.pdf, retrieved on 3 May 2011.

[172] NanoScope® III V5.31R1, © Digital Instruments 2006.

[173] L. N. Thibos, *Fourier Analysis for Beginners*. Visual Sciences Group, 2003. [Online]. Available: http://research.opt.indiana.edu/Library/FourierBook/ch08.html#H3

[174] L. A. Goodman, "On the exact variance of products," *Journal of the American Statistical Association*, vol. 55, pp. 708–713, 1960.

[175] P. Nicholls, "Christchurch quake map," http://www.christchurchquakemap.co.nz/all, retrieved on 17 May 2011.

[176] Z. Shi, V. Kochergin, and F. Wang, "193nm superlens imaging structure for 20nm lithography node," *Optics Express*, vol. 17, no. 14, pp. 11 309–11 314, July 2009.

[177] E. Betzig and J. K. Trautman, "Near-field optics: Microscopy, spectroscopy, and surface modification beyond the diffraction limit," *Science*, vol. 257, no. 5067, pp. 189–195, July 1992.